AD

TECHNICAL REPORT
67-36-ME

WIND TUNNEL TESTS AND ANALYSES FOR GROUND MOUNTED AIR-SUPPORTED STRUCTURES

by

A E Dietz, R B Proffitt
and R S Chabot

Hayes International Corporation
Birmingham, Alabama

Contract No DA19-129-AMC-129 (N)

October 1966

UNITED STATES ARMY
NATICK LABORATORIES
Natick, Massachusetts 01760

Mechanical Engineering Division

DISTRIBUTION OF THIS DOCUMENT IS UNLIMITED.

The findings in this report are not to be construed as an official Department of the Army position unless so designated by other authorized documents.

Citation of trade names in this report does not constitute an official indorsement or approval of the use of such items.

Destroy this report when no longer needed. Do not return it to the originator

Distribution of this document is unlimited. Release to CFSTI is authorized.

AD_____

TECHNICAL REPORT
67-36-ME

WIND TUNNEL TESTS AND ANALYSES FOR GROUND MOUNTED AIR-SUPPORTED STRUCTURES

by

A E Dietz, R. B. Proffitt and R S. Chabot

Hayes International Corporation
Birmingham, Alabama

Contract No DA19-129-AMC-129(N)

Project Reference 1K643303D546

October 1966

Mechanical Engineering Division
U S Army Natick Laboratories
Natick, Massachusetts 01760

FOREWORD

This manual for ground mounted air-supported single and double wall structures is prepared by Hayes International Corporation, Birmingham, Alabama. The manual presents information on wind tunnel tests conducted in support of design data and an analysis of tent fabric stresses. Configurations investigated included spherical and cylindrical single wall tents and cylindrical double wall tents with flat ends. Wind tunnel tests were conducted in the six foot stability tunnel at Virginia Polytechnic Institute, Blacksburg, Virginia. The work was conducted for the U S. Army Natick Laboratories, Natick, Massachusetts under Contract DA-19-129-AMC-129(N), during the period of July 1963 to October 1966

Mr Constantin J Monego of the Mechanical Engineering Division at the Natick Laboratories was the Army Project Engineer for this program. Mr A E Dietz was the Program Manager and Messrs. R B Proffitt and R S. Chabot were the principal investigators for the Hayes International Corporation The assistance provided by Mr. C. J Monego of the Natick Laboratories, Dr R T Keefe of the Virginia Polytechnic Institute and the personnel of the Technical Engineering Department of Hayes International Corporation are gratefully acknowledged

James H. Flanagan
Acting Chief
Mechanical Engineering Division

Approved

Dale H Sieling, Ph D.
Scientific Director

W M Mantz
Brigadier General, USA
Commanding

CONTENTS

	Page No.
LIST OF ILLUSTRATIONS	vii
SYMBOLS	x
GLOSSARY OF TERMS	xv
ABSTRACT	xvi
SECTION 1 INTRODUCTION	1
SECTION 2 GENERAL DISCUSSION	2
2.1 Background	2
2.2 General Characteristics	3
SECTION 3 WIND TUNNEL TESTS AND ANALYSIS	4
3.1 Test Facility	4
3.2 Data Corrections	4
3.2.1 Balance Corrections	4
3.2.2 Horizontal Buoyancy Corrections	5
3.2.3 Blockage Corrections	6
3.3 Test Articles	7
3.3.1 Model Configuration	7
3.3.2 Model Parameter	7
3.4 Model Installation	10
3.5 Aerodynamic Forces, Moments and Anchor Load	11
3.6 Tent Deflections and Stability	14
3.6.1 Deflection	14
3.6.2 Stability	15
3.7 Fabric Stress - Double Wall Tents	17
3.7.1 Geometry	17
3.7.2 Strength	20

CONTENTS (cont)

	PAGE NO.
3.7.3 Stability	23
3.7.4 Analysis	23
3.7.5 Conclusions	23
3.8 Fabric Stress - Single Wall Tents	25
3.8.1 Introduction	25
3.8.2 Application of Membrane Theory to Inflated Tents	25
3.8.3 Pressure Distribution Analysis	26
3.8.3.1 Truncated Spherical Shape	27
3.8.3.2 Cylindrical Shape with Spherical Ends	29
3.8.4 Membrane Stress Analysis	31
3.8.4.1 Truncated Spherical Shape	32
3.8.4.2 Cylinder with Spherical Ends	42
3.8.5 Results Truncated Spherical Shape	46
3.8.5.1 Calculations	46
3.8.5.2 Conclusions	46
3.8.6 Results - Cylindrical Shape with Spherical Ends	49
3.8.6.1 Calculations	49
3.8.6.2 Conclusions	50
3.9 Pressure Distribution	54
3.10 Data Reduction	54
3 10.1 Aerodynamic Coefficients	55
3.10.2 Pressure Coefficients	59
3.10.3 Anchor Load Coefficient	59
SECTION 4 FABRIC MATERIALS	61
4.1 Selection	61
4.2 Characteristics	62
SECTION 5 CONCLUSIONS	67
SECTION 6 RECOMMENDATIONS	69

CONTENTS (cont)

	PAGE NO.
SECTION 7 BIBLIOGRAPHY	70
SECTION 8 TABLES	73
SECTION 9 ILLUSTRATIONS	77
SUMMARY	174

LIST OF ILLUSTRATIONS

Figure		Page
1.	- Wind Tunnel Static Pressure Gradient	77
2.	- Tent Inflation Schematic	78
3.	- Pressure Instrumentation Schematic	79
4.	- Photographs of Single Wall Sphere	80
5.	- Photographs of Single Wall Cylinder - $W/\ell_h = 1/2$	81
6.	- Photographs of Single Wall Cylinder - $W/\ell_h = 1/2$	82
7.	- Photographs of Double Wall Cylinders	83
8.	- Photographs of Double Wall Cylinders	84
9.	- Boundary Layer Thickness	85
10.	- Typical Strain Gage Installation or the Ground Plane	86
11.	- Wind Axes System	87
12.	- Coordinate System for Transformation from Wind Axes to Body Axes	88
13.	- Variation of Lift Coefficient with Tent Shape - Single Wall Sphere	89
14.	- Variation of Lift Coefficient with Tent Shape - Single Wall Cylinders $W/\ell_h = 1\ 2$	90
15.	- Variation of Lift Coefficient with Tent Shape - Single Wall Cylinders $W/\ell_h = 1\ 4$	91
16.	- Variation of Lift Coefficient with Tent Shape - Double Wall Cylinders	92
17.	- Variation of Drag Coefficient with Tent Shape - Single Wall Spheres	93
18.	- Variation of Drag Coefficient with Tent Shape - Single Wall Spheres	94
19.	- Variation of Drag Coefficient with Tent Shape - Single Wall Spheres $W/\ell_h = 1{\cdot}4$	95
20.	- Variation of Drag Coefficient with Tent Shape - Double Wall Spheres	96

LIST OF ILLUSTRATIONS (cont)

Figure		Page
21.	- Variation of Moment Coefficient with Tent Shape - Single Wall Spheres	97
22.	- Variation of Moment Coefficient with Tent Shape - Single Wall Cylinders, $W/\ell_h = 1{\cdot}2$	98
23.	- Variation of Moment Coefficient with Tent Shape - Single Wall Cylinders, $W/\ell_h = 1{\cdot}4$	99
24.	- Variation of Moment Coefficient with Tent Shape - Double Wall Cylinders	100
25.	- Variation of Anchor Load Coefficient with Tent Shape - Single Wall Spheres and Cylinders	101
26.	- Variation of Anchor Load Coefficient with Tent Shape - Double Wall Cylinders	102
27.	- Variation of Guy Line Coefficients with Tent Shape	103
28.	- Tent Deflection Notation	104
29.	- Variation of Tent Deflection with Cell Pressure	105
30.	- Variation of Tent Deflection with Enclosure Pressure	106
31.	- Effect of Cell Size on Tent Deflection	107
32.	- Cell Size and Cell Number Relationship	108
33. - 41	- Variation of Meridional Stress Resultant with Impact Pressure	109
42.	- Variation of Web Stress with Impact Pressure	118
43.	- Variation of Hoop Stress with Cell Radius	119
44.	- Relationship between Cell Shape to Volume to Weight Ratio	120
45.	- Relative Sizes of Tent Cells	121
46.	- Forces on Tent Cell	22
47. - 49.	- Typical Stress Coefficients for Single Wall Spheres	122
50. - 52.	- Peak Stress Coefficients for Single Wall Spheres	125
53. - 55.	- Variation of Peak Stress Coefficient with Shape	128
56. - 59.	- Variation of Stress Ratio with Apex Angle	131

LIST OF ILLUSTRATIONS (cont)

Figure		Page
60.	- Variation of Stress Factor with Tent Height to Diameter Ratio	135
61. - 63.	- Typical Calculated Stress Coefficients - Model No. 8 - Spherical Ends.	136
64. - 66.	- Array of Calculated Stress Coefficients - All Tests - Model No. 8	139
67. - 68.	- Typical Annular - Longitudinal Stress Coefficient Distribution	142
69. - 70.	- Typical Maximum Peripheral Stress Coefficient Distribution	144
71. - 73.	- Maximum Design Stress Coefficient - Specific Dynamic Pressure	146
74. - 82.	- Maximum Design Stress Coefficients vs Tent Width to Length Ratio	149
83.	- Pressure Tap Locations, Model No. 1	158
84.	- Pressure Tap Locations, Model No. 17	159
85.	- Base Pressure Tap Locations, Model No. 19	160
86.	- Strain Gage Locations for Model No. 1	161
87.	- Strain Gage Locations for Model No. 17	162
88.	- Tenacity vs Elongation Diagram of Fiber	163
89.	- Load - Elongation Diagram of Fiber and Plain Weave Fabric - Polyester	164
90.	- Load - Elongation Diagram of Fiber and Plain Weave Fabric - Nylon	165
91.	- Weight of Coating for Single and Two Ply Coated Fabric	166
92.	- Typical Pressure Distribution as a Spherical Shell	167
93.	- Coordinate System and Membrane Stresses for a Spherical Shell	168
94.	- Coordinate System and Membrane Stresses for a Cylindrical Shell	169
95. - 97.	- Maximum Tent Deflection for Single Wall Tents	170
98.	- Maximum Tent Deflection for Double Wall Tents	173

SYMBOLS

A_o - Orifice area

A_c - Cross sectional area

A_s - Surface area

A_p - Planform Area

A_f - Floor area

A_e - Cell enclosed cross sectional area

AL - Anchor load

C_{AL} - Anchor load coefficient, single wall

C_{BL} - Base anchor load coefficient, double-wall

C_c - Coefficient of contraction

C_D - Drag coefficient

C_{GL} - Guy line coefficient

C_L - Lift coefficient

C_M - Pitching moment coefficient

C_N - Yawing moment coefficient

C_R - Rolling moment coefficient

C_Y - Side force coefficient

C_o - Orifice coefficient (0.65)

D - Drag

D_B - Data correction due to horizontal buoyancy

d - Reference length - Tent diameter

E - Modulus of elasticity

F - Force

f_b - Bending load

h - Tent height

h_r - Distance from ground plane to center of curvature

I - Moment of inertia about centroidal axis

K - Tent model shape factor

k_p - Impact pressure correction factor

L - Lift

L_B - Lift along body axis

ℓ_h - Length of tent

ℓ_m - Reference length for computing yawing moment coefficient

ℓ_r - Reference length for computing pitching moment coefficient

M - Moment

M_b - Initial buckling moment

M_c - Ultimate collapse moment

M_m - Yawing moment

M_y - Rolling moment

N_ϕ - Meridional stress resultant

$\overline{N}_\phi$ - Total meridional stress resultant

N_θ - Circumferential stress resultant

$\overline{N}_\theta$ - Total circumferential stress resultant

$N_{\phi\theta}$ - Shear stress resultant

N_{xe} - Stress resultant due to internal pressure

N_x - Longitudinal stress resultant

$N_{\theta x}$	-	Shear stress resultant
n	-	Number of cells in a tent
P	-	Static pressure
P_c	-	Cell Pressure
P_e	-	Tent enclosure pressure
P_{ext}	-	External pressure
$P_{(\phi, \theta)}$	-	Radial load
P_A	-	Axial load
P_r	-	External loading
P_T	-	Axial load + Pressure load
P_t	-	Stagnation pressure
P_y	-	Side force
P_{yB}	-	Side force in body coordinate system
q	-	Dynamic (impact) pressure
Q	-	Volume flow
r	-	Tent radius
r_o	-	Outside tent radius
r_i	-	Inside tent radius
r_c	-	Cell radius
R	-	Universal gas constant,
R_N	-	Reynolds number, dimensionless
S_ϕ	-	Arc length in ϕ direction
S_α	-	Arc length in α direction
S_β	-	Arc length in β direction

N_w - Web stress resultant

N_h - Hoop stress resultant

T - Absolute temperature

U - Velocity

$\overline{V}$ - Tent enclosed volume

V - Shear load

V_c - Cell volume

W - Tent width

w - Cell width

m - Distance from neutral axis

x,y,z - Cartesian coordinates

GREEK SYMBOLS

α_c - Cell reference angle

α - Tent reference angle

β - Tent reference angle

δ_F - Tent deflection - front

δ_H - Tent deflection, top

δ_B - Tent deflection, rear

ϵ_{SB} - Correction factor for solid blocking of wind tunnel due to presence of model

γ - Ratio of tent volume to tent weight

μ - Viscosity of air

θ - Curvelinear coordinate

ψ - Tent yaw angle

ρ - Density of air

ζ - Additional correction factor for wake gradients

ν - Poisson's ratio

λ - Tent geometry reference angle

ϕ - Curvelinear coordinate

Ω - Fabric weight/unit area

χ - Unit vector

ξ - Unit vector

Υ - Unit vector

ϵ_θ - Meridional strain

GLOSSARY OF TERMS

Reynold's Number - A dimensionless parametric ratio of th inertia forces and the viscous forces acting on a body immersed in a moving fluid. The mathematical expression for Reynold's Number is

$$R_N = \frac{\rho U l}{\mu}$$

Critical Reynold's Number - The Reynold's Number at which the boundary layer upstream of a point of separation changes from laminar to turbulent flow. The critical Reynold's Number for both spheres and cylinder is approximately 500,000.

Dynamic Pressure - Also referred to as impact pressure or velocity pressure and is that portion of the stagnation pressure which results from the motion of the fluid. The mathematical expression for dynamic pressure is

$$q = \frac{1}{2} \rho U^2$$

Potential Flow - A theoretical treatment of fluid flow which assumes the fluid to be inviscid. Consequently, a body in motion with potential flow has a symmetrical pressure distribution which results in zero drag forces.

Horizontal Bouyancy - The general tendency for the model in a closed jet wind tunnel to be "drawn" downstream due to the longitudinal static pressure gradient that exists in the test section.

Solid Blocking - The increase in air velocity due to the presence of a model in a wind tunnel test section caused by the reduction in the area through which the air is allowed to flow.

Planform Area - Maximum projected area in horizontal plane.

In. w g - Gage pressure expressed in inches of water

ABSTRACT

The objective of this program is to provide tentage information based on wind tunnel test data that can be applied either to the evaluation and and improvement of existing ground mounted air-supported tents or to the design of such future structures.

The program consisted of study, test and analytical investigation phases from July 1963 to October 1966. During the study phase, a review was made on pertinent literature on experimental techniques, data and analyses applicable to determining maximum aerodynamic force on and stresses in fabric structures. The wind tunnel investigations consisted of detailed testing of twenty-six tent models to include sixteen single wall tents (ten with non-porous and six with porous fabrics) and ten double-wall tents. Tests were conducted at stabilized wind speeds up to 105 miles per hour in the Virginia Polytechnic Institute's 6' x 6' stability tunnel. In the analytical phase, test data were used to develop fabric stress and aerodynamic coefficient data variation with tent parameters.

Results of the wind tunnel investigations and stress analyses have been incorporated and includes comprehensive, practical design data suitable for engineering reliable, stable, single and double-wall air-supported tents. Data, in general, are presented in non-dimensional coefficient form, and therefore, are applicable to full scale tents within the range of the parameters investigated. Design information is presented as charts and tables on tent aerodynamic force and moment coefficients, anchor and guy line coefficients, structural deflection, material stresses and packaged volume, and weight.

SECTION I

INTRODUCTION

In March 1956, a revised addition of the Design Manual for Spherical Air Supported Radomes was published by Cornell Aeronautical Laboratory Since its publication, air supported structures of other than spherical shapes have been adopted by the Army. Design and fabrication of these tents have generally been limited to the semi-empirical methods outlined in the revised Design Manual for Spherical Air Supported Tents and data estimated to cover other basic configurations

In order to assist the tentage engineer to more accurately define the criteria for design of air supported structures, the U S Army Natick Laboratories contracted with Hayes International Corporation to formulate practical design criteria for single and double-wall air supported structures The program included a comprehensive analytical study and model wind tunnel tests resulting in a Design Manual for ground mounted air supported tents A more rigorous solution to the analytical determination of fabric stresses is included in this investigation which, combined with the latest materials and accessory equipment information furnished by the Army, has produced more precise tentage design criteria than has heretofore been available to the Army designer

The Design Manual has been prepared in two parts for the convenience of the user. Wind Tunnel Tests contains a detailed description of the wind tunnel test investigations and data reduction techniques, together with a comprehensive analytical determination of maximum fabric stresses through use of measured tent pressure distributions Design Manual for Ground Mounted Air-Supported Tents (Single and Double Wall) presents the results of the tests and analyses of Part I in a concise form of design tables and curves for both single and double-wall tents and sample problems illustrating the use of the data.

SECTION 2

GENERAL DISCUSSION

2.1 BACKGROUND

The art of tent making is hundreds of years old. For centuries, through trial and error, man has constructed effective shelters for habitation and housing of equipment. The evolution of this art has covered myriad configurations, but only recently has a way been found to eliminate the cumbersome weight of the supports through the use of inflation techniques. The forerunner of air supported tents dates back to early World War II days when an external enclosure over a radar antenna was found desirable. This use was motivated by the necessity for protection of the radar installation from high winds. These early installations were small in size and the material used ranged from single sheets of molded plexiglas or plywood to multiple layers of sandwich-type construction. The first reported use of a resin-impregnated glass fabric as a radome material stemmed from an attempt to reduce the moisture absorption properties of plywood on the earlier models through the application of a thin protective overlay on the external surface of the radome.

Larger radomes were dictated for use on later World War II radar installations. The advent of radomes ranging in diameter from 35 to 55 feet arose from the necessity to extend the United States Air Defense after World War II to include radar detection systems located in arctic zones of operation. Operational radars of that time were designed to withstand only the wind loads and weather conditions encountered in temperate zones. Wind conditions in the Arctic were known to impose greater loads upon an antenna system, and upon its pedestal than those for which the structure was designed. Therefore, it was decided to utilize radomes for environmental protection. Up until this time the large radomes had been used an as expedient alternative to modification and strengthening of existing radar antenna structures. With the advent of arctic usage, the intrinsic merits of the light weight radome soon became obvious; i.e. environmental protection, reduction in power required to rotate large antenna systems in high winds and reduction in size and weight of structural members at the cost of a small degradation in system performance due to the presence of the radome.

Modern scientific and technological developments made in military equipment and in support of a mobile army have resulted in the need for new type tentage. The need for new tentage varies from highly specialized items for the missile program to large maintenance tents for ground vehicles and aircraft.

The use of air supported tents, other than radomes, represents one approach taken by the Army to provide shelters of reduced weight, cost and cubage which can be easily transported, erected and struck for more mobile army operations. With the development of these air supported shelters the technology of tent making is developing step by step from a traditional craft to a branch of scientific engineering.

Cornell Aeronautical Laboratories and Massachusetts Institute of Technology have performed several scale tests on radome and missile shelter models. Cornell has produced a Radome Design Manual for spherical radomes based on these tests. Design and fabrication of other than spherical tents has been accomplished largely by extrapolation of the design data contained in the Radome Design Manual and the individual designers personal "feel" for the problem. A wind tunnel program was initiated to investigate a wide variety of models both spherical and cylindrical single and double wall. The data obtained from these tests have been reduced and put in parametric form to facilitate future tent design.

2.2 GENERAL CHARACTERISTICS

Air supported tents present the modern mobile army with many advantages over rigid structures. Some of the more important advantages are listed below

RF Transmissibility - The air supported tent, as used to house radar antenna, due to its thin walled construction, very nearly approaches the ideal shelter, i.e. a thin walled homogeneous sphere. For this reason the same radome can be used for several radar systems of different frequencies.

Lightweight, Low Bulk and Cubage - The inherent characteristics of an air supported structure provides a high structural efficiency, which results in very low package weight. Use of thin flexible material for the envelope permits the entire unit to be folded into a small package which facilitates shipment and storage.

Ease of Handling and Logistic Support - Due to its low weight and compactness, the air supported structure is one of the most portable of all presently available shelters. The durability of the material used for the envelope minimized logistic requirements and maintenance. Standardization of the basic tent sizes reduces the inventory requirement and makes the air supported structure adaptable to nearly all shelter requirements.

SECTION 3

WIND TUNNEL TESTS AND ANALYSIS

3.1 TEST FACILITY

A series of wind tunnel tests was conducted in the Virginia Polytechnic Institute's 6 foot by 6 foot Stability Wind Tunnel under the direction of the Hayes International Corporation. The VPI 6 by 6 tunnel was designed and originally constructed at the Langley Aeronautical Laboratory of the National Aeronautics and Space Administration. The facility is classified as a continuous, closed jet, single return, subsonic wind tunnel with interchangeable round and square test sections. The tunnel is powered by a 600 hp d. c. motor driving a 14 foot propeller. Due to the presence of seven stainless steel turbulence screens in the settling chamber, the tunnel is capable of operating at a turbulence factor as low as 1.08. (Effects of turbulence in the air flow are seen as an increase in test Reynolds number as compared to a similar test in free air.

The tunnel is equipped with a six component automatic null balancing mechanical system for measuring forces and moments associated with models mounted through the floor or sidewall of the tunnel during static model tests. The output from this balance is fed into a readout printing system which allows the operator to read the six outputs as printed tabulation.

3.2 DATA CORRECTIONS

3.2.1 Balance Corrections

The results of the overall calibration of the wind tunnel installation at VPI indicated that there were several manufacturing and installation errors present in the machanical linkage of the balance system. These errors were evaluated as interaction corrections and were applied to the various balance readings as shown on the following page to give the true aerodynamic force and moment values.

Factor x Balance Readings	= True Readings
1.000 Lift Reading	= Lift
0.996 Drag Reading	= Drag
0.996 S. F. Reading + 0.004 Drag Reading	= Side Force

0.958 R.M. Reading + 0.015 Lift Reading + 0.054 S.F. Reading = Rolling Moment

0.953 P.M. Reading - 0.010 Lift Reading + 0.028 Drag Reading = 0.019 R.M. Reading = Pitching Moment

0.939 Y.M. Reading - 0.018 (Drag Reading - S.F. Reading) = Yawing Moment

These equations are presented in order to show that for the test runs where one or more of the balance units were inoperative, the other readings were not appreciably affected.

3.2.2 Horizontal Buoyancy Correction

The models tested were scaled only to the extent that the largest model permissible in the test section for each configuration considered was used.

The conditions imposed on the tent models tested in a wind tunnel are not the same as those found on full scale tents in free air. This test program had the models mounted to a fixed ground plane with the air moving past the model. The longitudinal static pressure gradient usually present in the test section produces extraneous forces that were corrected

Nearly all wind tunnels with closed test sections have a static pressure variation along the axis of the test section due to the thickening of the boundary layer as it progresses toward the exit cone. This pressure gradient is usually negative and hence there is a tendency for the model to be "drawn" downstream. This tendency of the model to be "drawn" downstream is known as "horizontal buoyancy" and is usually insignificant for wings and other relatively thin objects but may be of a significant value for more blunt objects. In this test program several pressure taps were installed along the tunnel walls adjacent to the model. For this special case, the longitudinal pressure gradient was a straight line and the equation for this correction becomes

$$D_B = \Sigma S_x \quad (dp/dl)\, dl$$

where S_x is the model cross section area at station x, l is the distance from the model nose and dp/dl is the slope of the longitudinal static pressure curve. Since the summation of the model area times the incremental distances $\Sigma S_x dl$, is the body volume, this equation reduces to·

$$D_B = - (dp/dl)\ (\text{Body Volume})$$

Figure 1 presents the longitudinal static pressure gradient for a representative model tested in the VPI 6 foot by 6 foot tunnel. Taking the slope of this curve and using the volume of a representative test model, it was found that D_B should be approximately 3.6 pounds.

3.2.3 Blockage Correction

The other correction required to be made on the test data is due to the presence of a model in the test section which effectively reduces the area through which the air must flow, and hence in accordance with Bernoulli's law increases the velocity of the air as it flows over the model. This increase of velocity in the vicinity of the model affects the dynamic pressure, Reynolds number, pitching moment coefficient, lift coefficient and drag coefficient. A simple form of this blockage correction is

$$\epsilon_{SB} = \frac{K\,(\text{model volume})}{S_c^{\;3/2}}$$

where K = 0.96 for a body of revolution and S_c is the wind tunnel section area. Again using the same representative test model as was used for the "horizontal buoyancy" correction it was determined that a representative value of ϵ_{SB} would be approximately 0.012.

The equations to be used for correction of the wall effects encountered in this program are summed below. The data with subscript "u" are uncorrected data based on free stream dynamic pressure, with the exception of drag which must have the buoyancy correction applied before final correction due to "solid blockage".

$$U = U_u\,(1 + \epsilon_{SB})$$

$$q = q_u\,(1 + 2\epsilon_{SB})$$

$$R_N = R_{N_u}\,(1 + \epsilon_{SB})$$

$$C_L = C_{L_u}\,(1 - \sigma - 2\epsilon_{SB})$$

$$C_M = C_{M_u}\,(1 - 2\epsilon_{SB}) + \frac{\sigma\, C_L}{4}$$

$$C_D = C_{D_u}\,(1 - 3\epsilon_{SB})$$

where $\sigma = \frac{\pi^2}{48}\left(\frac{d}{h}\right)^2$ is a model wake correction and "d" is the diameter of the model used.

3.3 TEST ARTICLES

3.3.1 Model Configurations

A series of 26 air-inflatable, single and double wall tents of various shapes were tested. The fabric used in the construction of the models was the lightest fabric available and corresponded to approximately 1/10 existing full scale values, while model scales varied from approximately 1/20th to 1/40th full size.

Internal pressure was maintained within the models for support. A remote air supply, regulated in the tunnel control room, was used to provide these pressures within the cells and enclosure (see Figure 2 & 3) The enclosure pressure, P_e, for single wall models was varied from 4/5 q to 5/4 q. Cell pressure, P_c, for the double wall models was varied from 5" to 30" $H_2 0$. Free stream total and static pressures were measured and referenced to cell and enclosure pressures as shown in Figure 3. Enclosure pressure for the double wall models was maintained at free stream static values.

Single wall models tested ranged in shape from spherical to cylindrical with spherical ends, with width to length ratios of 1 2, 1 3 and 1 4. The height to diameter ratios varied from 3/8 to 7/8. Envelope material varied in porosity from 0 to 15 cu. ft. /min. /ft.^{2}. Ten of the 16 single wall models were made of non-porous material.

Double wall models tested were all cylindrically shaped. Height to diameter ratios varied from 3/8 to 3/4 for the cylindrical models and width to length ratios varied from 1 1 to 1 4.

Table I summarizes all model configurations. Photographs of typical models are shown in Figures 4 thru 8.

3.3.2 Model Parameters

In the design of wind tunnel test models it is of paramount importance to insure that all principle non-dimensional parameters are scaled relative to one another in the model as they are found in the full scale tents. Wind tunnel models are also generally made to as large a scale as the test section of the tunnel will allow without inducing adverse tunnel blockage. In selecting the model designs for this program it was agreed that since the size of the full scale tent is variable, each model configuration should be designed to the tunnel blockage factor and made as large as possible without regard to scale. To accomplish this prior to the design of the ground plane, an arbitrary figure of one square foot was assumed for the projected frontal area

of the ground plane. Assuming a tunnel blockage factor of 10 percent, as recommended by Virginia Polytechnic Institute, and knowing the assumed ground plane frontal area, each model was designed to have maximum projected frontal area of 374 square inches. Using this frontal area, model dimensions for the various test configurations were computed and are presented in Table I.

The exact dimensions of all existing and proposed full scale tents being unknown, the models were designed allowing engineering judgement and experience to relax the requirements for some parameters known or felt to be unimportant and provide a wide variey of tent shapes of interest to the Army for present and future application.

The design of a flexible model for wind tunnel testing is considerably more complicated than a normal rigid model, whose shape essentially does not change. To obtain aerodynamic and dynamic similarity the following parameters had to be kept the same for scale as for the full size models.

Geometric Shape - For no wind conditions
Inflation Parameter - Ratio of inflation pressure to free system dynamic pressure
Reynold's Number - Ratio of inertia forces to viscous forces
Mach Number - Ratio of inertia forces to elastic forces
Froude Number - Ratio of inertia forces to gravity forces
Aeroelastic Parameter - Ratio of model diameter, fabric elongation and dynamic pressure to fabric stress
Dynamic Parameter - Ratio of model mass to air density and model diameter cubed

A model under conditions such that it has the same Reynolds and Mach numbers as its full scale counterpart will have forces and moments on it that can be directly scaled and flow patterns that are exactly the same. If the body in question is reacting to gravity, the model should also be maintained at the same Froude number as its full scale counterpart.

The inflation parameter is of importance because it governs tent stability. This parameter was investigated wherever possible to determine the limits of tent stability. The dynamic parameter was allowed to vary with model sizing as the fabric used was the lightest fabric available of sufficient strength to construct the models and the model size was dictated by the maximum allowable for the test section used. Based on the limited observations of the effects of this parameter during these tests, it is recommended that the inflation parameter be maintained at a minimum of 1.0.

The aeroelastic parameter is important in matching the model de-

flections with those of the full scale tents Based on the fabric stress data computer from the pressure distributions, this parameter can be compared. However, no attempt was made to do so because of the overriding considerations of fabric weight and model sizing as cited above. However, since the bending stiffness of the model fabric is negligible, deflections noted in the models are considered similar to those of full scale tents.

The Mach number parameter was irrelevant because of the low velocities used for this test series. Based on past experience, below a Mach number of 0 25, the elastic forces of air are at a minimum and can be neglected

Therefore, the similarity parameters considered to be of major importance were the inflation parameter and Reynolds number.

The values selected for the inflation parameter were 4/5 q, 1 0 q and 5/4 q. In some cases, an estimate was made as to the value of P_e/q that was required to stabilize the tent. It was found that this determination was an individual estimate and therefore only the more severe cases of tent instability were evaluated The single wall non-porous tents were tested at all three values of the inflation parameter. The single wall, porous tents were, in general, tested only at a value of 1.0 q. The double wall tents were tested at values of P_c/q equal to 3q, 4q, and 5q

The Reynolds number parameter determines the flow pattern as it is influenced by viscous effects As major variation in flow usually occurs below certain critical values of this parameter, it was desirable to test scaled models above this critical value in order to provide more accurate extrapolation of test data to full scale. At the lower test velocity of 35 mph, several models fall below this critical value of Reynolds number, hence the test data does not lend itself to extrapolation as readily as the data obtained from the other models. These conditions were adjusted to bring model Reynolds number above the critical value and thereby enable the data from all models to be scaled to full size tents The Reynold's number for these tents was based on the model diameter. Based on that reference length, past experience and aerodynamic theory predict the critical value of Reynold's number to be between 4 0 and 5 0 x 10^5 The critical Reynold's number establishes the lower values of test conditions in that major variation of flow occur below the test conditions specified by the critical Reynold's number Test data below the critical Reynold's number has little or no potential for extrapolation to full scale tents and therefore was eliminated from consideration in the design curves presented in Part 2.

The model fabric chosen was the finest gage possible considering fabric flexibility requirements and fabrication. The fabric chosen may be scaled to full size and is representative of those tents in service today. Fabric porosity was also varied in the construction of the tents to provide data of the influence of porosity on aerodynamic flow characteristics over the tent.

3.4 MODEL INSTALLATION

It was determined that more reliable data would be obtained by mounting the tent models on a ground plane suspended between the walls of the tunnel rather than by mounting them directly on the floor of the tunnel.

The optimum size of the ground plane for this particular tunnel is three times that of the longest model to be tested. The dimensions of the ground plane are, therefore, 72 inches wide by 195 inches long. The models, turntable etc., are mounted in the center of the ground plane within a 70 inch diameter circle. The boundary layer bleed flap was sized and located on the basis of the calculated boundary layer along the ground plane.

In order to better simulate the full scale tents, provision was made to enable the test conductor to exercise a limited amount of control, through adjustment of a bleed flap, over the boundary layer thickness in front of the model. To determine the desired setting for the bleed flap that best simulated actual conditions over the ground, a boundary layer survey was made. This survey investigated dynamic pressures at heights varying from the ground plane surface to approximately two inches above the surface for varying bleed flap settings.

These dynamic pressures were plotted versus the height above the surface. The height at which the dynamic pressure recovers to 90 percent of the free stream is defined to be the upper limit of the boundary layer. The results of this survey are presented in Figure 9. The curve corresponding to slot openings of 1.0" and 1.5" was chosen for subsequent use as it was felt that this produced a flow profile which more closely approximated actual free air conditions. Therefore, the data from these tests are restricted to ground mounted structures only.

The bases of the models were attached to the ground plane by means of cantilevered anchor springs fabricated from 17-4 PH steel heat treated to the TH1050 condition. Figure 10 shows typical strain gage installations at the anchor point and guy line positions. These anchors were spaced about the periphery of each model as shown in Figures 86 and 87. Double wall models were secured by guy wires in addition to the anchor springs.

The mounting plate loads were measured on the earlier tents by removing the tent and model base, covering the turn table and measuring the loads as the tunnel speed was varied through the test range. On the later models a dummy tent was constructed of plywood and fiberboard and suspended above the model base. Both methods were used at all test yaw angles and gave equally reliable results.

3.5 AERODYNAMIC FORCES, MOMENTS AND ANCHOR LOADS

The aerodynamic forces and moments were recorded in pounds and foot-pounds respectively in the wind axis system. The wind axis system has three orthogonal axes, one oriented in the direction of the wind with drag positive in the downstream direction, another oriented in the vertical direction with lift positive in the upward direction, and a third oriented in the lateral direction normal to the former two with side force positive to the right when looking upstream. See Figure 11. These axes are fixed in the wind tunnel and do not vary with yaw angle. The sign convention for yaw angle measurement is also included in Figure 11.

The anchor load data were recorded on an SR-4 Strain Scanner and Recording Unit. The deflections measured by this unit were then transferred to computer load sheets for automatic data reduction. The reduced data were presented as individual anchor load and anchor load coefficient and total anchor load corrected for both inflation pressure and the ratio of total number of tent anchors to the number of instrumented anchors used.

The aerodynamic force and anchor load data were reduced to dimensionless coefficient form by dividing the force in pounds by the product of dynamic pressure times the reference area. The aerodynamic moment data were similarly reduced to coefficient form by dividing by the product of dynamic pressure times the reference area times a reference length. These coefficients are defined as follows

Coefficient	Equation
Lift	$C_L = L/qS$
Drag	$C_D = D/qS$
Sideforce	$C_Y = Y/qS$
Pitching Moment	$C_M = M/qS_m$

Coefficient	Equation
Rolling Moment	$C_R = R/qS_t$
Yawing Moment	$C_N = Y/qs$
Anchor Load	$C_{AL} =$ Anchor load/qS

Corrections for tunnel bolckage were applied to the data in coefficient form

The static pressure distribution data was reduced to coefficient form in accordance with the following equation

$$C_P = \frac{P_\ell - P_\infty}{q_\infty}$$

where

P_ℓ = Local static pressure (at tent surface)

P_∞ = Free stream static pressure

q_∞ = Free stream dynamic pressure

The maximum values of the aerodynamic and anchor load coefficients computed were determined and plotted as functions of tent height to tent diameter and the tent width to length ratio

Twenty-six single and double wall tents were tested to 105 miles per hour. It should be noted that the single wall cylindrical shapes tested differed from the double wall shapes in that the ends were spherical for single wall and flat for double wall The aerodynamic force data are discussed below

Lift

From the lift coefficient, defined as $C_L = L/qS$, it can be seen in Figure 13 that C_L increases almost linearly with the ratio of height to diameter for single wall spheres. Fabric porosity of 10 - 15 cu. ft /min. sq. ft resulted in the minimum C_L for this shape.

Cylindrical single wall tents exhibit a minimum lift coefficient at a height to diameter ratio of 0. 5, as shown in Figures 14 and 15. However, a width to length ratio of 1 2 results in a more moderate C_L at $h/d < 0.5$ than the W/ℓ_h of 1 4. The reverse is true in the case of $h/d > 0.5$.

Double wall, cylindrical shapes show a moderate decrease in lift coefficient as h/d increases, as can be seen from Figure 16 Width to length ratios of 1 4 resulted in a considerably higher C_L than that of 1 2.

Drag

Single wall, spherical shapes show an increase in drag coefficient with increasing h/d as presented in Figure 17. Slight fabric porosity 0-5 cu. ft / min. sq. ft., reduces C_D moderately whereas a further increase in the porosity increases C_D back to non porous values.

Single wall cylindrical shapes of 1 2 width to length ratios (Figure 18), indicate a moderate increase in C_D with increasing h/d but have C_D's considerably lower than shapes of W/ℓ_h = 1 4 at lower h/d values. (Fig 19) Increasing fabric porosity increases the C_D for cylindrical shapes.

Double wall shapes with an h/d less than 0. 5 exhibited lower drag coefficients than did the single wall shapes (Figure 20). However an increase in h/d above 0. 5 resulted in much higher C_D's for the double wall shapes. Variation in width to length ratio caused a moderate increase in C_D with an increase in W/ℓ_h.

In summary, it appears that spherical shapes exhibit lowest drag coefficient with h/d An increase in W/ℓ_h or h/d results in an increase in drag coefficient for cylindrical models.

Moments

Moment coefficients for single wall spherical tents were quite low at low h/d values, and increased to a fairly constant value at h/d> 0. 5. Increasing porosity to 0-5 resulted in the lowest values of C_M while a further increase in porosity increased C_M to near the non-porous values. (See Figure 21).

Single wall cylindrical shapes show a slight increase in C_M with increasing h/d values. Increasing w/1 ratios raise C_M values markedly Fabric porosity values of 0-5 and 10-15 reduced the C_M considerable in W/ℓ_h ratios of 1 2 and cause a moderate decrease in C_M at W/ℓ_h ratios of 1 4 (See Figures 22 and 23

Double wall shapes reflected a moderate, linear increase in C_M with increasing h/d ratios, (See Figure 24). The moment coefficients decreased slightly with a change in W/ℓ_h ratio from 1 1 to 1 2, but showed a marked decrease with a W/ℓ_h ratio of 1 4.

Anchor Loads

Anchor loads of a fabric shelter are the result of aerodynamic forces acting on the tent external surface and the enclosure pressure within the body. The anchor load coefficient is defined as $C_{AL} = F/qS_t$. These are plotted in figures 25 and 26.

A guy line coefficient, defined as C_{GL} = guy line load/qS_t, is used to determine vertical loads on the guy lines for double wall models. These are plotted in figure 27 . These coefficients represent maximum aerodynamic loading with inflation pressure effects eliminated. Enclosure pressure is another variable which further influences anchor loads and must be considered jointly when determining total anchor loading.

3.6 TENT DEFLECTION AND STABILITY

3.6.1 Tent Deflections

Tent deflection due to wind load was measured through use of a (fixed-position still) camera Film negatives of no-wind and test-wind conditions having the same enclosure (and cell) pressures were superimposed to provide accurate deflection measurement. Data were measured using a background grid and recorded for deflection areas at the front, top and rear of each tent using the symbols and sign conventions of figure 28. Corrections were made to the measured data for camera position relative to tent and grid locations. Maximum deflection data were then plotted as a ratio of tent deflection to tent radius, δ/r, versus the ratio of tent height to tent diameter, h/d, for all twenty-six models.

The effect of porous fabric on reducing single wall tent deflection was investigated, however, only non-porous fabric was used in the construction of the double wall tents. Also, the independent effects of cell size, cell pressure and enclosure pressure on test deflection for the 3/4 cylindrical, double wall tent with 1 1 width to length ratio were determined. Table II shows relative cell sizes for these double wall tents. The deflection data curves are presented in Figures 29, 30, 31, 95, 96, 97 and 98

A more comprehensive number of tent shapes and sizes of the single wall non-porous variety were tested, hence, it is felt that these data are more conclusive. In the case of double wall tents, the curves appear as a straight line connecting two data points. Additional double wall configuration tents are required to better define curve variation, however, due to the general concave curve shape for single wall tents it is believed the double wall data is conservative in the h/d range of 0.5 - 0.6, but less conservative at higher ratios

With respect to deflections, the following general conclusion may be made· Tents with low-porosity fabric, 0-5 cu. ft. /min. /sq. ft. @ 6" w. g. pressure, showed measurable reductions in deflections. Tents with a h/d of approximately 0. 5 have the smallest deflections. Spherical single wall tents have smaller overall deflections than the cylindrical tents. For the double wall tents, an increase in cell size, cell pressure and enclosure pressure provide greater tent rigidity and result in less tent deflection. Also a double wall tent guy line configuration with lines attached at 0. 80 and 0. 40 tent height, with angled corner guy lines, produced smallest deflections.

3. 6. 2 Stability

As part of the test program, tent stability was qualitatively investigated by defining instability as any set of conditions producing tent deflection and vibration which, when coupled together provided objectionable tent motion. Degree of motion determined visually during testing and from motion picture reruns of tests. The effects of changes of fabric porosity, enclosure pressure, cell size and pressure and guy line location were evaluated where applicable. The following general conclusions may be made relative to tent stability.

The single wall tent configurations, with the exception of the 7/8 sphere and all 1 4 width to length ratio cylindrical tents were found to be very stable. For these tents, motion is more pronounced with a wind at 45 degrees attitude. Other spherical and the 1 2 width to length ratio cylindrical configurations exhibited very stable properties at all test conditions.

The double wall tents had flat ends which contributed to flow separation and lesser stability than the single wall tents with spherical ends. The 3/4 cylindrical, 1 1 width to length tents were not 'true' cylindrical tents but, rather, had flat sides which may have contributed to this configuration's lower stability.

When some deflection and vibration is acceptable, the tent shapes tested withstood hurricane force winds without the use of guy lines. Double wall tent anchor loads were not measured for the no-guy line condition.

To minimize double wall tent corner deflection and motion, which occurs primarily when the tent is oriented 45 degrees to the wind (corner into the wind), guy lines angle 45 degrees to the tent side should be attached to each corner of the tent at a point 0. 8 tent height and make an angle of approximately 45 degrees with the ground. Corner and end deflections were more pronounced on the double wall tents, believed aggravated by the flat ends, and no complete elimination of corner deflection at the 45 degree attitude was found.

The best guy line configuration consists of a combination high (0.8 tent height) and low (0.4 tent height) line arrangement, with the upper guy lines angled 45 degrees to the tent side and the lower guy lines perpendicular to the tent side when viewed from the top of the tent.

Cell pressure (enclosure pressure for single wall tents) is an important factor in controlling tent motion. Although permissible tent deflection, as required by tent usage, could establish pressure requirements, tests indicated that only for cell pressures equal to or in-excess-of the tent dynamic pressure did both good stability and deflection characteristics exist From a stability standpoint at 105 miles per hour, no significant gains were achieved beyond an inflation pressure of 16 inches water gage. Also only small deflection reductions occurred for higher pressures up to 30 inches water gage.

Tent cell size was also observed to be a factor in providing better tent stability since an increase in cell size was more rigid for the same cell inflation pressure. A prime consideration in increasing cell size, is that, for the same enclosure volume the tent overall size and weight increase rapidly

Single wall tents with low fabric porosity (0-5 cu ft./min./sq ft @ 6" w.g.) exhibited lower deflections, in general, than non-porous tents and possessed equal or better stability characteristics

Double wall tent enclosure pressure should be maintained at ambient or low positive pressure to preclude cell buckling. Test with enclosure pressure less than ambient exhibited a critical buckling tendency on the windward (forward) side of the tent.

3.7 DOUBLE WALL TENTS

In the design of a double wall tent, weight and enclosed volume are of prime importance. For this reason, weight to volume ratio is theoretically optimized in the following study. Results of the study provide relationship between number of cells and cell sizing (see figure 44). Over-all tent dimensions are dictated by functional requirements. Continued effort is necessary for true optimization of weight to volume and strength.

Study of strength requirements is summarized in paragraph 3.7 2 and insludes stress theory which is utilized in analysis of models tested. The results of stress analyses of tents subjected to wind tunnel airloads are presented in curve form on figures 33 thru 43.

It is anticipated that a more general approach to double wall tent design will be included in a later revision. The revised approach should provide for cell sizing and weight optimization such as indicated by application of Figure 44 and should also facilitate sizing and analyses of cylindrical double wall tents of variable geometries within the proportions tested.

3.7 1 Geometry Study

To effect a least weight analysis, it is necessary to derive approximate relations for the weight and enclosed volume of a tent The cross-sectional area inside the tent shown in Figure 32 is approximately

$$A_c = r(r\phi_B + 2h_r \csc\phi_B) + (r^2 + h_r^2)\cot\phi_B \qquad (1)$$

The enclosed volume is $A_c \ell_h$ or

$$V = 2n\, r_c \sin\alpha_c \left[r\,(r\phi_B + 2h_r \csc\phi_B) + (r^2 + h_r^2)\cot\phi_B\right] \qquad (2)$$

The weight of the fabric used to form n cells is

$$Wt = 4\Omega\left[r_c\ 2n\ \alpha_c + (n+1)\cos\alpha_c\right]\left[(r + r_c)(\phi_B + \cot\phi_B) + h_r \csc\phi_B\right] \qquad (3)$$

where Ω = fabric weight per unit surface area. The other parameters are shown in Figure 32.

To obtain a least weight design, we require the maximum volume to weight ratio. Dividing equation (2) by equation (3), and defining $\gamma = V/Wt$,

$$\gamma = \frac{n \sin \alpha \left[r_c(r\phi_B + 2h_r \csc \phi_B) + (r^2 + h_r^2) \cot \phi_B\right]}{2 \left[2 n \alpha_c + (n+1) \cos \alpha_c\right]\left[(r + r_c)(\phi_B + \cot \phi_B) + h_r \csc \phi_B\right]} \tag{4}$$

The intended use of the tent would set certain of the parameters, r, ϕ_B, h, and n, which would be a function of the length, and strength requirements would determine Ω The two remaining independent variables, α_c and r_c, determine the cell configuration directly. To establish whether or not γ obtains a finite maximum with regard to α_c and r_c, we take the partial derivatives of γ with respect to α_c and r_c, and set them equal to zero

From $\frac{\partial \gamma}{\partial r_c} = 0$, we find that no maximum exists, so for minimum weight, the smallest radius practical should be used. The radius will therefore be dictated by strength and stability criteria.

Taking the partial derivative of γ with respect to α_c, and defining

$$C = \frac{\left[n \ r \ (r\phi_B + 2h_r \csc \phi_B) + (r^2 + h_r^2) \cot \phi_B\right]}{2 \Omega \left[(r + r_c)(\phi_B + \cot \phi_B) + h_r \csc \phi_B\right]}, \tag{5}$$

we obtain

$$\frac{\partial \gamma}{\partial \alpha_c} = C \ \frac{2n (\alpha_c \cos \alpha_c - \sin \alpha_c) + n + 1}{2 n \alpha_c + (n+1) \cos \alpha_c^2} \tag{6}$$

Setting equation (6) equal to zero, we find that

$$\sin \alpha_c - \alpha_c \cos \alpha_c = \frac{n+1}{2n} \tag{7}$$

The maximum (if it is a maximum) value of γ is, then, dependent only upon the number of cells, n. As a limiting value,

$$\lim_{n \to \infty} \frac{n+1}{2n} = 1/2, \tag{8}$$

so that for large values of n,

$$\sin \alpha_c - \alpha_c \cos \alpha_c = 1/2 \tag{9}$$

A trial and error solution yields $\alpha_c = 68° - 54'$. Obviously, for n = 1, $\alpha_c = 90°$.

Since there is only one root of equation (9) for $0 \leq \alpha_c \leq 90°$, to determine if this is a maximum value, we examine the sign of $\partial\gamma/\partial\alpha_c$ on both sides of our solved value of α_c. Setting n = 10, from equation (6)

$$\frac{\partial\gamma}{\partial\alpha_c} = \frac{C}{(20\ \alpha_c + 11\cos\alpha_c)^2}\ (20\ \alpha_c\cos - 20\sin\alpha_c + 11) \tag{10}$$

Since the brackets in equation (10) will always be positive, and we are uninterested in the magnitude of equation (10), we examine only

$$20\ (\alpha_c\cos\alpha_c - \sin\alpha_c) + 11. \tag{11}$$

Setting (11) equal to zero, we find that $\alpha_c \simeq 71.5°$ for n = 10. Now setting $\alpha_c = 50°$ in (11) yields a positive sign, and $\alpha_c = 85°$ results in a negative sign. Simialr results are obtained for all values of n, so we have the desired maximum volume to weight ratio in terms of α_c as a function of n. Figure 44 illustrates the variance of α_c and n for maximum γ

As an illustration, consider an existing tent which we shall refer to as Tent 1. It has the following parameters n = 12, = 15 oz./sq. yd., r = 9' - 6", h_r = 2' - 6", $\phi_B = 81°$, r_c = 10", and $\alpha_c = 35° - 48'$. Using equations (2) and (3), we find that V = 2234.1 cu. ft. and Wt = 166.5 #. The tent is 140 4" long. The weight, as given in the above reference is 264# for the shelter section. This extra 97.5# is comprised of such items as carrying handles, zippers, weather seal flaps, local reinforcement, stitching, etc.

We shall now redesign Tent 1, varying only α_c and n and call it Tent 2 This way we can retain approximately the same volume, and reduce the weight. Our cell width will be approximately 2 $r_c \sin 70°$ = 18.8". We require then, that $n \geq 140.4/18.8 = 7.5$. From Figure 44, for n = 8, $\alpha_c = 72°$ Again using equations (2) and (3), V = 2421.6 cu. ft., and Wt = 149.3#. The length of Tent 2 is 152.5". Since the weight of the miscellaneous items on Tent # 1 will be approximately the sam for Tent #2, we wind up with a shelter section weight of 246.8#. These changes are tabulated below for easy comparison, and Figure 45 shows the relative sizes of the tent cells.

	Tent 1	Tent 2	Absolute Difference	Percent Difference
n	12	8	Down 4	33
α_c	35° - 48'	72° - 00'	Up 36° -12'	101
Volume	2234.1 ft.^{3}	2421.6 ft.^{3}	Up 187.5 ft.^{3}	8
Weight	264.0#	246.8#	Down 17.2#	7
Length	140.4"	152 2"	Up 11 8"	8

3.7.2 Strength Study

It is apparent that geometric optimization alone is insufficient for complete weight control. Selection of fabric must be made with full consideration of material strength to weight ratio. While no formal procedure is developed herein for fabric selection it is recognized that proper fabric design and/or selection can have paramount effect on the attempts to minimize weight. Study of physical properties of fabric is a significant and separate endeavor which should merit additional research and development outside the scope of this contract. Principal criteria for fabric weight optimization should require high strength to weight ratio and minimum safety margin

Stresses in a cellular structure can be fairly accurately predicted by ordinary methods of structural mechanics so long as tensile stress is maintained throughout the fabric. Since fabric is ineffective in compression, initial buckling occurs when one principal stress is positive (tensile) and the other principal stress is zero. An inflated cellular structure with cross section as shown in figure 45 when subjected to applied loads will commence initial buckling when the compression stress due to applied loads equals the tensile prestress due to cell inflation. In the tent structure, the meridional stress resultant (pounds per inch) due to applied load is

$$N_\phi = \frac{P_A}{A_c} \pm \frac{Mr_c}{I}$$

and the meridional inflation stress resultant is $P_c A_e / A_c$.

where

I is the moment of inertia (in.^{3})
r_c is the cell radius (in.)

P_A is meridional force (pounds) resulting from applied load

M is meridional moment (inch-pounds) resulting from applied load.

A_c is fabric length in cross section (in.).

P_c is inflation pressure (psi)

A_e is cell enclosed area (in^2)

Specifically, referencing figure 32,

$$I = 2r_c^3 \; n\,(\alpha_c + \sin\alpha_c \cos\alpha_c) + 1/3\,(n+1)\cos^3\alpha \qquad (1)$$

$$A_e = 2\,r_c^2\,n\,(\alpha_c + \sin\alpha_c \cos\alpha_c) \qquad (2)$$

$$A_c = 4\,n\,r_c\,\alpha_c + 2\,(n+1)\,r_c \cos\alpha_c \qquad (3)$$

The initial buckling moment (M_b) is reached when the stress resultant due to meridional moment equals the net stress resultant from inflation pressure and meridional force due to loads. Equating stress resultant from applied load to stress resultant from inflation pressure,

$$\frac{M_b r_c}{I} + \frac{P_A}{A_c} = \frac{P_c A_e}{A_c}$$

Transposing and solving,

$$M_b = \frac{(P_c A_e - P_A)\,I}{r_c A_c} \qquad (4)$$

Substituting equations 1, 2, and 3,

$$M_b = \frac{r_c(2\,r_c^2\,n\,P_c)(\alpha_c + \sin\alpha_c \cos\alpha_c) - P_A \quad n\,(\alpha_c + \sin\alpha_c \cos\alpha_c) + 1/3\,(n+1)\cos^3\alpha_c}{2n\alpha_c + (n+1)\cos\alpha_c} \qquad (5)$$

The ultimate collapse moment is reached when wrinkles have progressed across the cross-section a distance $b = r_c\,(1 + \alpha_c + \cos\alpha_c - \sin\alpha_c)$ as shown in Figure 46. The width of the cross-section at collapse is assumed unchanged since all but the end cells are restrained from lateral expansion At ultimate collapse the total meridional force is carried by the surface skin. The total meridional force acts as a couple with moment arm equal to $b - r_c = r_c(\alpha_c + \cos\alpha_c - \sin\alpha_c)$ as indicated in Figure 46. The ultimate collapse moment is

$$M_c = (P_A + P_c A_e)(\alpha_c + \cos\alpha_c - \sin\alpha_c)\, n\, r_c \qquad (6)$$

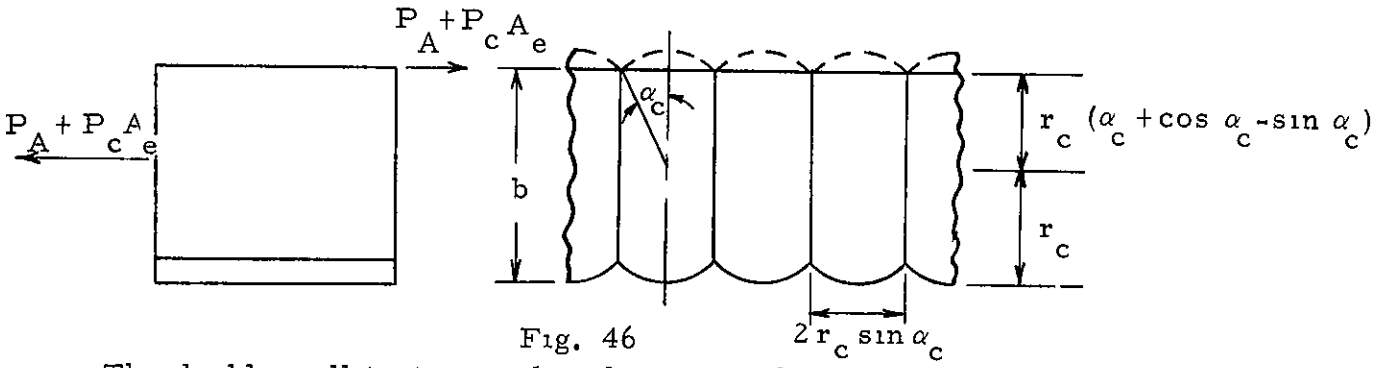

Fig. 46

The double wall tent is analysed as an arch structure comprised of a series of connecting beam elements of arbitrary lengths chosen to fit the load pattern and also to provide a smooth pattern of discrete valves of internal forces, meridional moment, meridional force, and radial shear Analysis utilizes the theorem of least work and is programmed on the Hayes IBM 1620 computer. The tent is first analysed with no buckled section When analysis indicates that a buckled section exists according to relation (5), a new flexibility coefficient is inserted at the buckled section and computer analysis is continued. The new flexibility coefficient allows a near-pinned condition at that point.

Results are then printed out in keeping with the following relations

Meridional stress resultant,

$$N_\phi = \frac{M\ r_c}{I} + \frac{P_A + P_c A_e}{A_c} \qquad (7)$$

Hoop stress resultant,

$$N_h = (P_c - P_r)\, r_c \qquad (8)$$

where P_c is internal pressure

P_r is external pressure

Web stress resultant,

$N_w = N_h\,(2 \sin\alpha_c)$, By equilibrium of the skin-web junction

$$N_w = (P_c - P_r)\, 2\, r_c \sin\alpha_c \qquad (9)$$

3.7.3 Stability

Static instability of an "m" times redundant structure will occur when (m + 1) points have buckled. Since the tent fabric cannot carry compression load, static instability is also assumed to occur when the axial compression load equals the axial tension load due to inflation pressure.

3.7.4 Analysis

Three arbitrary tent sizes were used as analytical models. They are identified as

Tent #1 - h/d = .5, d = 238 inches
Tent #2 - h/d = .75, d = 194 inches
Tent #3 - h = 163 inches, d = 266 inches, this tent has flat sides 9° from vertical

All analytical models had guy lines attached at approximately 0.80 tent height.

Pressure coefficients were taken from wind tunnel data and converted into a two-dimensional pressure distribution around the tents for q = .6, 3, and 6 inches of water (gage). It was assumed that the wind load did not vary along the length of the tent, and average values of the pressures along the tent length were used in the analysis. Shear, moment and meridional forces were obtained for each loading by the theorem of least work using the IBM 1620 computer. The collapse moments and axial loads were computed for all combinations of w/d = 0.080, 0.12, 0.16, P_c = 3q, 4q, 5q, and $\alpha_c = 30^{\circ}, 60^{\circ}$. When the actual moment exceeded the collapse moment for any condition, new flexibility coefficients for the collapsed point were inserted into the computer program until the actual moment was lowered to equal the collapse moment. The load redistribution by the above method did not give additional collapsing moments, therefore, model instability due to moment did not exist. When the meridional compression force exceeded the tension force due to inflation pressure p_c, the tent was assumed unstable.

For all stable conditions, the maximum fabric stress resultants were computed and graphed vs. q in inches of water (gage). Fabric web and hoop stress resultants calculated and graphed as a function of cell radius, internal pressure and cell angle, α_c.

3.7.5 Conclusions

When using the design curves as derived from this study, the designer should not deviate significantly from the over-all tent proportions from which the curves are determined. It is anticipated that a more general design

approach will be provided in a later revision The revised approach should allow more latitude in cell sizing and weight optimination Results of the weight optimization study are presented on Figure 44 which shows optimum values for α_c between 69° and 90°, however, for least fiber loading, α_c should be equal to or less than 30°. Therefore, in the final design approach, trade-off must be made between weight/volume optimization and strength.

In the strength analyses, the maximum stress resultants were found in either the hoop or web stresses. For a cell angle, α_c equal to or less than 30°, the hoop force is greater. For cell angle greater than 30°, the web force is greater. In each model analyzed, the meridional stress resultant is least of the three components tabulated.

It was also observed from the strength analyses that the maximum fabric loading does not vary appreciably with height to diameter ratio, but does vary significantly with cell width to tent diameter ratio, w/d, and with cell internal pressure, P_c, as evidenced by the curves of results obtained As w/d is increased, wind load capability is increased by virtue of increased stability. As P_c is increased, wind load capability is increased by virtue of increased pre-stress and hence, increased stability. Increase in w/d or P_c also effects increase in maximum design stress.

Analysis results indicate that most models with w/d ratio of 0.08 were unstable according to the criteria of paragraph 3.7 3, that is, calculated meridional compression force ($-P_A$) is greater than meridional inflation force ($P_c A_e$). However, since these models did not collapse during the test, it can only be concluded that these designs are marginal in acceptability and analysis as performed herein is considered inadequate for these models. Results of all successful analyses are presented in Figures 33 thru 43. These curves are suitable for use as design curves.

3.8 FABRIC STRESS - SINGLE WALL TENTS

3.8.1 Introduction

The analytical determination of stress distribution in any membrane under non-uniform pressure loading requires a satisfactory analytical representation of the pressure distribtuion which can then be applied to a suitable shell theory. Expressions for wind loading on spherical and cylindrical shaped surfaces are obtained which are considered to be reasonable approximations, relative to the experimental pressure data, for the purposes of this analysis.

In the past, the tent designer has used a crude stress analysis and a large factor of safety to conveniently provide structure capable of carrying a given wind load. However, the need to optimize tent structures had created the desire for a more refined analysis of stresses Although the present analysis is approximate, it is a significant step in refining the structural analysis of air supported tents.

3.8.2 Application of Membrane Theory of Inflated Tents

Although this analysis uses the membrane theory to determine internal loads in the fabric structure of inflated tents under wind load, there are some obvious errors in its application. Whereas the membrane theory is predicated on a homogeneous, elastic material having inherent shear resistance and an equilibrium condition which assumes no distortion of the membrane, a single-ply fabric is inherently capable of resisting only bi-axial tension loads in the directions of the weave fibers. However, in the case of an inflated fabric structure, when tensile stresses are present due to internal pressure, external compressive loads may be taken by a reduction in tensile stress. If tensile stress is relieved to the point where the material fibers try to go into compression, the fabric in this area will develop wrinkles normal to the direction of zero stress.

Although typical past design criteria have required the inflation pressure to be maintained at a sufficiently high level to keep the fabric in tension in all areas in order to prevent such wrinkles, such a requirement may be unnecessarily severe. The relief of tensile stress in one principle direction of the fabric weave, due to external compressive load, may cause some increase in tensile stress in the other weave direction from load redistribution; but this increased stress will be no greater, and probably considerably less, than the additional stress induced by increasing the inflation pressure to eliminate wrinkles. It is further noted that local buckling of this type may be

readily tolerated, especially under extreme operating conditions, since the deflections do not constitute failure and would be expected to bring about reduction in peak stress values.

To accommodate shear load as a component of diagonal tension without the excessive distortion caused by reorientation of the weave fibers, the usual practice in tentage design is to select a fabric of two-ply construction with the bias ply oriented at an angle of 45 degrees with respect to the other ply. Although this appreciably reduces the distortion, the fabric does not follow the linear membrane theory. A non-linear theory has been initiated, but much work remains to be done to make it a practical analysis technique. Despite the inadequacies of the linear membrane theory in its application to inflated fabric structures, it is the best analysis technique presently available.

3.8.3 Pressure Distribution Analysis

The fabric loads analysis which follows was based on measured external pressure distributions obtained during the wind tunnel test series. The method of measurement chosen was to section the tent off by rows and columns. At the intersection of each row and column a light weight tube was attached to the fabric on the inside of the envelope. A small orifice was then drilled through the fabric and into the tube thereby forming a surface static pressure tap. The number of pressure taps per tent model was determined primarily by the model size with some consideration being given to areas of constant pressure distribution. The locations of the pressure taps for two models are presented in Figs. 83 and 84.

The method of measurement of the test pressures was discussed in Paragraph 3.1 and the details of data reduction in Paragraph 3.9. These tests indicate somewhat different pressure distributions than those around tower mounted radomes due to the presence of the ground plane. The boundary layer associated with the ground plane is discussed in Paragraph 3 1, however, it is noted that the boundary layer thickness was adjustable and was set at values deemed reasonable for ground mounted structures A discussion of model similarity and data extrapolations is also discussed in Paragraph 3.1.

Past work on spherical radomes has approximated wind load distribution with a three term trigonometric series, assuming symmetry about the wind axis. Comparison with higher degree series utilizing wind tunnel data shows that a considerably better approximation can be obtained with an eight term expansion.

3.8.3.1 Truncated Spherical Shape

To express the pressure distribution analytically, it is necessary to determine the angles ϕ and θ They were determined from the models as follows.

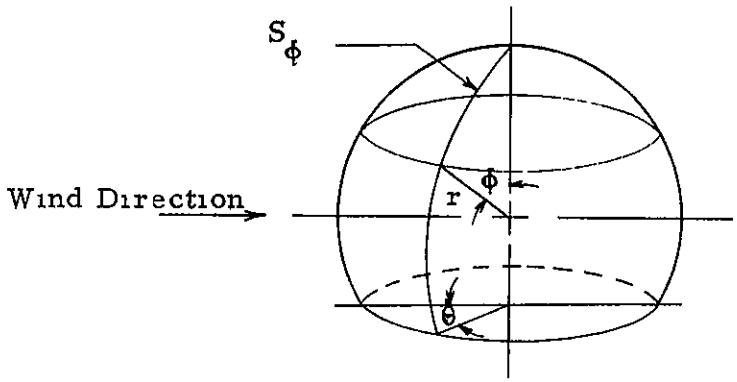

S_ϕ = Arc length from vertical axis of rotation to angle ϕ in a meridional plane containing vertical axis of rotation.

$$\phi = \frac{S_\phi}{r}$$

$$\theta = 2\pi N$$

where N = No. of columns from stagnation plane $\theta = 0$ to given θ divided by total no. of columns around the spherical model Columns are the grid lines in the meridional direction.

$$\sin \phi_B = \left[1 - \left(\frac{d-2_h}{d}\right)^2 \right]^{\frac{1}{2}}$$

$$\cos \phi_B = \frac{d-2_h}{d}$$

For the purpose of spherical shell membrane analysis, the wind load can be expressed as a trigonometric series in the angles ϕ and θ (assuming symmetry about the plane $\theta = 0°$, $\theta = 180°$),

$$\frac{P}{q}(\phi, \theta) = \sum_{0}^{N} A_n \sin^n \phi \cos^n \theta = \sum_{0}^{N} p_n(\phi) \cos n\theta$$

where P = pressure on shell surface minus free stream static pressure

q = dynamic pressure ($1/2\ \rho\ U^2$)

Through a computerized curve-fit program using the principle of least squares, it was determined that N = 7 yields optimum results with regard to accuracy of fit and time expended. The computer program uses polynominal curves of the form

$$\frac{P}{q}(\phi, \theta) = \sum_{0}^{N} A_n X^n.$$

So setting $X^n = \sin^n \phi \cos^n \theta$, N = 7, we have

$$X^\circ = 1$$

$$X = \sin\phi \cos\theta$$

$$X^2 = \frac{1}{2} \sin^2 \phi\,(1 + \cos 2\theta)$$

$$X^3 = \frac{1}{4} \sin^3 \phi\,(3 \cos\theta + \cos 3\theta)$$

$$X^4 = \frac{1}{8} \sin^4 \phi\,(3 + 4 \cos 2\theta + \cos 4\theta)$$

$$X^5 = \frac{1}{16} \sin^5 \phi\,(10 \cos\theta + 5 \cos 3\theta + \cos 5\theta)$$

$$X^6 = \frac{1}{32} \sin^6 \phi\,(10 + 15 \cos 2\theta + 6 \cos 4\theta + \cos 6\theta)$$

$$X^7 = \frac{1}{64} \sin^7 \phi\,(35 \cos\theta + 21 \cos 3\theta + 7 \cos 5\theta + \cos 7\theta)$$

Collecting like terms of cos n θ, we find that

$$P_o(\phi) = A_o + \frac{1}{2} A_2 \sin^2 \alpha_1 + \frac{3}{8} A_4 + \frac{5}{16} A_6 \sin^6 \phi$$

$$P_1(\phi) = A_1 \sin\phi + \frac{3}{4} A_3 \sin^3\phi + \frac{5}{8} A_5 \sin^5\phi + \frac{35}{64} A_7 \sin^7\phi$$

$$P_2(\phi) = \frac{1}{2} A_2 \sin^2\phi + \frac{1}{2} A_4 \sin^4\phi + \frac{15}{32} A_6 \sin^6\phi$$

$$P_3(\phi) = \frac{1}{4} A_3 \sin^3\phi + \frac{5}{16} A_5 \sin^5\phi + \frac{21}{64} A_7 \sin^7\phi$$

$$P_4(\phi) = \frac{1}{8} A_4 \sin^4\phi + \frac{3}{16} A_6 \sin^6\phi$$

$$P_5(\phi) = \frac{1}{16} A_5 \sin^5\phi + \frac{7}{64} A_7 \sin^7\phi$$

$$P_6(\phi) = \frac{1}{32} A_6 \sin^6\phi$$

$$P_7(\phi) = \frac{1}{64} A_7 \sin^7\phi$$

3.8.3.2 Cylindrical Shape with Spherical Ends

The broadside wind load is considered to be the most critical for the cylindrical portion of a tent There is assumed to be no variation in the wind load to x (the distance along the axis of the cylinder) so that we take the pressure coefficient expression in the form

$$\frac{P}{q}(\phi) = \sum_{0}^{N} A_n \sin^n\phi$$

As was done for the spherical shell distribution, the assumed curve is fitted to the wind tunnel data through a least squares analysis

To express the pressure distribution on the spherical ends of the cylindrical models, it was necessary first to determine the angles α and β, and then convert to ϕ, θ coordinates. The angles α and β were found from the models as follows.

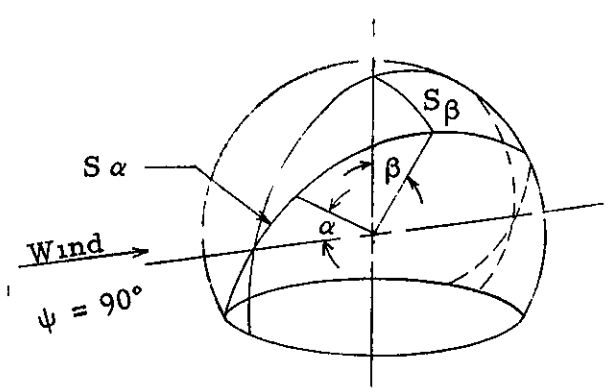

S_α = Arc length from stagnation axis for yaw angle equals 90° to angle α in a meridional plane containing stagnation axis

$$\alpha = \frac{S_\alpha}{r}$$

S_β = Arc length from vertical axis of rotation to angle β in the plane normal to the stagnation axis and containing vertical axis

$$\beta = \frac{S_\beta}{r}$$

The conversion from α, β to ϕ, θ coordinates takes the following form

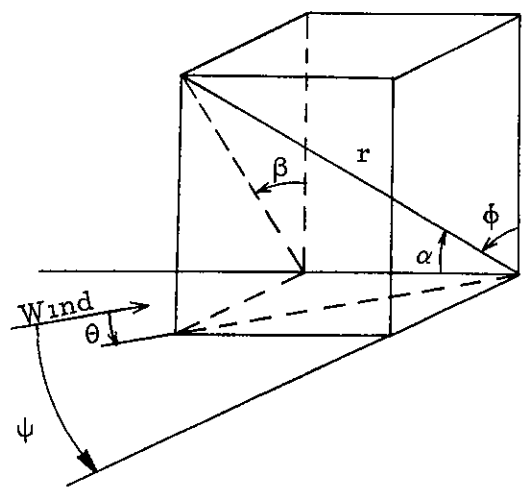

ψ = Yaw Angle

Note ψ and θ are positive counter-clockwise from wind direction

$$\cos\alpha = \sin\phi\cos 9\left(\frac{\pi}{2} - \psi + \theta\right)$$

$$\sin\alpha\sin\beta = \sin\phi\sin\left(\frac{\pi}{2} - \psi + \theta\right)$$

$$\cos^2\left(\frac{\pi}{2} - \psi + \theta\right) = 1 - \sin^2\left(\frac{\pi}{2} - \psi + \theta\right) = \frac{\cos^2\alpha}{\sin^2\phi} \qquad (1)$$

$$\sin^2\left(\frac{\pi}{2} - \psi + \theta\right) = \frac{\sin^2\alpha\sin^2\beta}{\sin^2\phi} \qquad (2)$$

Adding equations (1) and (2) gives

$$\frac{\cos^2 \alpha + \sin^2 \alpha \sin^2 \beta}{\sin^2 \phi} = 1.$$

$$\sin^2 \phi = 1 - \cos^2 \phi = \cos^2 \alpha + \sin^2 \alpha \sin^2 \beta$$

$$\cos^2 \phi = 1 - \cos^2 \alpha - \sin^2 \alpha \sin^2 \beta = \sin^2 \alpha (1 - \sin^2 \beta)$$

$$\cos \phi = \sin \alpha \cos \beta \tag{3}$$

$$\phi - \cos^{-1} (\sin \alpha \cos \beta)$$

Equation (1) by identity is

$$\cos^2 \left(\frac{\pi}{2} - \psi + \theta\right) = \frac{\cos^2 \alpha}{1 - \cos^2 \phi}$$

By substitution of equation (3)

$$\cos^2 \left(\frac{\pi}{2} - \psi + \theta\right) = \frac{\cos^2 \alpha}{1 - \sin^2 \alpha \cos^2 \beta}$$

$$\cos \left(\frac{\pi}{2} - \psi + \theta\right) = \frac{\cos \alpha}{(1 - \sin^2 \alpha \cos^2 \beta)^{\frac{1}{2}}}$$

$$\theta = \cos^{-1} \left[\frac{\cos \alpha}{(1 - \sin \alpha \cos \beta)^{\frac{1}{2}}}\right] + \psi - \frac{\pi}{2} \tag{5}$$

For $(1 - \sin^2 \alpha \cos^2 \beta)^{\frac{1}{2}}$, take positive root

Now we can express our pressure data in terms of ϕ and θ, and proceed with the solution just as is done for the truncated spherical models

3.8.4 Membrane Stress Analysis

The analysis of stress resultants as presented here is not entirely original. The governing system of differential equations and their general solutions can be found in many texts on the theory of shells. They are reiterated here, in anticipation that not every designer has this literature readily available, nor is proficient in the mathematics involved.

The results of this analysis are presented as stress coefficients, N_ϕ/qr, N_θ/qr, $N_{\phi\theta}/qr$, N_x/qr, and N_{xp}/qr on the computer print-out sheets. In addition, graphs of these stress coefficients are presented as functions of ϕ, θ, and x.

3.8.4.1 Truncated Spherical Shape

Stress Resultants

The equations of equilibrium for a spherical shell element with a distributed radial load are

$$\frac{\partial}{\partial\phi}(N_\phi \sin\phi) + \frac{\partial}{\partial\theta}(N_{\phi\theta}) - N_\theta \cos_\phi = 0, \tag{1}$$

$$\frac{\partial}{\partial\phi}(N_{\phi\theta} \sin\phi) + \frac{\partial}{\partial\theta}(N_\theta) + N_{\phi\theta}\cos\phi = 0, \tag{2}$$

$$N_\phi + N_\theta = - P(\phi, \theta) r, \tag{3}$$

where

N_ϕ = meridional stress resultant (pounds per inch)

N_θ = circumferential stress resultant (pounds per inch)

$N_{\phi\theta}$ = shear stress resultant (pounds per inch)

$P(\phi, \theta)$ = radial load (pounds per square inch)

r = tent radius (inches).

From equation (3),

$$N_\theta = - N_\phi - P(\phi, \theta) r$$

Substituting equation (4) into equations (1) and (2), we eliminate N_θ, yielding

$$\frac{\partial}{\partial\phi}(N\phi \sin\phi) + \frac{\partial}{\partial\theta}(N_{\phi\theta}) + \left[N_\phi + P(\phi,\theta) r\right] \cos\phi = 0 \tag{5}$$

$$\frac{\partial}{\partial\phi}(N_{\phi\theta} \sin\phi) + \frac{\partial}{\partial\theta}\left[- N_\phi - P(\phi, \theta) r\right] + N_{\phi\theta}\cos\phi = 0 \tag{6}$$

For a wind load, which is symmetric with respect to the plane $\theta = 0°$, $\theta = 180°$, the general solution of equations (5) and (6) may be

represented by

$$N_\phi = r\,q \sum_{0}^{N} S_{\phi n}(\phi) \cos n\,\theta \tag{7}$$

$$N_{\phi\theta} = r\,q \sum_{1}^{N} S_{\phi\theta n}(\phi) \sin n\,\theta \tag{8}$$

with N = 7 because the pressure distribution sequence terminates at n = 7

$$P(\phi, \theta) = q \sum_{0}^{7} p_n(\phi) \cos n\,\theta \tag{9}$$

Substituting the n-th general term from equations (7), (8), and (9) into the differential equations (5) and (6), we obtain after simplification,

$$\frac{d}{d\phi}\left[S_{\phi n}(\phi)\right] \sin\phi + 2\,S_{\phi n}(\phi) \cos\phi + n\,S_{\phi\theta n}(\phi) + p_n(\phi) \cos\phi = 0 \tag{10}$$

$$\frac{d}{d\phi}\left[S_{\phi\theta n}(\phi)\right] \sin\phi + 2\,S_{\phi\theta n}(\phi) \cos\phi + n\,S_{\phi n}(\phi) + n\,p_n(\phi) = 0 \tag{11}$$

Adding equations (10) and (11), we obtain

$$\frac{d}{d\phi}\left[S_{\phi n}(\phi) + S_{\phi\theta n}(\phi)\right] + \left(\frac{2\cos\phi + n}{\sin\phi}\right)\left[S_{\phi n}(\phi) + S_{\phi\theta n}(\phi)\right]$$

$$= -\left(\frac{\cos\phi + n}{\sin\phi}\right) p_n(\phi). \tag{12}$$

Subtracting equation (11) from equation (10) yields

$$\frac{d}{d\phi}\left[S_{\phi n}(\phi) - S_{\phi\theta n}(\phi)\right] + \left(\frac{2\cos\phi - n}{\sin\phi}\right)\left[S_{\phi n}(\phi) - S_{\phi\theta n}(\phi)\right]$$

$$= -\left(\frac{\cos\phi - n}{\sin\phi}\right) p_n(\phi) \tag{13}$$

Substituting

$$U_{1n} = S_{\phi n}(\phi) + S_{\phi\theta n}(\phi) \tag{14}$$

$$U_{2n} = S_{\phi n}(\phi) - S_{\phi\theta n}(\phi) \tag{15}$$

into equations (12) and (13) results in two ordinary linear differential equations of first order.

$$\frac{d}{d\phi}(U_{1n}) + \left(\frac{2\cos\phi + n}{\sin\phi}\right) U_{1n} = -\left(\frac{\cos\phi + n}{\sin\phi}\right) p_n(\phi) \tag{16}$$

$$\frac{d}{d\phi}(U_{2n}) + \left(\frac{2\cos\phi - n}{\sin\phi}\right) U_{2n} = -\left(\frac{\cos\phi - n}{\sin\phi}\right) p_n(\phi) \tag{17}$$

From ordinary differential equations the general solution of equation (16) is

$$U_{1n} e^{\int\left(\frac{2\cos\phi + n}{\sin\phi}\right) d\phi} = \int -\left(\frac{\cos\phi + n}{\sin\phi}\right) p_n(\phi)\, e^{\int\left(\frac{2\cos\phi + n}{\sin\phi}\right) d\phi} d\phi + C_{1n} \tag{18}$$

where C_{1n} is the n-th general constant of integration Performing the indicated operations in equation (18), we obtain

$$U_{1n} = -\frac{(1 + \cos\phi)^n}{(\sin\phi)^{n+2}} \left[I_{1n}(\phi) + C_{1n} \right] \tag{19}$$

where

$$I_{1n}(\phi) = \int p_n(\phi)\,(\cos\phi + n)(1 - \cos\phi)^n (\sin\phi)^{1-n}\, d\phi \tag{20}$$

The general solution of equation (17) is

$$U_{2n} e^{\int\left(\frac{2\cos\phi - n}{\sin\phi}\right) d\phi} = \int -\left(\frac{\cos\phi - n}{\sin\phi}\right) p_n(\phi)\, e^{\int\left(\frac{2\cos\phi - n}{\sin\phi}\right) d\phi} d\phi + C_{2n} \tag{21}$$

From equation (24) we obtain

$$U_{2n} = \frac{(1 - \cos\phi)^n}{(\sin\phi)^{n+2}} \left[I_{2n}(\phi) + C_{2n} \right]$$

where

$$I_{2n}(\phi) = \int p_n(\phi)\,(n - \cos\phi)\,(1 + \cos\phi)^n (\sin\phi)^{1-n}\, d\phi$$

Finally from equations (14) and (15),

$$S_{\phi n}(\phi) = \frac{1}{2}\,(U_{1n} + U_{2n})$$

or

$$S_{\phi n}(\phi) = -\frac{1}{2}\left[\frac{(1+\cos\phi)^n}{(\sin\phi)^{n+2}}\left(I_{1n}(\phi) + C_{1n}\right) - \frac{(1-\cos\phi)^n}{(\sin\phi)^{n+2}}\left(I_{2n}(\phi) + C_{2n}\right)\right] \tag{22}$$

$$S_{\phi\theta n} = \frac{1}{2}\,(U_{1n} - U_{2n})$$

or

$$S_{\phi\theta n} = -\frac{1}{2}\left[\frac{(1+\cos\phi)^n}{(\sin\phi)^{n+2}}\,(I_{1n}(\phi) + C_{1n}) + \frac{(1-\cos\phi)^n}{(\sin\phi)^{n+2}}\,(I_{2n}(\phi) + C_{2n})\right] \tag{23}$$

The stresses are,

$$N_\phi = qr\sum_0^7 S_{\phi n}(\phi)\cos n\theta \tag{24}$$

$$N_\theta = -N_\phi - qr\sum_0^7 p_n(\phi)\cos n\theta \tag{25}$$

$$N_{\phi\theta} = qr\sum_0^7 S_{\phi\theta n}(\phi)\sin n\theta \tag{26}$$

The above results represent the general solution of the equilibrium equations (1), (2) and (3). Evaluation of the integration constants in U_{1n} and U_{2n} is

accomplished by examining each load term independently and defining boundaries to assure finite stress values and strain compatibility at the tent base ($\phi = \phi_B$).

In each load term there exists two arbitrary constants, C_{1n} and C_{2n}. We can determine C_{1n} for all values of n from equation (19) by requiring that stress resultants, hence U_{1n} be finite at the apex ($\phi = o$) In equation (19), there is a zero of order n + 2 in the denominator. As can be verified by repeated application of L'Hospital's Rule, a finite value of U_{1n} is given at the apex by setting,

$$C_{1n} = -I_{1n}(o) \text{ for } 0 \leq n \leq 7$$

Similarly for U_{2n} we obtain from equation (21)

$$C_{2n} = I_{2n}(o) \quad n = o \text{ and } 1 \text{ only*}$$

* When $n \geq 2$ the above relation becomes indeterminate and C_{2n} ($2 \leq n \leq 7$) remain arbitrary constants

For evaluation of constants C_{2n} ($2 \leq n \leq 7$) we will require strain compatibility at the base ($\phi = \phi_B$) where hoop strain, $\epsilon_\theta = 0$

The compatibility equation is

$$\epsilon_\theta = \frac{N_\theta}{E} - \nu \frac{N_\phi}{E} \qquad \text{(a)}$$

where E is elastic modulus

ν is poissons ratio

$$\frac{N_\theta}{E} - \nu \frac{N_\phi}{E} = 0 \qquad \text{(b)}$$

$$N_\theta = \nu \; N_\phi \tag{c}$$

Substituting

$N_\phi = - N_\theta - q\,r \sum_0^N p_n(\phi) \cos n\theta$ from equations (3) and (9), equation (c) becomes for each load term $N_{\phi n}(\phi_B) = - \frac{1}{1+\nu} \; q\,r\; p_n\,(\phi_B) \cos n\theta$

or

$$\frac{N_{\phi n}(\phi_B)}{q\,r} = - \frac{1}{1+\nu} \; p_n\,(\phi_B) \cos n\theta \tag{d}$$

From equations (24) for each load term evaluated at ϕ_B,

$$\frac{N_{\phi n}(\phi_B)}{q\,r} = S_{\phi n}(\phi_B) \cos n\theta \tag{e}$$

Substituting (d) into (e)

$$\frac{1}{1+\nu} \; p_n\,(\phi_B) = S_{\phi n}(\phi_B)$$

$$S_{\phi n}(\phi_B) = \frac{1}{1+\nu} \; p_n\,(\phi_B) \tag{f}$$

Evaluating equation (22) at ϕ_B -

$$S_{\phi n}(\phi_B) = - \frac{1}{2} \left[\frac{(1 + \cos\phi_B)^n}{(\sin\phi_B)^{n+2}} \left(I_{1n}\,(\phi_B) + C_{1n} \right) - \frac{(1 - \cos\phi_B)^n}{(\sin\phi_B)^{n+2}} \left(I_{2n}\,(\phi_B) + C_{2n} \right) \right] \tag{g}$$

Substituting relation (f) and (g) and solving, when $2 \le n \le 7$,

$$C_{2n} = \frac{(1 + \cos\phi_B)^n}{(1 - \cos\phi_B)^n} \left(I_{1n}(\phi_B) + C_{1n} \right) - I_{2n}(\phi_B)$$

$$- \frac{2}{(1 + \nu)} \frac{(\sin\phi_B)^{n+2}}{(1 - \cos\phi_B)^n} p_n(\phi_B) \qquad \text{(h)}$$

All constants of integration are thus evaluated. Integrated values for $I_{1n}(\phi)$ are as follows

$$I_{10}(\phi) = A_o\left(\frac{1}{2}\sin^2\phi\right) + A_2\left(\frac{1}{8}\sin^4\phi\right) + A_4\left(\frac{1}{16}\sin^6\phi\right)$$

$$A_6\left(\frac{5}{128}\sin^8\phi\right)$$

$$I_{11}(\phi) = A_1\left(-\cos\phi + \frac{1}{3}\cos^3\phi\right)$$

$$+ A_3\left(-\frac{3}{20}\cos\phi\sin^4\phi - \frac{3}{5}\cos\phi + \frac{1}{5}\cos^3\phi\right)$$

$$+ A_5\left(-\frac{5}{56}\cos\phi\sin^6\phi - \frac{3}{28}\cos\phi\sin^4\phi - \frac{3}{7}\cos\phi\right.$$

$$\left. + \frac{1}{7}\cos^3\phi\right)$$

$$+ A_7\left(-\frac{35}{576}\cos\phi\sin^8\phi - \frac{5}{72}\cos\phi\sin^6\phi - \frac{1}{12}\cos\phi\sin^4\phi\right.$$

$$\left. - \frac{1}{3}\cos\phi + \frac{1}{9}\cos^3\phi\right)$$

$$I_{12}(\phi) = A_2\left(-\cos\phi - \frac{1}{2}\sin^2\phi - \frac{1}{8}\sin^4\phi\right)$$

$$+ A_4\left(-\cos\phi + \frac{1}{3}\cos^3\phi - \frac{1}{4}\sin^4\phi - \frac{1}{12}\sin^6\phi\right)$$

$$+ A_6\left(-\frac{3}{4}\cos\phi + \frac{1}{4}\cos^3\phi - \frac{3}{16}\cos\phi\sin^4\phi - \frac{5}{32}\sin^6\phi - \frac{15}{256}\sin^8\phi\right)$$

$$I_{13}(\phi) = A_3 \left(-\frac{4}{5}\cos\phi - \frac{2}{5}\cos^3\phi - \sin^2\phi + \frac{1}{20}\cos\phi\sin^4\phi \right)$$

$$+ A_5 \left(-\frac{9}{7}\cos\phi + \frac{3}{7}\cos^3\phi - \frac{5}{8}\sin^4\phi + \frac{17}{56}\cos\phi\sin^4\phi \right.$$

$$\left. + \frac{5}{112}\cos\phi\sin^6\phi \right)$$

$$+ A_7 \left(-\cos\phi + \frac{1}{3}\cos^3\phi - \frac{1}{4}\cos\phi\sin^4\phi - \frac{7}{16}\sin^6\phi \right.$$

$$\left. + \frac{11}{48}\cos\phi\sin^6\phi - \frac{7}{192}\cos\phi\sin^8\phi \right)$$

$$I_{14}(\phi) = A_4 \left(-\frac{1}{2}\cos\phi - \frac{5}{6}\cos^3\phi - \frac{3}{2}\sin^2\phi + \frac{1}{4}\sin^4\phi \right.$$

$$\left. + \frac{1}{48}\sin^6\phi \right)$$

$$+ A_6 \left(-\frac{3}{2}\cos\phi + \frac{1}{2}\cos^3\phi - \frac{9}{8}\sin^4\phi + \frac{3}{4}\cos\phi\sin^4\phi \right.$$

$$\left. + \frac{1}{4}\sin^6\phi + \frac{3}{128}\sin^8\phi \right)$$

$$I_{15}(\phi) = A_5 \left(-\frac{1}{7}\cos\phi - \frac{9}{7}\cos^3\phi - 2\sin^2\phi + \frac{5}{8}\sin^4\phi - \frac{9}{56}\cos\phi\sin^4\phi \right.$$

$$\left. - \frac{1}{112}\cos\phi\sin^6\phi \right)$$

$$+ A_7 \left(-\frac{5}{3}\cos\phi + \frac{5}{9}\cos^3\phi - \frac{7}{4}\sin^4\phi + \frac{4}{3}\cos\phi\sin^4\phi \right.$$

$$\left. + \frac{35}{48}\sin^6\phi - \frac{29}{144}\cos\phi\sin^6\phi - \frac{7}{576}\cos\phi\sin^8\phi \right)$$

$$I_{16}(\phi) = A_6 \left(\frac{1}{4}\cos\phi - \frac{7}{4}\cos^3\phi - \frac{5}{2}\sin^2\phi + \frac{9}{8}\sin^4\phi \right.$$

$$\left. - \frac{7}{16}\cos\phi\sin^4\phi - \frac{3}{32}\sin^6\phi - \frac{1}{256}\sin^8\phi \right)$$

$$I_{17}(\phi) = A_7 \left(\frac{2}{3}\cos\phi - \frac{20}{9}\cos^3\phi - 3\sin^2\phi + \frac{7}{4}\sin^4\phi \right.$$

$$- \frac{5}{6}\cos\phi\sin^4\phi - \frac{7}{24}\sin^6\phi + \frac{1}{18}\cos\phi\sin^6\phi$$

$$\left. + \frac{1}{576}\,\text{cso}\,\phi\sin^8\phi \right)$$

$$I_{20}(\phi) = - I_{10}(\phi)$$

$$I_{21}(\phi) = I_{11}(\phi)$$

$$I_{22}(\phi) = A_2 \left(-\cos\phi + \frac{1}{2}\sin^2\phi + \frac{1}{8}\sin^4\phi \right)$$

$$+ A_4 \left(-\cos\phi + \frac{1}{3}\cos^3\phi + \frac{1}{4}\sin^4\phi + \frac{1}{12}\sin^6\phi \right)$$

$$+ A_6 \left(-\frac{3}{4}\cos\phi + \frac{1}{4}\cos^3\phi - \frac{3}{16}\cos\phi\sin^4\phi + \frac{5}{32}\sin^6\phi \right.$$

$$\left. + \frac{15}{256}\sin^8\phi \right)$$

$$I_{23}(\phi) = A_3 \left(-\frac{4}{5}\cos\phi - \frac{2}{5}\cos^3\phi + \sin^2\phi + \frac{1}{20}\cos\phi\sin^4\phi \right)$$

$$+ A_5 \left(-\frac{9}{7}\cos\phi + \frac{3}{7}\cos^3\phi + \frac{5}{8}\sin^4\phi + \frac{17}{56}\cos\phi\sin^4\phi \right.$$

$$\left. + \frac{5}{112}\cos\phi\sin^6\phi \right)$$

$$+ A_7 \left(-\cos\phi + \frac{1}{3}\cos^3\phi - \frac{1}{4}\cos\phi\sin^4\phi + \frac{7}{16}\sin^6\phi \right.$$

$$\left. + \frac{11}{48}\cos\phi\sin^6\phi + \frac{7}{192}\cos\phi\sin^8\phi \right)$$

$$I_{24}(\phi) = A_4 \left(-\frac{1}{2} \cos\phi - \frac{5}{6} \cos^3\phi + \frac{3}{2} \sin^2\phi - \frac{1}{4} \sin^4\phi - \frac{1}{48} \sin^6\phi \right)$$

$$+ A_6 \left(-\frac{3}{2} \cos\phi + \frac{1}{2} \cos^3\phi + \frac{9}{8} \sin^4\phi + \frac{3}{4} \cos\phi \sin^4\phi \right.$$

$$\left. - \frac{1}{4} \sin^6\phi - \frac{3}{128} \sin^8\phi \right)$$

$$I_{25}(\phi) = A_5 \left(-\frac{1}{7} \cos\phi - \frac{9}{7} \cos^3\phi + 2 \sin^2\phi - \frac{5}{8} \sin^4\phi - \frac{9}{56} \cos\phi \sin^4\phi \right.$$

$$\left. - \frac{1}{112} \cos\phi \sin^6\phi \right)$$

$$+ A_7 \left(-\frac{5}{3} \cos\phi + \frac{5}{9} \cos^3\phi + \frac{7}{4} \sin^4\phi + \frac{4}{3} \cos\phi \sin^4\phi \right.$$

$$\left. - \frac{35}{48} \sin^6\phi - \frac{29}{144} \cos\phi \sin^6\phi - \frac{7}{576} \cos\phi \sin^8\phi \right)$$

$$I_{26}(\phi) = A_6 \left(\frac{1}{4} \cos\phi - \frac{7}{4} \cos^3\phi + \frac{5}{2} \sin^2\phi - \frac{9}{8} \sin^4\phi - \frac{7}{16} \cos\phi \sin^4\phi \right.$$

$$\left. + \frac{3}{32} \sin^6\phi + \frac{1}{256} \sin^8\phi \right)$$

$$I_{27}(\phi) = A_7 \left(\frac{2}{3} \cos\phi - \frac{20}{9} \cos^3\phi + 3 \sin^2\phi - \frac{7}{4} \sin^4\phi - \frac{5}{6} \cos\phi \sin^4\phi \right.$$

$$\left. + \frac{7}{24} \sin^6\phi + \frac{1}{18} \cos\phi \sin^6\phi + \frac{1}{576} \cos\phi \sin^8\phi \right)$$

3.8.4.2 Cylindrical Shape with Spherical Ends (Broadside Wind Load)

Considerable effort has been expended in attempting an integrated solution of the entire tent which is without precedent It has been necessary within the scope of the present contract to explore alternate analytical techniques in lieu of optimum procedures The following is considered the most realistic of the simplified approaches and should afford adequate basis for establishing future designs even when low safety factors are employed

The cylindrical portion of the tent is considered to be loaded by three separate loads, 1) internal pressure, 2) external pressure from wind load and 3) equilibrium membrane force of the hemispherical section at each end of the cylinder The forces resulting from the three separate loads are then superimposed to find the maximum membrane stress in each direction. It is theorized that the resulting stresses are conservative because, at lines of force discontinuity, the maximum stress values would be relieved if displacement compatibility were attained between adjoining free bodies.

Stresses in the hemispherical ends are analysed as though the two ends were joined together forming a truncated sphere. Analysis is then identical to the preceding spherical shape. Load data is taken from the actual cylindrical tent tests

Loads on Cylinder

1. Radial Loads

Radial loads include

Internal pressure, $P_e = q A_e$

External pressure, $P_{ext} = q \sum_{0}^{N} A_n \sin^n \phi$

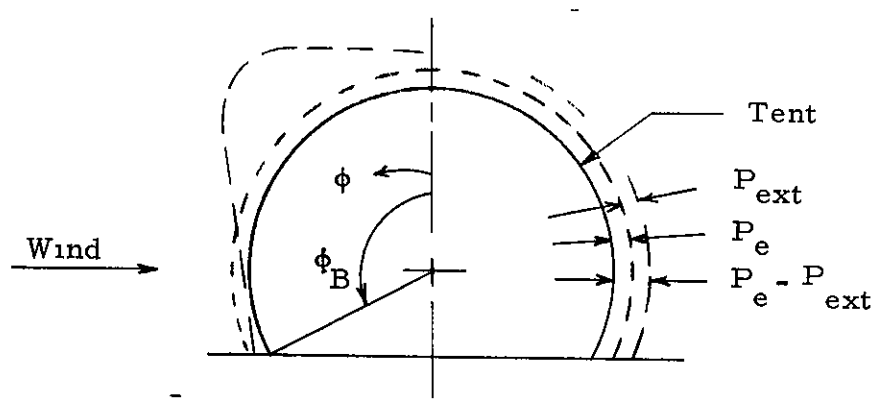

The radial loads are combined as indicated giving a resultant radial load, $P_e - P_{ext}$.

The cylindrical membrane when subjected to a radial load varying with ϕ should distort freely such that the circumferential force is constant. This is because we have assumed that there are no tangential loads and that the fabric has zero bending stiffness It must then follow that the radius would be variable with ϕ in order that equilibrium be maintained thru the relation

$$N_{\phi(const)} = (P_e - P_{ext})\ r\ \phi$$

or

$$r(u) = \frac{N_{\phi(const)}}{P_e - P_{ext}}$$

The resulting deformation would inversely simulate the load magnitude as shown below

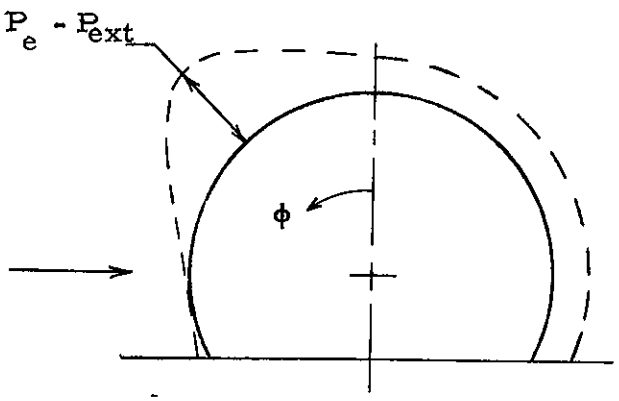

Load

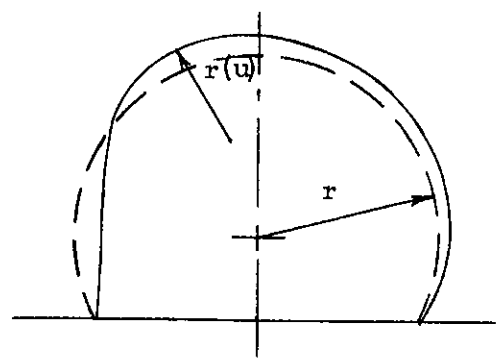

Deformation

To evaluate N_ϕ we will consider equilibrium of a cylindrical body of unit length radial load varying with ϕ.

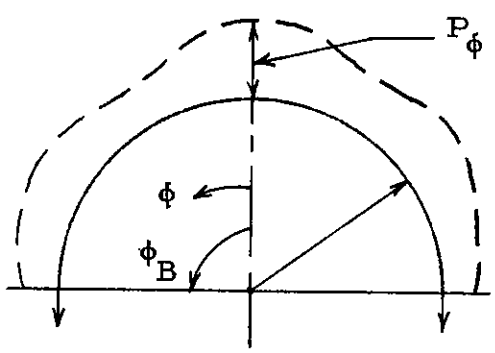

$N_\phi(const)$ $N_\phi(const)$

Summation of Vertical Forces

$$2 N_\phi \sin\phi_B = \int_{-\phi_B}^{\phi_B} r\, p(\phi) \cos\phi \, d\phi$$

where

$$p(\phi) = P_e - P_{ext}$$

and

$$P_{ext} = q \sum_0^N A_n \sin^n \phi$$

$$\therefore \quad N_\phi = \frac{r}{2 \sin\phi_B} \int_{-\phi_B}^{\phi_B} (P_e - q \sum_0^N A_n \sin^n \phi) \cos\phi \, d\phi$$

since

$$N_\phi = \text{const.}$$

then

$$N_\phi = \frac{R}{\sin\phi_B} \int_0^{\phi_B} (P_e - q \sum_0^N A_n \sin^n \phi) \cos\phi \, d\phi$$

which reduces to

$$\frac{N_\phi}{q\, r} = \frac{P_e}{q} - \frac{1}{\sin\phi_B} \sum_0^N \frac{A_n \sin^{n+1}\phi_B}{n+1}$$

let

$$C = \frac{P_e}{q} - \frac{N_\phi}{q\, r},$$

$$C = \sum_0^N \frac{A_n \sin^{n+1}\phi_B}{n+1}$$

$$\frac{\partial C}{\partial \phi_B} = 0 = \frac{n A_n \cos \phi_B \sin^{n-1} \phi_B}{n+1}$$

$$\therefore \quad \cos \phi_B \sin^{n-1} \phi_B = 0$$

$$\phi_B = + \frac{\pi}{2}, \quad n = 0, 1, 2, \quad . N \qquad \text{(maximum)}$$

Since flexibility is apparent and distortion conforms to minimum energy principles, utilization of maximum ϕ_B ($\frac{\pi}{2}$) in the calculation of all n values in the expression for C is reasonable and conservative.

$$\therefore \quad C = \sum_0^N \frac{A_n}{n+1}$$

and

$$\frac{N_\phi}{q\,r} = \frac{P_e}{q} - \sum_0^N \frac{A_n}{n+1}$$

2. Axial Loads

Axial loads on the cylinder are taken as the loads necessary for equilibrium of the hemispherical ends and are determined by use of the spherical tent solution. The spherical ends are assumed to be joined together to form a sphere with load distribution as determined by the actual test data. The resulting N_θ at $\theta = 0$ and $\theta = \pi$ must then be applied to each end of the cylinder The only additional axial load on the cylinder is that due to internal pressure or

$$N_{xe} = \frac{P_e r}{2}$$

Total axial stress for body equilibrium is given by

$$N_x = N_\theta^{(\phi, \theta = 0, \pi)} + \frac{P_e r}{2}$$

or

$$\frac{N_x}{q\,r} = \frac{N_\theta^{(\phi, \theta = 0, \pi)}}{q\,r} + \frac{P_e}{2q}$$

It is recognized that the above analysis does not provide for displacement compatibility at the sphere-cylinder junction It is quite apparent that a compatibility solution should provide a reduction in the calculated peak value because of the edge flexibility of the supporting cylinder It is also noted that the peak stress values for N_θ (necessary for end equilibrium are consequently regarded as slightly conservative

It is also recognized that no evaluation of shear ($N_{x\phi}$) is attempted in the cylindrical shell section. The analysis of shear is not considered critical since the material can buckle in shear without consequent failure (rupture) of the fabric. The critical stress components are taken to be tensile membrane forces

3 8.5 Results - Truncated Spherical Shape

Pressure data from all tests on tent models 1, 4, 7, 10, 13, and 21, have been analysed for curve fitting and model stress analysis in keeping with paragraphs 3.8 3 and 3 8.4.

3.8.5 1 Calculations

Stress coefficients (N_ϕ/qr, N_θ/qr, $N_{\phi\theta}/qr$) were calculated on Hayes' IBM 1620 Computer. Stresses were calculated at 15° intervals, from ϕ = 15° to $\phi = \phi_B$ and from $\theta = 0$ to $\theta = 180°$. Typical stress coefficients are illustrated on Figures 47, 48 and 49 for Test Number 173 on tent model number 4 where dynamic air pressure, q, = 0.6 and tent internal pressure, p_e = 4/5 q.

All valid peak stress coefficients for the non porous spherical model tests (Models 1, 4, 7, and 21) are plotted on Figures 50, 51 and 52 Peak stress values are the maximum occurring in the tent Peak N_ϕ usually occurs at $\phi = 15°$ and $\theta = 75°$. Peak N_θ usually occurs at $\phi = 15°$ and $\theta = 0$ (See Figures 47 and 48)

As is evident on Figures 50 thru 52 the stress coefficient curves are drawn above the plotted points and represent maximum peak stress values where internal pressure is varied from 5/4 q No pattern of stress coefficients is discernable due to varying internal pressure within the selected range

3 8 5 2 Conclusions

The curves of peak stress coefficients are utilized to prepare design curves as shown in Figures 53, 54, and 55 These design curves provide a direct reading of peak stress coefficients for any given h/d and design dynamic, or impact, pressure, q, where internal tent pressure is approximately

equal to q.

Since wind loading can be from any direction, stress variations with θ becomes inconsequential in the spherical design. However it may be advantageous or desirable that the designer be able to determine stress variations with apex angle, ϕ. Figures 56 thru 59 have been derived from test data maximum values and provide a ratio of $N_\theta(\phi)$ to N_θ(peak) for use in design calculations. No comparable curve is prepared for $N_\phi(\theta)$ because the variation in N_ϕ with ϕ is slight. (See Figure 47 at $\theta = 75°$).

Poissons Ratio

In the boundary condition (paragraph 3.8.4.1) requiring strain compatibility at the tent base ($\phi = \phi_B$), Poisson's ratio (ν) is inherent. Because no information is available on Poisson effects in tent fabrics and also because different weaves and fabric compositions would affect the strain characteristics, the analyses have employed a somewhat arbitrary poisson ratio equal to one. Since the true value of Poisson's ratio may be significantly less than the assumed value, design curves have been developed (Figure 60) to provide correction factors for Poissons ratio, $\nu = 0.5$. These curves were determined by ratio of calculated stress results when ν was varied in test case solutions for each h/d represented in the test program.

Design Curve Summary and Application

The design curves generated in this study and analysis are presented herein as Figures 53 thru 60 inclusive.

Utilization of the design curves in tent analysis is as follows·

1) From design requirements determine tent size and shape and design value for dynamic (or impact) pressure

2) Enter Figure 53, 54, or 55 with required h/d on the appropriate curve for dynamic pressure and read stress coefficients,

$$\frac{N_\phi}{q\,r} \text{ and } \frac{N_\theta}{q\,r} .$$

3) Enter Figure 60 and read stress factors,

$$\frac{N_\phi\,(\nu = 0.5)}{N_\phi\,(\nu = 1.0)} \quad \text{and} \quad \frac{N_\theta\,(\nu = 0.5)}{N_\theta\,(\nu = 1.0)} .$$

4) Multiply respective stress factors (from 3) by stress coefficients (from 2) to get stress factors for material with poissons ratio, $\nu = 0.5$. Products are corrected stress coefficients,

$$\frac{N_\phi}{q\,r} \quad \text{and} \quad \frac{N_\theta}{q\,r}$$

5) Multiply corrected stress coefficients (from 4) by design dynamic pressure, q, in p. s. i. and tent radius, r, in inches. Products are Stress Resultants N_ϕ and N_θ in pounds per inch.

6) If variation in N_θ with apex angle, ϕ, is desired, determine stress ratio,

$$\frac{N_\theta(\phi)}{N_\theta\,(\text{peak})},$$

from Figure 56, 57, 58 or 59 depending on appropriate h/d. Multiply stress ratios (from 6) by N_θ (from 5) to get variable values of N_θ versus apex angle, ϕ.

7) Total stress resultants are·

$$\overline{N_\phi} = N_\phi\,(\text{from } 5) + \frac{P_e r}{2}$$

$$\overline{N_\theta} = N_\theta\,(\text{from } 6) + \frac{P_e r}{2}$$

where P_e is internal pressure in p. s. i.

r is radius in inches.

3.8.6 Results - Cylindrical Shape with Spherical Ends (Broadside Wind Load)

All tests on tent models 2, 5, 6, 8, 9, . . . have been analyzed in accordance with paragraphs 3.8.3 and 3.8.4. The effects of internal pressure was inherently accounted for in these tests. The internal tent model pressure was set at 4/5 q, 1q, and 5/4 q for each series of tests for each wind velocity used. Broadside wind direction, normal to the cylindrical section centerline, creates the most severe loading condition and the largest fabric stresses. The aerodynamic pressure data gathered from these tests indicated much lower values for any wind direction other than broadside which substantiates what may be assumed by observation. The results of the calculations and conclusions are presented in the following two paragraphs.

3.8.6.1 Calculations

The maximum resulting stress coefficients

$$\frac{N_\phi}{q\,r}\ ,\quad \frac{N_\theta}{q\,r}\ \text{and}\ \frac{N_{\phi\theta}}{q\,r}$$

were calculated on Hayes IBM 1620 computer and are listed in tabular form in Table III for each test model considered. Test model No. 8 was chosen as being typical within the set and calculated values of stress coefficients versus the angle θ for test No. 118, tent pressure 4/5 q, q = .6, are presented in Fig. 61, 62, and 63 as calculated by methods outlined in paragraph 3.8.4.2. These results are typical of all models tested and thus presents all the necessary information required to develop design curves for tents that exist within the set, i.e., h/d ranging from 3/8 to 3/4 and w/ℓ_h ranging from 1/4 to 1.

The calculated results of $N_\phi/q\,r$ versus q are plotted in Figure 64 for all tests on Model No. 8 for both the cylindrical section and the spherical ends. The scatter of all results are included within the shaded area and a line of maximums bounding the upper limits describe the maximum stress level for any wind velocity up to 105 mph.

The calculated results of $N_\theta/\,q\,r$ versus q are plotted in Fig. 65 for all tests on Model No. 8 for the spherical ends. These results are interpreted as above, with one addition, the cylindrical section peak values are assumed constant longitudinally (in the direction of x) except at the interface.

The calculated results of $N_{\phi\theta}/q\,r$ versus q are plotted in Figure 66 for all tests on Model No. 8 for the spherical ends. These results are interpreted as before except the shear is assumed to be zero at the interface

and anywhere on the cylindrical section away from the base.

Figure 67 presents an illustration of all maximum values of $N_\phi / q r$ stress coefficients as typically presented in Figure 61 for Model No. 8 combined with the maximum calculated value for the cylindrical section for all tests at all wind velocities for every ϕ from 15° to 75.5°. The abscissa is divided as a function of d, the basic tent diameter, and the radius projection of various positions of θ in 15° intervals from 0° reference point to $\theta = 180°$ The purpose of this division is to allow a plot of maximum stress coefficients showing the distribution around an end, through the discontinuity region at the interface, and continuity in the cylindrical section. The rear side is split out and rotated 180° in order to better show the distribution. Only one half of the model is presented because of symmetric loading and results.

Figure 68 presents an illustration of all maximum values of $N_\theta / q r$ stress coefficients as typically presented in Figure 61 for Model No. 8 combined with the extension assumption that the cylindrical equilibrium forces are constant in the cylindrical section for all tests at all wind velocities for every ϕ from 15° to ϕ_B. The remaining explanation of the figure is stated in the preceding paragraph.

Figure 69 presents a cross plot of maximum $N_\phi / q r$ stress coefficient as a function of the angular position from $\phi = 0°$ to $\pm \phi_B$. These values are representative of all tests of Model No. 8 maximum interface stress coefficients considering discontinuity effects at the junction of the cylindrical section and the spherical ends where $\theta = 0°$ and 180°.

Figure 70 presents a cross plot of maximum $N_\theta / q r$ stress coefficient as a function of the angular position from $\phi = 0°$ to $\pm \phi_B$. These values are again representative of all tests of Model No. 8 maximum interface stress coefficients combined with the extension assumption that the cylindrical equilibrium forces are constant in the cylindrical section for all tests at all wind velocities at the junction of the cylindrical section and the spherical ends where $\theta = 0°$ and 180°.

3.8.6.2 Conclusions

The purpose of this presentation, as outlined previously is to develop design data curves from which the design of a cylindrically shaped tent with spherical ends can be made without undue labor or theoretical analysis of stresses. The figures presented in this part enable the design to predict maximum stress coefficients for various cylindrically shaped spherical ended tent sizes for wind velocities up to 105 mph.

Figures 71 thru 73 present a typical plot of stress coefficients

for specific dynamic pressures for W/ℓ_h equal to 1/2. These results represent an attempt to present design data to use as a means to arrive at interpolated values of the stress coefficients for various wind velocities. The curves thus presented represent a minimum of data points and cannot be relied upon to give accurate results. The final design curves described in the following paragraphs constitute the evaluation of data herein presented and should be used in any design problem

Maximum stress coefficients presented in Table III represent all maximums for all combinations of sizes and wind velocities. The scatter of results as illustrated in Fig. 64, Fig 65 and Fig. 66 proved that the maximum stress at any point can be predicted for any wind velocity by using a line of maximums which bound the scatter region for any specific model.

The resulting design curves (Ref Figs. 74 thru 82) presented herein utilize this method to predict maximum stress coefficients. The calculated stress coefficient maximums of all tests on all models include all of the specific results within its set and therefore the scatter of the maximums represent all of the results for any specific variation in proportional size.

Resulting stress coefficients in any portion of a cylindrically shaped spherical ended tent can be obtained by using the design stress coefficient curves presented in Figs. 74 thru 82. To use these curves, the designer would decide upon the proportions of size of the tent to be designed, either by aerodynamic considerations or other requirements, and choose the figure for the specific h/d ratio which applied to the given problem. After this the designer would then enter the graph upon the abscissa at the predetermined W/ℓ_h and read upward to either the curve labeled cylindrical section or spherical ends and determine the corresponding stress coefficient by reading across to the ordinate index.

Figure 71 presents the variation of maximum stress coefficient, $(N_\phi/q\,r)$ maximum, versus h/d for a constant $W/\ell_h = .5$, for any specific dynamic pressure (q), in the spherical ends.

Figure 71 presents the variation of maximum stress coefficient, $(N_\phi/q\,r)$ maximum, versus h/d for a constant $W/\ell_h = .5$, for any specific dynamic pressure (q), in the cylindrical section.

Figure 72 presents the variation of maximum stress coefficient, $(N_\theta/q\,r)$ maximum, versus h/d for a constant $W/\ell_h = .5$, for any specific dynamic pressure (q), in the spherical ends and the cylindrical section, assuming the extension of equilibrium forces to be constant.

Figure 73 presents the variation of maximum stress coefficient, $(N_{\phi\theta}/q\,r)$ maximum, versus h/d for a constant $W/\ell_h = .5$, for any specific dynamic pressure (q), in the spherical ends. The shear stress coefficients in the cylindrical section are assumed to be zero and their calculation has herein been neglected.

Figure 74, 75 and 76 present maximum stress coefficients, $(N_\phi/q\,r)$ maximum, versus W/ℓ_h ratios from $W/\ell_h = .25$ to 1.0 for both spherical ends and the cylindrical section of the tents for all broadside wind loads for h/d ratios of h/d = 3/8, 1/2 and 3/4 respectively. These design data curves will provide accurate results of stress coefficients for any tent with these particular proportional sizes for all load conditions. It must be remembered that the stress coefficients depicted from these curves do not represent the total stress condition. The effects of internal pressure must be added to these results

Figures 77, 78, and 79 present maximum stress coefficient, $(N_\theta/q\,r)$ maximum, versus W/ℓ_h ratios as stated in the preceding paragraph with the equilibrium extension applying throughout the cylindrical section.

Figures 80, 81 and 82 present maximum stress coefficients, $(N_{\phi\theta}/\,q\,r)$ maximum, versus W/ℓ_h ratios as stated above except in the cylindrical section where the assumed shear stress is zero.

Poissons Ratio

Poisson's effect upon the fabric stresses are discussed in preceding paragraph 3.8.5.2 and resulting design curves furnished in Fig. 60 The results given and manner in which the designer applied this to the cylindrically shaped spherical ended tent is exactly the same.

Design Curve Summary and Application

The design curves presented in this study and analysis are included as Figures 74 thru 82.

Utilization of the design curves in tent analysis is as follows

1) From design requirements determine tent size and shape and dynamic (or impact) pressure design value

2) Enter Figs 74 thru 79 (choosing the appropriate figure by knowing the h/d ratio) with the required W/ℓ_h and read stress coefficients, $N_\phi/q\,r$ maximum and $N_\theta/q\,r$ maximum for both the cylindrical section

and the spherical ends. For stress coefficient values which would exist for other sizes than those presented, linear interpolation within the range given will yield corresponding results.

3) Enter Fig. 60 and read stress factors N_ϕ (ν = 0.5) / (N_ϕ (ν = 1.0) and N_θ (ν = 0.5) / N_θ (ν = 1.0).

4) Multiply respective stress factors (from 3) by stress coefficients (from 2) to get stress factos for material with Poissons ratio, ν = 0.5. Products are corrected stress coefficients, $N_\phi / q\,r$ and $N_\theta / q\,r$.

5) Multiply corrected stress coefficients (from 4) by design dynamic pressure, q, in p.s.i. and tent radius, r, in inches. Products are stress resultants N_ϕ and N_θ in pounds per inch.

6) Total stress resultants are·

$\overline{N}_\phi = P_e r + N_\phi$ (from 5) Cylinder

$\overline{N}_\phi = P_e r/2 + N_\phi$ (from 5) Sphere

$\overline{N}_\theta = N_x = P_e r/2 + N_\theta$ (from 5) Both

3.9 PRESSURE DISTRIBUTION

The fabric loads analysis presented in Paragraph 3.8.2 was based on measured external pressure distributions obtained during the wind tunnel test series. The method of measurement chosen was to section the tent off by rows and columns. At the intersection of each row and column, a light weight tube was attached to the fabric on the inside of the envelope. A small orifice was then drilled through the fabric and into the tube thereby forming a surface static pressure tap. The number of pressure taps per tent model was determined primarily by the model size with some consideration being given to areas of constant pressure distribution. The location of the pressures taps for several models is presented in Fig. 83 and 84.

The method of measurement of the test pressures was discussed in Paragraph 3.1 and the details of data reduction in Paragraph 3 8. These tests indicate somewhat different pressure distributions than those around tower mounted radomes due to the presence of the ground plane. The boundary layer associated with the ground plane is discussed in Paragraph 3.1, however, it is noted that the boundary layer thickness was adjustable and was set at a value deemed reasonable for ground mounted structures A discussion of model similarity and data extrapolations is also discussed in Paragraph 3.1.

3.10 DATA REDUCTIONS

The data reduction program was divided into four categories aerodynamic balance data, anchor load data, external pressure distribution and tent model deflections. The data collected during each test was transferred to a prepared computer load sheet for automatic data reduction on the IBM 1620 computer located at Hayes International Corporation, Birmingham, Alabama. The equations, etc., used for this reduction are presented in the following sections.

3.10.1 Aerodynamic Coefficients

The total aerodynamics load and moment coefficients are defined as follows

Coefficient	Equation
Lift	$C_L = \frac{L}{qA_p}$
Drag	$C_D = \frac{D}{qA_p}$
Sideforce	$C_Y = \frac{P_y}{qA_p}$
Pitching Moment	$C_M = \frac{M}{qA_p \ell_m}$
Rolling Moment	$C_R = \frac{M_y}{qA_p \ell_r}$
Yawing Moment	$C_N = \frac{M_m}{qA_p \ell_m}$

The aerodynamic loads and moments used for computing the above coefficients are as follows

Component	Equation
Lift	$L = L_r - L_p - L_j$
Drag	$D = D_r - D_p - D_j$
Sideforce	$P_y = P_{yr} - P_{yp} - P_{yj}$
Pitching Moment	$M = M_r - M_p - M_j$
Rolling Moment	$M_y = M_{yr} - M_{yp} - M_{yj}$
Yawing Moment	$M_m = M_{mr} - M_{mp} - M_{mj}$

where

subscript "r" values are the total reading including contributions due to plate loads and jet flow loads, subscript "p" values are the plate loading contributions only. Subscript "j" values are the reactions due to the additional air flow into the tent enclosure during porous model tests. These values are slopes calculated from the data points in lbs. (or foot-lbs.) per in H_2O.

This program also computes the actual velocity from the tunnel indicated velocity, corrected for pressure, temperature, and Reynolds number as follows·

$$U = \sqrt{\frac{2q}{\rho}} \qquad \text{Velocity}$$

$$R_N = \frac{\rho U d}{\mu} \qquad \text{Reynolds Number}$$

Additional corrections were made to the data for the effects of the wind tunnel boundary conditions. The boundary corrections required for the special case of a model mounted on a ground plane were reduced to two These were solid blocking and horizontal bouyancy. The equations used are as follows

$$U_\infty = U_u \quad (1 + \epsilon_{SB})$$

$$q_\infty = q_u \quad (1 + 2\epsilon_{SB})$$

$$R_{N\infty} = R_{Nu} \quad (1 + \epsilon_{SB})$$

$$C_L = C_{Lu} \quad (1 - \sigma - 2\epsilon_{SB})$$

$$C_M = C_{Mu} \quad (1 - 2\epsilon_{SB}) + \frac{\sigma C_L}{4}$$

$$C_D = C_{Du} \quad (1 - 3\epsilon_{SB})$$

where

subscript "u" terms are the uncorrected data based on wind tunnel upstream conditions.

$$\epsilon_{SB} = \frac{K(\text{model volume, } \overline{V})}{(A_c)^{3/2}}$$

$$\sigma = \frac{\pi^2}{4^2} \left(\frac{d}{h}\right)^2$$

where

K - is a constant = 0 96 for bodies of revolution

A_c - wind tunnel cross section area

d - diameter of model used

h - height of wind tunnel test section

The drag coefficient, C_{Du}, based on free stream conditions includes a correction for horizontal bouyancy. This correction was made as follows

$$C_{Du} = \frac{D - D_B}{q_u A_p}$$

where

$$D_B = -\frac{dp}{dl} \quad \text{(model volume)}$$

$\frac{dp}{dl}$ = slope of tunnel longitudinal static pressure curve

D = net drag

q_u = free stream dynamic pressure

A_p = reference area, maximum planform.

Model volume for single wall models was computed as follows

$h > d/2$,

$$\overline{V} = \frac{\pi}{6} d^3 - \frac{\pi}{48} d^3 + \frac{\pi}{3} r_B^2 (h - d/2) + \pi r_2 (\ell - 2r) - \frac{r_2}{2} (\theta - \sin\theta) (\ell - 2r)$$

where

$$r_B = r^2 - (h - d/2)^2$$

$h < d/2$,

$$\overline{V} = \frac{2}{3} \pi h \left(\frac{d}{2}\right)^2 - \frac{\pi}{3} r_B^2 (d/2 - h) + \frac{r^2}{2} (\theta - \sin\theta) (\ell - 2r_B)$$

where

$$r_B = r^2 - (h - d/2)^2$$

$h = d/2$

$$\overline{V} = \frac{\pi}{12} d^3 + \frac{\pi}{2} (r)^2 (\ell - 2r)$$

where

r = model radius

h = model tent height, feet

d = model diameter, feet

r_B = base radius

θ = base angle

ℓ = length

The maximum planform area for single wall models was computed as follows

$$A_p = \pi r^2 + 2r (\ell - 2r)$$

where

r = model radius, in feet

A_p = planform area

In the equations for volume and the equations for planform area, model radius and diameter divided by 2 were considered independent numbers in order to make the equations apply to both spherical and cylindrical models.

The final correction made to the aero balance data was to transform from wind axes to body axes for models oriented at yaw angles of $\psi = 45°$. The relationship between wind axis and body axis is presented in Figure 12". For $\psi = 0°$ and $90°$ no correction was necessary.

The equations used were as follows

Coefficient	Equation
Lift	$C_{LB} = C_L$
Drag	$C_{DB} = C_D \cos\psi - C_Y \sin\psi$
Sideforce	$C_{YB} = C_Y \cos\psi - C_D \sin\psi$
Pitching Moment	$C_{MB} = C_M \cos\psi - C_R \sin\psi$
Rolling Moment	$C_{RB} = C_R \cos\psi - C_M \sin\psi$
Yawing Moment	$C_{NB} = C_N$

3 10 2 Pressure Coefficients

The pressure distribution data were reduced to coefficient form in accordance with the following equation·

$$C_p = \frac{P - P_\infty}{q_\infty}$$

where

C_p - pressure coefficient

P - pressure at model surface

P_∞ - tunnel static pressures

The values of pressure at the model surface were measured at many points on the model surface. The relative locations of these points varied from model to model. Typical locations are presented in Figures 83 and 84.

3.10.3 Anchor Load Coefficients

Individual anchor loads and anchor load coefficients were computed for each active anchor used. The anchor loads were computed by first calibrating each active anchor with four (4) known loads of 1 lb., 6 lb , 11 lb., and 16 lb. The slope of the calibration curve obtained was then computed in lb. /micro inches per inch load and multiplied times the strain recorded for that anchor under the test condition considered. The anchor load coefficient was then computed as follows

$$C_{AL} = \frac{AL}{q A_p}$$

where

P_{AL} - anchor load, lbs.

q - dynamic pressure, lbs /ft.^{2}

A_p - reference area, ft.^{2} (Projected Frontal Area)

The anchor loads were summed for all test conditions and printed on the output sheet as total anchor loads. These loads were corrected for inflation loads and printed out as aerodynamic loads. The aerodynamic loads shown include a correction for the fact that not all anchors were "active", or measured strain. This correction was a multiplication factor composed of a ratio of total to active anchor points employed.

The inflation loads used were computed by recording the strain for each anchor corresponding to tent pressures of 2 in., 4 in., and 6 in. of water and converting these anchor loads by multiplying by the slope of the calibration curve for each gage. These individual loads were then summed to give total inflation loads for all test conditions. Figures 81 and 89 present the planform lay-out of the active anchor locations for two models.

SECTION 4

FABRIC MATERIALS

4 1 SELECTION

The increasing use of fabrics for engineering materials in air supported structures where weight, durability, and reliability are important has emphasized the need for, first, the careful selection of fabrics for mechanical strength, and second, the selection of coatings for seam strength, cold weather flexibility, and increased durability In addition, good quality control is essential to insure uniformity of product The structural data presented in this design manual show that each structure and its intended use presents special and unique engineering problems The full potential of lightness in weight, durability and reliability of a structure can only be realized by engineering a fabric to match the exacting mechanical and environmental conditions of use specified for the tent

The selection of a fabric meeting the exacting and use conditions for a tent must be based on a critical evaluation of all fiber and fabric properties A comprehensive review of even the most essential fabric characteristics is beyond the scope of this manual The information relative to fabric properties can best be obtained from fiber and fabric manufacturers, military specifications and from literature (11, 12, 13, 14) However, fabric engineering can be only as effective as the extent that information relative to the desired characteristics of a fabric is known Since this manual provides the necessary information to determine the strength of fabric required for a given structure, the stress-strain behavior of fibers and fabrics is considered pertinent and is included for ready reference The relationship between tensile strength and weight of fabrics is also given The strength-weight relationship is necessary to establish the weight of fabric required for the tent, and to estimate the weight of the final structure Two other fabric properties which can restrict the selection of coated fabrics for air supported tents are mentioned briefly because of their interest to the Military and the satelite and communications industry The two fabric properties are low temperature flexibility and dielectric constant

Fiber Type The Army and Air Force have to date found nylon and polyester fibers more satisfactory for air-supported tent fabrics than fiberglas, acrylic, modacrylic and cellulose type fabrics Both fibers have a high strength to weight ratio. The two fibers can be used to produce thin, flat fabrics of high strength Thin, relatively flat

fabrics are essential for light weight coated fabric, since the thickness of fabric controls the amount and therefore the weight of coating compound required to fill the interstices and protect the fabrics Nylon and polyester fibers are still considered the more acceptable fibers to use for air supported tents. However, fiber producers are continually improving their fibers, and the three other fiber types which show promise for future use are included The additional fibers are glass fiber, acrylic, and polypropylene. Of these, glass fiber is not new It is a high strength, low elongation fiber It has better weathering and chemical resistance properties than either nylon or polyester It has been used as a radome fabric, but was found to crack on sharp creases which occurred in the fabric as a result of folding the tent for storage. Glass fiber technology has improved, and modern glass fabrics show an improved resistance to cracking in folds Acrylic fibers are included because of their better weathering resistance and radio frequency transmission characteristics when compared to nylon and polyester. The potential field of applications for acrylic fibers is in the relm of extremely low porosity, uncoated fabrics for single wall air supported tents. High tenacity polypropylene is included because of its high resistance to abrasion and good mechanical properties. For a plain weave polypropylene fabric, the strength to weight ratio was found to be higher than that of nylon and polyester fabrics However, its strength degrades rapidly on weathering and the fabric can only be used with a protective coating. To date, difficulty is experienced in attaining a satisfactory adhesion of coatings to polypropylene. As soon as a satisfactory solution can be found for coating polypropylene fabrics, its high strength to weight ratio will make possible still lighter weight fabrics than can be attained with present day nylon and polyester fibers.

4 2 CHARACTERISTICS

Fiber Strength Characteristics - The load-elongation behavior of the five fiber types are shown in Figure 88 The unit for load in both figures is fiber tenacity in grams per denier. To convert the load-elongation curves to the standard engineering stress-strain curves, it is necessary to convert fiber tenacity in grams per denier to tensile strength in pounds per square inch. The conversion factor for this is shown in the Wellington Sears Handbook -11 as follows

$$\text{Tensile Strength (psi)} = 12,800 \times \text{sp gr} \times \text{Tenacity (gpd)}$$

It is readily apparent from the load-elongation curves that, except for glass fibers, the fiber elongation is not linearly proportional to the applied load. Each curve shows an initial elastic region at

low elongation followed by a complex flow and stiffening characteristic as the fiber is elongated to rupture. To obtain an appreciation for fibers with non-linear load elongation characteristics, reference is made to Dr Susich's work on the mechanical conditioning of fibers In his paper, Dr Susich compares the load-elongation characteristics of fibers after repeated loading at several predetermined extensions The results are reported in terms of the length recovered after the load is removed The results are given in percent of initial length Dr Susich uses three terms to describe the load recovery properties of fibers, the first is percent of length recovered immediately after removal of the load, Immediate Elastic Recovery (IER), the second term represents the contraction of fiber length at some time after the removal of load, Delayed Recovery, (DR), the third term represents a permanent extension of the fiber after the load is removed, Permanent Set (PS) The results Dr Susich found for the fibers considered in this manual were extracted from his report and presented in Table IV It should be noted that the relative proportion of each type of deformation varies with percent of elongation, the higher the percent of elongation, the lower the elastic recovery and the higher the permanent set. This is characteristic of viscoelastic material A detailed interpretation of the fiber load elongation curve is beyond the scope of this manual This information is summarized in the Wellington Sears Handbook (11) and in selected individual papers

The information provided by the fiber load-elongation curve is useful for predicting, as a first approximation, the strength and energy absorbing characteristics of the fabric Hence these can be used to select the fiber type which will best fulfill the particular engineering application

Fabric Strength Characteristics - The load elongation characteristics of a fabric differs from that of its component fiber The load elongation curves for nylon fiber and fabric is shown in Figure 89 and that for Polyester on Figure 90. The unit for load is given as a percent of rupture load for convenience in comparing fiber and fabric curves. In order to obtain a better understanding of the difference in fiber and fabric curves, a brief review of the behavior of fabrics under stress is in order

Dr Haas considered the deformation of a plain weave fabric to be the result of three distinct but mutually interacting mechanisms The first of these is thread shear, where the mutually perpendicular warp and filling yarn rotate, changing the angles between the yarns, the second mechanism is termed thread straightening and results from the over and under characteristics of the plain weave, each set of yarns

bending over the other set This bending is also known as crimp When the loads are applied to the two yarn systems, the system under the highest stress will tend to straighten transferring part of its crimp to the other set of yarns This mechanism is termed crimp interchange The third mechanism is that of yarn extension within the weave Pierce and others have identified a fourth mechanism which will influence the load elongation behavior of a plain weave fabric This is concerned with the compressive properties and the bending stiffness of the yarn Each yarn is subjected to both lateral compression and bending at every thread crossing Lateral compression causes the yarn to flatten under load and allows the weave to extend, and bending rigidity in increased resistance to extension of the weave

The sequence with which the interacting mechanism operates is assumed to be as follows when the load is first applied, the mechanisms of shear and crimp interchange predominate These two mechanisms operate by a geometric rearrangement of the yarns in the weave rather than by yarn extension Thus, the results of initial fabric deformation under load is independent of the rheological properties of the fiber. This mechanism is indicated in Figure 89 and 90, by the fabric exhibiting a greater extension at break than the fiber This is due primarily to the crimp in the yarns Filling yarns having a greater initial crimp will show a greater extension at all loads As the loads are increased, the strain due to shear and crimp interchange reaches a limiting value which is governed by the limiting extension of the fabric The limiting extension is reached sooner in a densly woven fabric, such as the polyester, Figure 89 than in fabrics of a looser construction such as the nylon fabric, Figure 90 This phenomenon is best illustrated by examining the filling yarn extension for both fabrics The polyester filling yarn curve shows a steeper slope at low loads than the nylon filling curve Increasing the load at this point will lead to yarn extension and yarn flattening The latter two mechanisms predominate as the stress applied approaches the rupture load Also tensile fibers are viscoelastic material. Hence, where fabric loads reach a level where yarn extension occurs within the fabric, the results of strain becomes time dependent and thus extension results can vary with the rate of loading of the material. This is particularly important when rupture strain is considered. If the rate of increase of loading is slow, there is more time for creep to occur and the breaking extension can be reached at a lower load

From the above, it is evident that the load elongation response of a fabric can be highly influenced by the modes with which the loads are applied and the time rate of loading Further, the mechanical behavior of fabrics in air supported structures, where the fabrics are

simultaneously stressed in all directions, cannot be fully predicted on the basis of uniaxial stress data shown above. It is in this area of study, relative to the mechanical behavior of fabrics under biaxial stress condition, that much work remains to be done A more comprehensive and accurate theory of the mechanism of fabric stress behavior at low loads, and at increasing loads to rupture, would be of considerable value in developing fabrics of minimum weight for a given structural application Studies in this area are underway and will be included in this section as results become available

To provide the fabric weight relationships required for this manual, it is necessary to evaluate the rupture load of a series of plain weave fabrics for each of the fiber types listed below The rupture load for each fabric is divided by the fabric weight Therefore the units of the weight-strength relationship developed are pounds-square yard per inch-ounce

In this manual safety factors will be introduced which will enable the use of the full fabric values shown in Table III.

It should be recognized that the strength in pounds per inch per ounce of fabric represents the fabric rupture loads The percent of rupture load which can be fully utilized in order to reduce the weight of the fabric cannot at this time be accurately determined Experience with radome construction has indicated that base fabric loads, as determined from the radome manual and before the addition of a safety factor, can be as high as 20% of the rupture load of the fabric At this level of rupture load, fabric extensions are easily obtained and found to vary considerably even with fabrics produced according to a given Military specification. Hence, it is difficult to determine the percent of yarn extension from fabric load elongation curves alone With the development of an accurate theory of the mechanism of fabric deformation it may be possible for the designer to exercise his engineering judgement and use a higher percentage of the breaking load, leading to lighter weight fabrics However, each of these problems becomes an individual determination relying fully upon the load elongation characteristic of the fabrics and the fiber

Low Temperature Flexibility The military requirement for tents to be operational at -65F is a difficult one to meet for coated fabrics. MIL-C-43086 is the specification for vinyl coated nylon fabric developed for air supported tents for use in the temperate zone. It is recommended for use with temperatures no lower than -10F The weight of thermoplastic vinyl coating for both durability and seam strength is 8 ounces per square yard for light weight fabrics and 15

ounces for heavier fabrics as shown in Figure 91 The solid line shows the estimated amount of vinyl coating required as a function of base fabric weight for single ply fabrics The dashed line shows the estimated amount of coating required for two ply fabrics

MIL-C-43285 is the specification for chloroprene-chlorosulfonated polyethylene coated nylon or polyester fabric developed for tents designed for arctic use The weight of thermosetting chloroprene base coating and chlorosulfonated polyethylene top coating was found to be 10 ounces per square yard as shown in Figure 91 The small dash line represents a single fabric, the dash dot line represents the 2 ply fabric

It should be pointed out that the coating weights as shown in Figure 91 represent an estimated average weight The actual amount and the distribution of coating face to back of the fabric depends on end use conditions Each problem becomes a matter for individual determination relying fully on durability and seam strength data, which must be obtained to insure integrity of the tent

It should be noted that while the chloroprene, chorosulfonated polyethylene coating is considered by the Army to be the best cold weather coating for air supported tents, the flexing of this coated fabric, is restricted to temperatures no lower than -40F There is an urgent need for a durable low temperature coating compounds which will remain flexible at -65 and which can be joined with a seam strong enough to withstand the tension loads developed by air supported tents

Dielectric Constant A low dielectric constant is necessary for good radio frequency (RF) transmission, an essential requirement for air supported radomes housing operating radar equipment. In the past the rough rule of thumb guide to good RF transmission was to keep the thickness of the fabric small in comparison to the wavelength and to use fabrics and coatings with low dielectric constants Reference is made to the publication "Studies of Quantitative Correlation between Bulk Density and Thickness of Fabrics and their Radar Transmission Characteristics," for a more complete coverage of the electrical characteristics of fabrics

SECTION 5

CONCLUSIONS

As a result of the wind tunnel tests and analyses represented herein, certain conclusions relative to ground mounted air supported tent design and operation may be made These conclusions are listed below in very brief form

1. Stable single and double wall air-supported tent configurations have been successfully tested up to wind velocities of 105 miles per hour.

2. Of the major design variables investigated (other than type and shape factors), which included fabric porosity, operating pressures, cell size and guy line arrangement, operating pressures are most important.

3. The use of porous fabric in single wall tent construction produced the following general tent characteristics.

   a. Tent lift increased with an increase in fabric porosity for spherical and cylindrical tents with a 1 2 W/ℓ_h and decreased for tents with a 1 4 W/ℓ_h.

   b. Tent drag decreased with increased porosity for spherical tents and increased for cylindrical tents.

   c. Low porosity fabric reduced tent deflection slightly with no marked improvement in tent stability.

4. The following tent deflection characteristics prevailed

   a. Minimum tent deflections for single wall tents occurred at a height to diameter ratio of one-half for all tent configurations.

   b. As would be expected, tent deflection was greatest in the frontal, windward sector of the tent.

   c. Spherical single wall tents have smaller overall deflections than the cylindrical tents.

   d. For the double wall tents, an increase in cell size, i.e., cell width to enclosure diameter ratio, increased tent rigidity and resulted in less tent deflection.

   e. For the double wall tents, a guy line configuration wherein lines are attached at 0.80 and 0.40 tent height and have angled corner

lines produced smallest deflections

5. Tent enclosure and cell pressures and cell size are all important factors affecting tent stability. Tests concluded that

   a. For satisfactory tent stability characteristics, single wall enclosure and double wall cell pressures of at least free streams dynamic pressure are required

   b. Enclosure pressures equal to ambient static or greater pressure must be maintained in double wall tents to preclude early tent buckling

   c. The stability of cylindrical double wall tents was found to be less than for cylindrical single wall tents, believed to result from flow conditions around the double wall tent flat ends

   d. No significant gains in double wall tent stability were achieved beyond a cell pressure of sixteen inches water gage.

   e. Proper guy line arrangement provides some additional stability at recommended operating pressures. The best guy line configuration tested consisted of a combination high (0.8 tent height) and a low (0.4 tent height) line arrangement.

6 Stress analyses of spherical and cylindrical single wall tents within proportions tested can be accomplished using the design curves developed in this study for the Design Manual for Ground Mounted Air-Supported Structures (single and double wall). Basic design curves are based on an assumed fabric poissons ratio of 1.0. Provision is included for stress evaluations when poissons ratio is 0.5. Stress variation with apex angle, ϕ, can be determined for spherical shaped tents. Additional theory development and analysis is needed to refine stress profiles on cylindrical models.

7. In the strength analysis of the double wall tent, the maximum stress resultants were found in either the hoop or web stresses. Hoop stresses were greatest when cell angle, α_c was greater than 30° and when α_c was less than 30°, the web stress is greatest. Meridional stress resultants were smaller than the other components in both cases.

   Fabric stresses were found to increase with an increase in cell width to tent diameter ratio and with an increase in cell pressure.

SECTION 6

RECOMMENDATIONS

The following areas of investigation warrant further study and testing as a result of the information obtained from this program in order to increase the utility and accuracy of the design data presented herein.

1. Additional double wall tent tests are required to as firmly establish the data variation with tent shape parameters as for the single wall case

2. The effects of adjacent tents or structures on tent loads and stability characteristics were not measured during these tests and possibly should be evaluated in future tests.

3. Wind tunnel tests should be performed on selected single and double wall tents configurations to obtain vibrational characteristics which can be used to evaluate fabric fatigue.

4. Full scale tentage tests should be made to evaluate Reynold's member effects on tentage data presented in Part II of the design manual

5. Short radius (ends) single and double wall tents should be wind tunnel tested to determine design feasibility, especially any beneficial deflection and stability characteristics when replacing double wall flat end tents.

BIBLIOGRAPHY

1 Bird, Walter W , "Design Manual for Spherical Air Supported Radomes", (Revised) Report No UH-909-D-2, Cornell Aeronautical Laboratory, March, 1956

2. Bicknell, J and Yeghiayan, R , "Wind Tunnel Tests on an Air Supported Tent Model," Report No 1024, Massachusetts Institute of Technology, June, 1963

3 Pope, Alan, "Wind Tunnel Testing," Second Edition, John Wiley and Sons, Inc

4 Liepmann, H W and Roshko, A , "Elements of Gasdynamics," John Wiley and Sons, Inc , 1957

5 Dwinnell, J H , "Principles of Aerodynamics," McGraw-Hill Book Company, Inc , 1949

6 "Ground Radome Study, Final Report," WDL-TR-1936, Philco Western Development Laboratories, Palo Alto, Calif , December 1962

7 Sevin, Eugene, "Analytical and Experimental Studies of Spherical Rigid Ground Radomes," Final Report 8154, Armour Research Foundation, February 1961

8 Foerster, A F., "Stress Distribution and Stability Criteria of Spherical Ground Radomes Subjected to Wind Loads," Proceedings of the OSU-WADC Radome Symposium, WADC-TR58-272, Vol 1, Ohio State University, June 1958

9 Timeshenko, S , Theory of Plates and Shells, McGraw Hill Book Company, Inc , New York, 1940

10 Flugge, Wilhelm, Stresses in Shells, Springer-Verlag, Berlin/Gottingen/Heidelberg, 1962

11. Wellington Sears Handbook of Industrial Textiles, Wellington Sears Company Inc., 1963

12 ASTM Committee D-13 ASTM Standards on Textile Materials, American Society for Testing Materials, 1964, Philadelphia, Pa

13 American Association of Textile Chemist and Colorists, Technical Manual of the American Association of Textile Chemist and Colorists, Vol 40, Howes Publishing Co., Inc , New York, 1964

14 Federal Specifications, Textile Test Methods CCCT191, General Services Administration, Business Service Center, Region 3, Washington 25, D C , 1951

15 Cornel Aeronautical Laboratory, Inc , Design Manual for Spherical Air Supported Radomes Revised Contract AF 30(602)-976, Rome Air Development Center, Griffiss Air Force Base, Rome, New York, ASTIA Report No UB-909-D-2 (1958)

16 Monego, C J , Air Supported Tents for Military Use

17 Monego, C J , Studies of Quantitative Correlation Between Bulk Density and Thickness of Fabrics and Their Radar Transmission Characteristics, U S Materiel Command, U S Army Natick Laboratories, Natick, Mass

18 Susick, G and Barker, S , Tensile Recovery Behavior of Textile Fibers, Textile Research Journal 21, pg 482, 1951

19 Hamburger, W J., Morgan, H M., and Platt, M M , Mechanics of Elastic Performance of Textile Materials, Part X, Some Aspects of Elastic Behavior at Low Strains, Textile Research Journal 22, pg 695, 1952

20 Dupont, E I de Nemours & Co , Tensile Stress-Strain Properties of Fibers, Bulletin X-82, May 1958

21 Haas, R Dietzem, National Advisory Committee for Aeronautics Report No 16, Anual Report, 1917, pg 144-271, Published by Springer Verlag Berlin, 1912, translated by Darrow, K K originally

22 Pierce, F T , "The Geometry of Cloth Structure," Journal Textile Institute, 28 p T45, 1937

23 Monego, C J , "The Biaxial Stress-Strain Behavior of Fabrics," Presentation Before the Fiber Society in Wilmington, Delaware, 5 October 1964

24. Textile World, Man-Made Fiber Chart, McGraw Hill Publishing Company, Inc , New York, 1964

25 Crory, F , Reed, R , Tezzard, W , and Font-Journey, G , Installation and Testing of Arrowhead Universal Ground Anchors in Frozen and Thawed Ground, U S Army Cold Region Research and Engineering Laboratory, Hanover, New Hampshire, 1964.

26 Marks, Lionel, S , Mechanical Engineers Handbook, McGraw Hill Book Company, Inc , New York 1941

TABLE I

TENT MODEL SIZES FOR PHASE I TESTS

Single-Wall Tents										
Model No	1	2	3, 15	4, 10, 13	5, 11, 14	6	7	8	9, 12	21
Configuration	3/4 Sphere	3/4 Cyl	3/4 Cyl	1/2 Sphere	1/2 Cyl	1/2 Cyl	3/8 Sphere	3/8 Cyl	3/8 Cyl	7/8 Sphere
Width to Length Ratio	-	1 2	1 4	-	1 2	1 4	-	1 2	1 4	-
Width	27 0	15 8	11 2	30 8	19 4	13 8	37 2	22 0	15 4	23 4
Length	-	34 9	46 1	-	42 8	57 1	-	49 6	66 5	-
Height	20 3	11 9	8 4	15 4	9 7	6 9	13 9	8 6	6 0	20 5
Radius	13 5	7 9	5 6	15 4	9 7	6 9	18 6	11 4	8 0	11 7

Double Wall Tents					
Model	16	17, 22-26	18	19	20
Configuration	3/8 Cyl	3/4 Cyl	3/4 Cyl	1/2 Cyl	1/2 Cyl
Width to Length Ratio	1 1	1 1	1 2	1 2	1 4
Width	31 1	22 4	15 8	19 4	13 8
Length	31 1	22 4	34 9	42 8	57 8
Height	12 1	16 8	11 9	9 7	6 9
Radius	16 1	11 2	7 9	9 7	6 9

NOTES

1 All dimensions are in inches

2 Models 1 thru 9 and model 21 are non porous, single wall

3 Models 10 thru 15 are porous, single wall

4 Models 16 thru 20 and 22-26 are non porous, double wall

TABLE II

Comparison of Double Wall Model Cell Sizes

Model	Enclosure Diameter	Cell Width	Cell Width / Enclosure Diameter	Cell Size / Model No 17 Cell Size
# 17*	19 5"	1 60"	0 082	1
# 22	19 5"	1 60"	0 082	1
# 23	18 25"	2 25"	0 123	1 5
# 24	17 00"	2 80"	0 164	2
# 25	18 25"	2 25"	0 123	1 5
# 26	19 5"	1 60"	0 082	1

* Reference Model #17

Note All the above tents had overall width of 22. 4".

TABLE III - MAXIMUM STRESS COEFFICIENTS
ALL TESTS - MODELS LISTED

CYLINDRICAL SHAPE WITH SPHERICAL ENDS
CONDITION BROADSIDE WIND LOAD

Model No.	h/d	W/ℓ_h	*	(N_ϕ/qr) Max.			(N_θ/qr) Max			$(N_{\phi\theta}/qr)$ Max.		
				q = .6	q = 3.0	q = 6.0	q = .6	q = 3 0	q = 6 0	q = .6	q = 3.0	q = 6.0
2	3/4	1/2	S	1.436	1.447	1.532	1.339	1.384	1 464	1.356	1.249	1.306
			C	.737	.820	.818	1.339	1.384	1.464	0	0	0
5	1/2	1/2	S	1.433	1.322	1.159	1.382	1.217	1.108	.669	.646	.546
			C	.796	.494	.571	1.382	1.217	1.108	0	0	0
6	1/2	1/4	S	1.235	1.503	-	1.100	1.418	-	.615	.679	-
			C	.525	.651	-	1.100	1.418	-	0	0	0
8	3/8	1/2	S	1.237	1.167	1.177	1.251	1.256	1 296	.548	.491	.520
			C	.907	.679	.712	1.251	1.256	1.296	0	0	0
9	3/8	1/4	S	1.485	1.829	-	1.552	1.936	-	.659	805	-
			C	.804	.789	-	1.552	1.936	-	0	0	0

*S - Spherical Results, C - Cylindrical Results

Table IV

Load Recovery Properties of Fibers

From Susich & Backer

Cond \ Fiber	Polyester	Nylon	Spun Acrylic	Filament Acrylic*	Glass Fiber**	Polypropylene*
	At 5 % Strain					
IER***	38	38	42	NA	-	NA
DR***	52	59	30	NA	-	NA
PS***	10	3	28	NA	-	NA
	At 10% Strain					
IER	27	28	27	NA	-	NA
DR	46	67	43	NA	-	NA
PS	27	5	30	NA	-	NA
	At 50% of Elongation at Break					
IER	28	27	30	NA	78	NA
DR	50	67	45	NA	19	NA
PS	22	6	25	NA	3	NA
	At 50% of Breaking Tenacity					
IER	33	29	33	NA	78	NA
DR	52	67	52	NA	19	NA
PS	15	4	15	NA	3	NA

* Data not available

** Breaking extension 5%

*** IER Immediate Elastic Recovery, DR Delayed Recovery, PS Permanent Set.

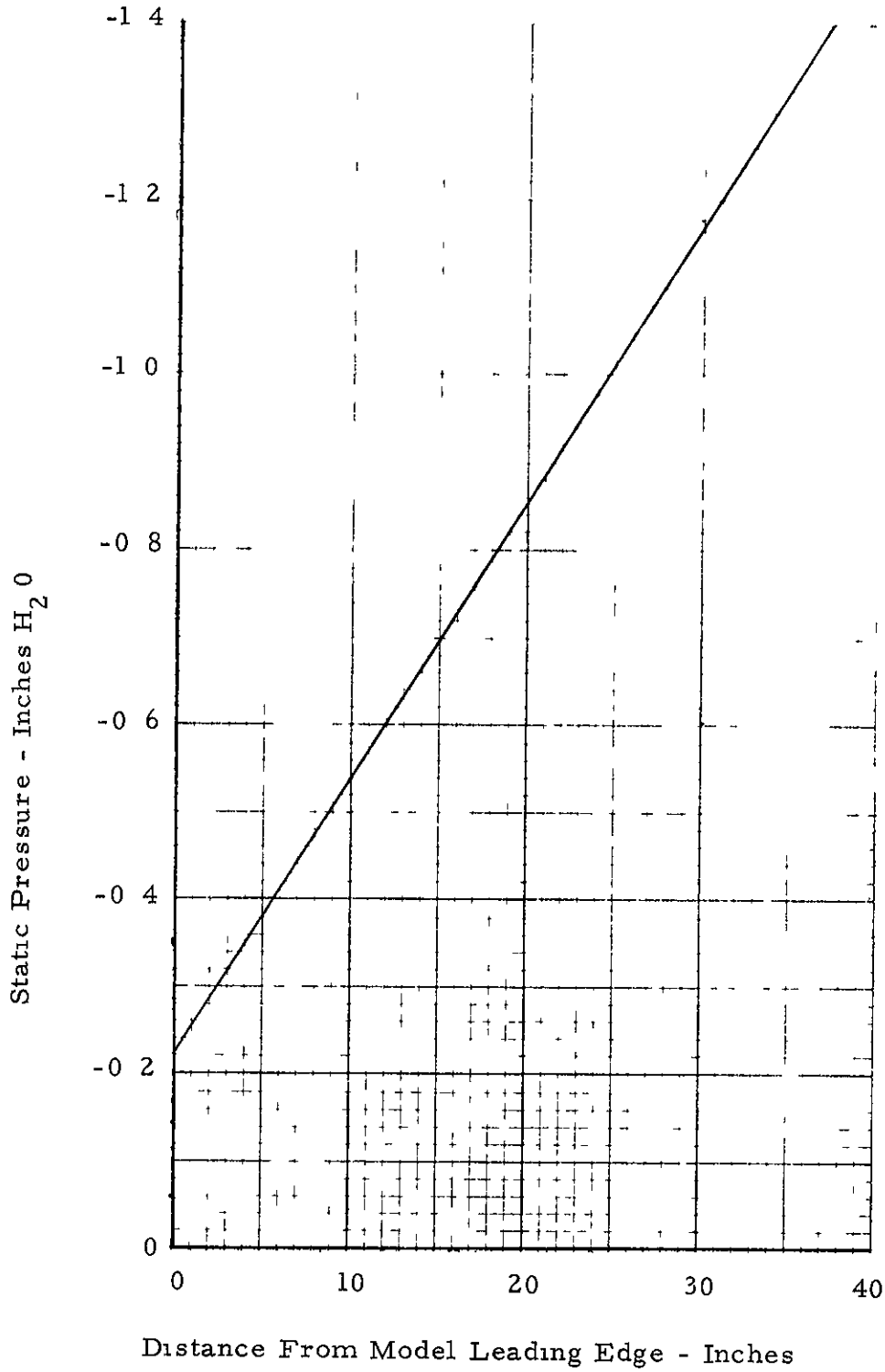

Figure 1 - Wind Tunnel Static Pressure Gradient

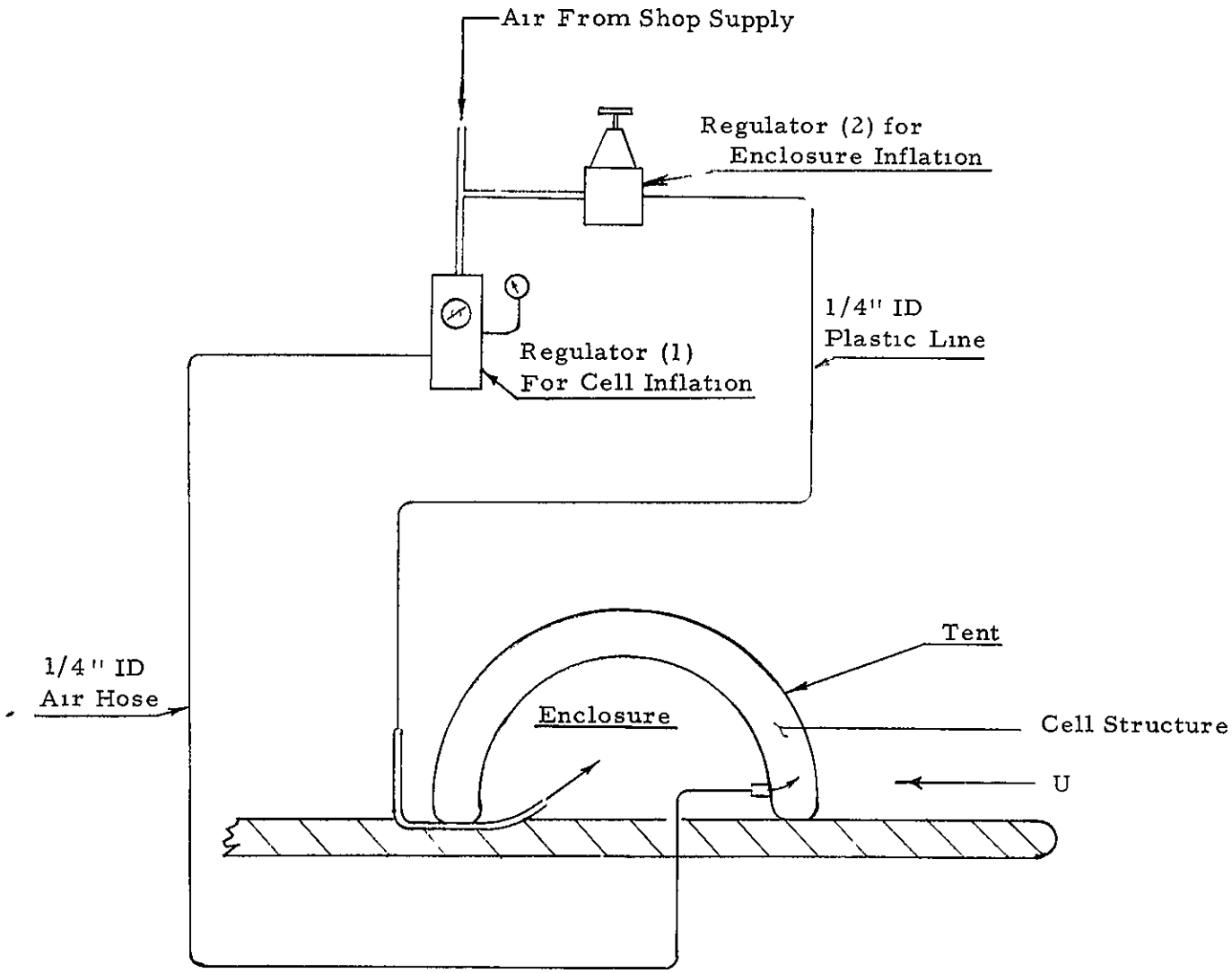

Figure 2 - Tent Inflation Schematic

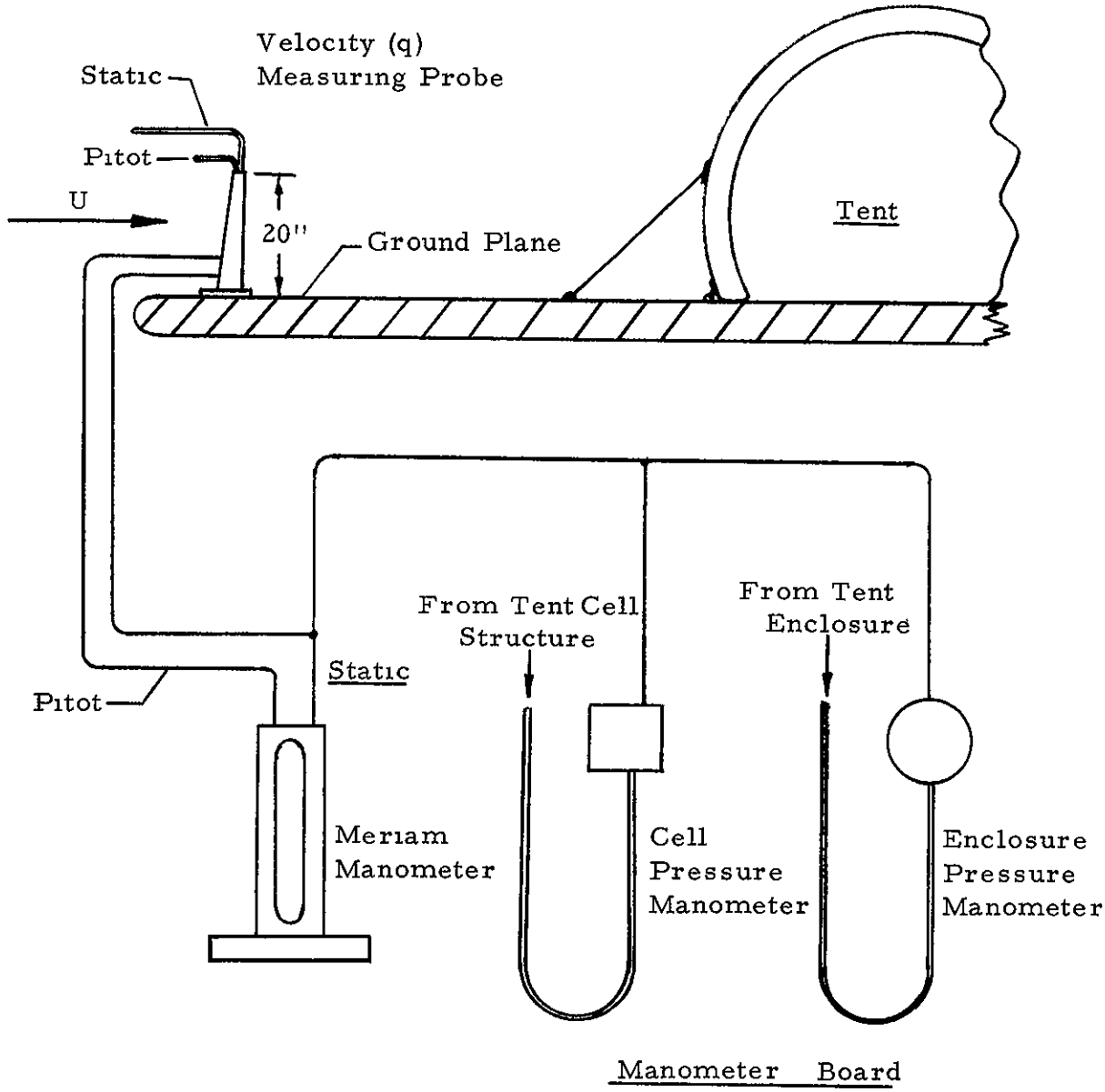

Figure 3 - Pressure Instrumentation Schematic

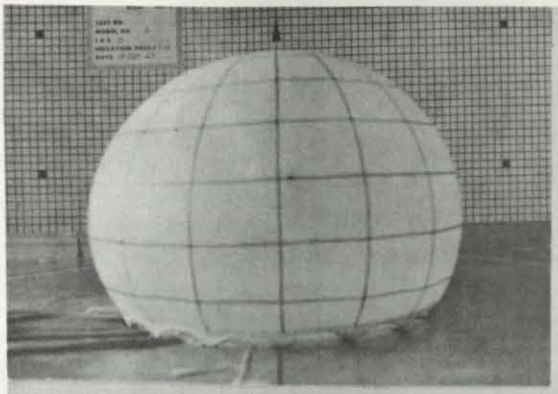

Model No. 1
3/4 Sphere

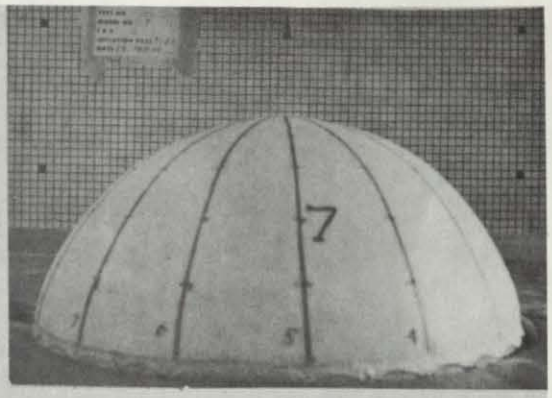

Model No. 7
3/8 Sphere

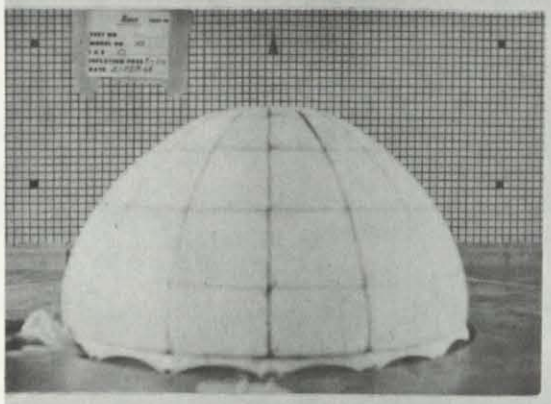

Model No. 10
1/2 Sphere

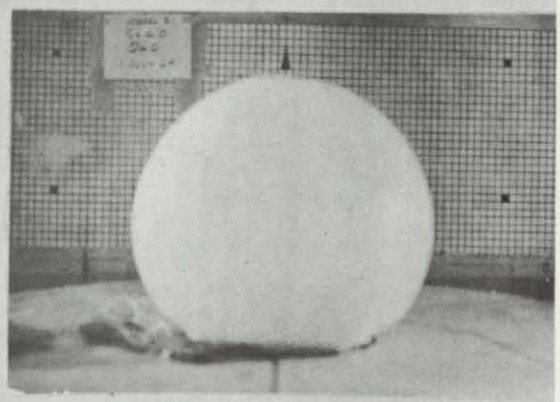

Model No. 21
7/8 Sphere

Figure 4. – Photographs of Single Wall Spheres

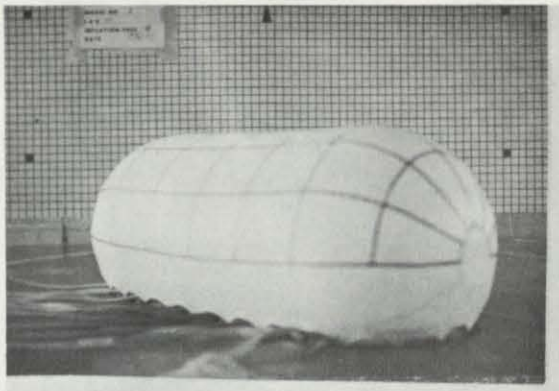

Model No. 2
3/4 Cylinder

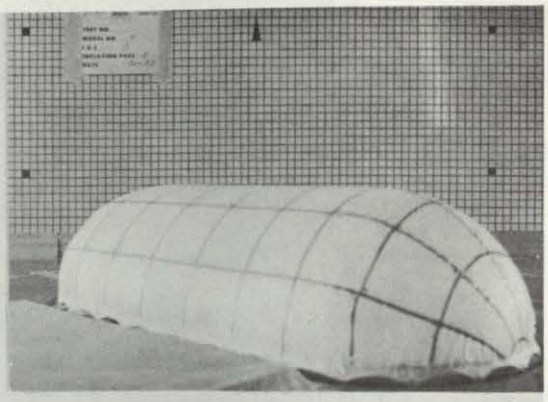

Model No. 5
1/2 Cylinder

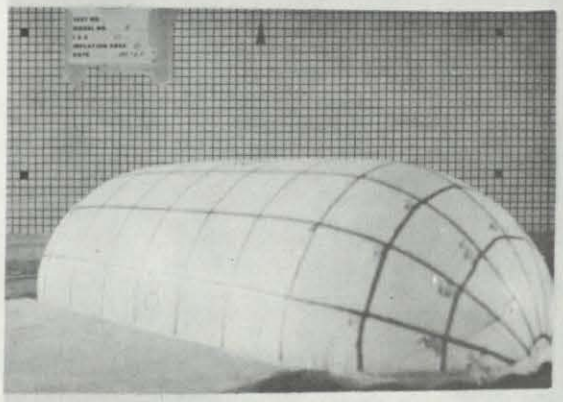

Model No. 8
3/8 Cylinder

Figure 5. — Photographs of Single Wall Cylinder, $W/\ell_h = 1/2$

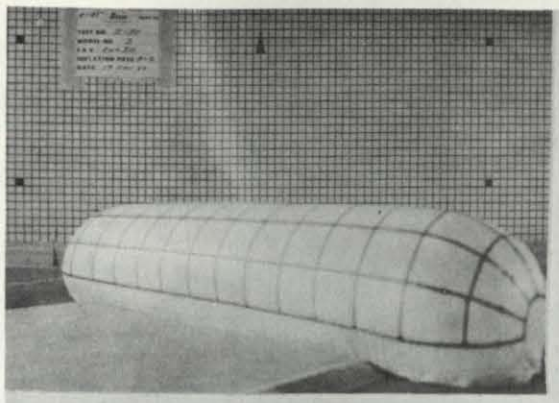

Model No. 3
3/4 Cylinder

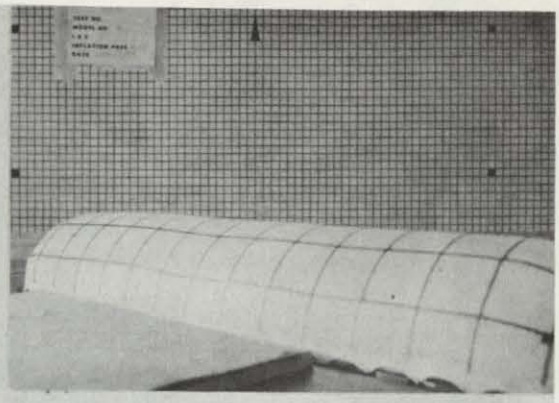

Model No. 6
1/2 Cylinder

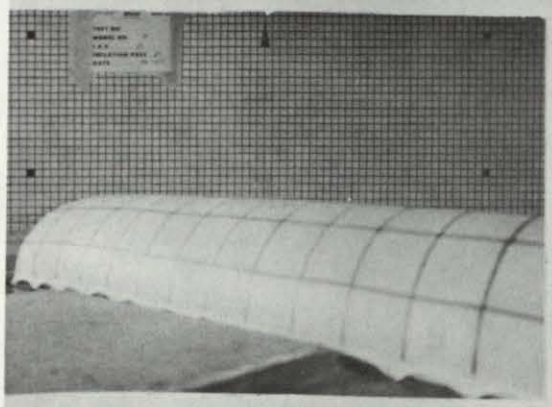

Model No. 9
3/8 Cylinder

Figure 6. — Photographs of Single Wall Cylinder, $W/\ell_h = 1/4$

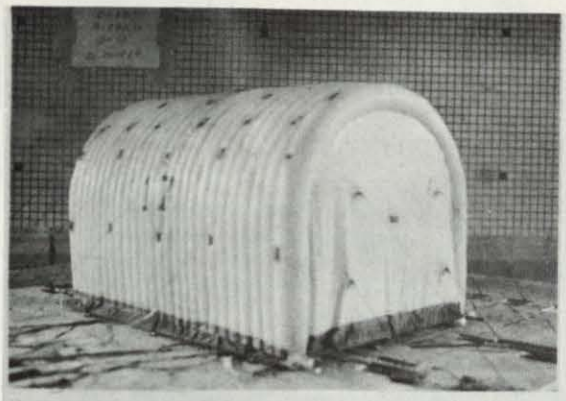

Model No. 17
3/4 Cylinder
Cell Width/Enclosure Dia. = 0.082

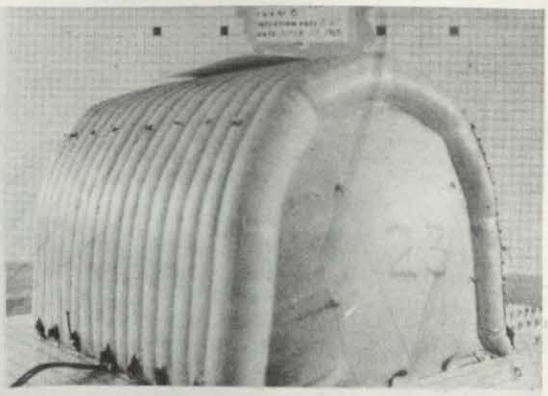

Model No. 23
3/4 Cylinder
Cell Width/Enclosure Dia. = 0.123

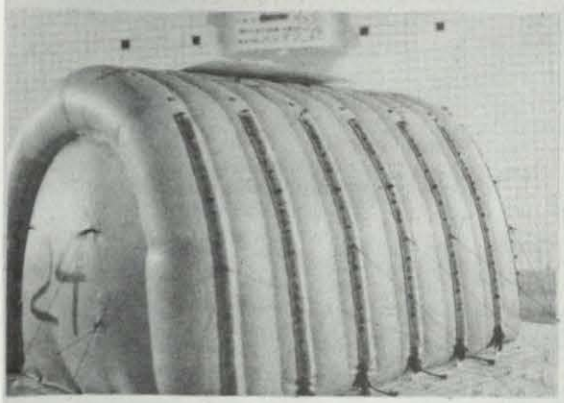

Model No. 24
3/4 Cylinder
Cell Width/Enclosure Dia. = 0.164

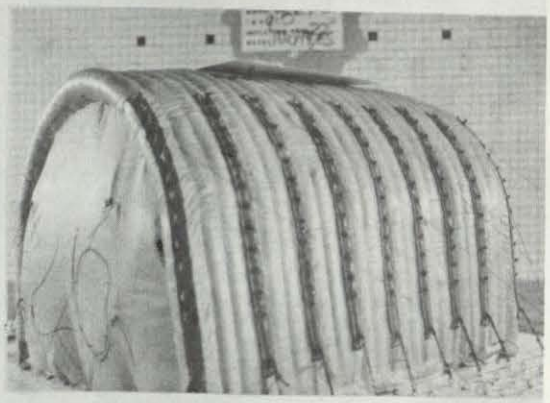

Model No. 26
3/4 Cylinder
Cell Width/Enclosure Dia. = 0.082

Figure 7. — Photographs of Double Wall Cylinder $W/\ell_h = 1/1$

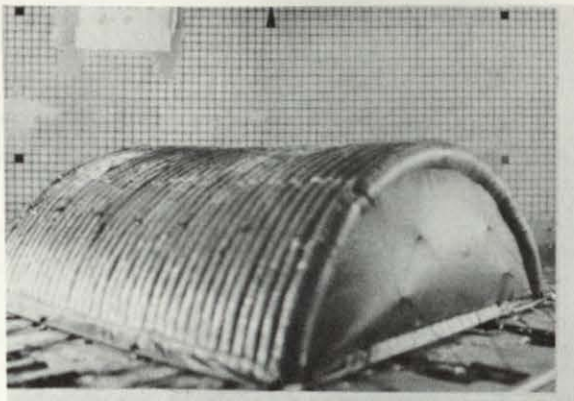

Model No. 16
3/8 Cylinder
$W/\ell_h = 1/1$

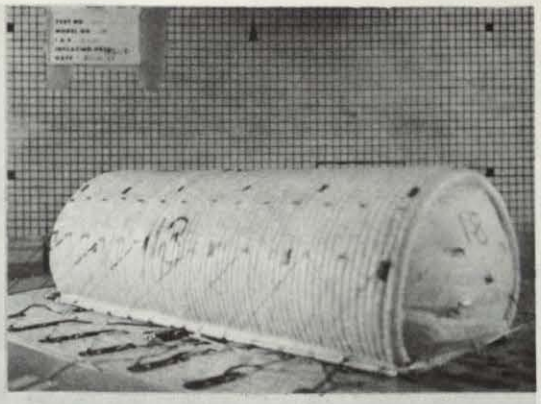

Model No. 18
3/4 Cylinder
$W/\ell_h = 1/2$

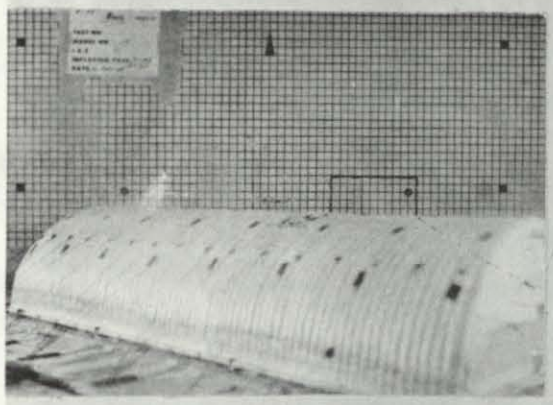

Model No. 19
1/2 Cylinder
$W/\ell_h = 1/2$

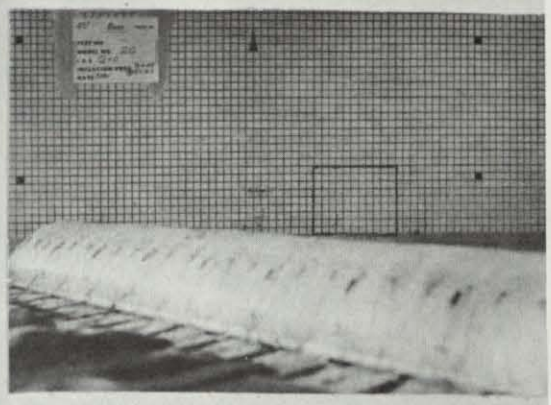

Model No. 20
1/2 Cylinder
$W/\ell_h = 1/4$

Figure 8.—Photographs of Double Wall Cylinders, $W/\ell_h = 1/1$, 1/2 & 1/4

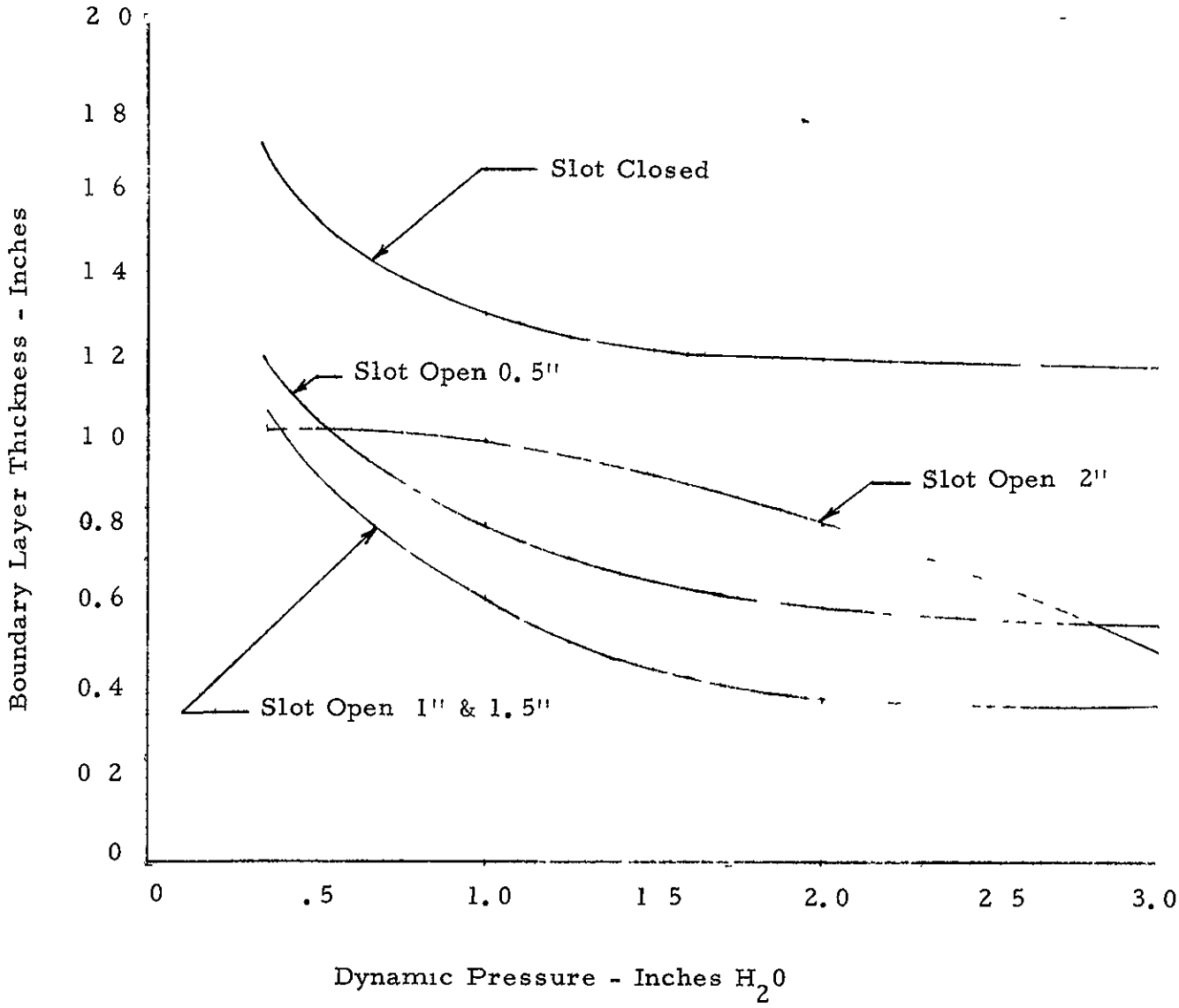

Figure 9 . - Boundary Layer Thickness

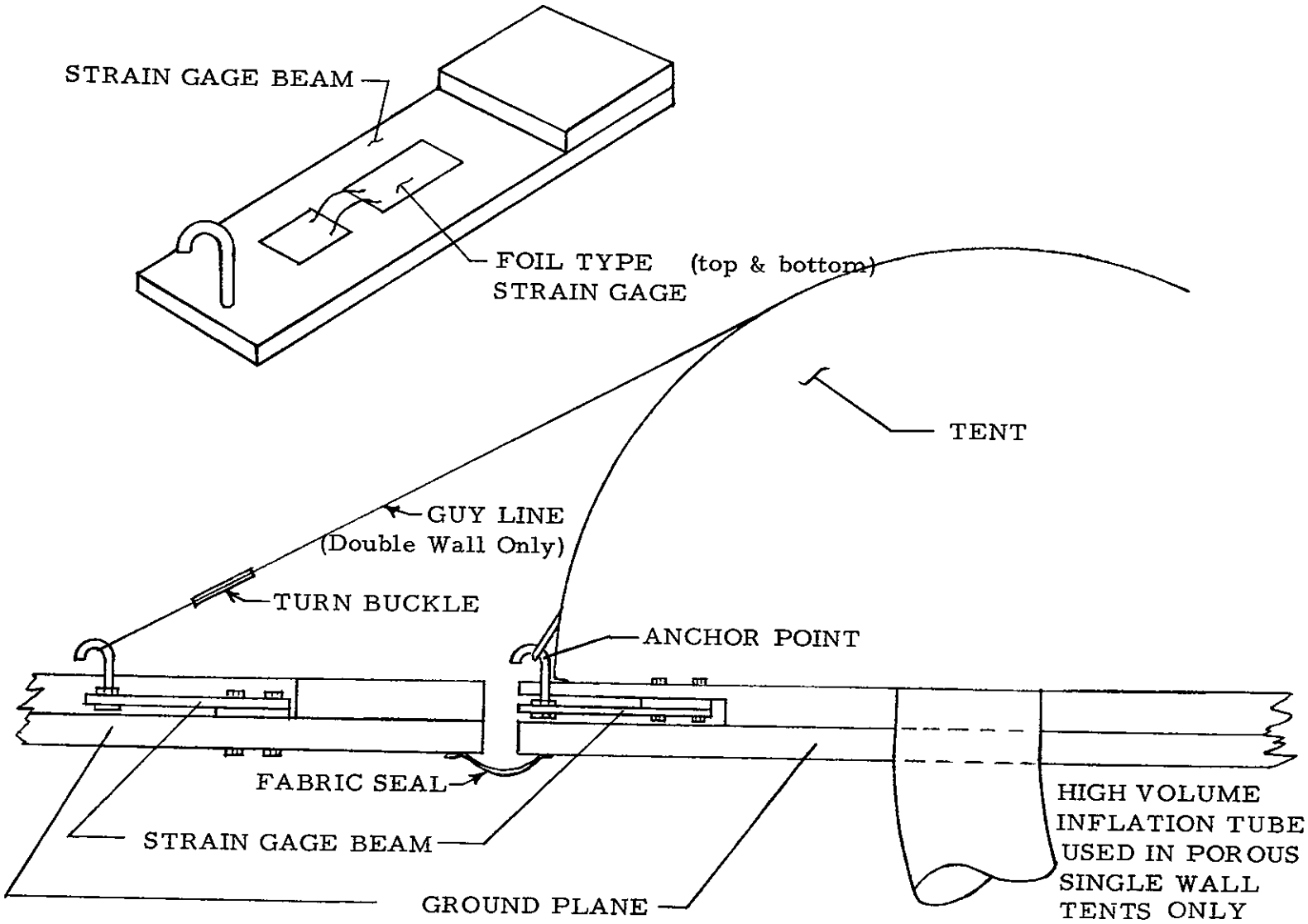

Figure 10. - Typical Strain Gage Installation on the Ground Plane

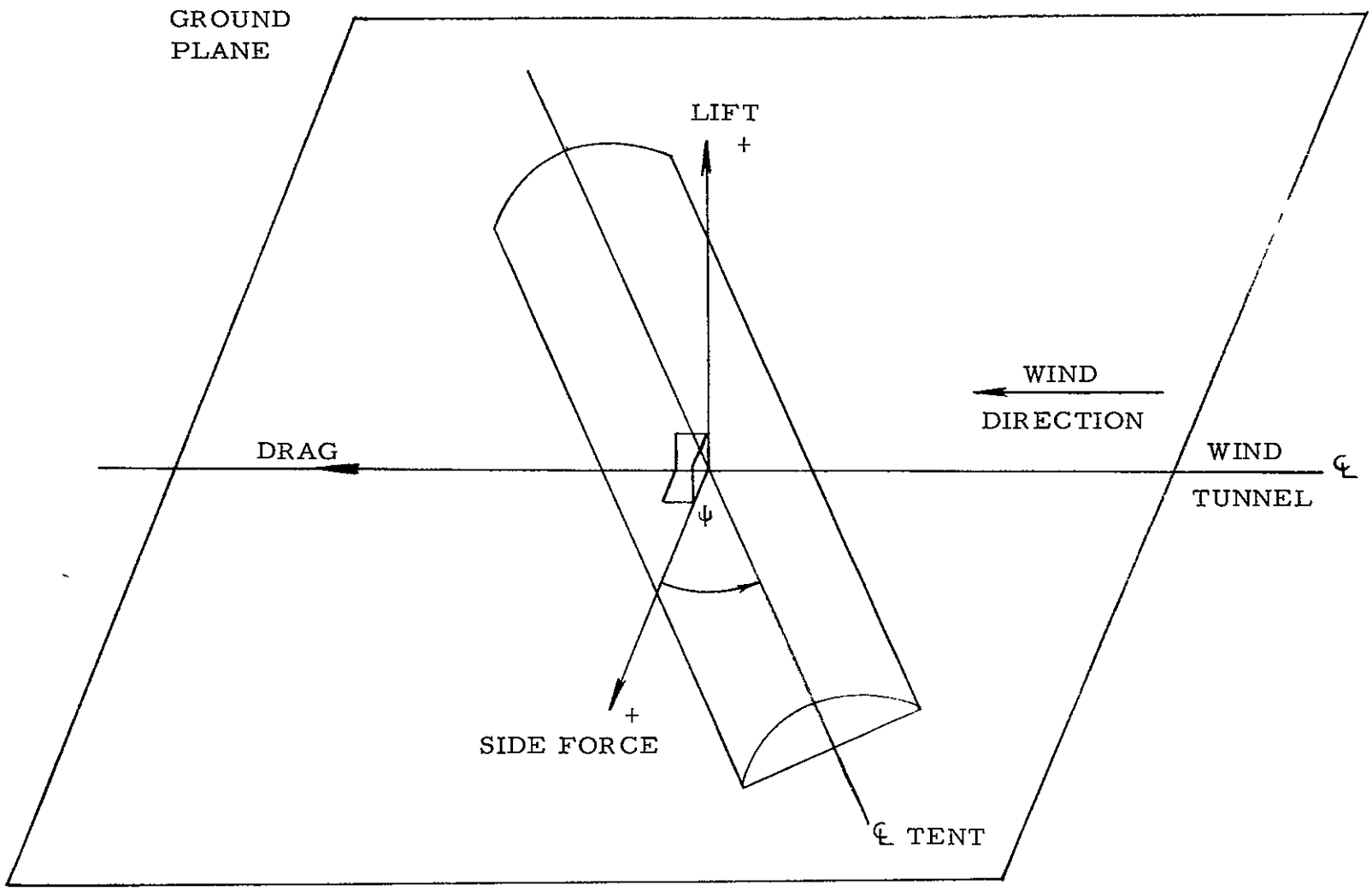

Figure 11. - Wind Axes System

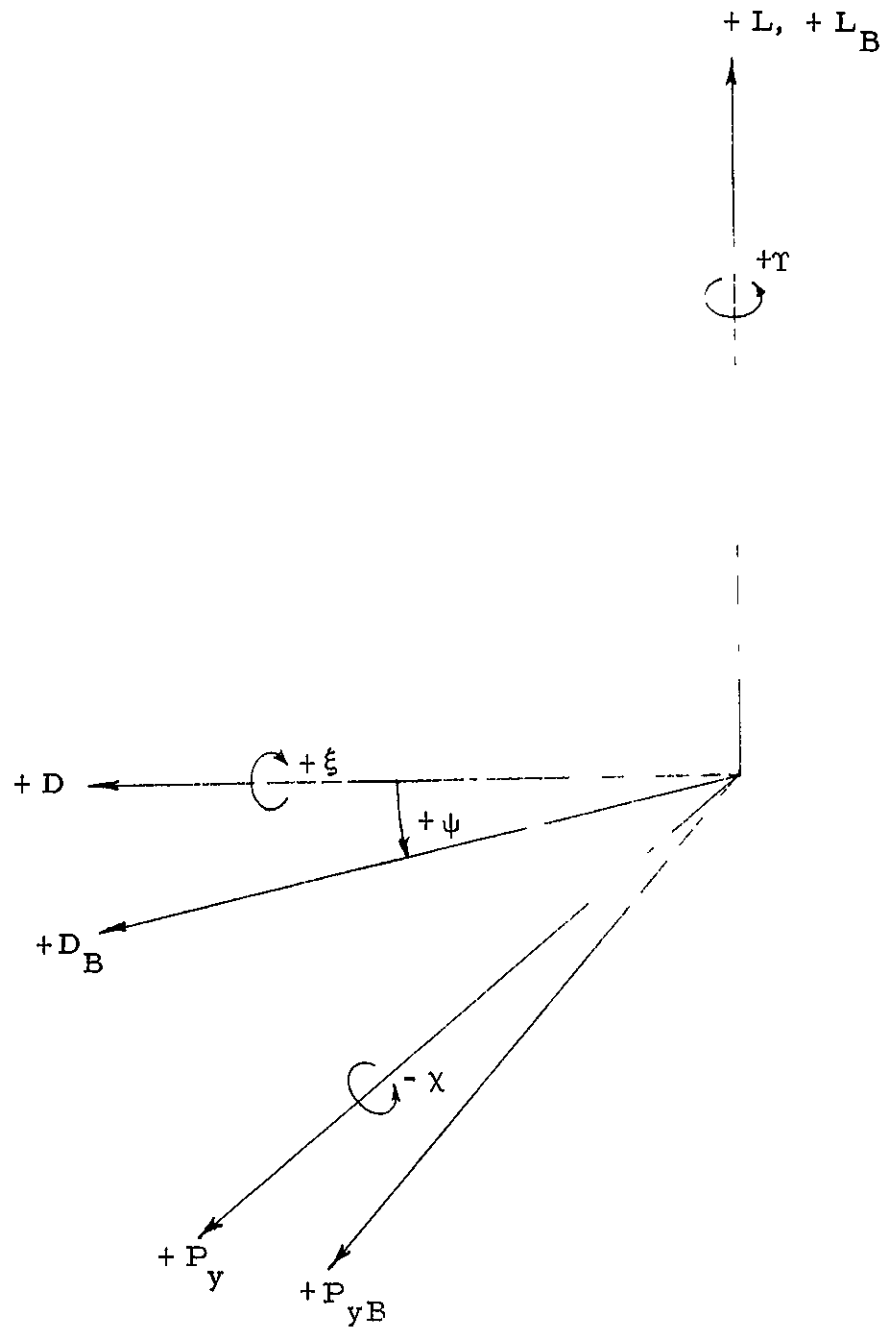

Figure 12. - Coordinate System for Transformation from Wind Axes to Body Axes

MAXIMUM LIFT COEFFICIENT
SINGLE WALL SPHERES

Note

(*) Fabric porosity, cu. ft /min /sq. ft. @ 6 in w g

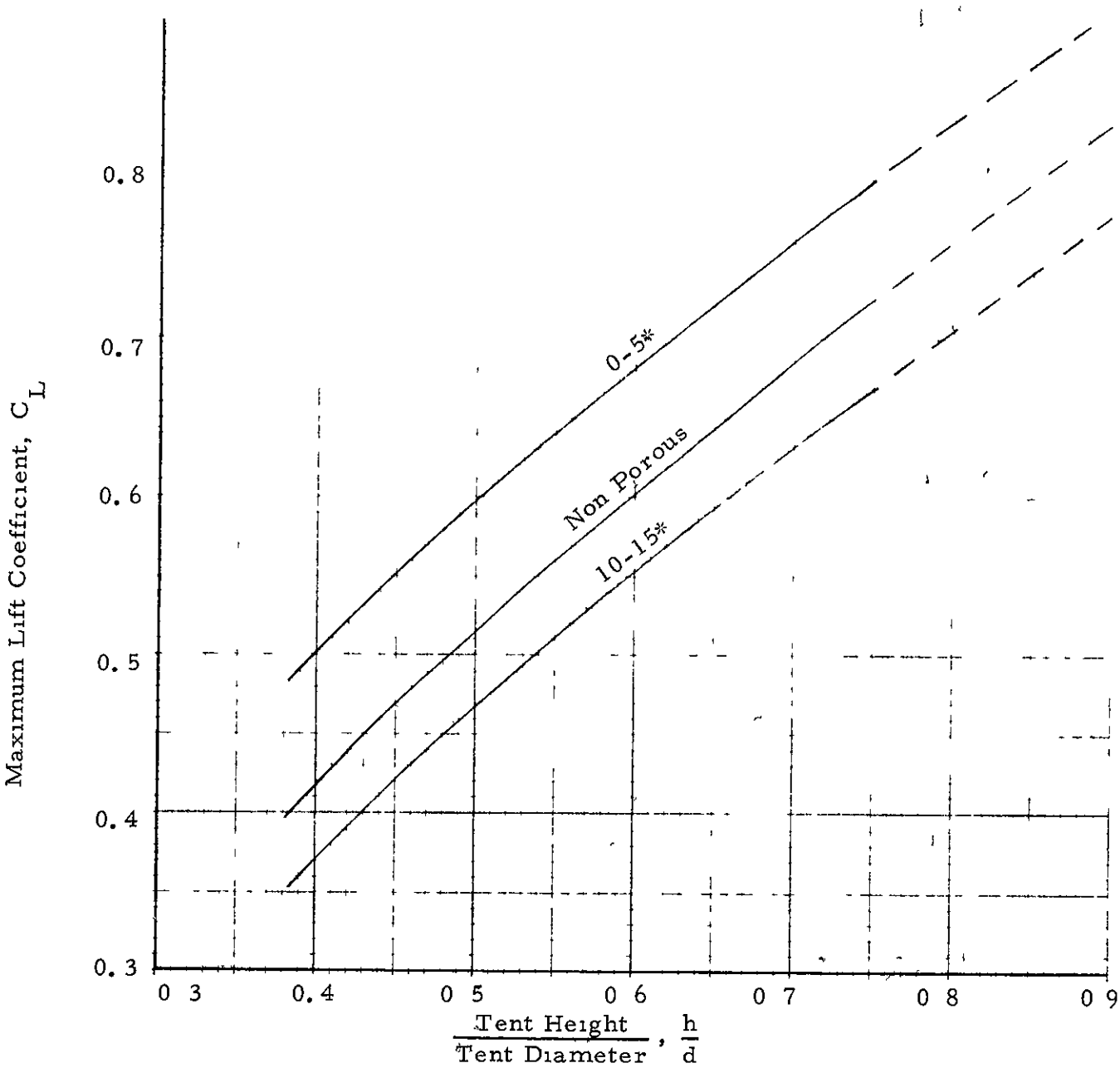

Figure 13. - Variation of Lift Coefficient with Shape and Fabric Porosity (Spherical Single Wall Tents).

MAXIMUM LIFT COEFFICIENT
SINGLE WALL 1 2 CYLINDERS

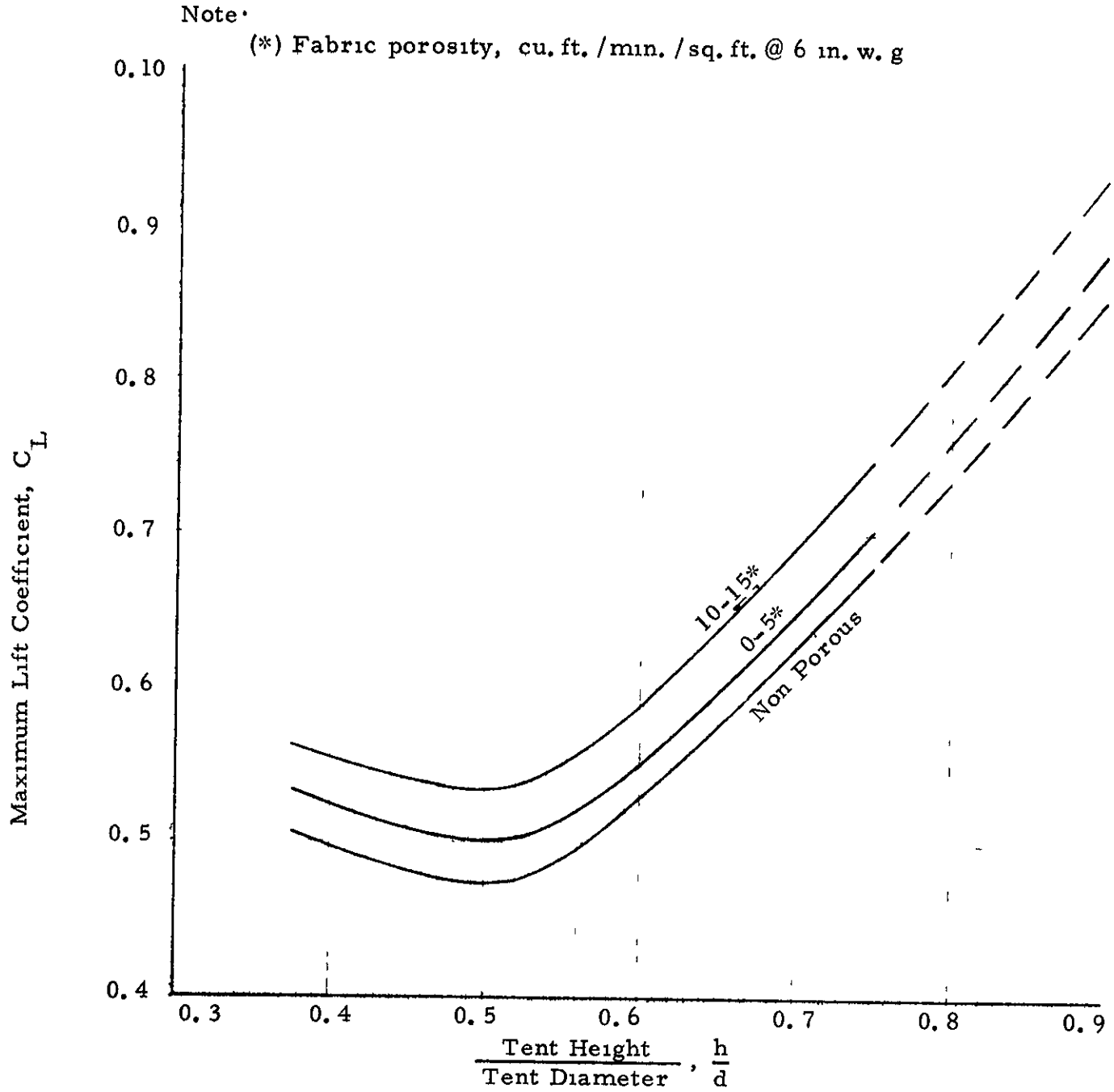

Figure 14. - Variation of Lift Coefficient with Shape and Fabric Porosity (Cylindrical Single Wall Tents, 1·2 W/ℓ_h).

MAXIMUM LIFT COEFFICIENT
SINGLE WALL 1 4 CYLINDERS

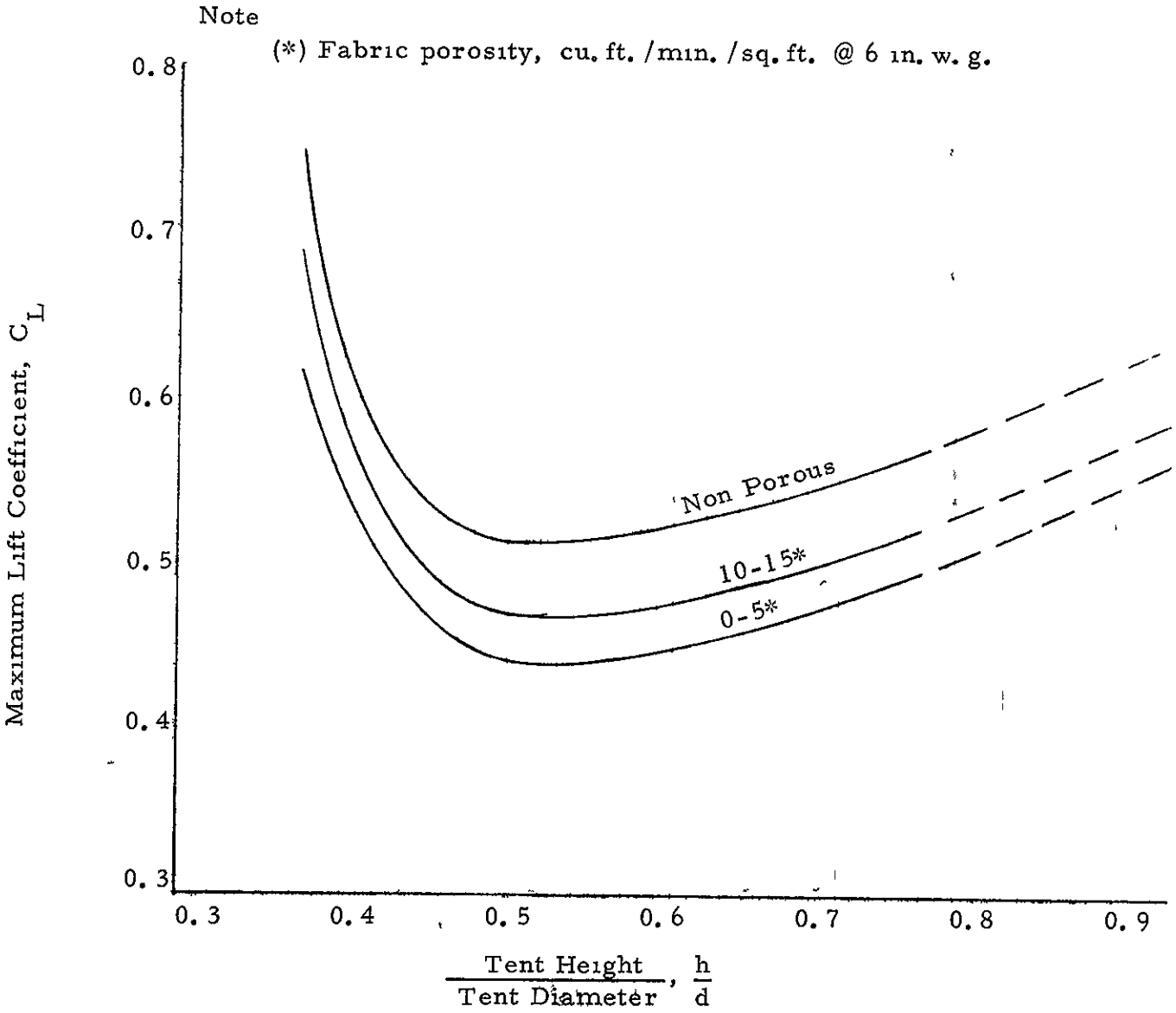

Figure 15. - Variation of Lift Coefficient with Shape and Fabric Porosity (Cylindrical Single Wall Tents, 1 4 W/ℓ_h)

MAXIMUM LIFT COEFFICIENT

DOUBLE WALL CYLINDERS

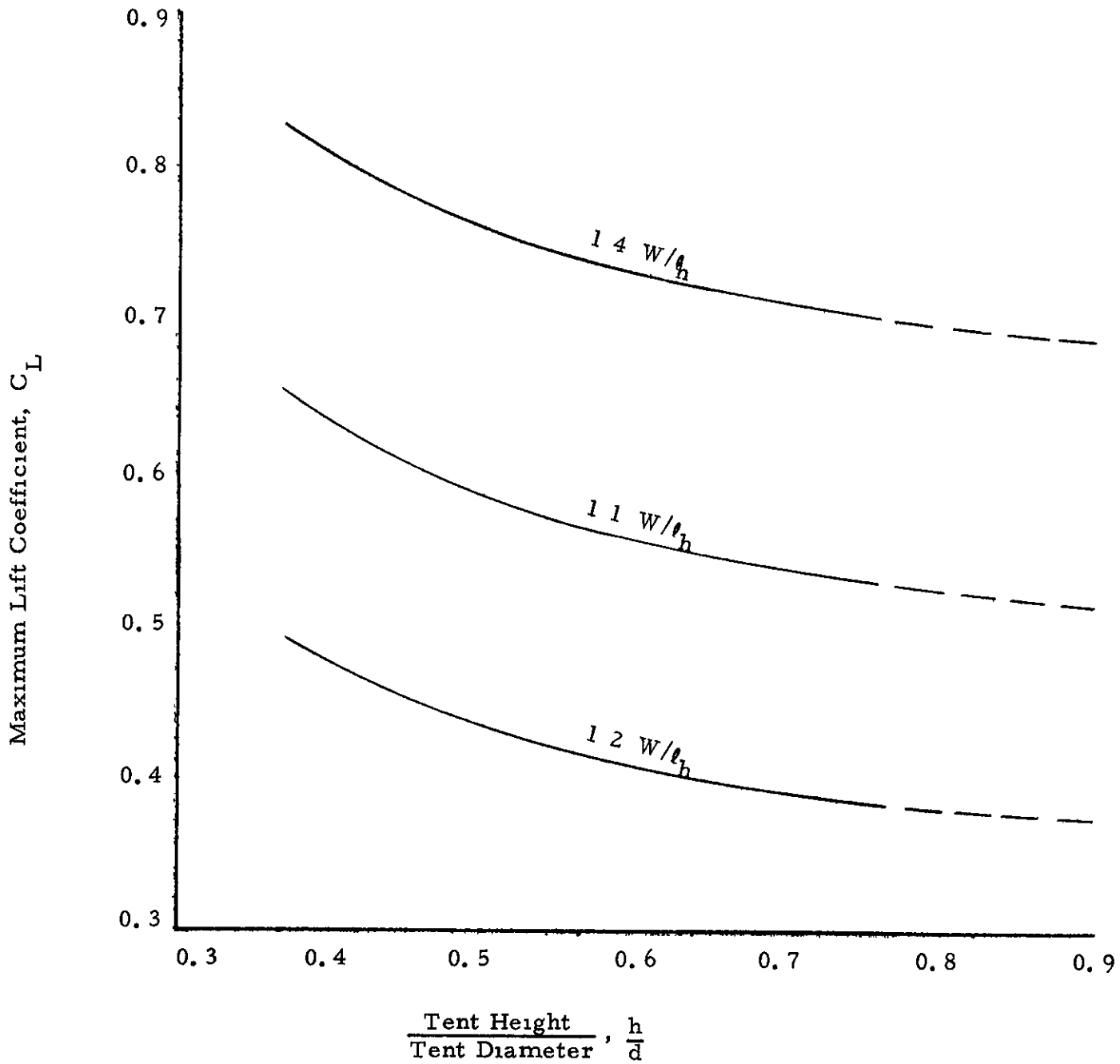

Figure 16 . - Variation of Lift Coefficient with Shape (Non Porous Double Wall Tents, 1 1, 1·2, 1·4, W/ℓ_h)

MAXIMUM DRAG COEFFICIENT
SINGLE WALL SPHERES

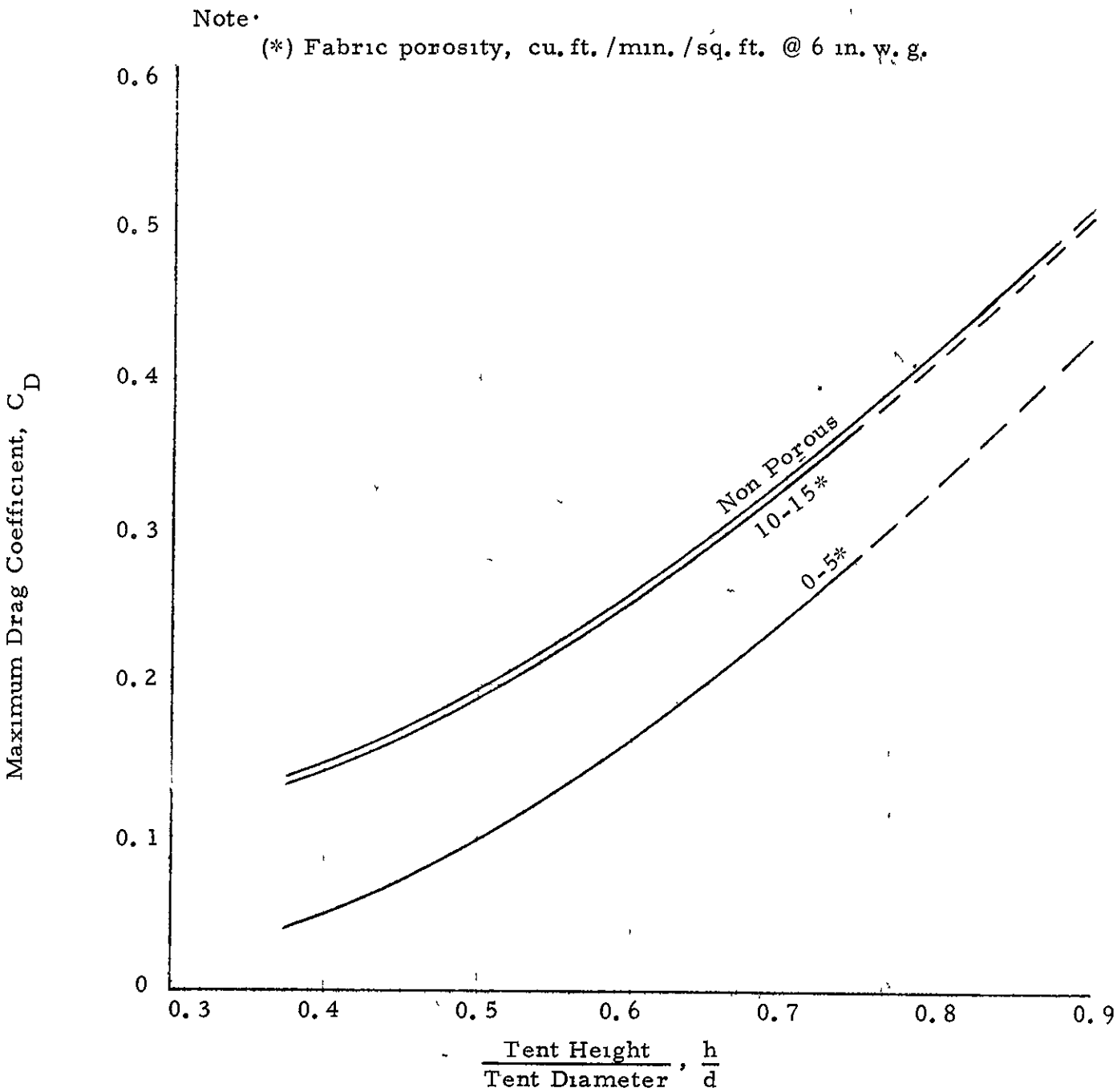

Figure 17. - Variation of Drag Coefficient with Shape and Fabric Porosity (Spherical Single Wall Tents).

MAXIMUM DRAG COEFFICIENT
SINGLE WALL 1·2 CYLINDERS

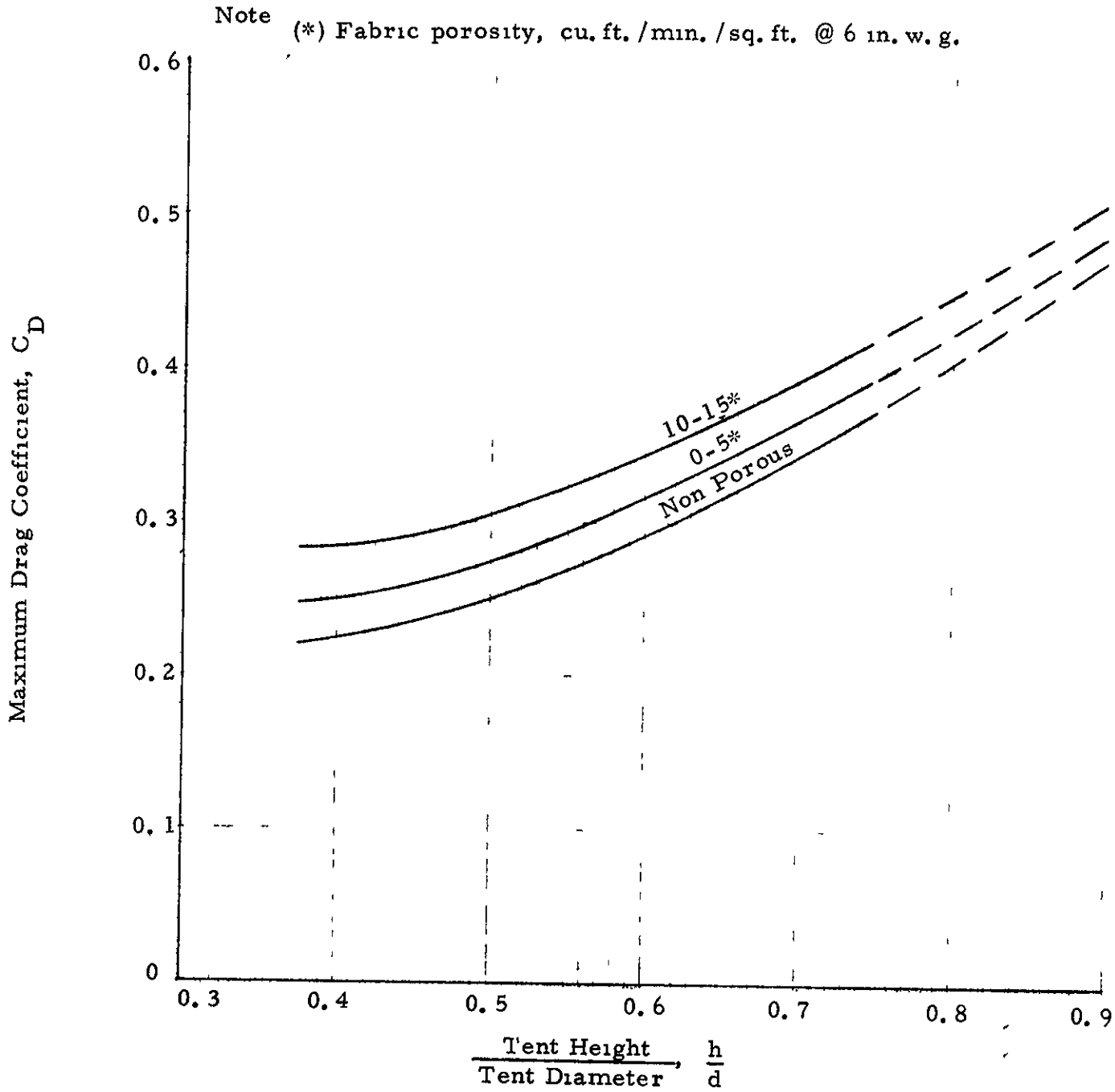

Figure 18. - Variation of Drag Coefficient with Shape and Fabric Porosity (Cylindrical Single Wall Tents, 1 2 W/ℓ_h)

MAXIMUM DRAG COEFFICIENT
SINGLE WALL 1 4 CYLINDERS

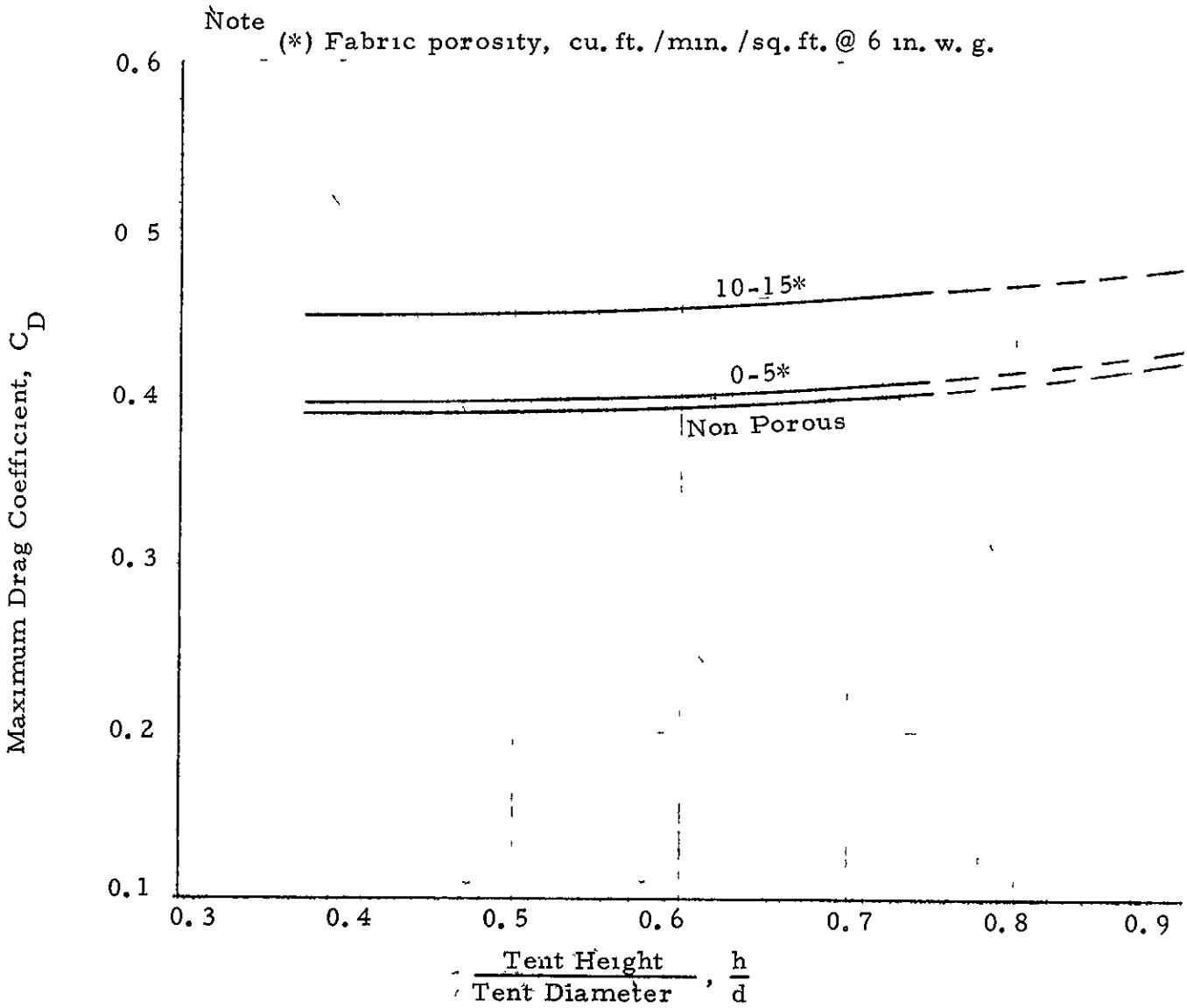

Figure 19. - Variation of Drag Coefficient with Shape and Fabric Porosity (Cylindrical Single Wall Tents, 1 4 W/ℓ_h).

MAXIMUM DRAG COEFFICIENT
DOUBLE WALL CYLINDERS

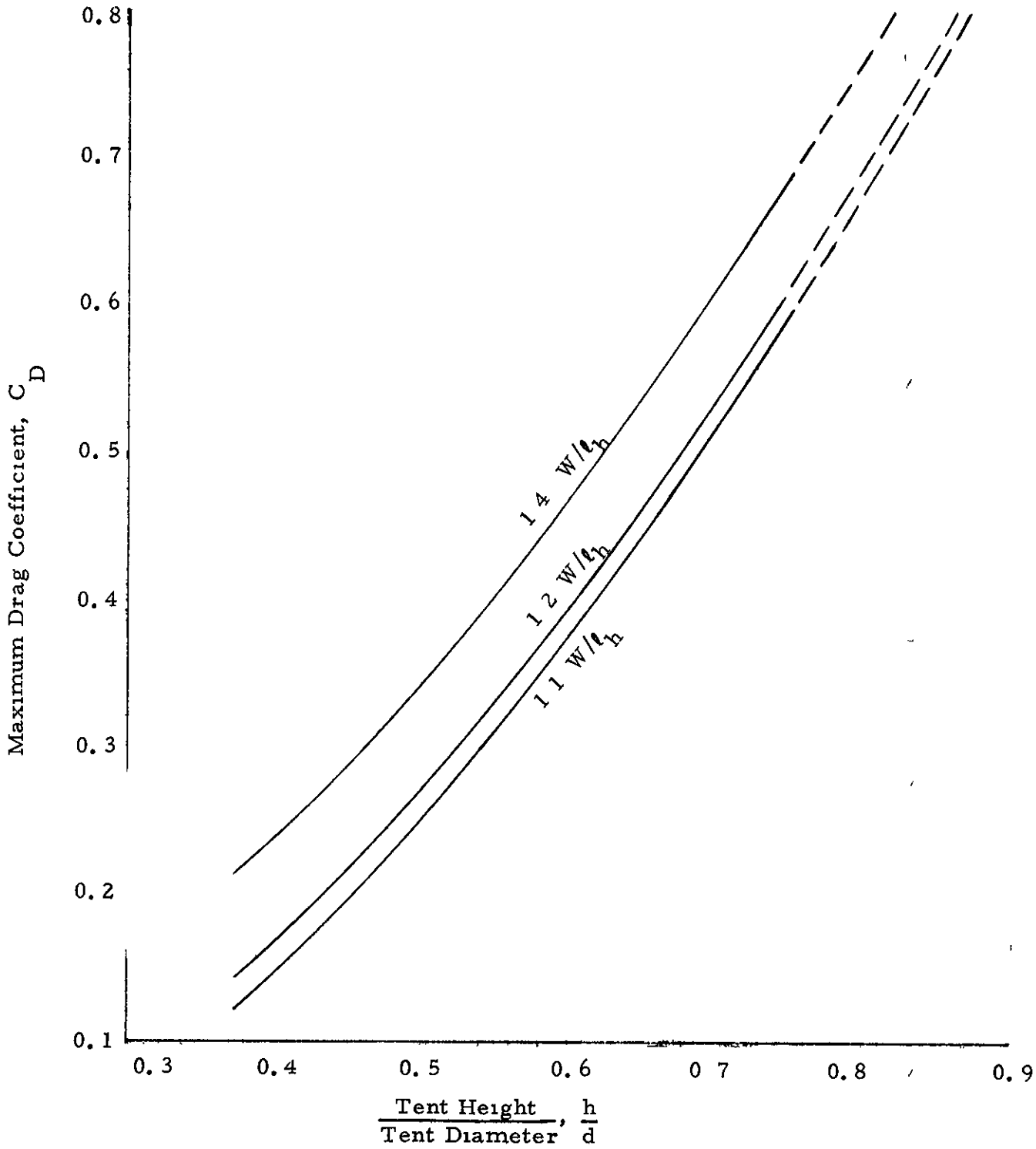

Figure 20. - Variation of Drag Coefficient with Shape (Non Porous Double Wall Tents, 1 1, 1 2, 1 4, W/ℓ_h).

MAXIMUM MOMENT COEFFICIENT
SINGLE WALL SPHERES

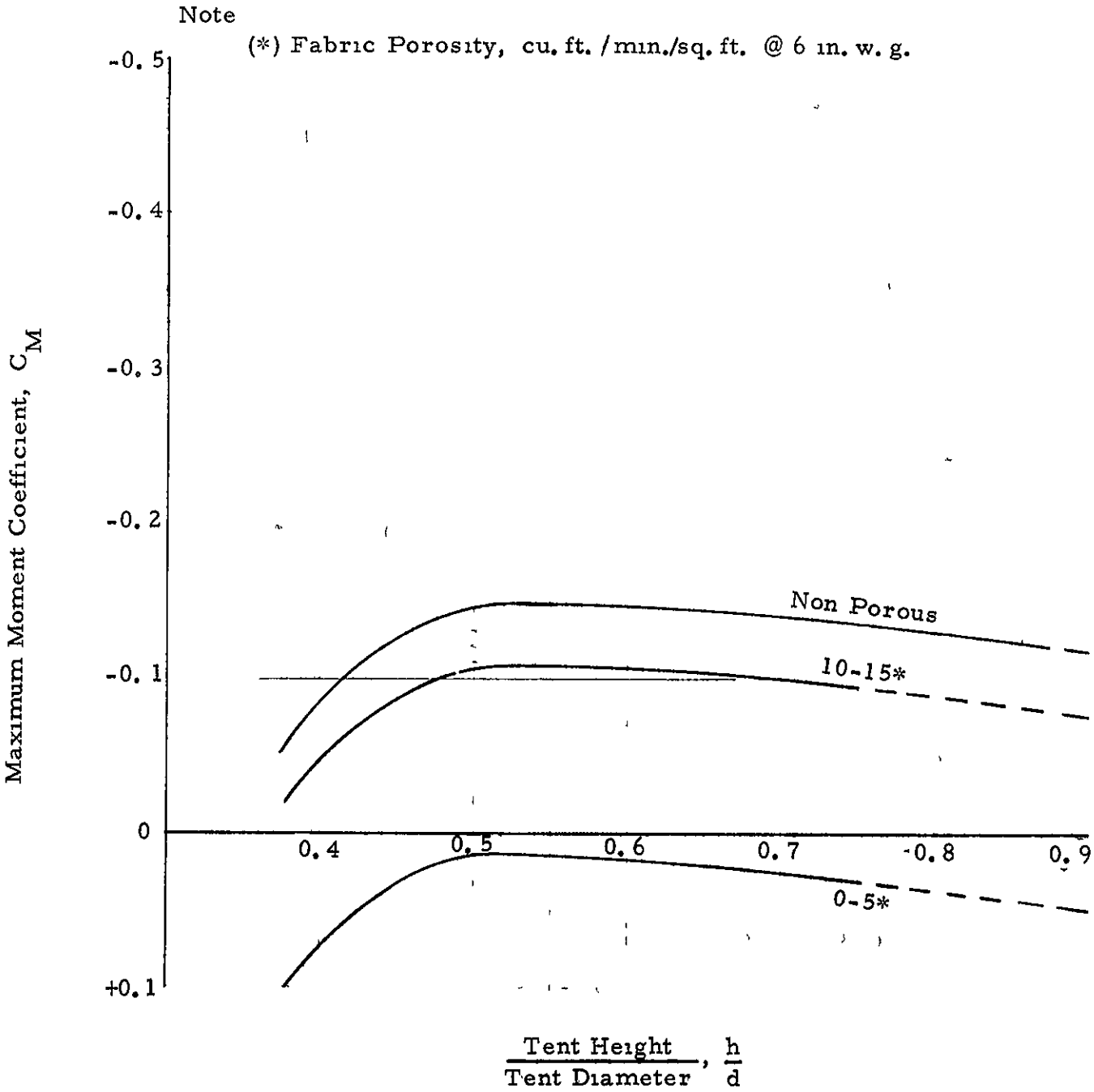

Figure 21. - Variation of Moment Coefficient with Shape and Fabric Porosity (Spherical Single Wall Tents).

MAXIMUM MOMENT COEFFICIENT
SINGLE WALL 1 2 CYLINDERS

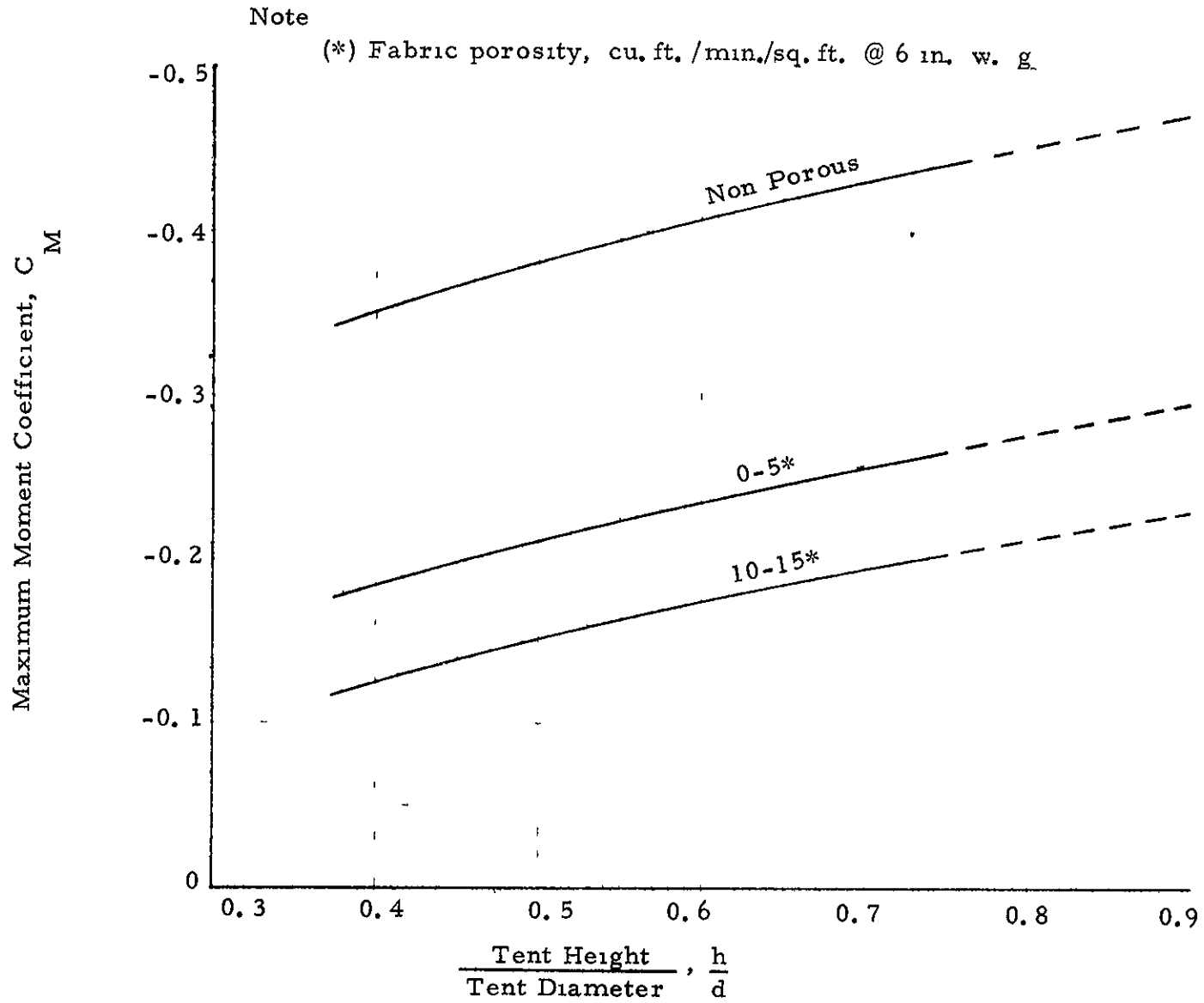

Figure 22. - Variation of Moment Coefficient with Shape and Fabric Porosity (Cylindrical Single Wall Tents, 1 2 W/ℓ_h)

MAXIMUM MOMENT COEFFICIENT
SINGLE WALL 1 4 CYLINDERS

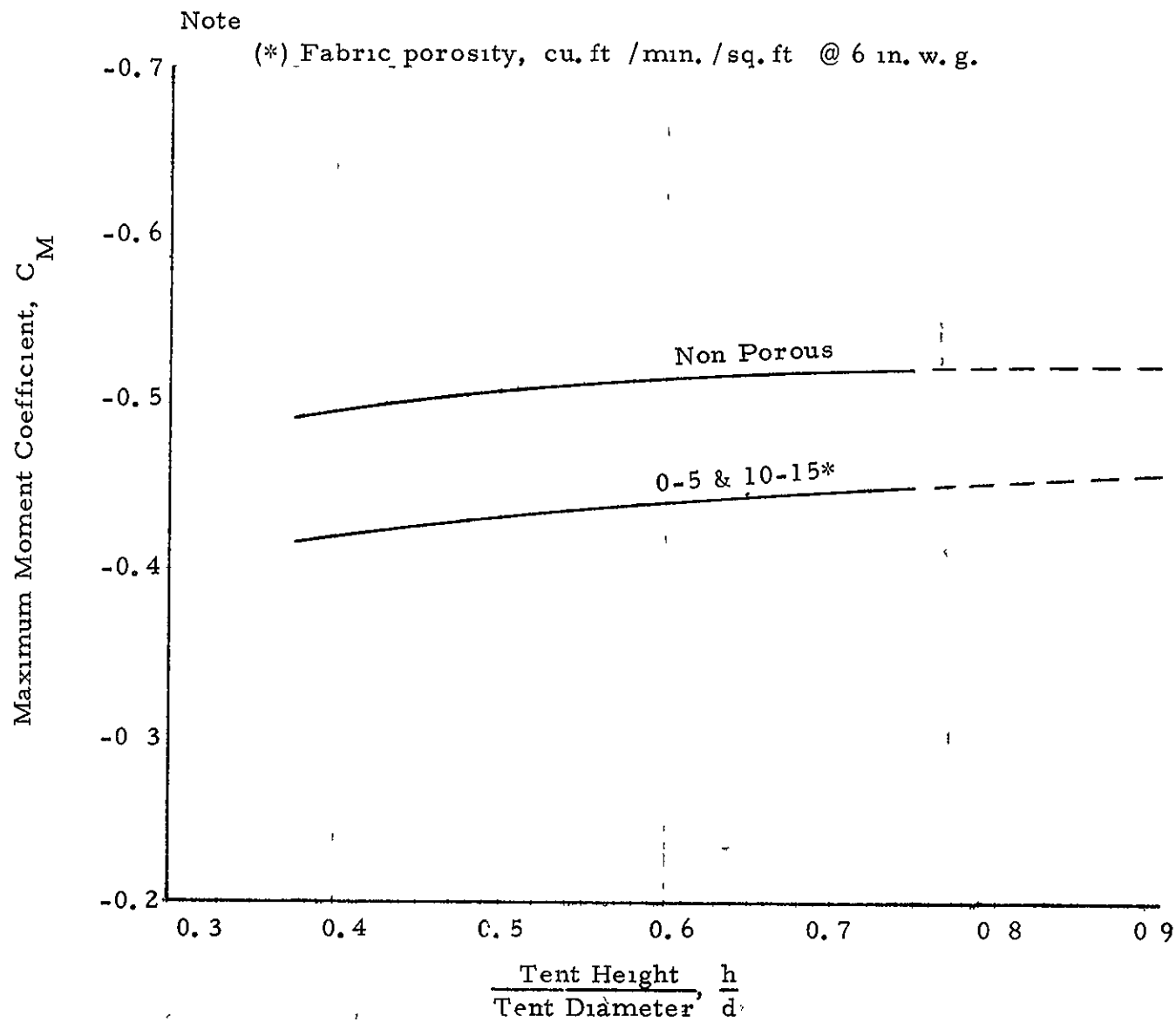

Figure 23. - Variation of Moment Coefficient with Shape and Fabric Porosity (Cylindrical Single Wall Tents, 1 4 W/ℓ_h).

MAXIMUM MOMENT COEFFICIENT
DOUBLE WALL CYLINDERS

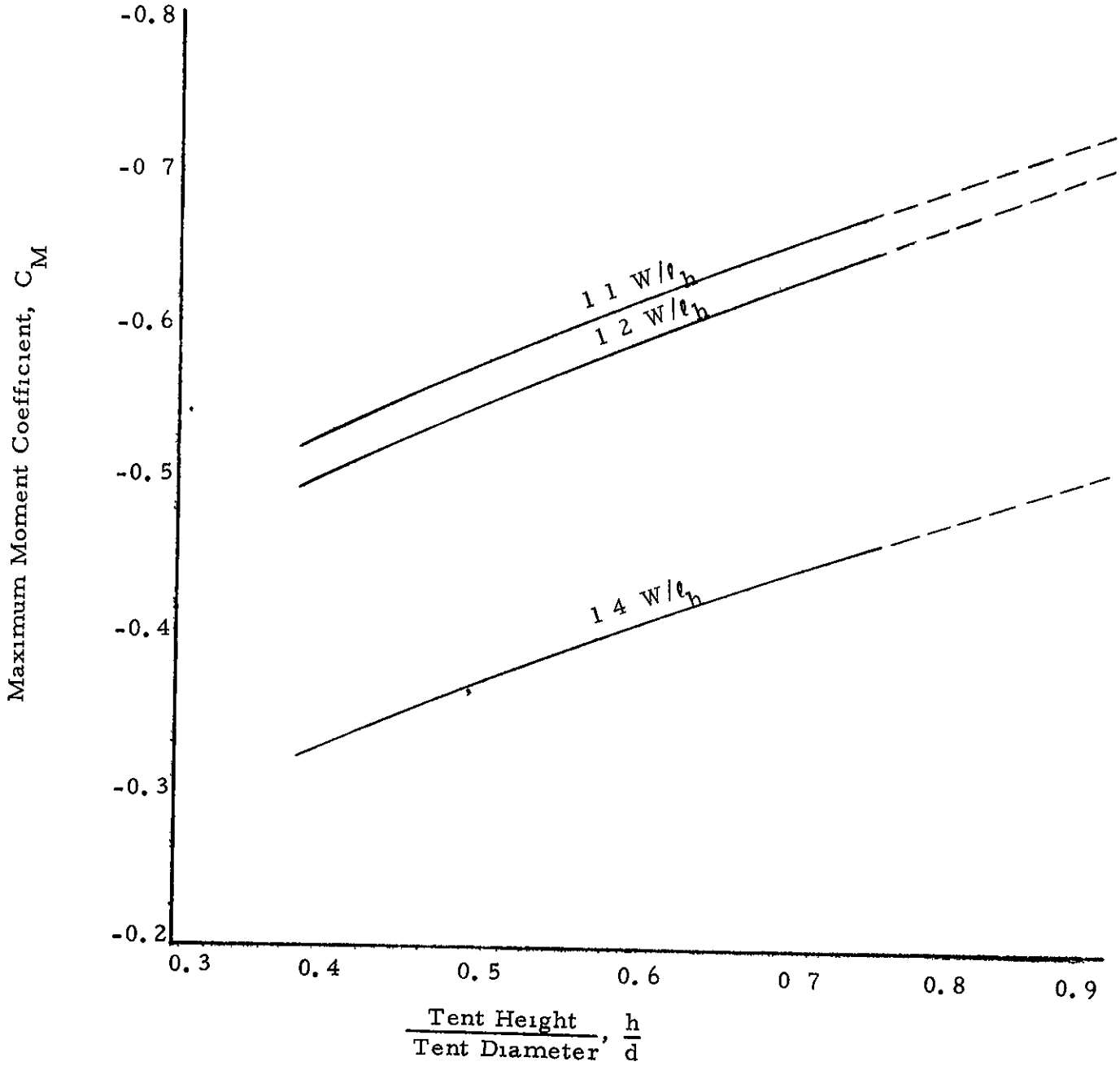

Figure 24. - Variation of Moment Coefficient with Shape (Non Porous Double Wall Tents, 1 1, 1·2, 1 4, W/ℓ_h).

MAXIMUM AERODYNAMIC ANCHOR LOAD COEFFICIENT
SINGLE WALL SPHERES AND CYLINDERS

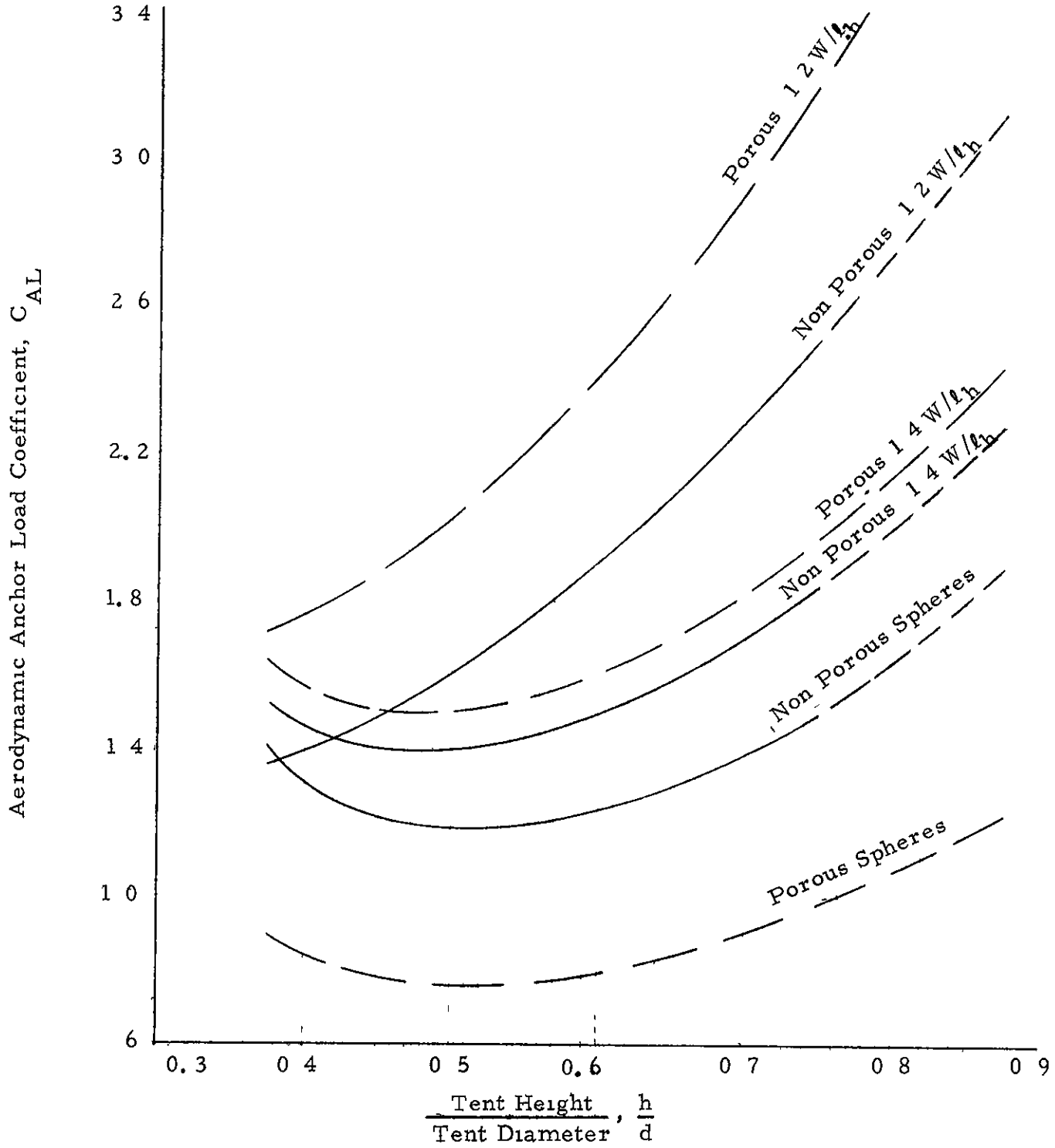

Figure 25. - Variation of Anchor Load Coefficient With Shape

MAXIMUM BASE ANCHOR LOAD COEFFICIENT
DOUBLE WALL CYLINDERS

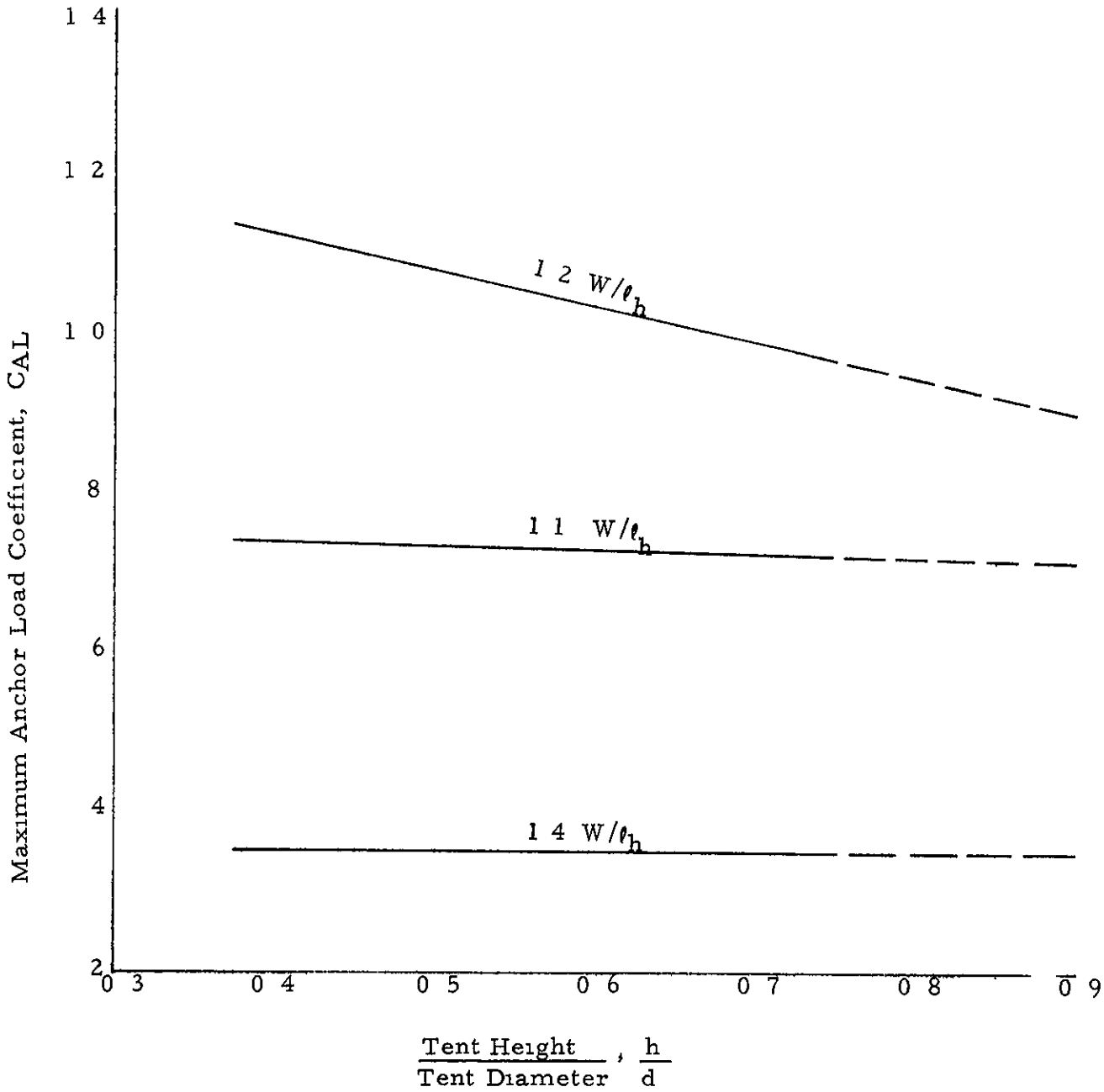

Figure 26 - Variation of Base Anchor Load Coefficient With Shape

MAXIMUM GUY LINE LOAD COEFFICIENT
DOUBLE WALL CYLINDER

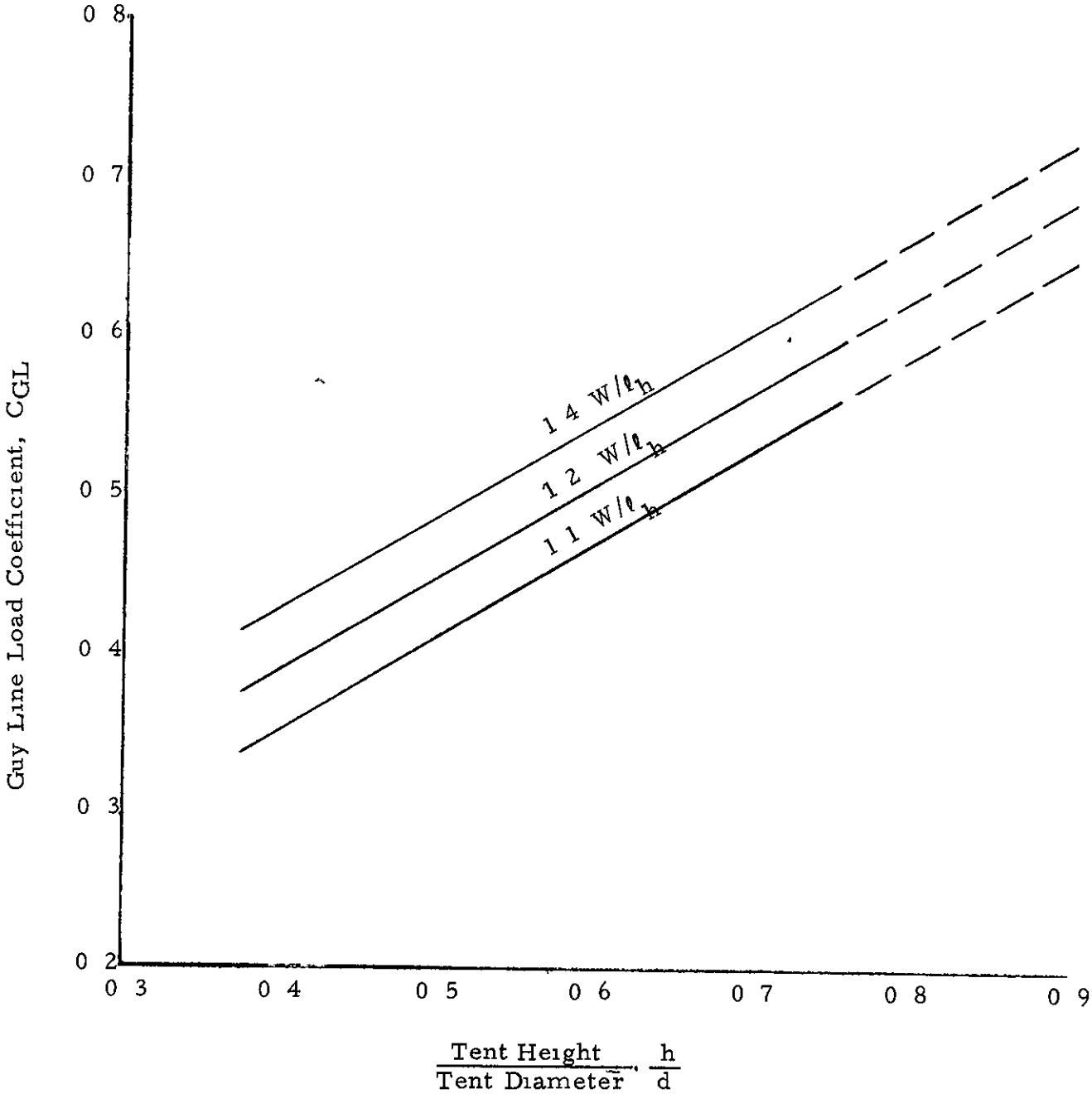

Figure 27 - Variation of Guy Line Load Coefficient With Shape

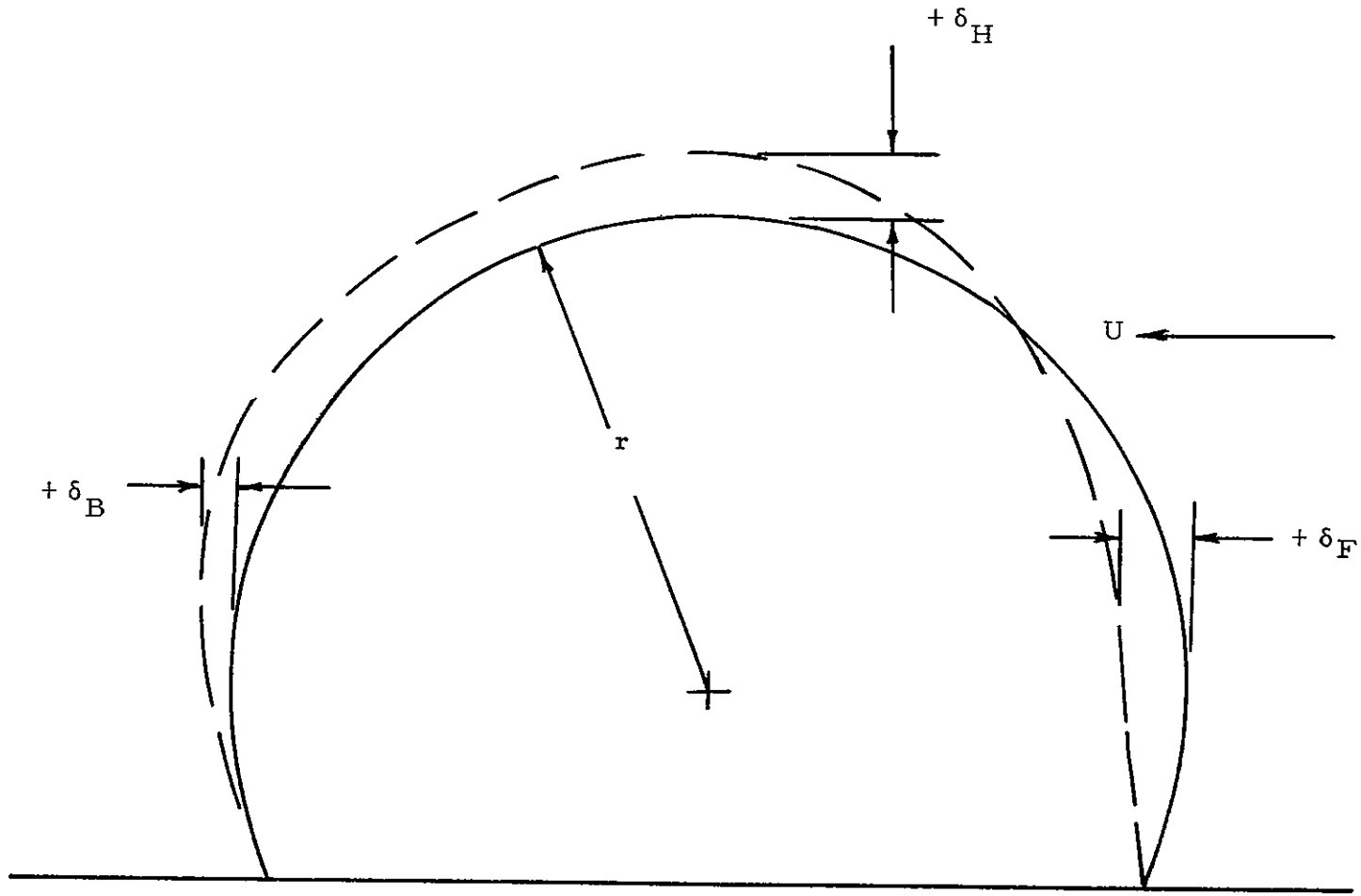

Figure 28. - Tent Deflection Notation

DOUBLE WALL, 3/4 CYLINDER, 1 1 WIDTH/LENGTH RATIO
GUY LINES ATTACHED 0.80 and 0.40 TENT HEIGHT

Note Cell Width/Enclosure Diameter = 0.123

Cond q = 6.0" w.g.

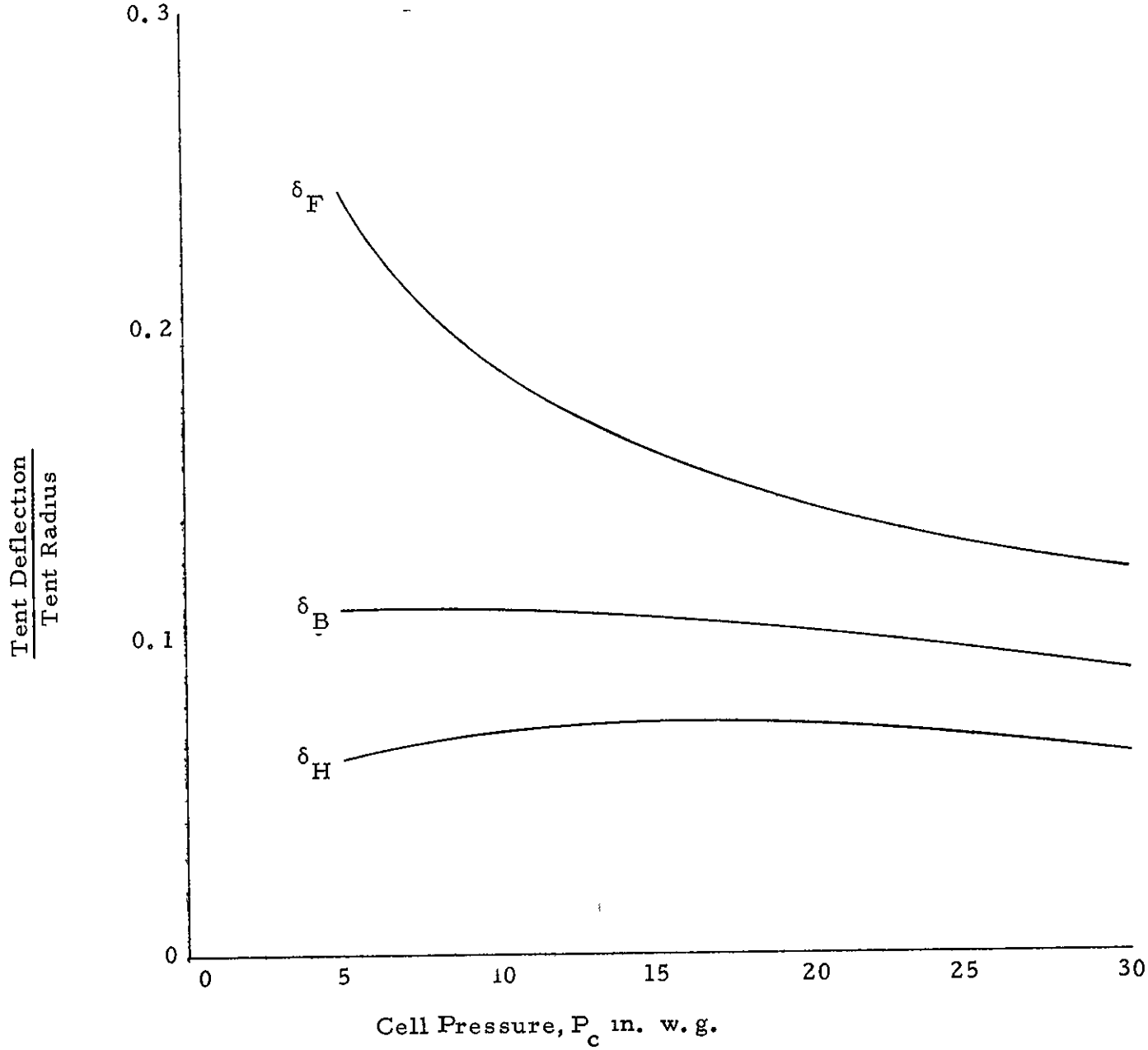

Figure 29. - Variation of Tent Deflection with Cell Pressure. Guy Lines Attached at 0 80 and 0.40 Tent Height.

DOUBLE WALL, 3/4 CYLINDER, 1 1 WIDTH/LENGTH RATIO

Cond $q = 6.0''$ w. g.
$P_c = 5.0''$ w. g.

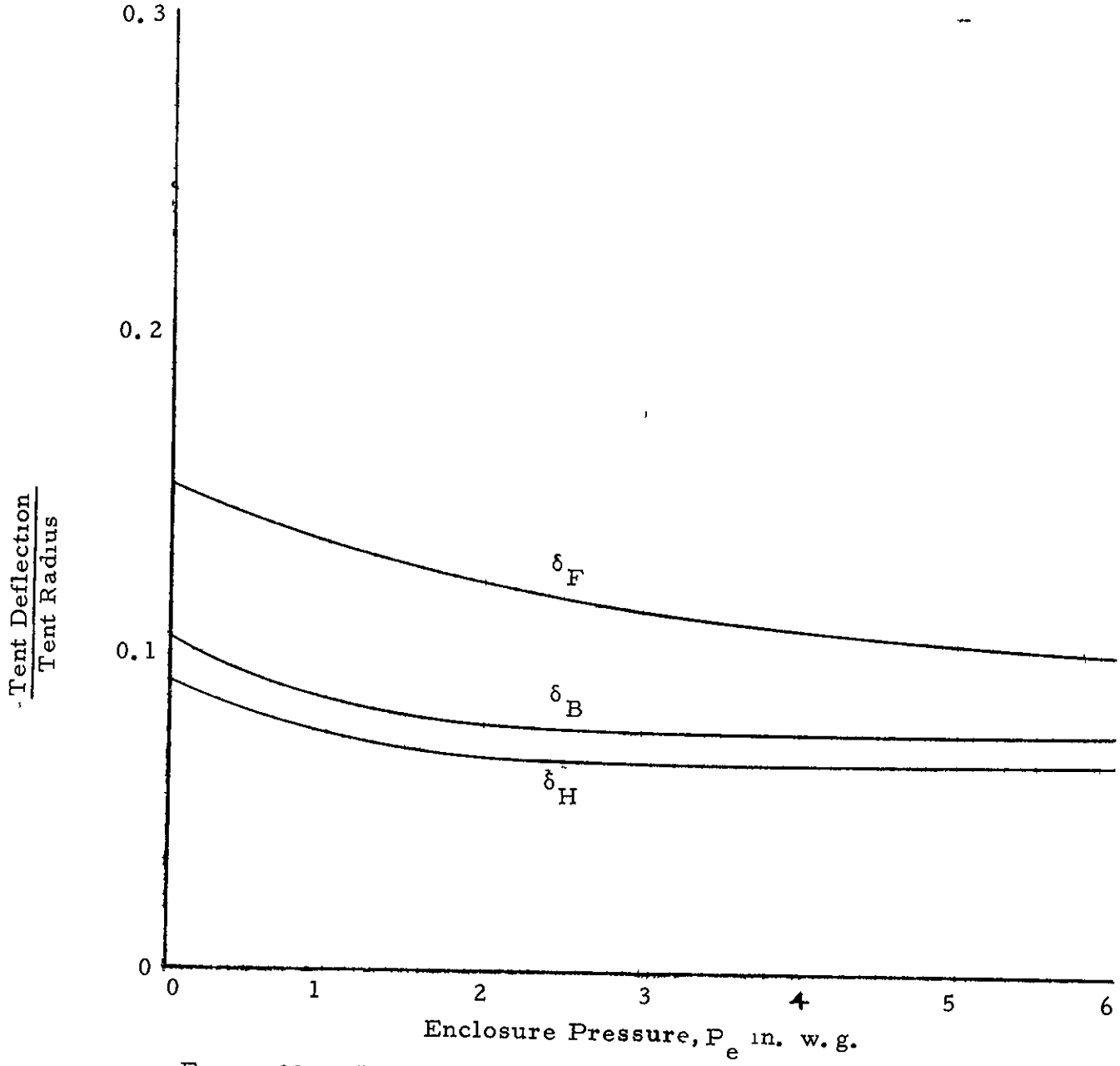

Figure 30. - Variation of Tent Deflection With Enclosure Pressure. No Guy Lines, Constant Cell Pressure = 5.0"w. g., Broadside to Wind ($\psi = 0°$).

DOUBLE WALL, 3/4 CYLINDER, 1 1 WIDTH/LENGTH RATIO
GUY LINES ATTACHED 0 80 TENT HEIGHT

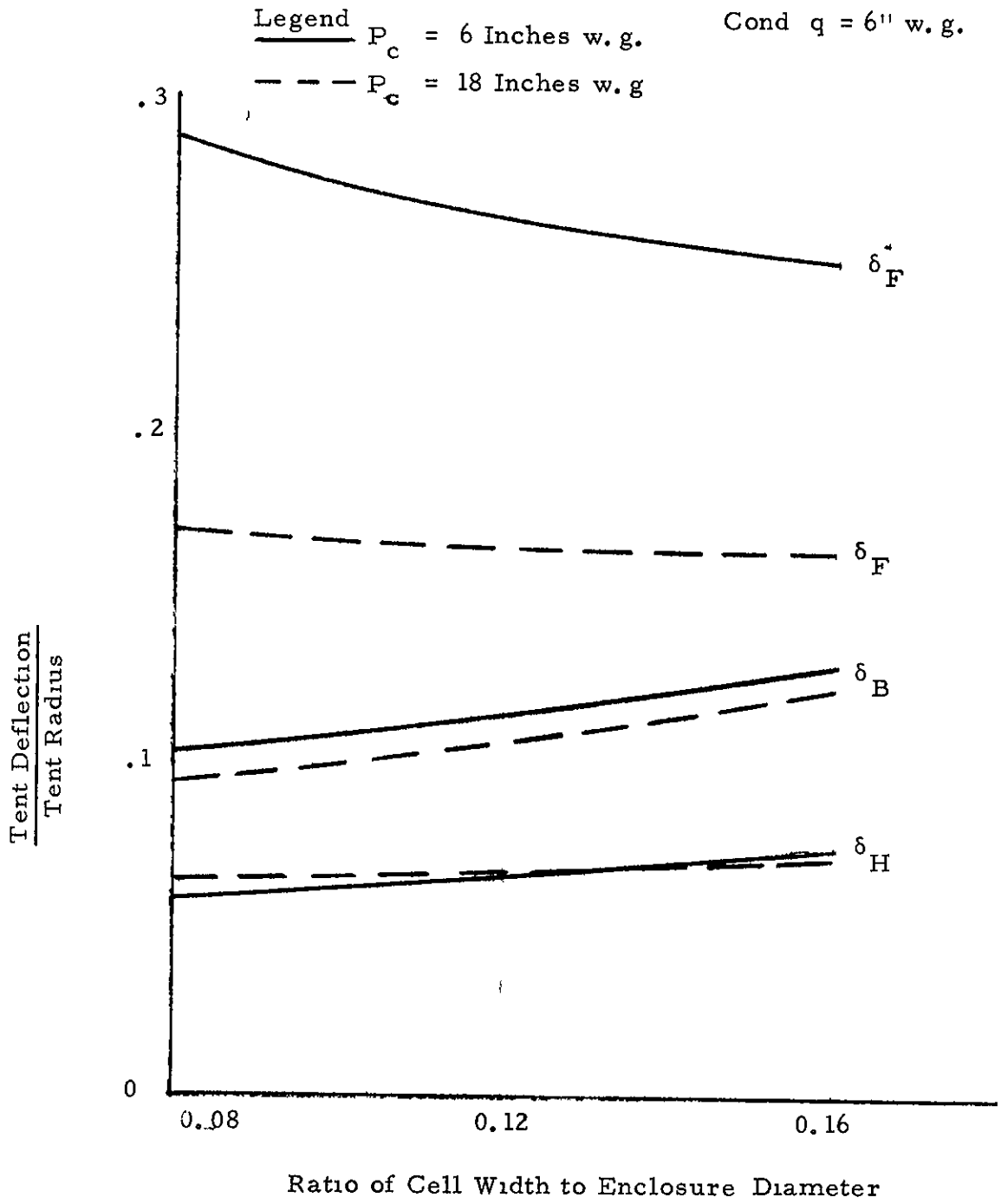

Figure 31 . - Effect of Cell Size on Tent Deflection.

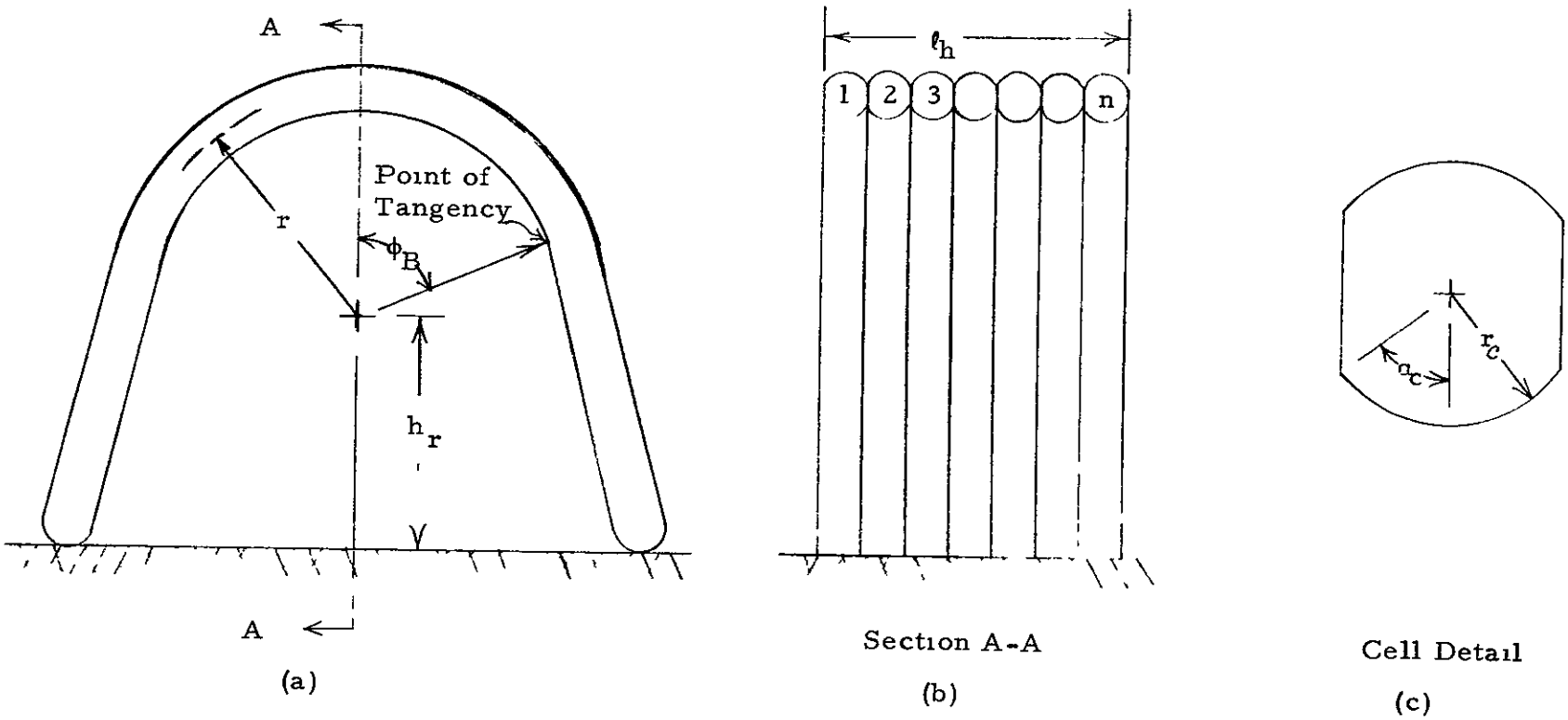

Figure 32 - Cell Size and Cell Number Relationship

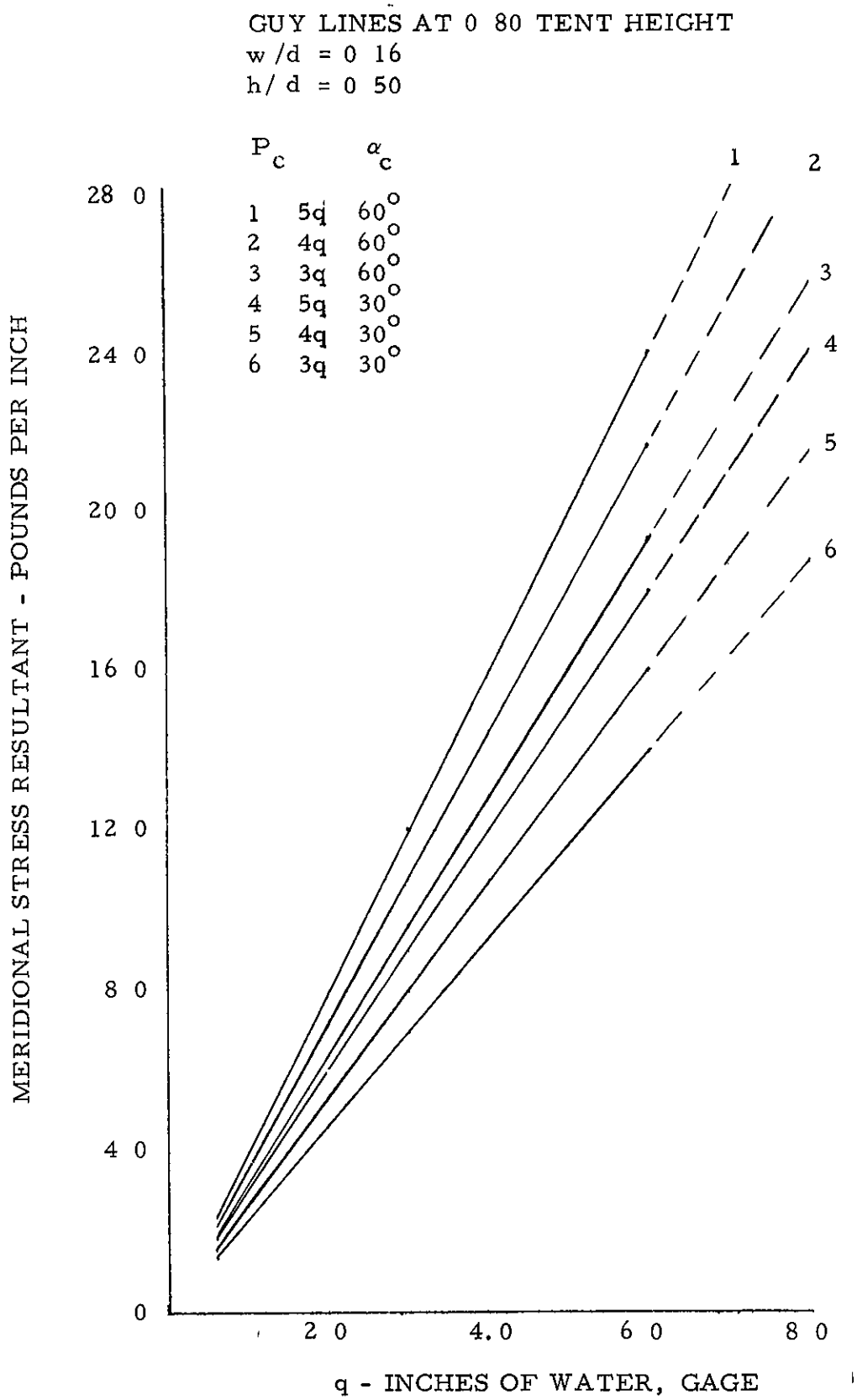

FIGURE 33. - VARIATION OF MERIDIONAL STRESS RESULTANT WITH IMPACT PRESSURE, q - DOUBLE WALL CYLINDERS.

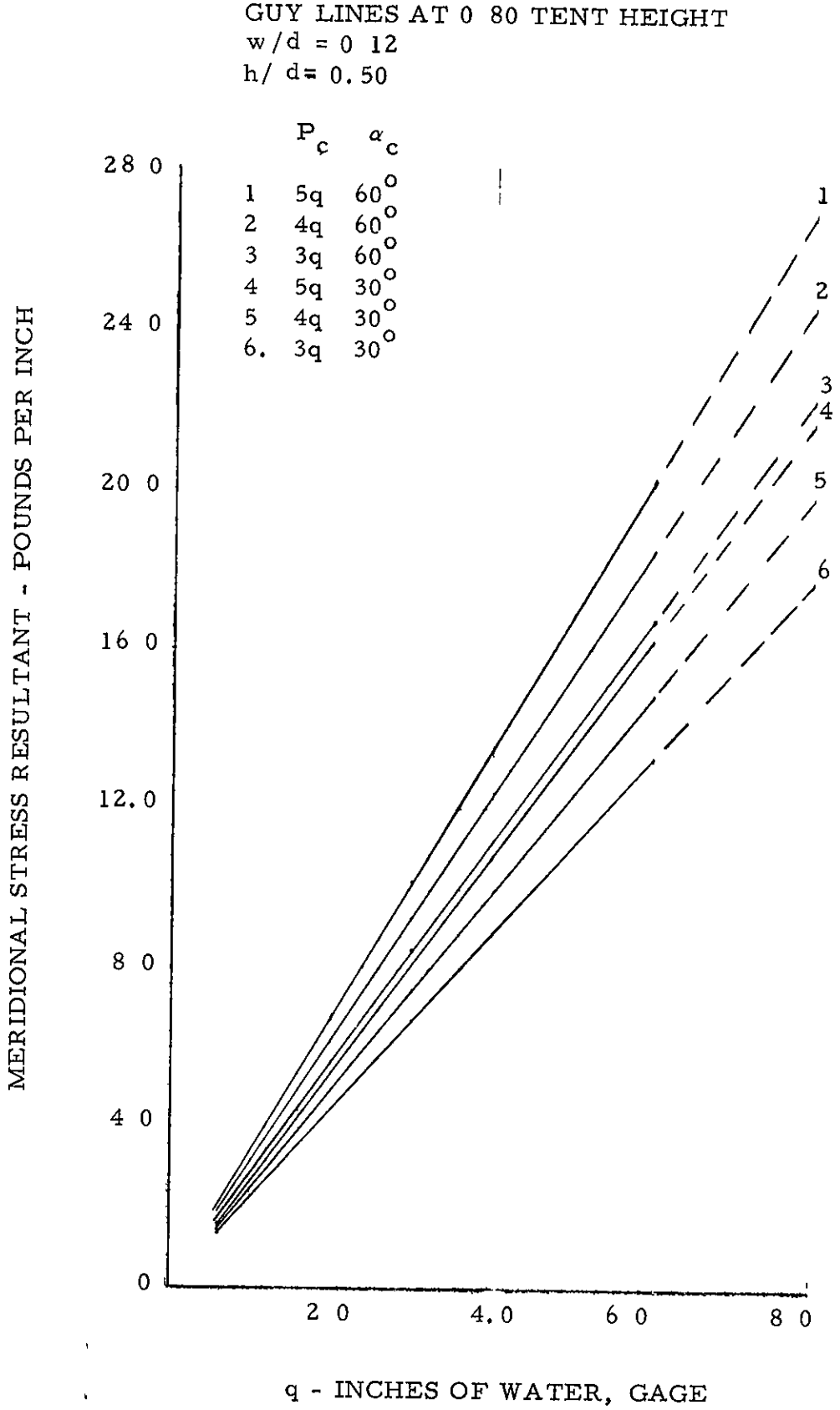

FIGURE 34. - VARIATION OF MERIDIONAL STRESS RESULTANT WITH IMPACT PRESSURE, q - DOUBLE WALL CYLINDERS.

GUY LINES AT 0 80 TENT HEIGHT
w/d = 0 080
h/d = 0.50

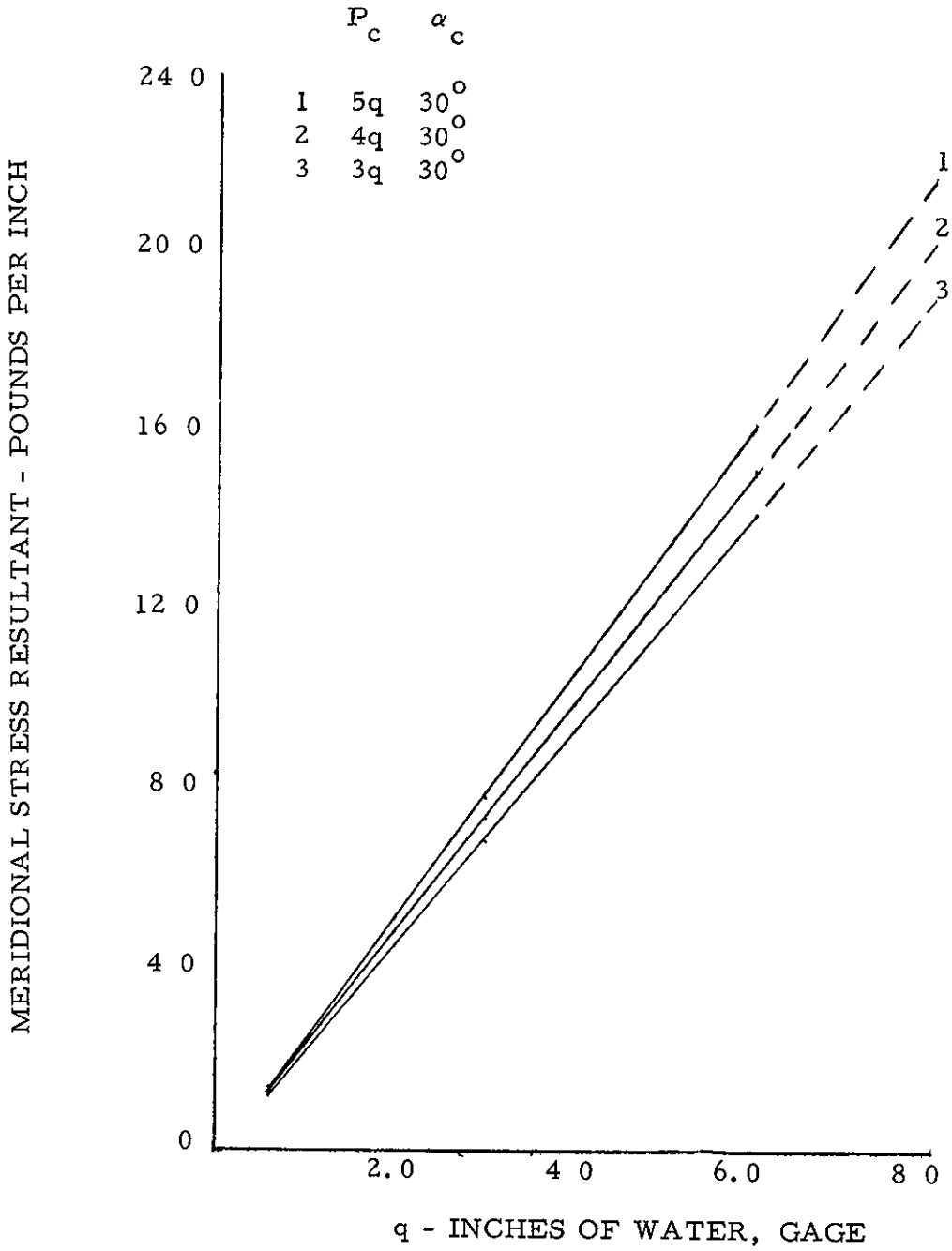

FIGURE 35. - VARIATION OF MERIDIONAL STRESS RESULTANT WITH IMPACT PRESSURE, q - DOUBLE WALL CYLINDERS

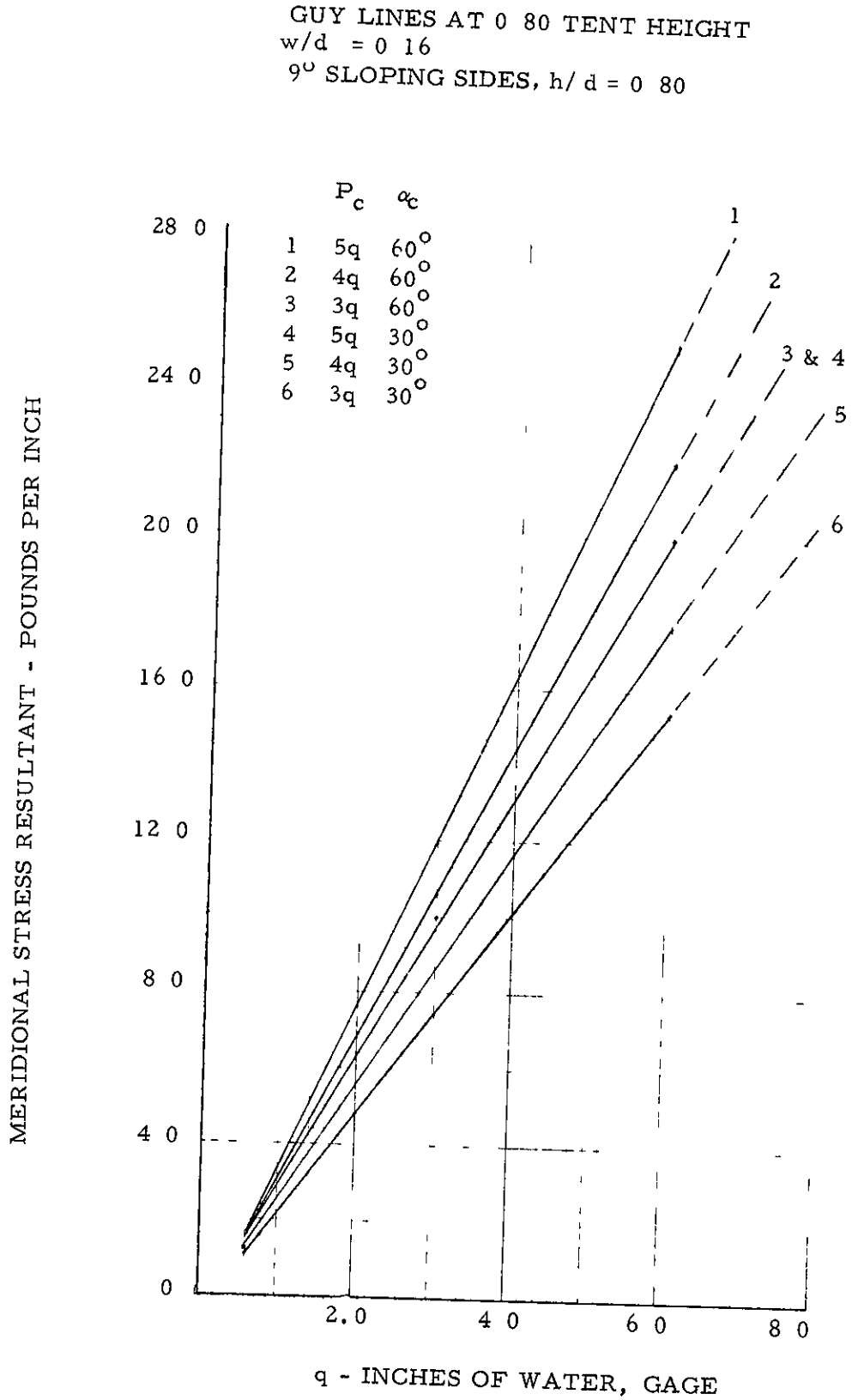

FIGURE 36 - VARIATION OF MERIDIONAL STRESS RESULTANT WITH IMPACT PRESSURE, q - DOUBLE WALL CYLINDERS

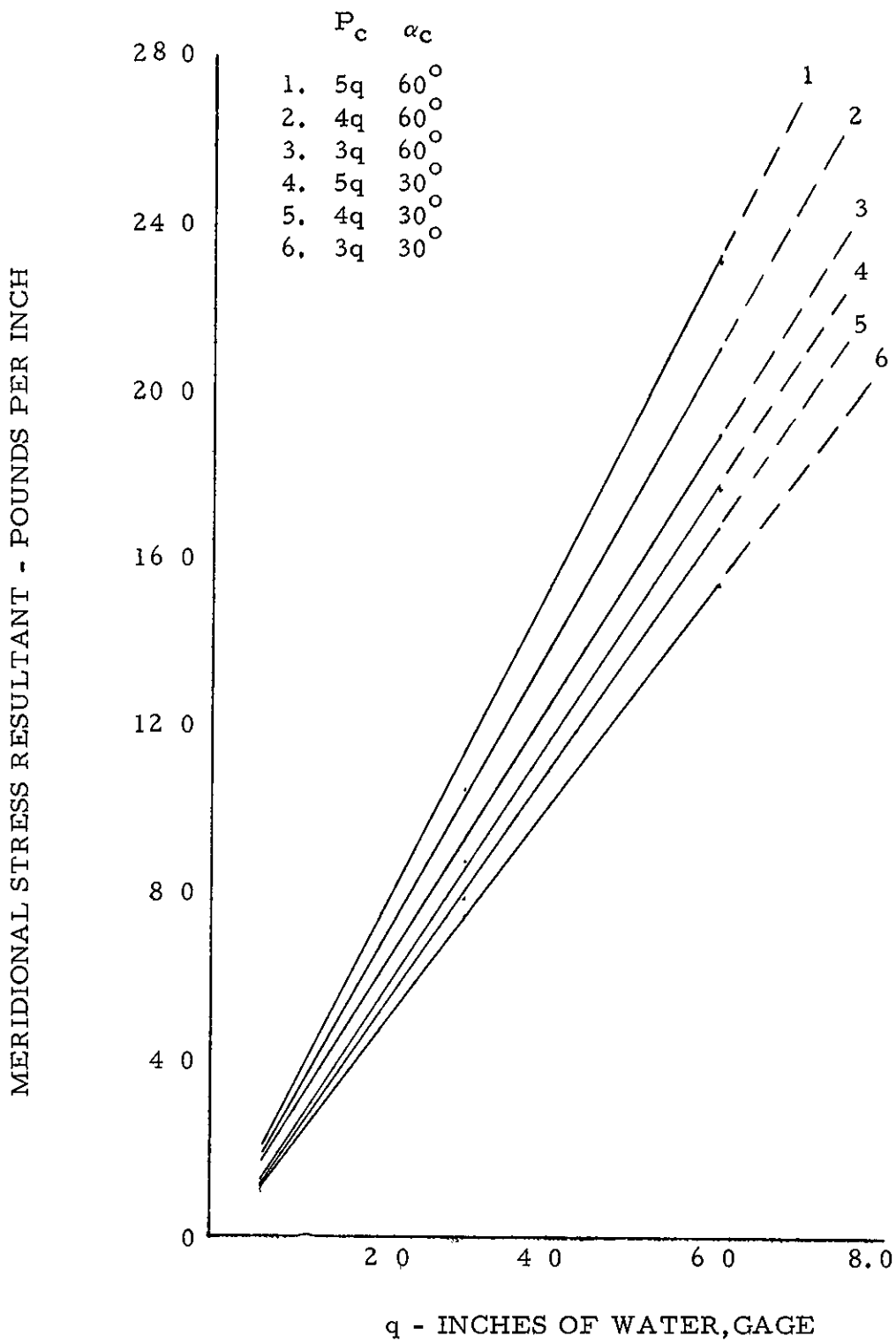

FIGURE 37. - VARIATION OF MERIDIONAL STRESS RESULTANT WITH IMPACT PRESSURE, q - DOUBLE WALL CYLINDERS.

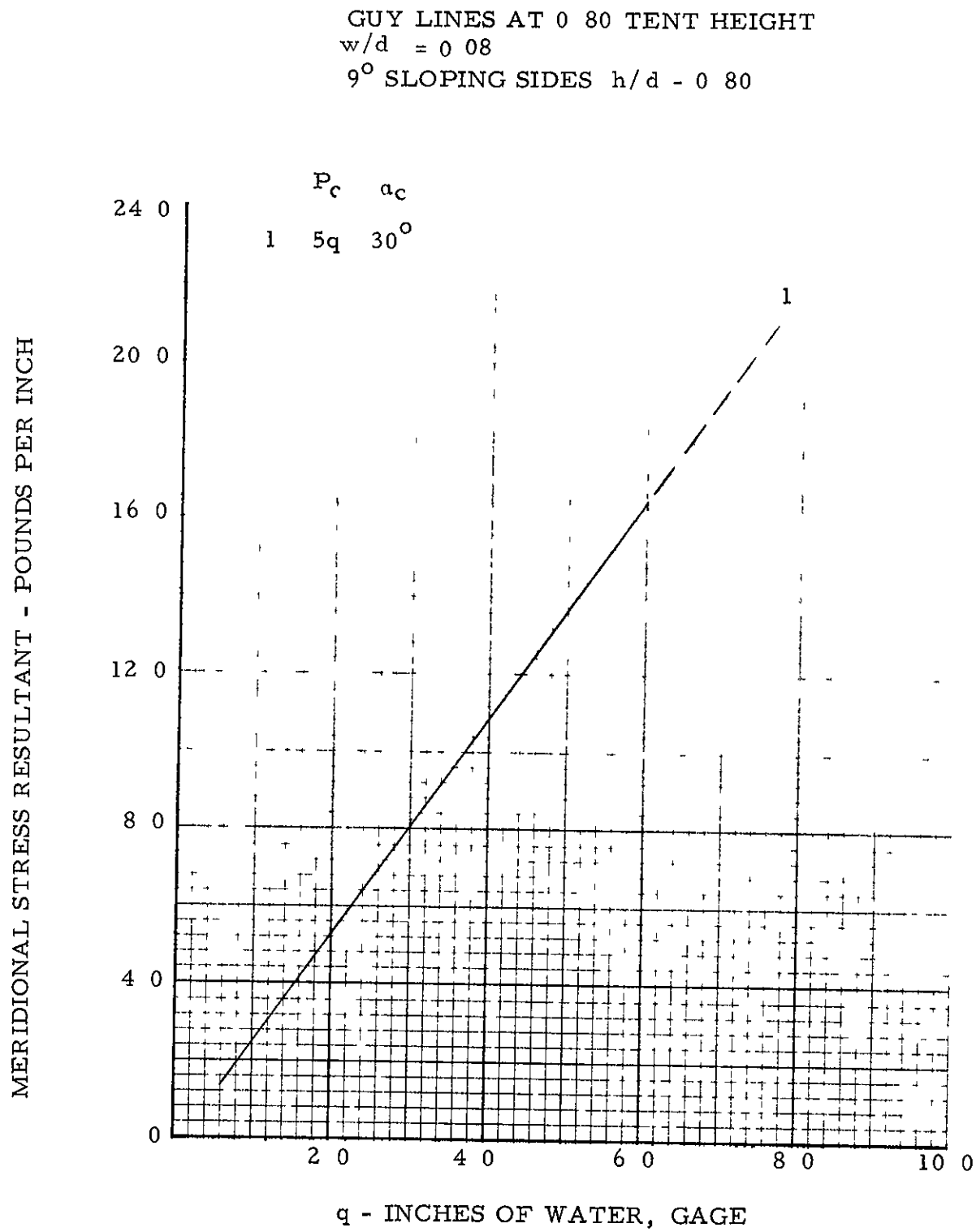

FIGURE 38. - VARIATION OF MERIDIONAL STRESS RESULTANT WITH IMPACT PRESSURE, q - DOUBLE WALL CYLINDERS

GUY LINES AT 0.80 TENT HEIGHT
w/d = 0 16
h/d = 0 75

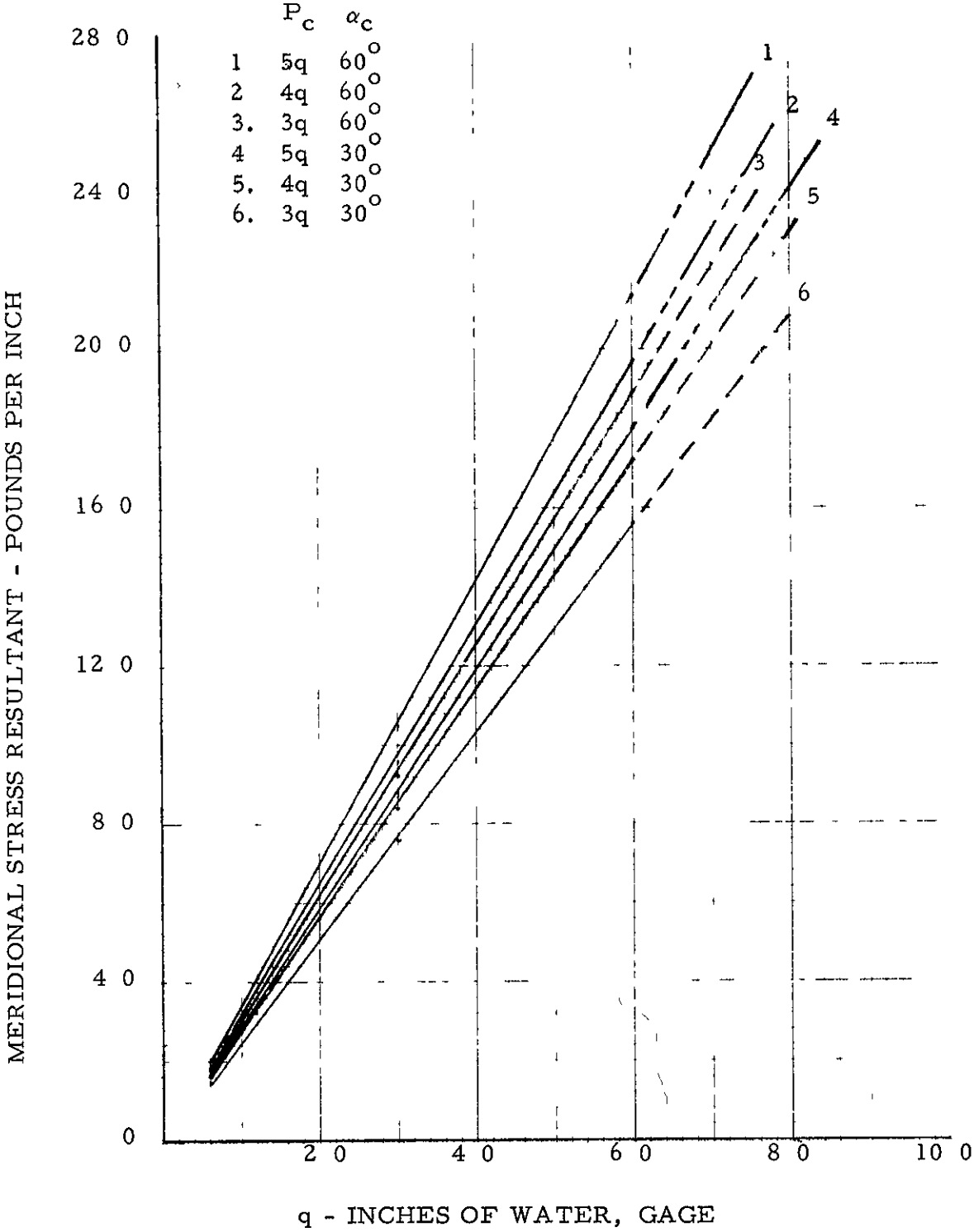

FIGURE 39 - VARIATION OF MERIDIONAL STRESS RESULTANT WITH IMPACT PRESSURE, q- DOUBLE WALL CYLINDERS

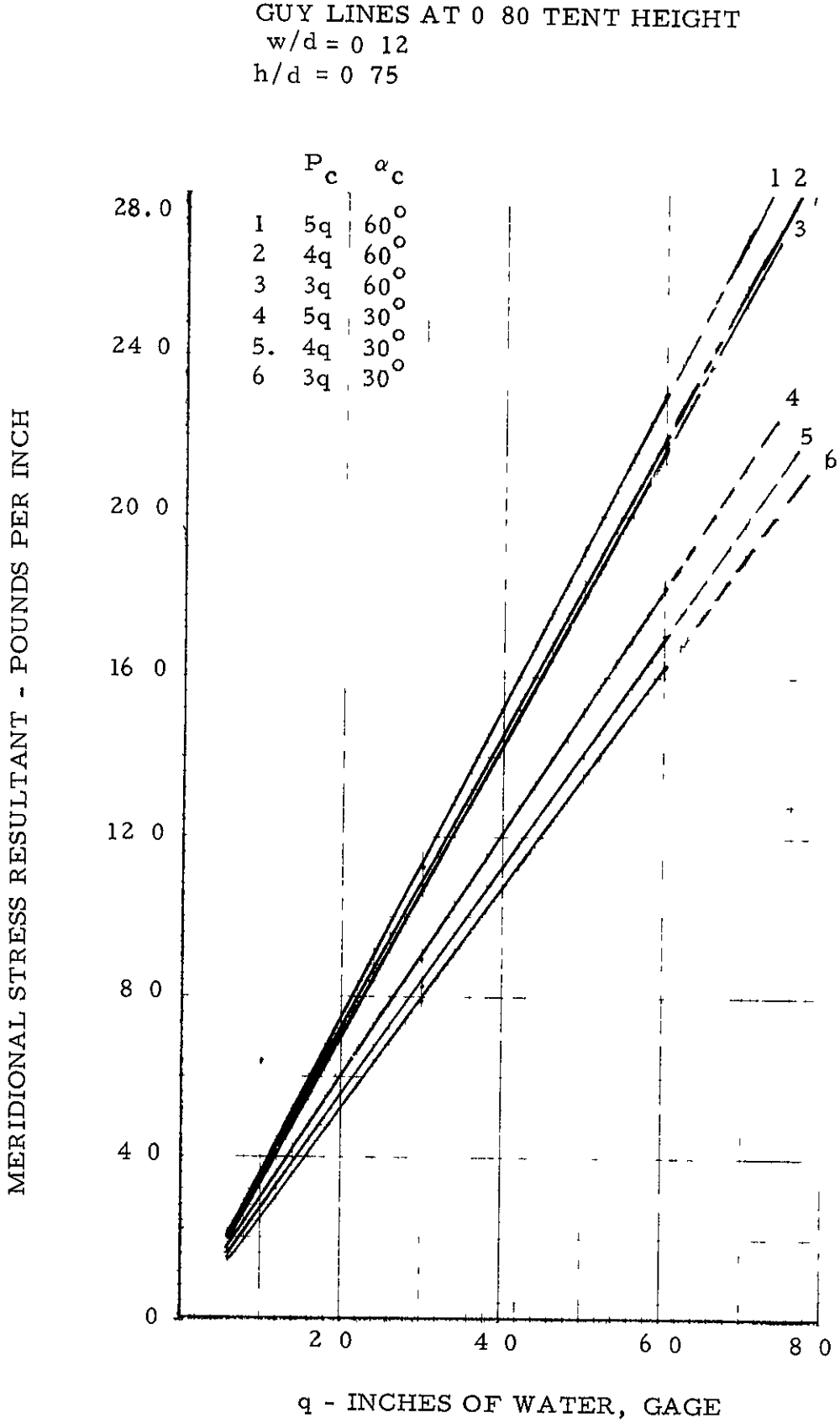

FIGURE 40. - VARIATION OF MERIDIONAL STRESS RESULTANT WITH IMPACT PRESSURE, q - DOUBLE WALL CYLINDERS

GUY LINES AT 0 80 TENT HEIGHT
w/d = 0 08
h/d - 0 75

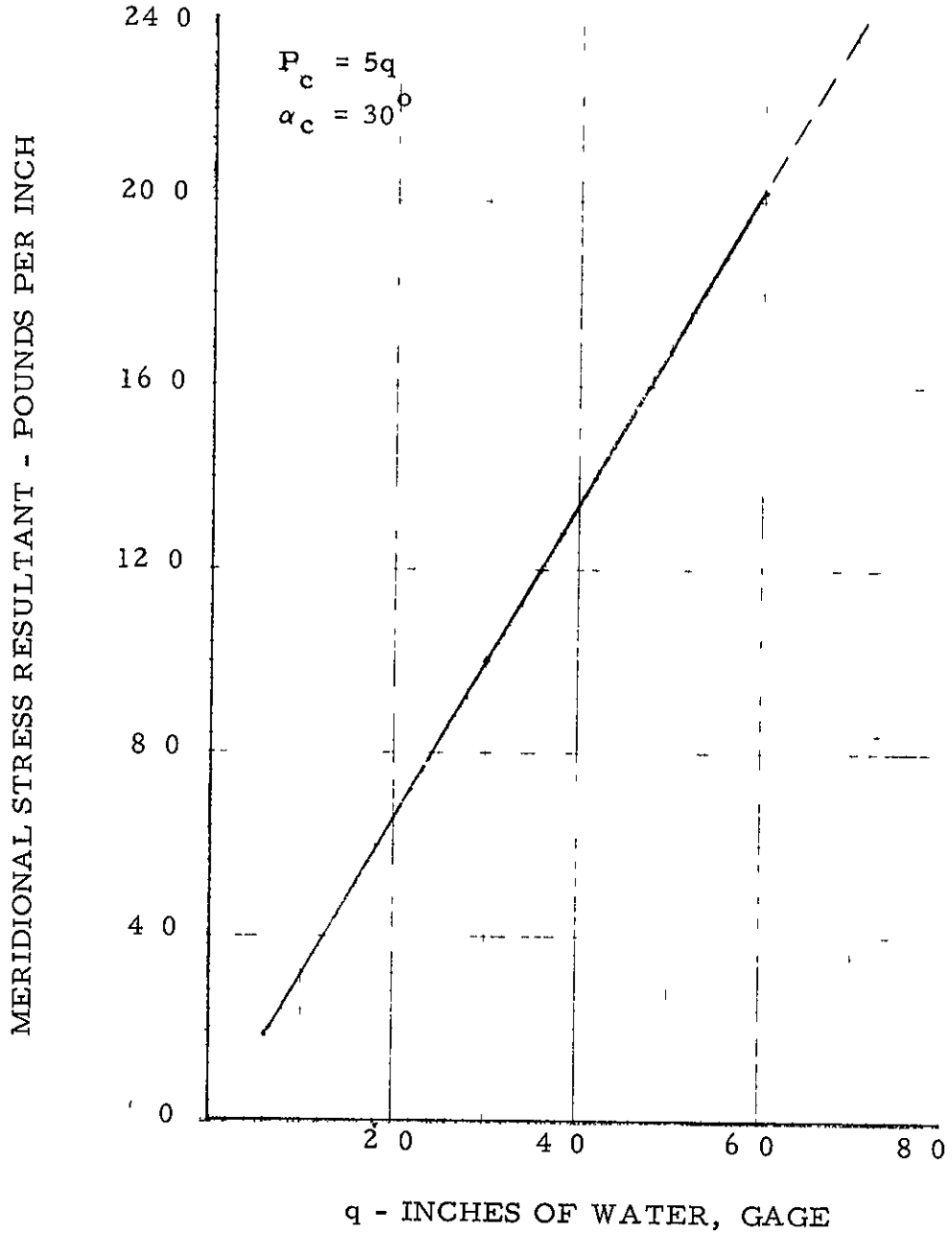

FIGURE 41. - VARIATION OF MERIDIONAL STRESS RESULTANT WITH IMPACT PRESSURE, q - DOUBLE WALL CYLINDERS

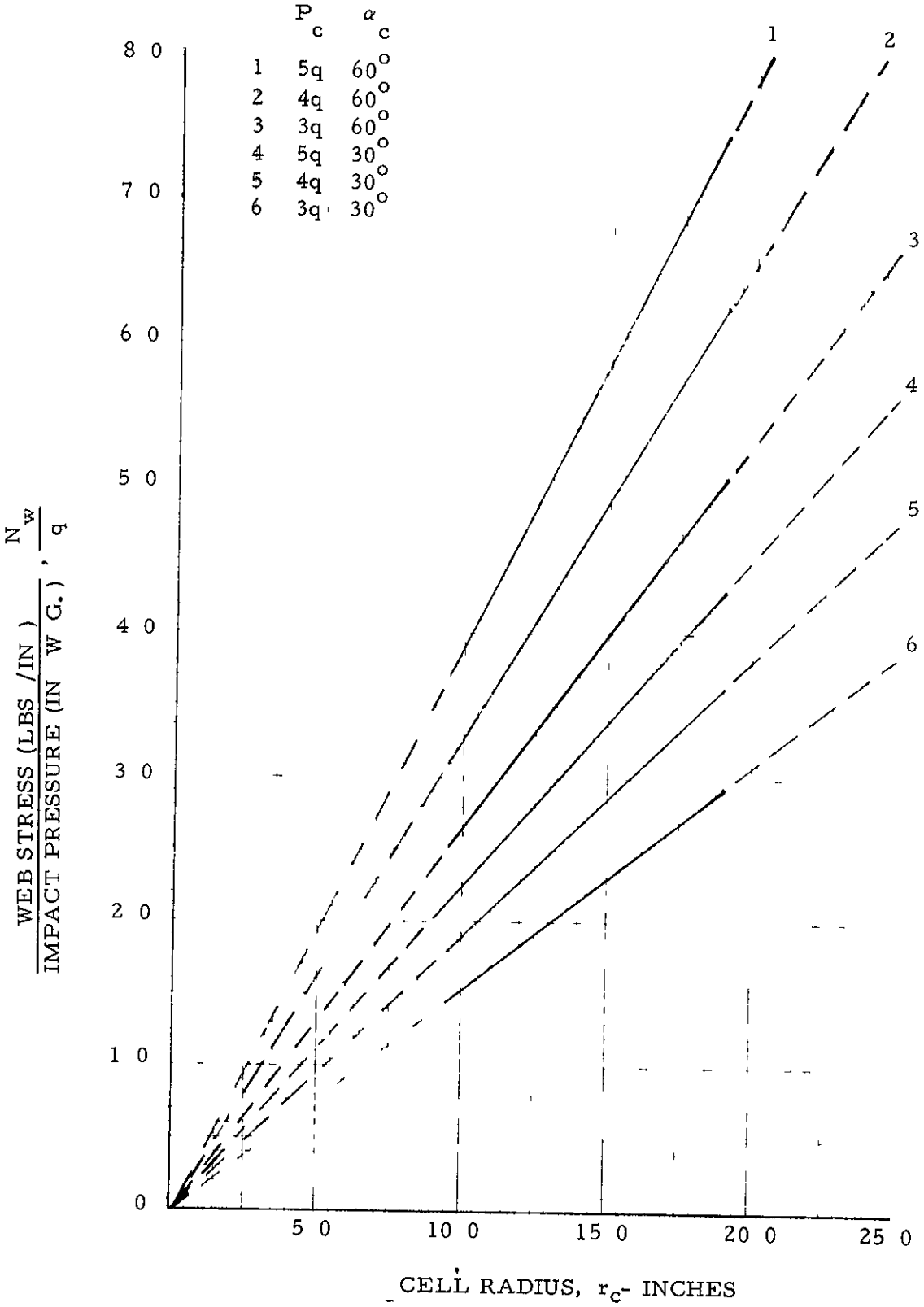

FIGURE 42 - VARIATION OF RATIO OF WEB STRESS TO IMPACT PRESSURE WITH CELL RADIUS - DOUBLE WALL CYLINDERS

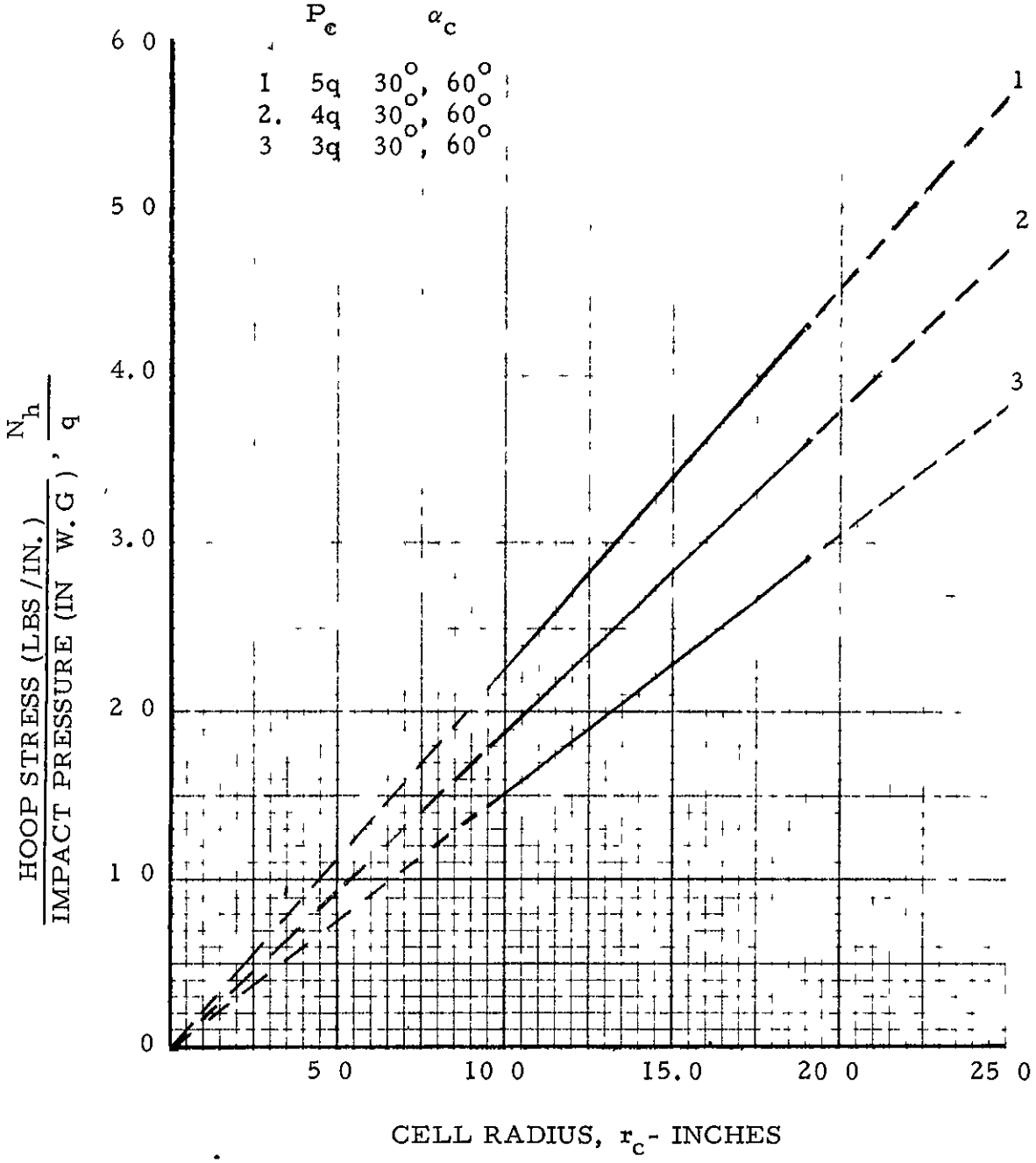

FIGURE 43 - VARIATION OF RATIO OF HOOP STRESS WITH IMPACT PRESSURE WITH CELL RADIUS - DOUBLE WALL CYLINDERS

α_c n Relationship for Maximum Volume to Weight Ratio Double Wall Tent

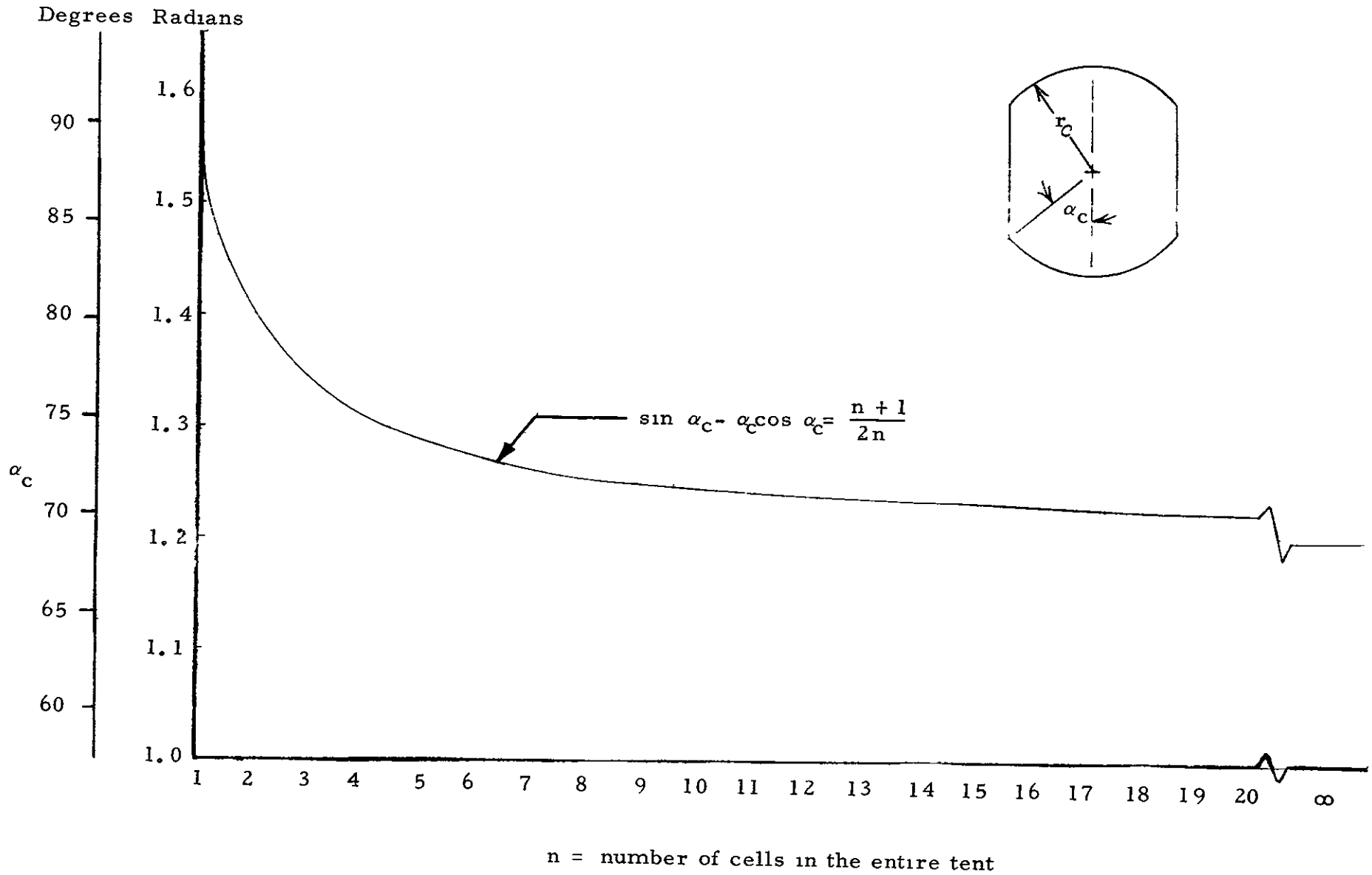

FIGURE 44

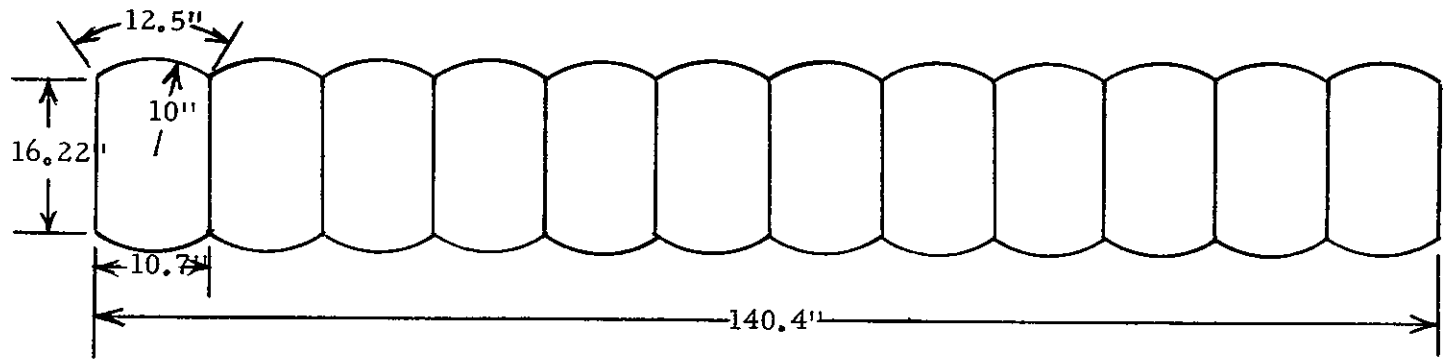

Cell Size, Tent # 1 Scale 1/20

(a)

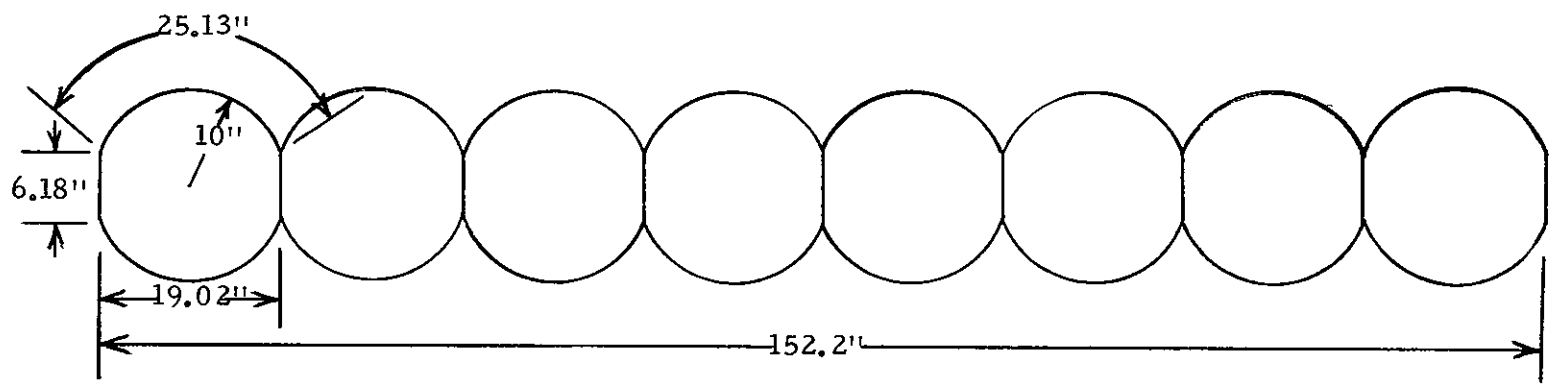

Cell Size, Tent # 2 Scale 1/20

Figure 45. - Relative Sizes of Tent Cells.

SINGLE WALL SPHERES
MODEL NO 4
TEST NO. 173

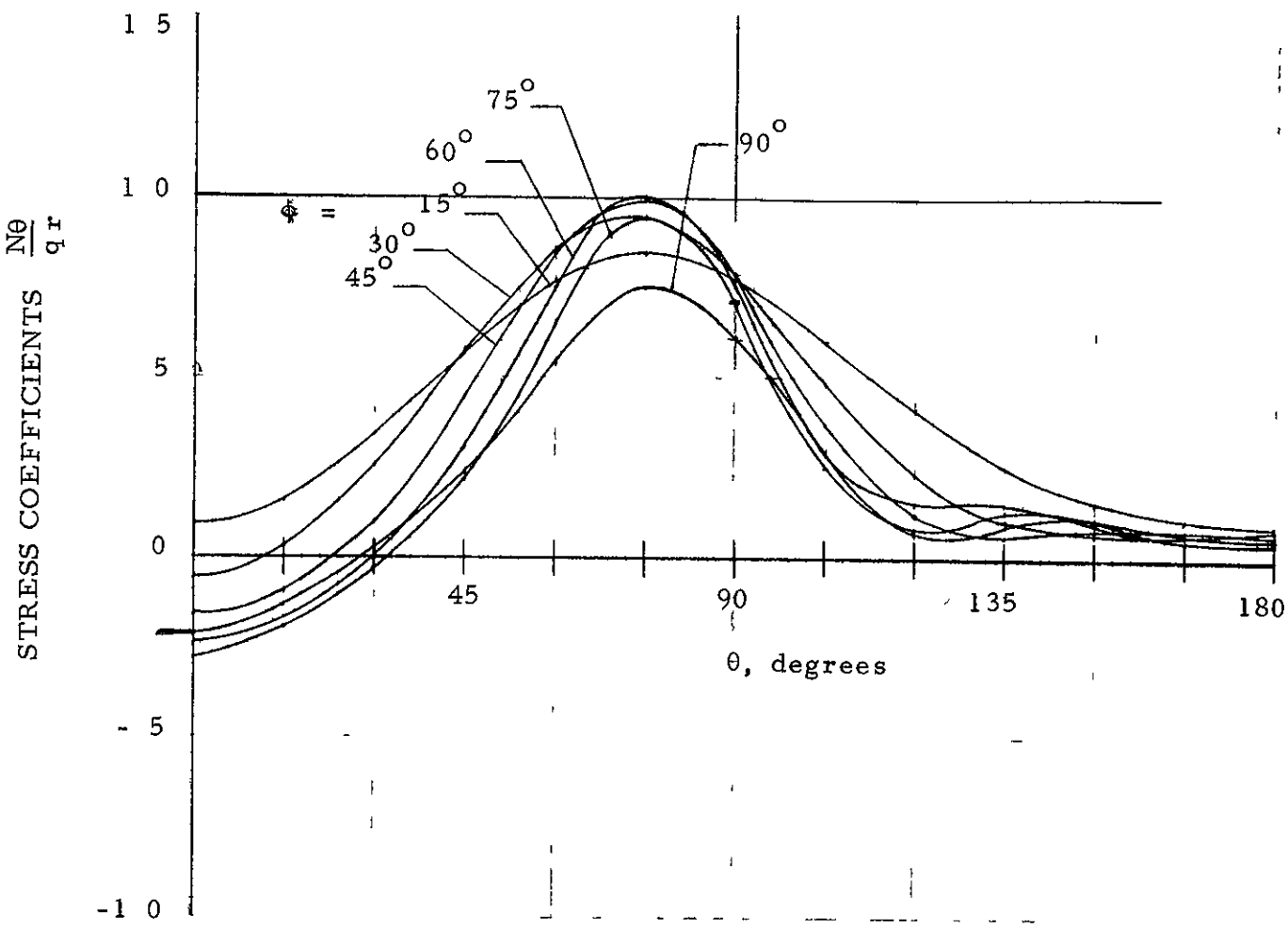

FIGURE 47 - TYPICAL STRESS COEFFICIENTS

SINGLE WALL SPHERES
MODEL NO. 4
TEST NO. 173

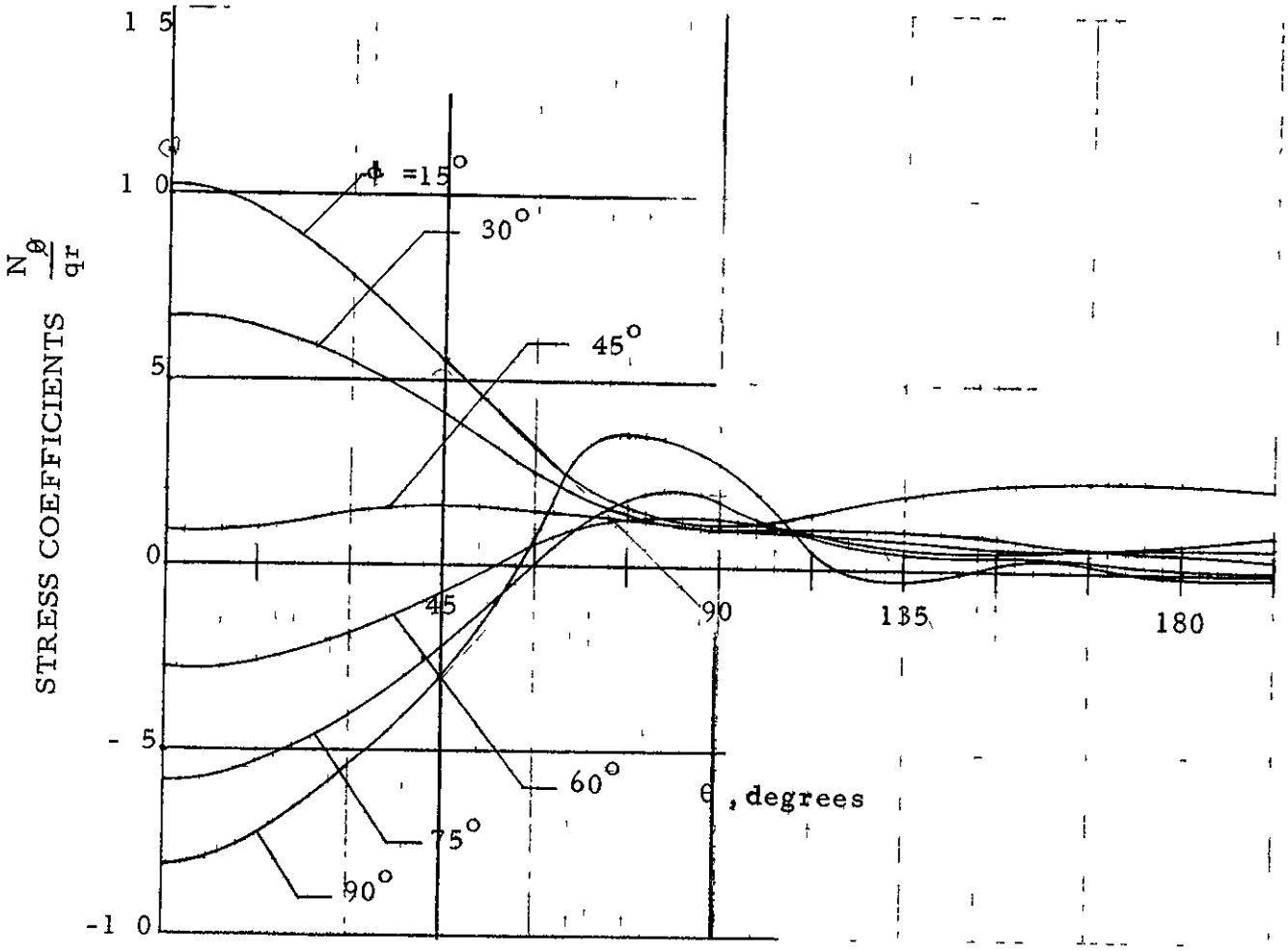

FIGURE 48 - TYPICAL STRESS COEFFICIENTS.

SINGLE WALL SPHERES
MODEL NO 4
TEST NO. 173

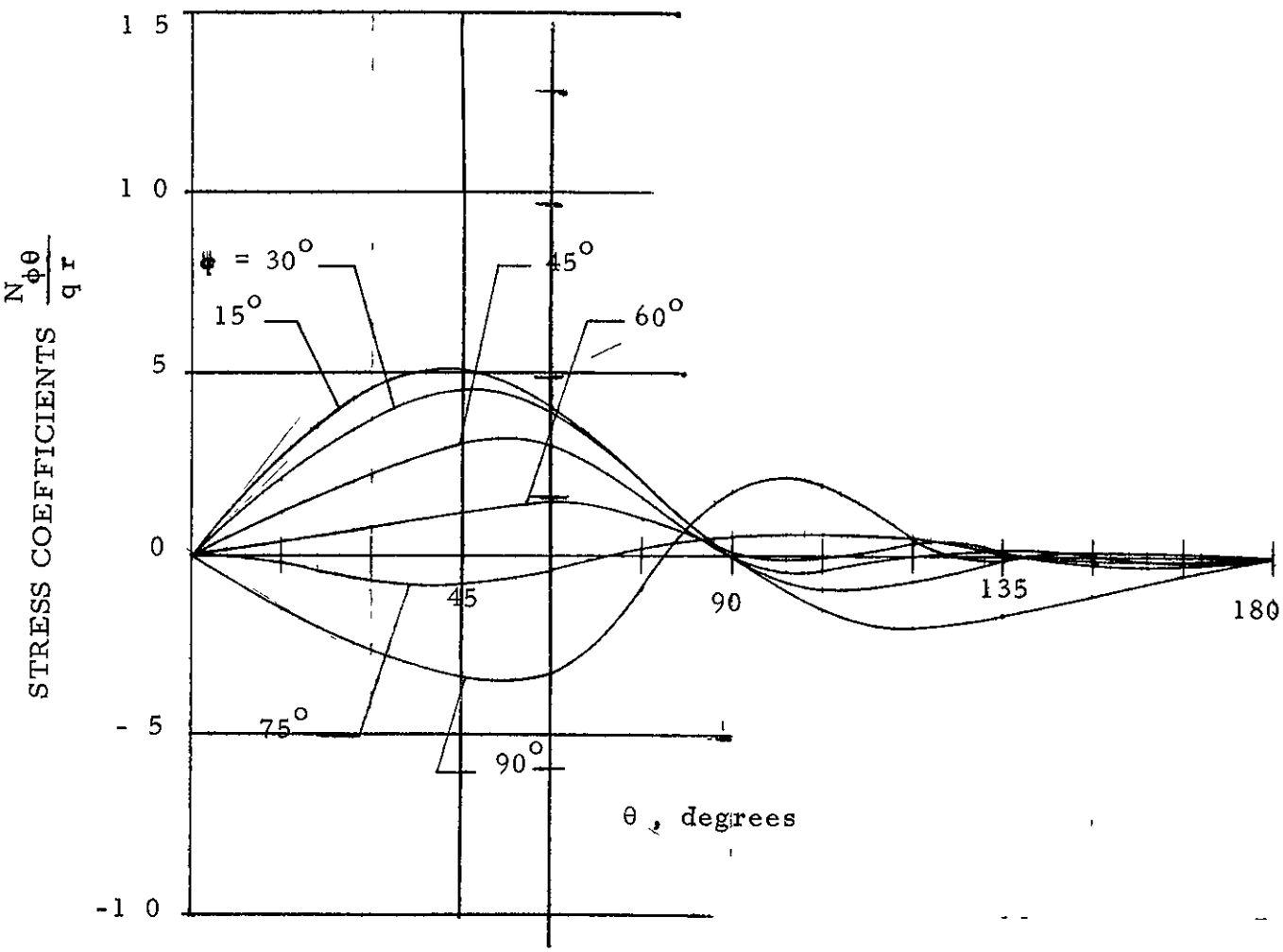

FIGURE 49 - TYPICAL STRESS COEFFICIENTS

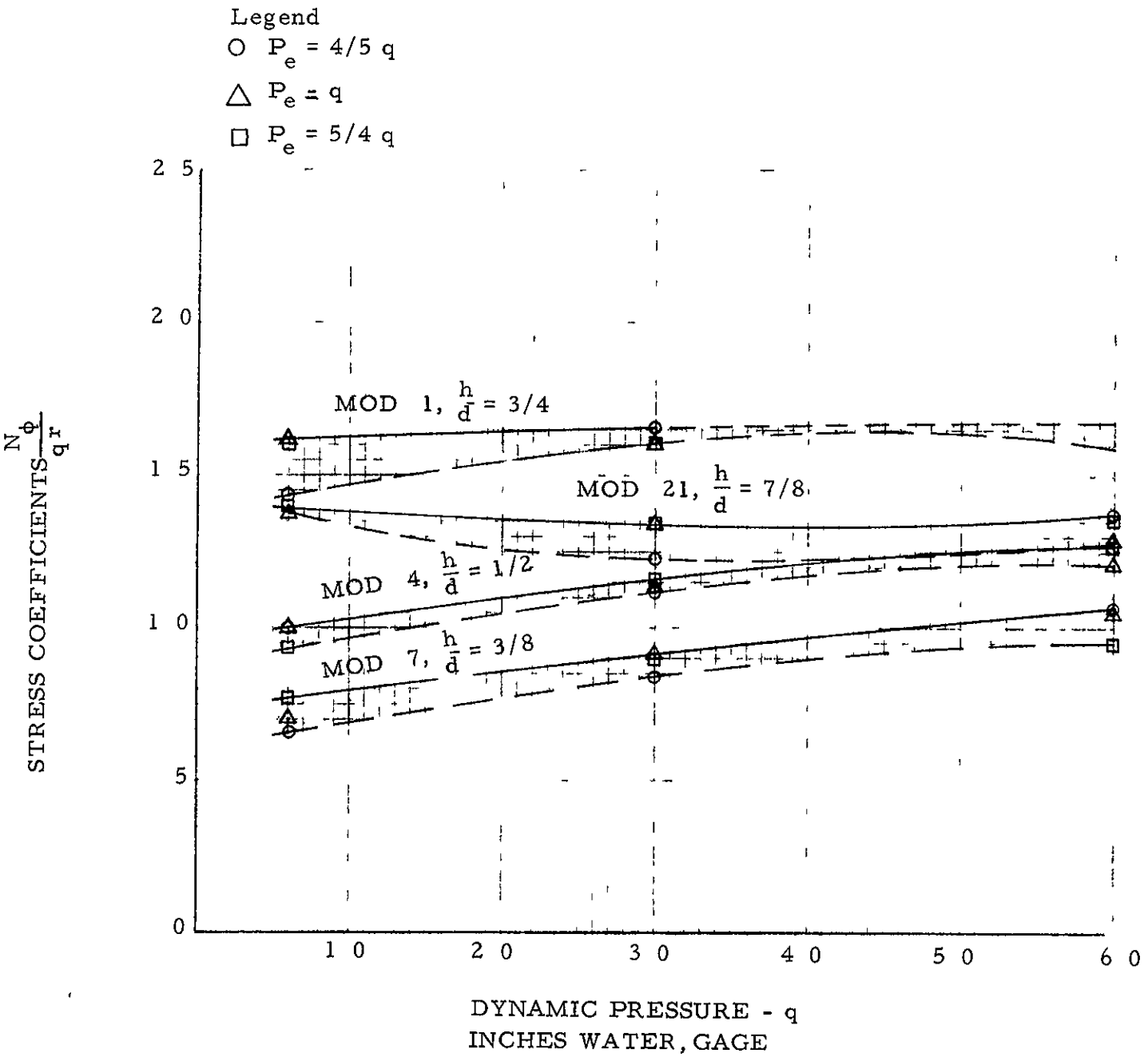

FIGURE 50. - CALCULATED PEAK STRESS COEFFICIENTS, $\frac{N_\phi}{qr}$

SINGLE WALL SPHERES

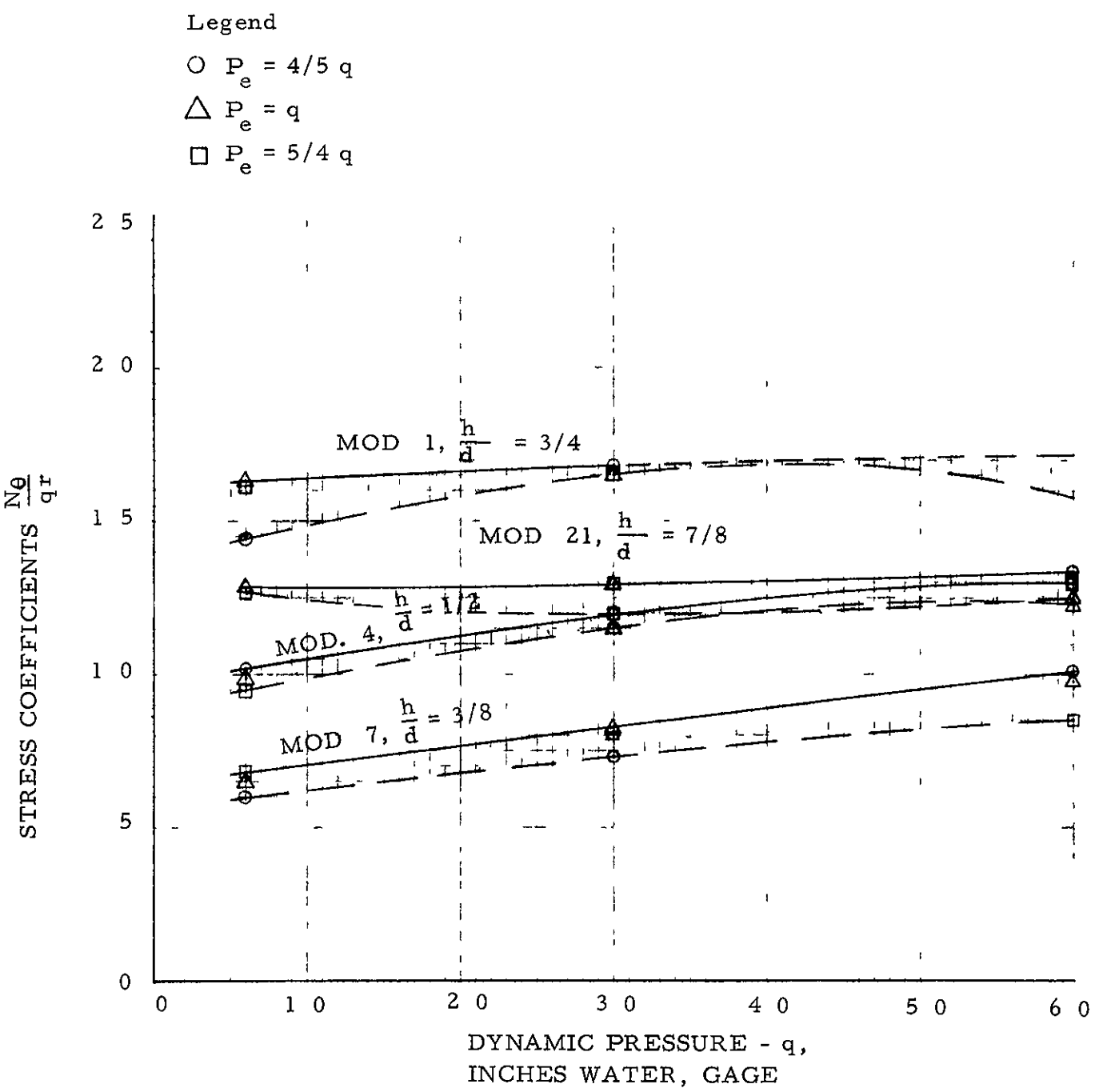

FIGURE 51. - CALCULATED PEAK STRESS COEFFICIENTS, $\frac{N_\theta}{q\,r}$

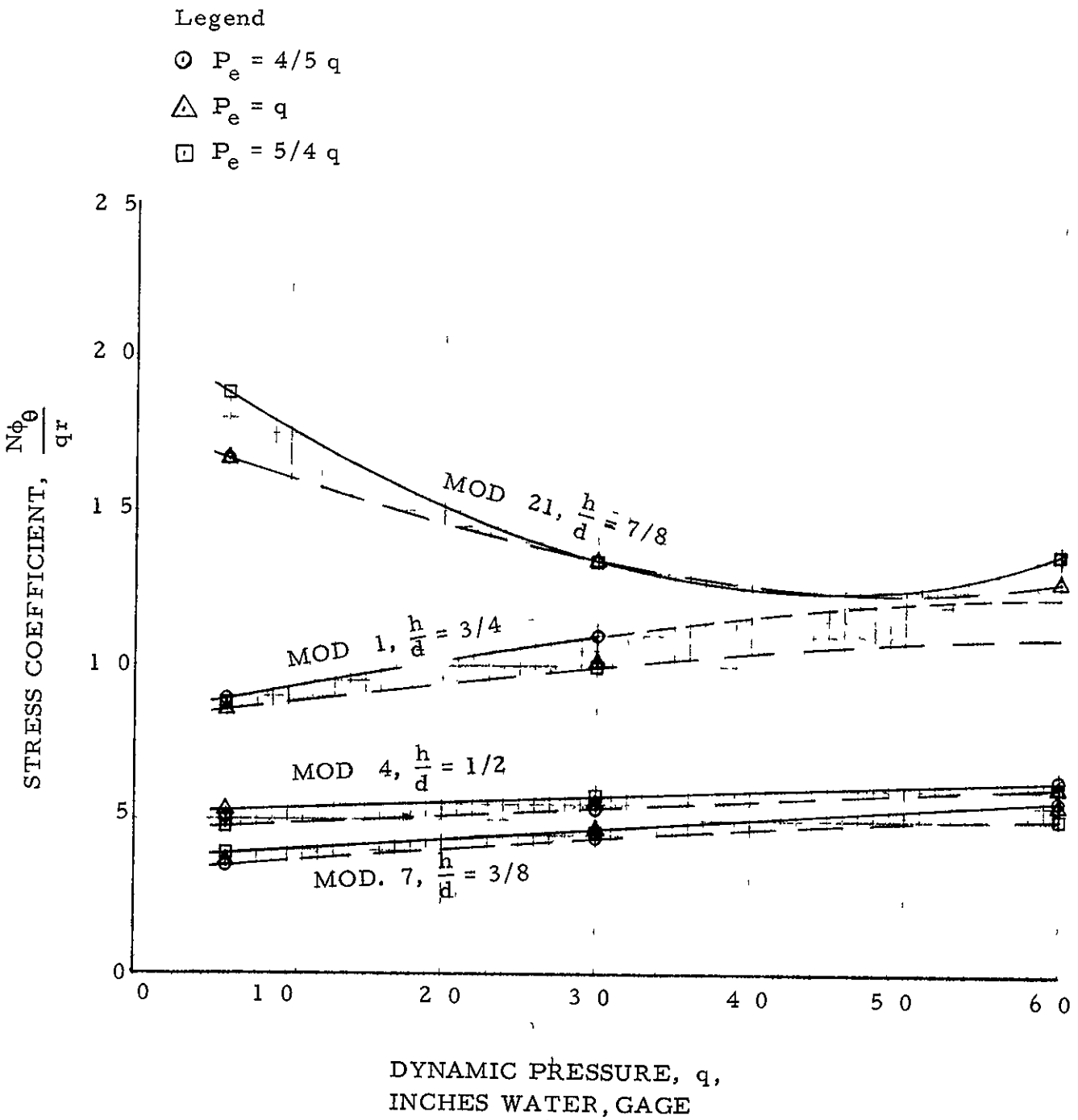

FIGURE 52. - CALCULATED PEAK STRESS COEFFICIENTS, $\frac{N_{\phi\theta}}{qr}$

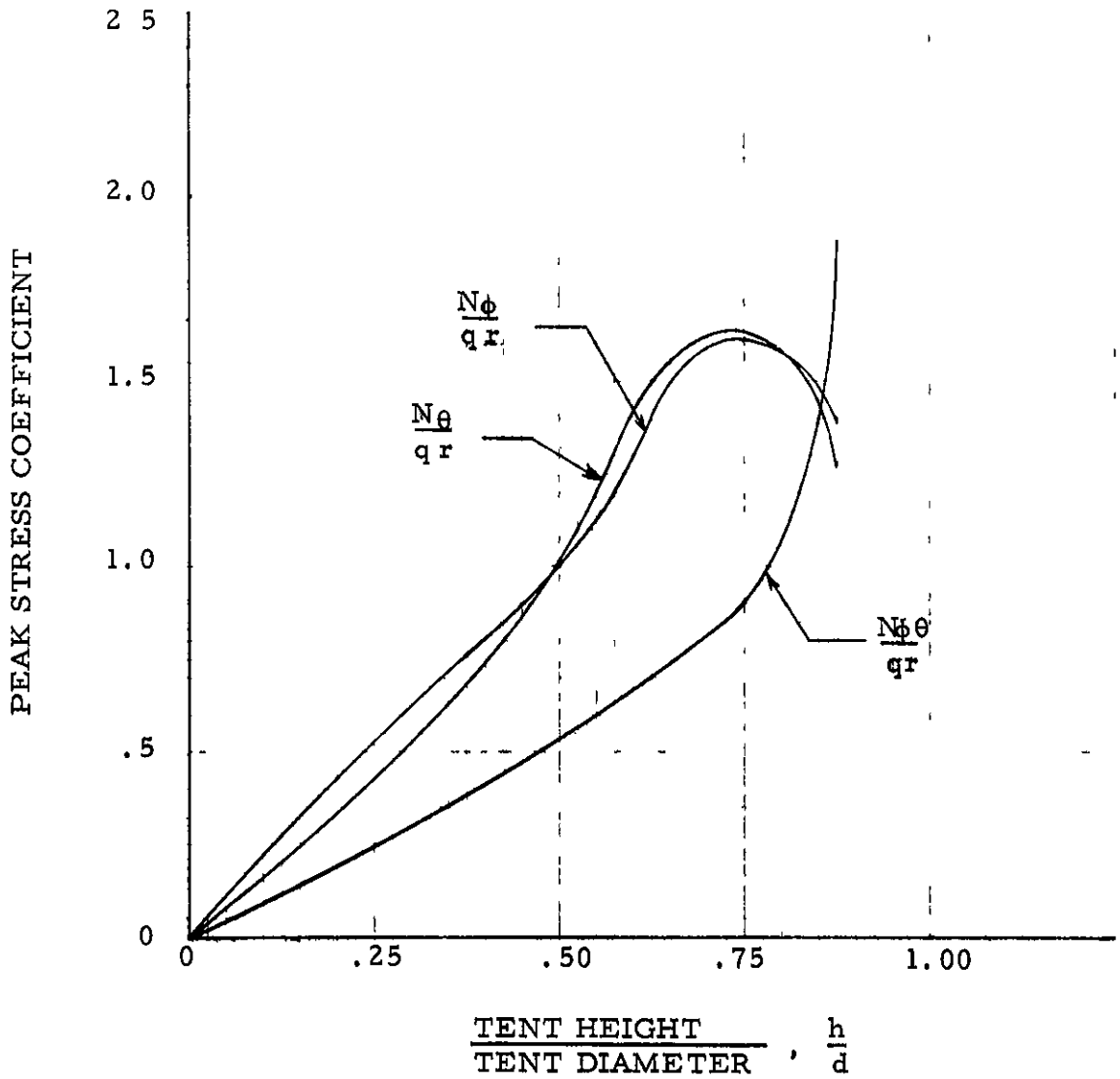

FIGURE 53. - VARIATION OF PEAK STRESS COEFFICIENT WITH SHAPE AT q = 0.6 INCHES OF WATER GAGE, NON POROUS SINGLE WALL SPHERES.

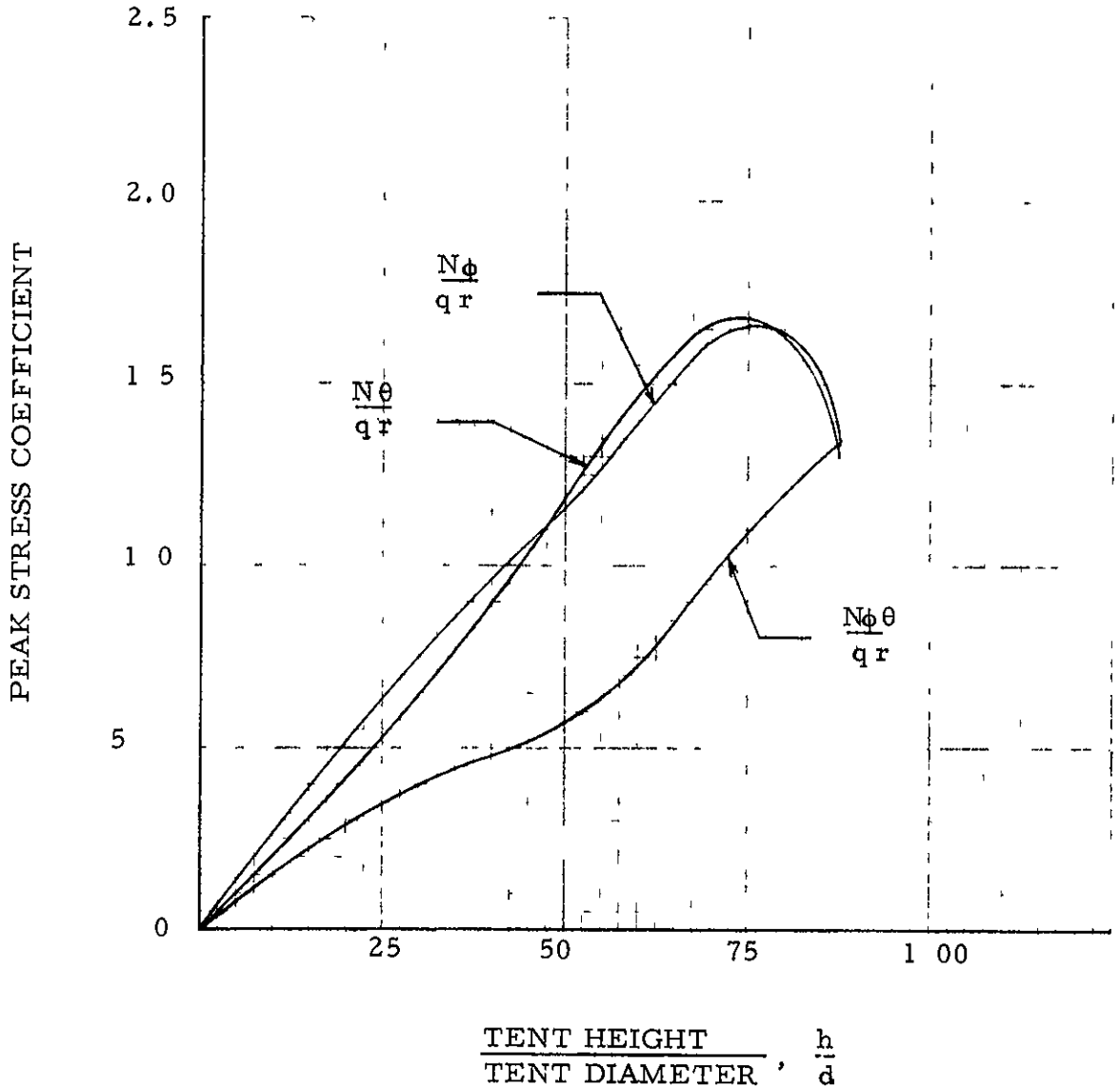

FIGURE 54. - VARIATION OF PEAK STRESS COEFFICIENT WITH SHAPE AT q = 3.0 INCHES OF WATER GAGE, NON POROUS SINGLE WALL SPHERES.

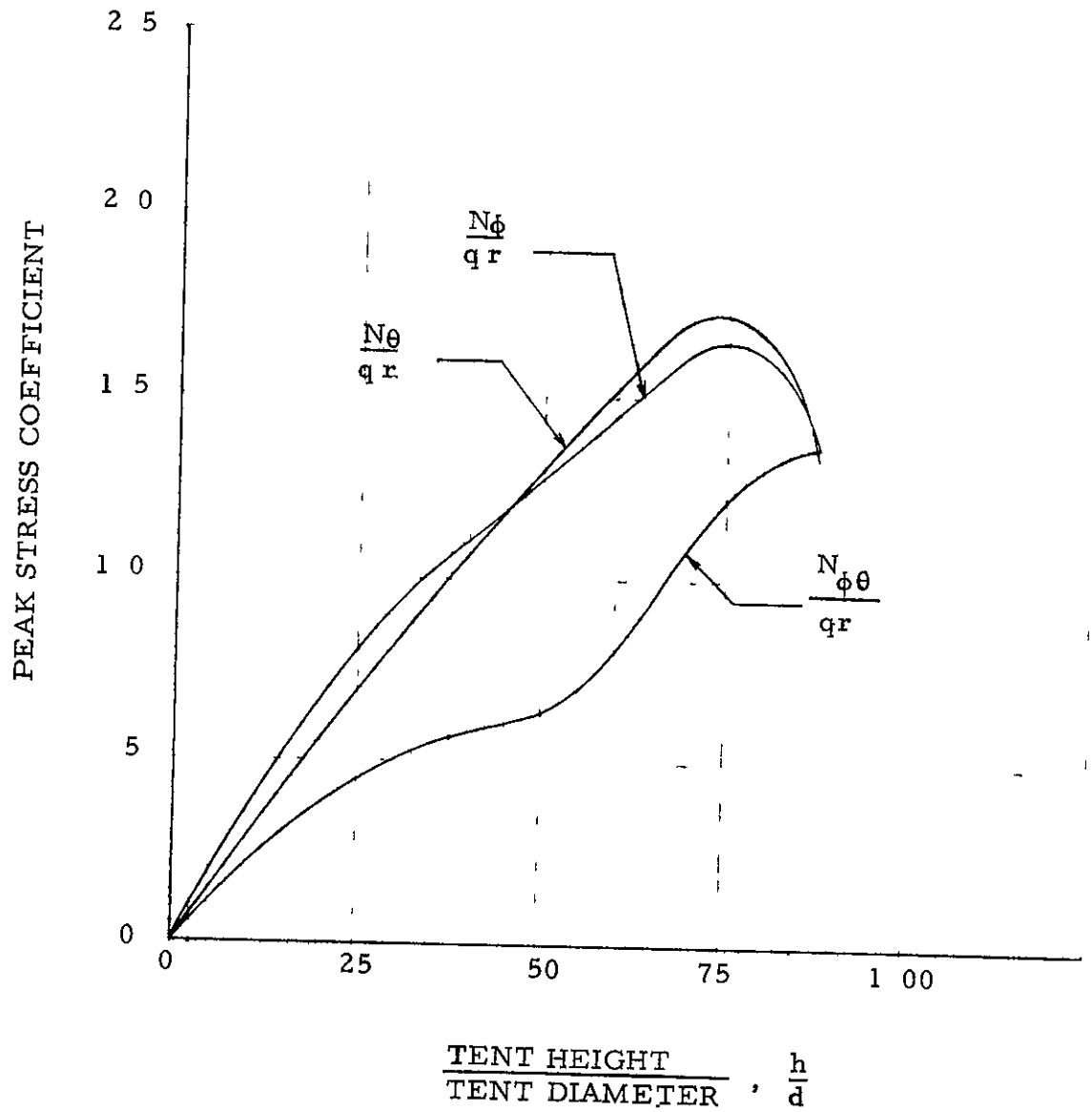

FIGURE ' 55 - VARIATION OF PEAK STRESS COEFFICIENTS WITH SHAPE AT q = 6.0 INCHES OF WATER, GAGE, NON POROUS SINGLE WALL SPHERES

SINGLE WALL SPHERES

$\frac{h}{d} = \frac{3}{8}$

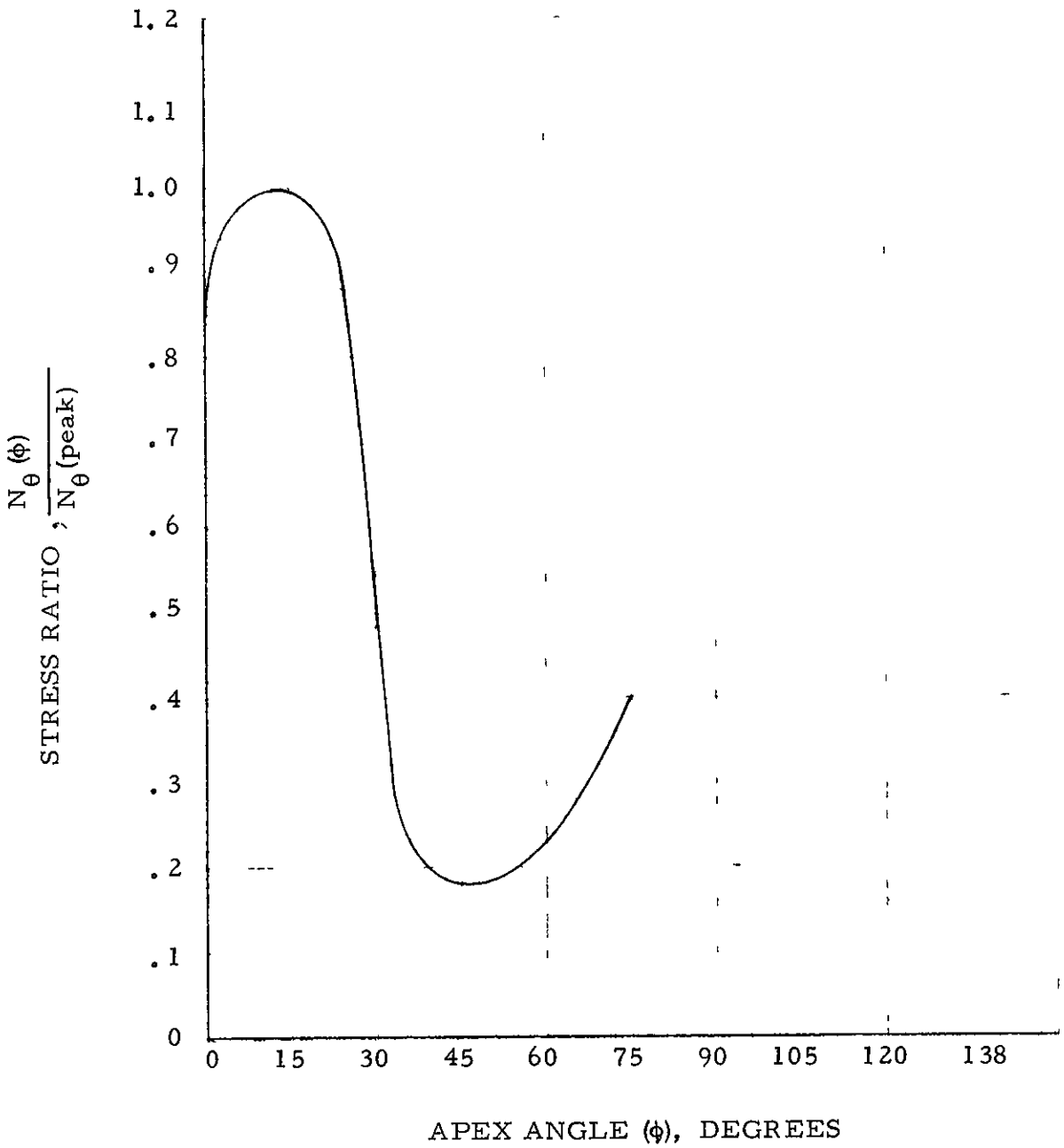

FIGURE 56 - STRESS RATIO, $\frac{N_\theta(\phi)}{N_\theta(\text{peak})}$ VS. APEX ANGLE, ϕ

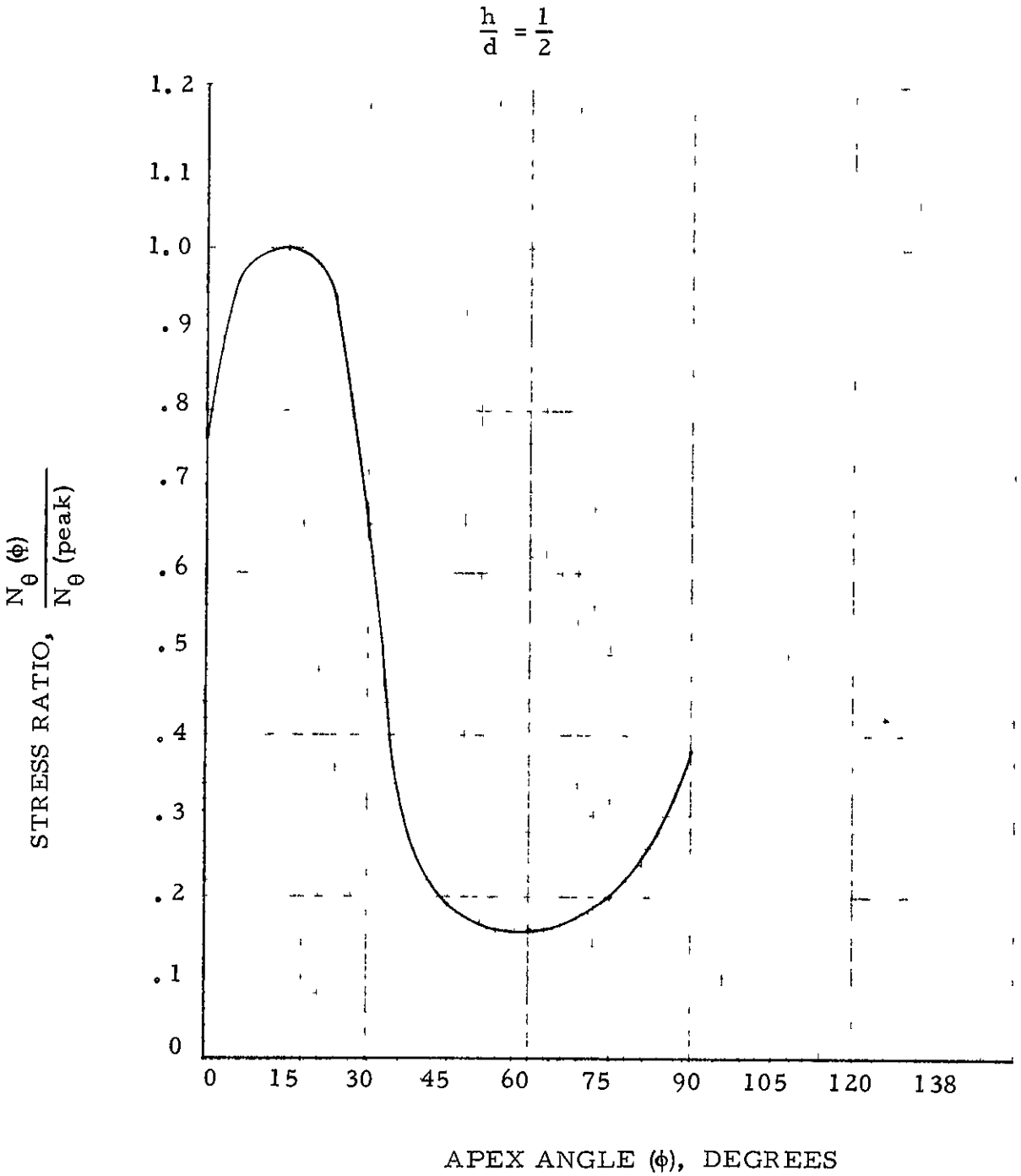

FIGURE 57. - STRESS RATIO, $\frac{N_\theta(\phi)}{N_\theta(\text{peak})}$ VS. APEX ANGLE, ϕ

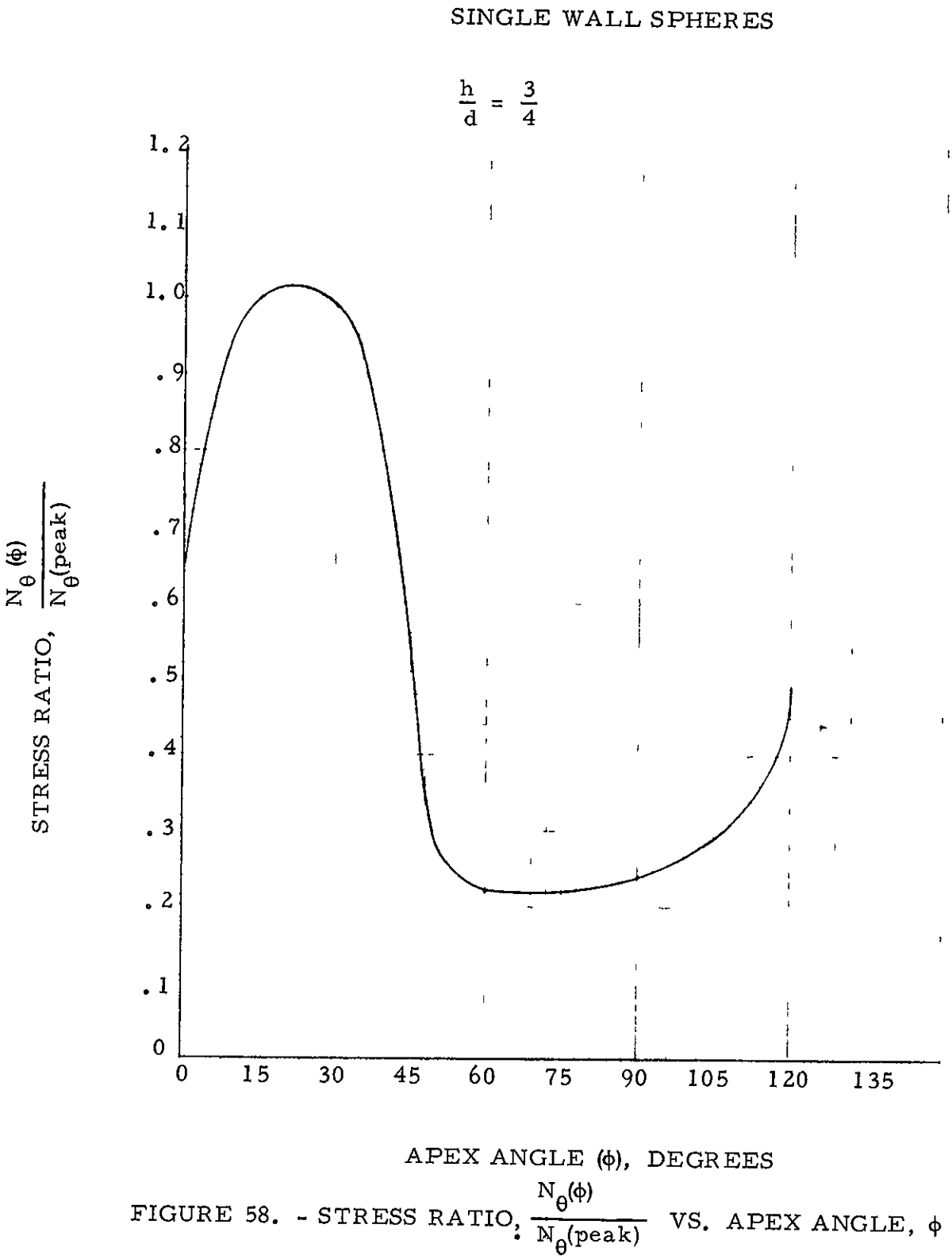

FIGURE 58. - STRESS RATIO, $\frac{N_\theta(\phi)}{N_\theta(\text{peak})}$ VS. APEX ANGLE, ϕ

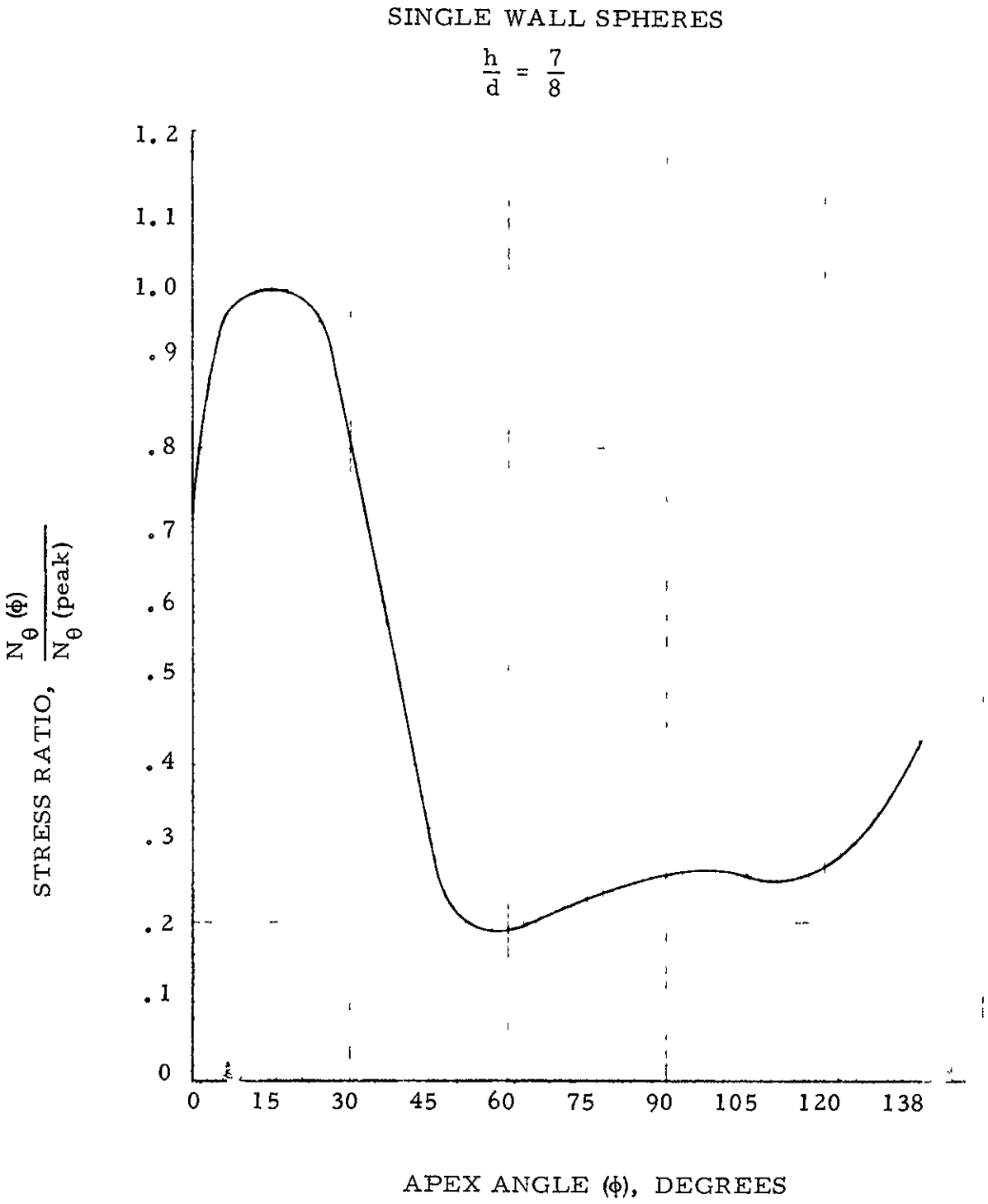

FIGURE 59. - STRESS RATIO, $\frac{N_\theta(\phi)}{N_\theta(\text{peak})}$ VS. APEX ANGLE, ϕ

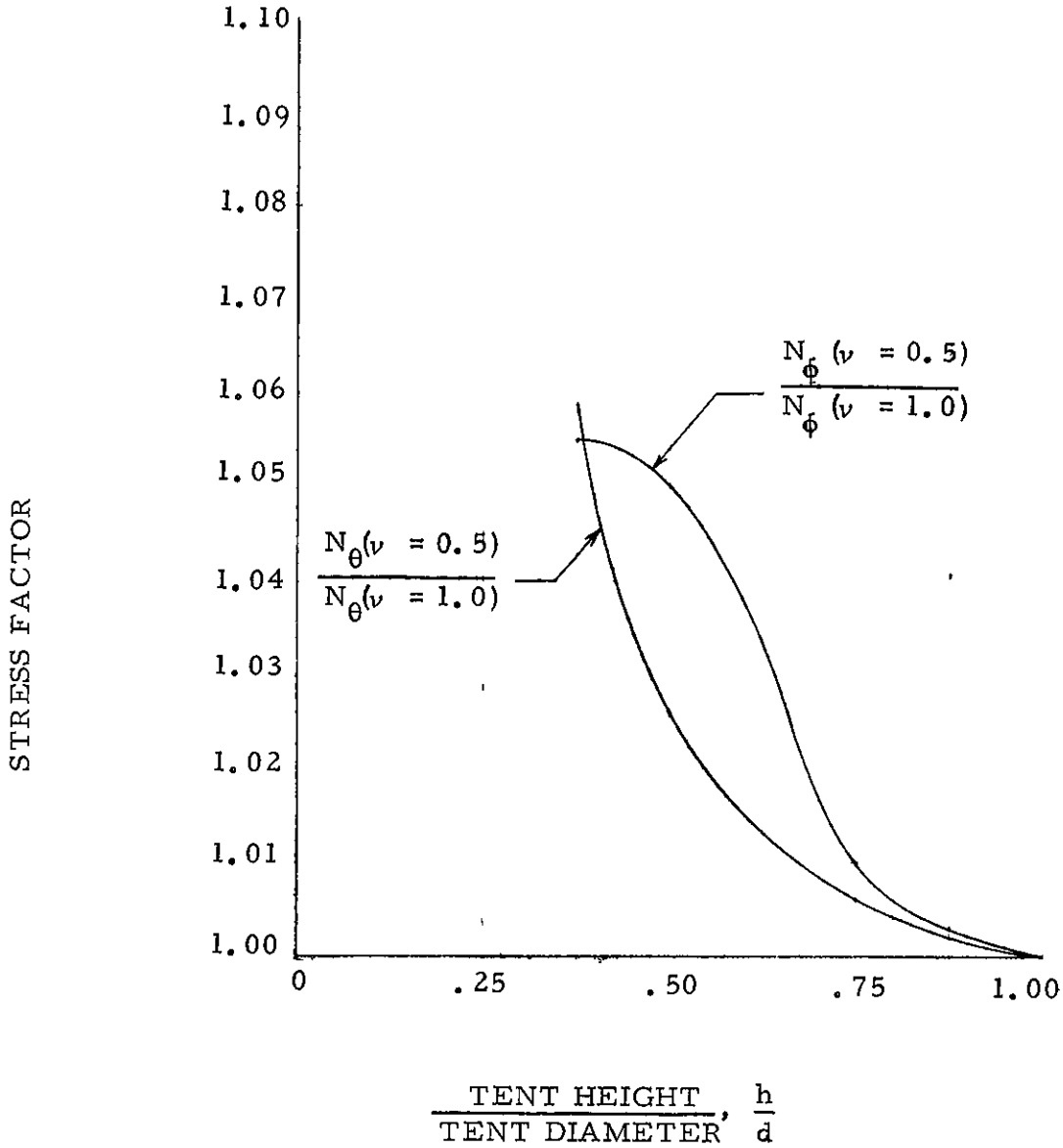

FIGURE 60 - STRESS FACTOR FOR TENT FABRIC WITH POISSONS RATIO, $\nu = 0.5$

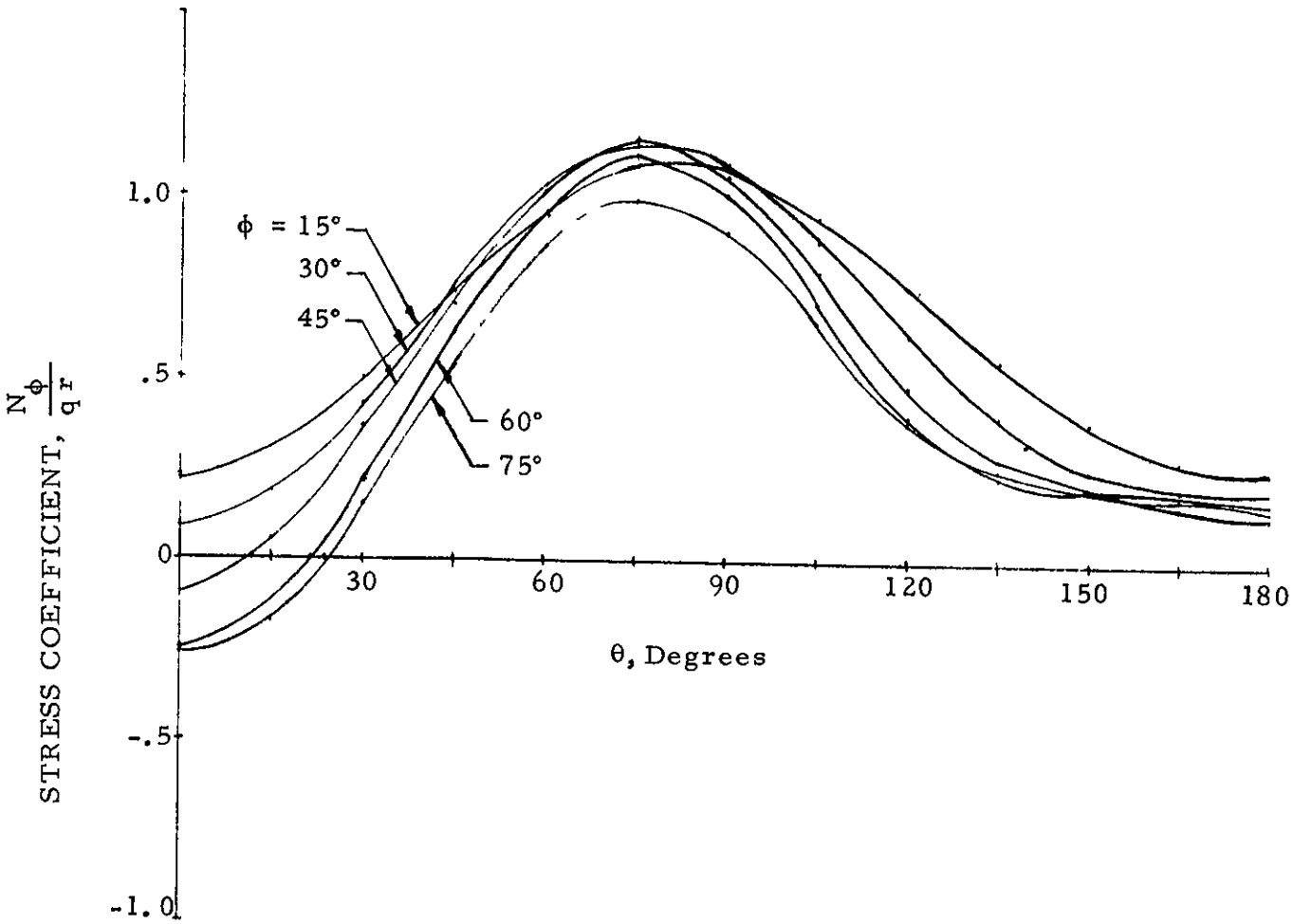

FIGURE 61 - TYPICAL CALCULATED STRESS COEFFICIENTS
MODEL NO. 8 - SPHERICAL ENDS
TEST NO 118 - P_e = 4 /5 q, q = 6

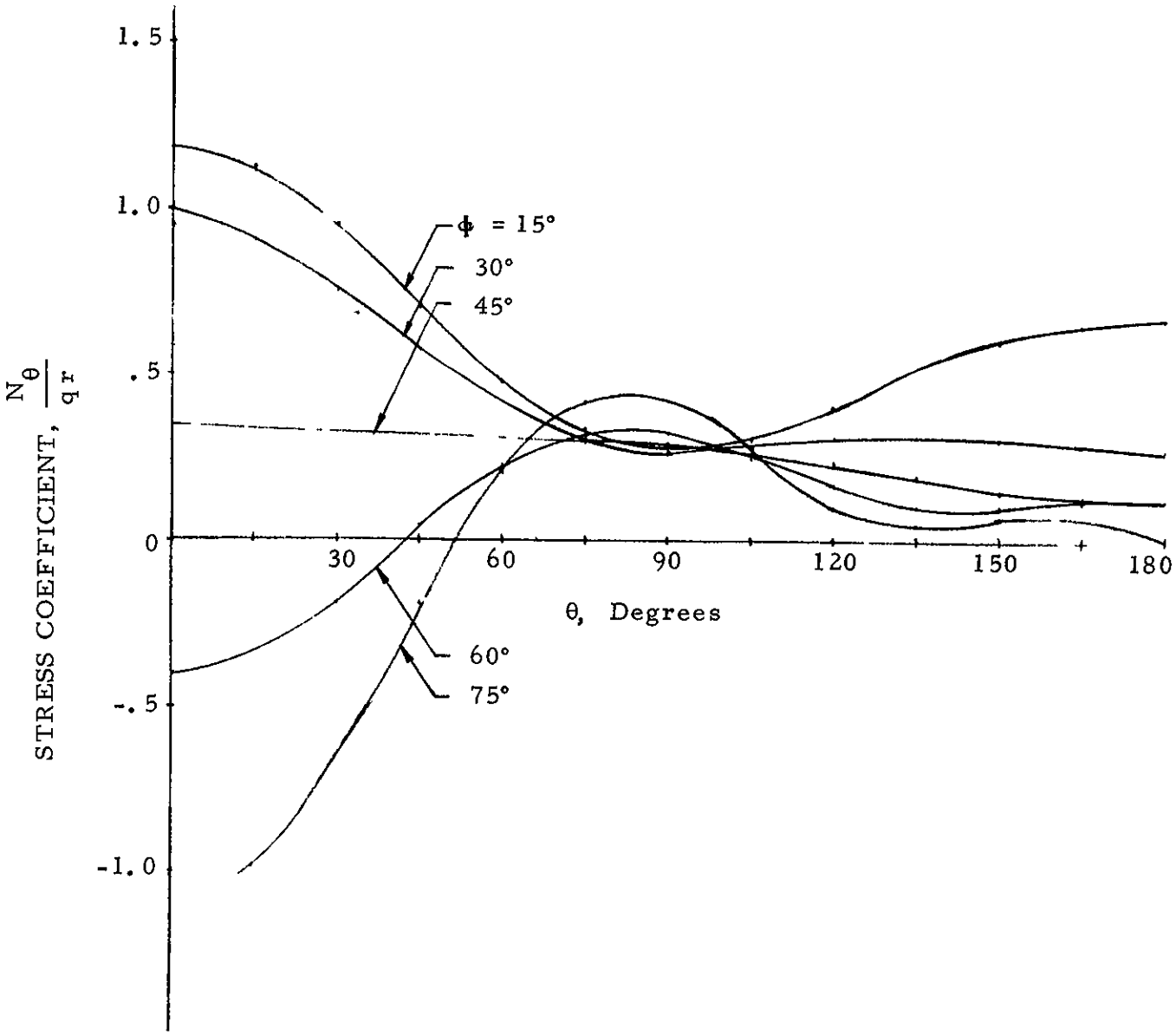

FIGURE 62. - TYPICAL CALCULATED STRESS COEFFICIENTS
MODEL NO 8 - SPHERICAL ENDS
TEST NO 118 - $P_e = 4/5\ q$, $q = .6$

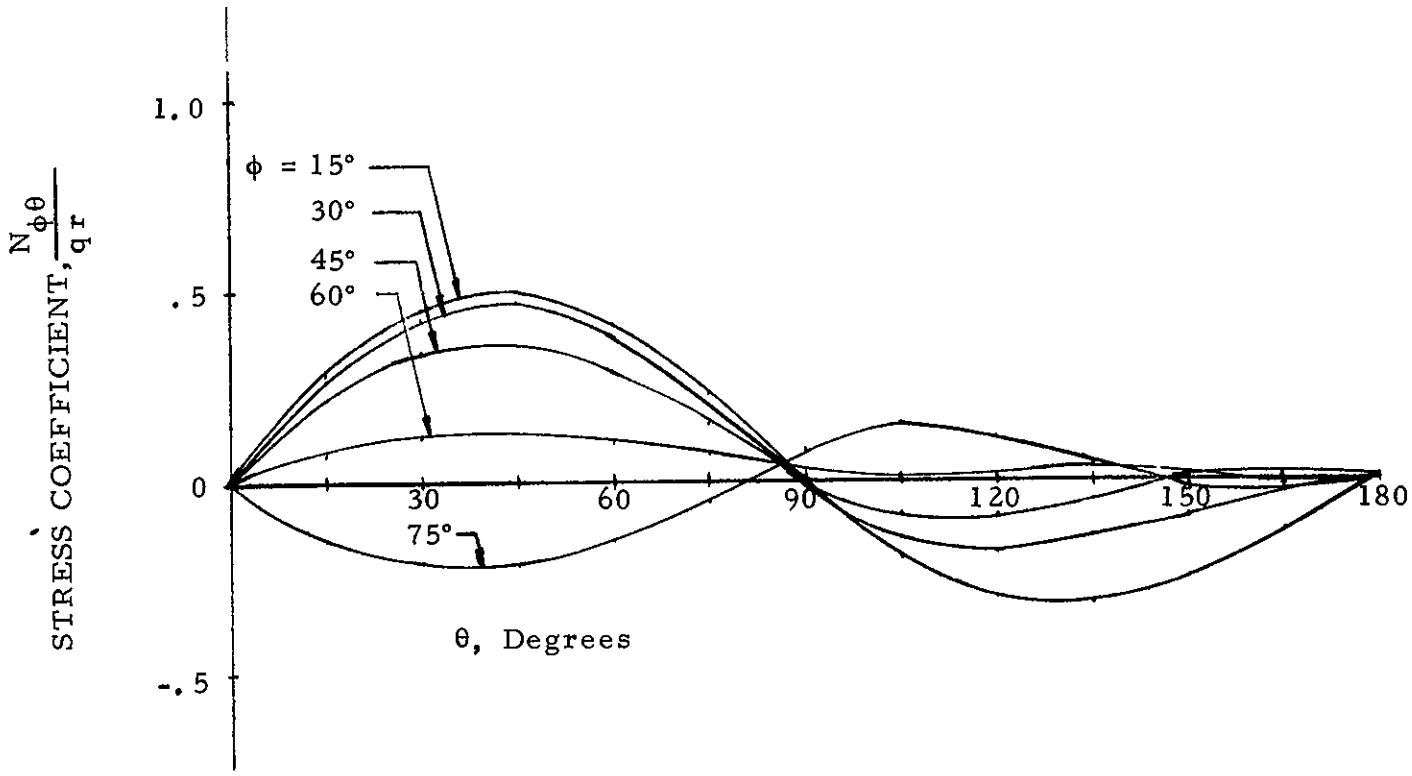

FIGURE 63. - TYPICAL CALCULATED STRESS COEFFICIENTS
MODEL NO. 8 - SPHERICAL ENDS
TEST NO. 118 - $P_e = 4/5\ q$, $q = .6$

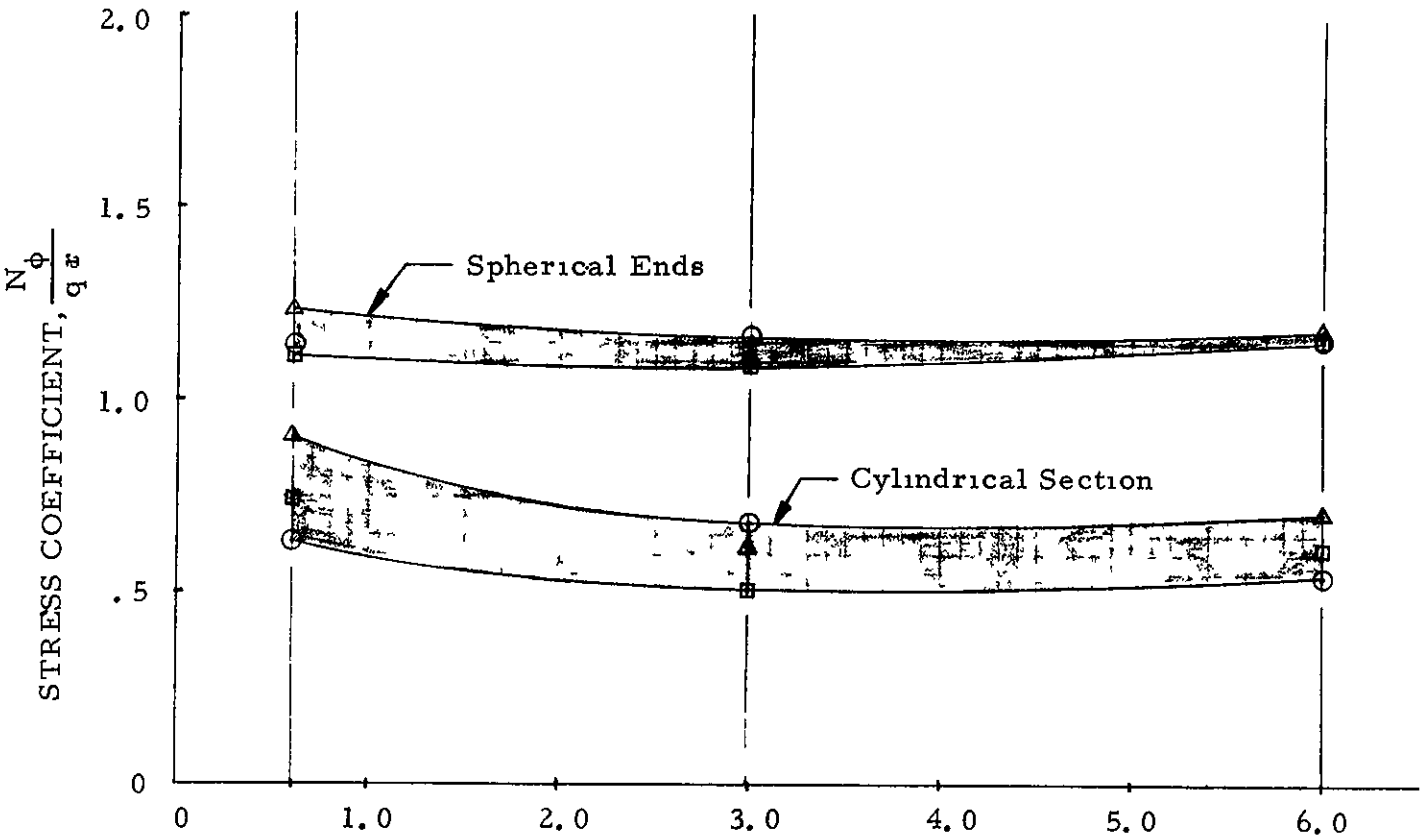

SYM	P_e	TEST NO
⊙	4/5 q	118, 121, 124
△	1 q	119, 122, 125
⊡	5/4 q	120, 123, 126

FIGURE 64. - ARRAY OF CALCULATED STRESS COEFFICIENTS
ALL TESTS - MODEL NO 8

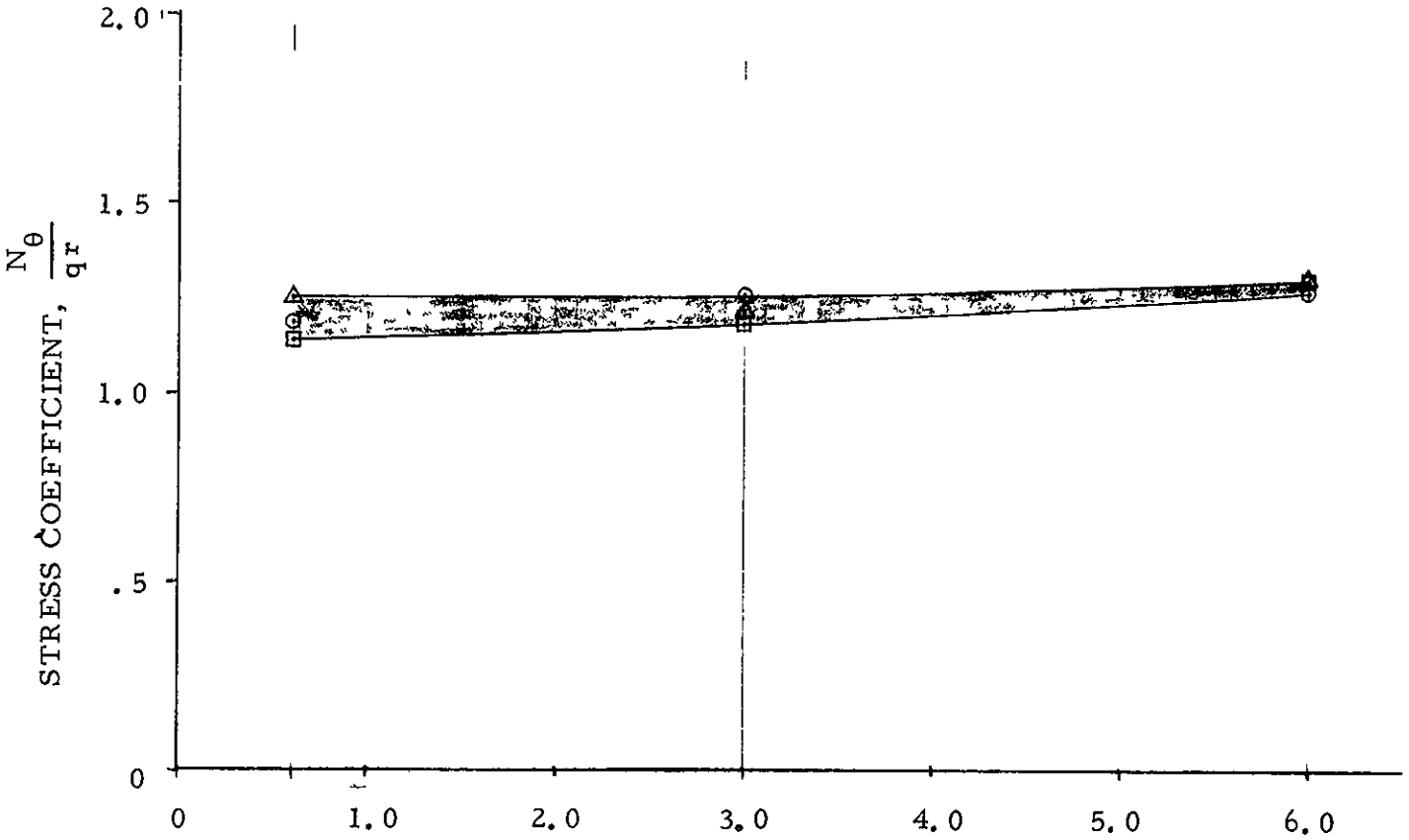

DYNAMIC PRESSURE, q, INCHES OF WATER, GAGE

SYM	P_e	TEST NO.
○	4/5 q	118, 121, 124
△	1 q	119, 122, 125
□	5/4 q	120, 123, 126

FIGURE 65. - ARRAY OF CALCULATED STRESS COEFFICIENTS
ALL TESTS - MODEL NO 8

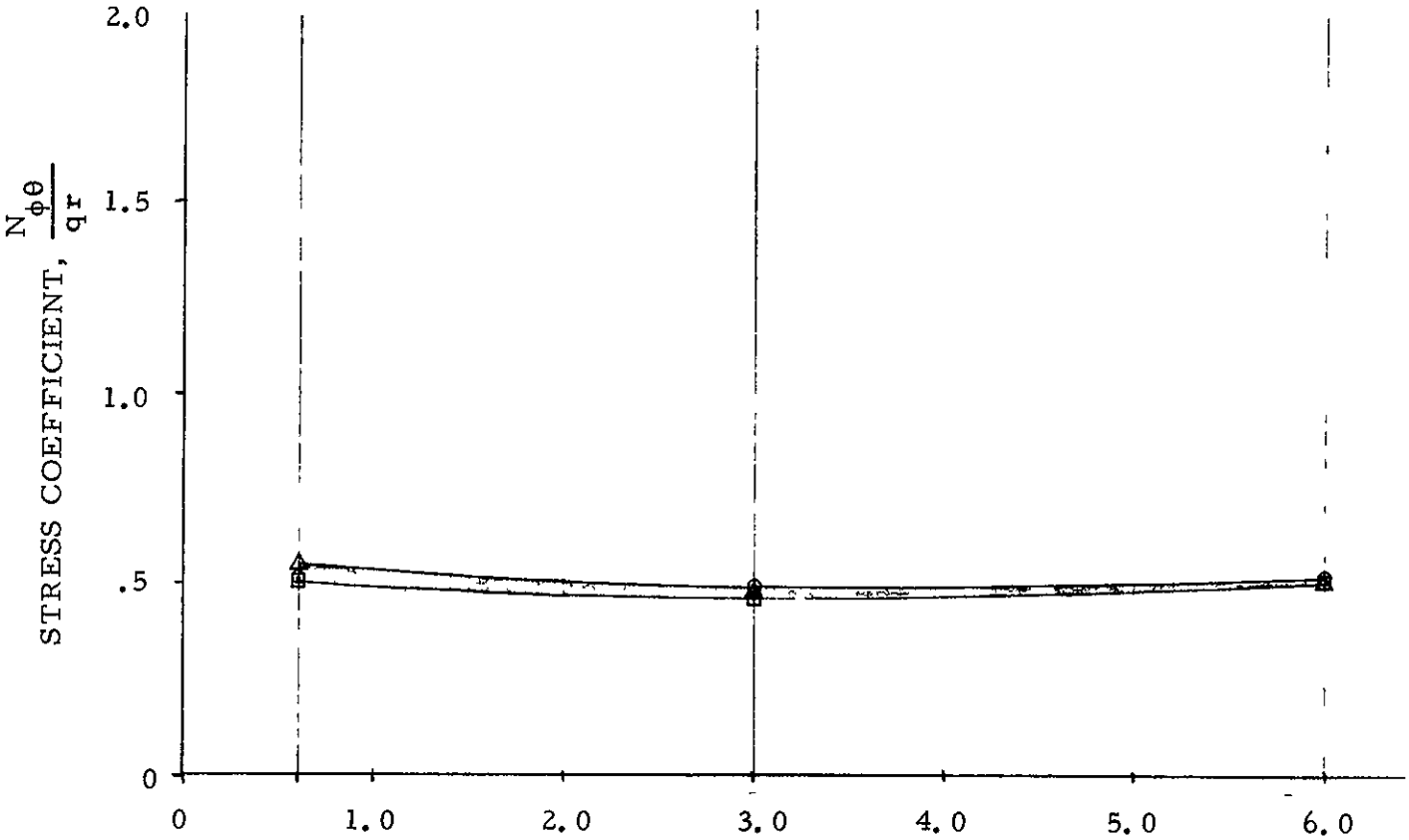

DYNAMIC PRESSURE q, INCHES OF WATER, GAGE

SYM	P_e	TEST NO.
○	4/5 q	118, 121, 124
△	1 q	119, 122, 125
□	5/4 q	120, 123, 126

FIGURE 66 - ARRAY OF CALCULATED STRESS COEFFICIENTS
ALL TESTS - MODEL NO. 8

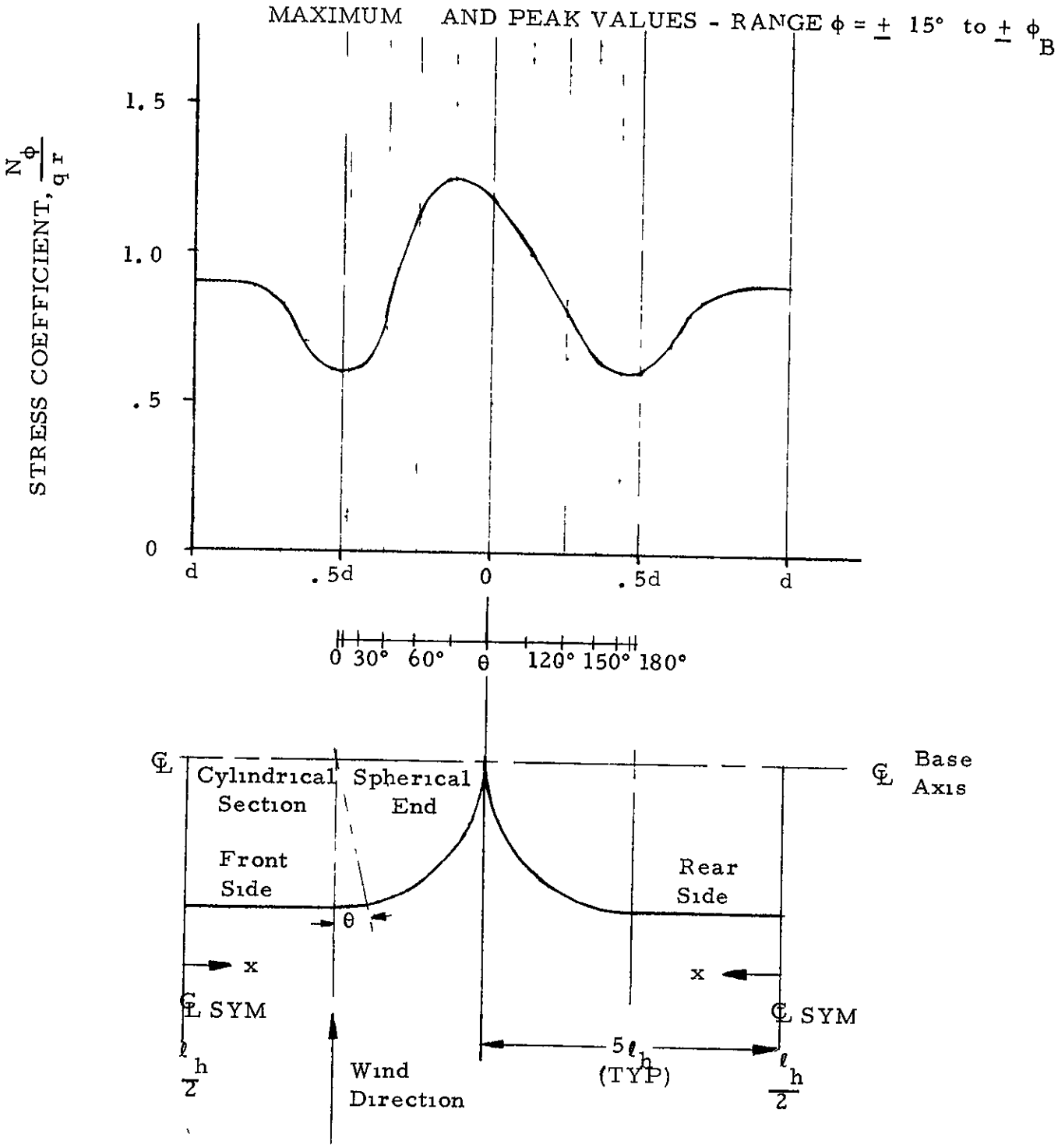

FIGURE 67. - TYPICAL ANNULAR - LONGITUDINAL STRESS COEFFICIENT DISTRIBUTION MODEL NO. 8 - ALL TESTS.

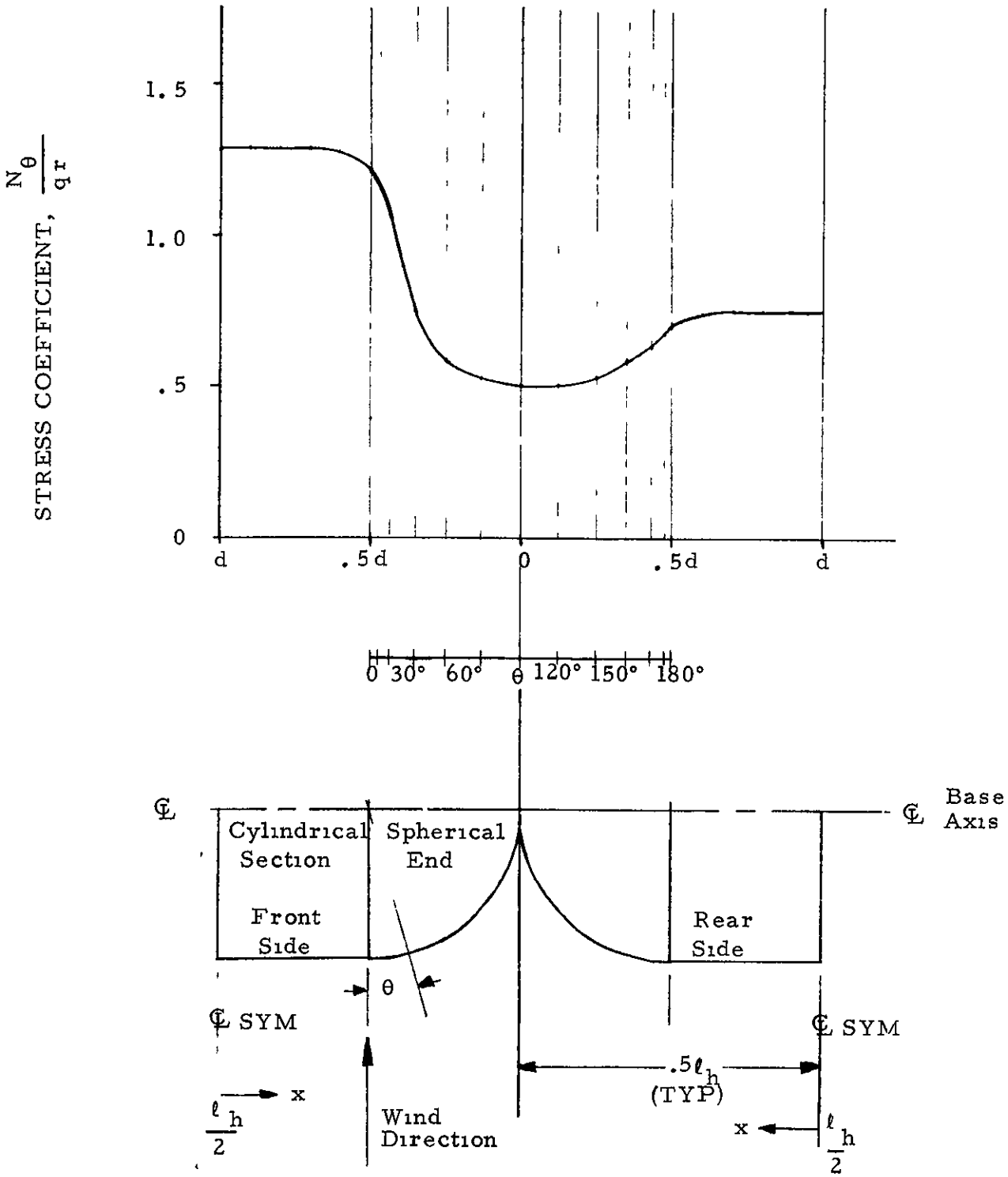

FIGURE 68. - TYPICAL ANNULAR - LONGITUDINAL STRESS COEFFICIENT DISTRIBUTION MODEL NO. 8 - ALL TESTS.

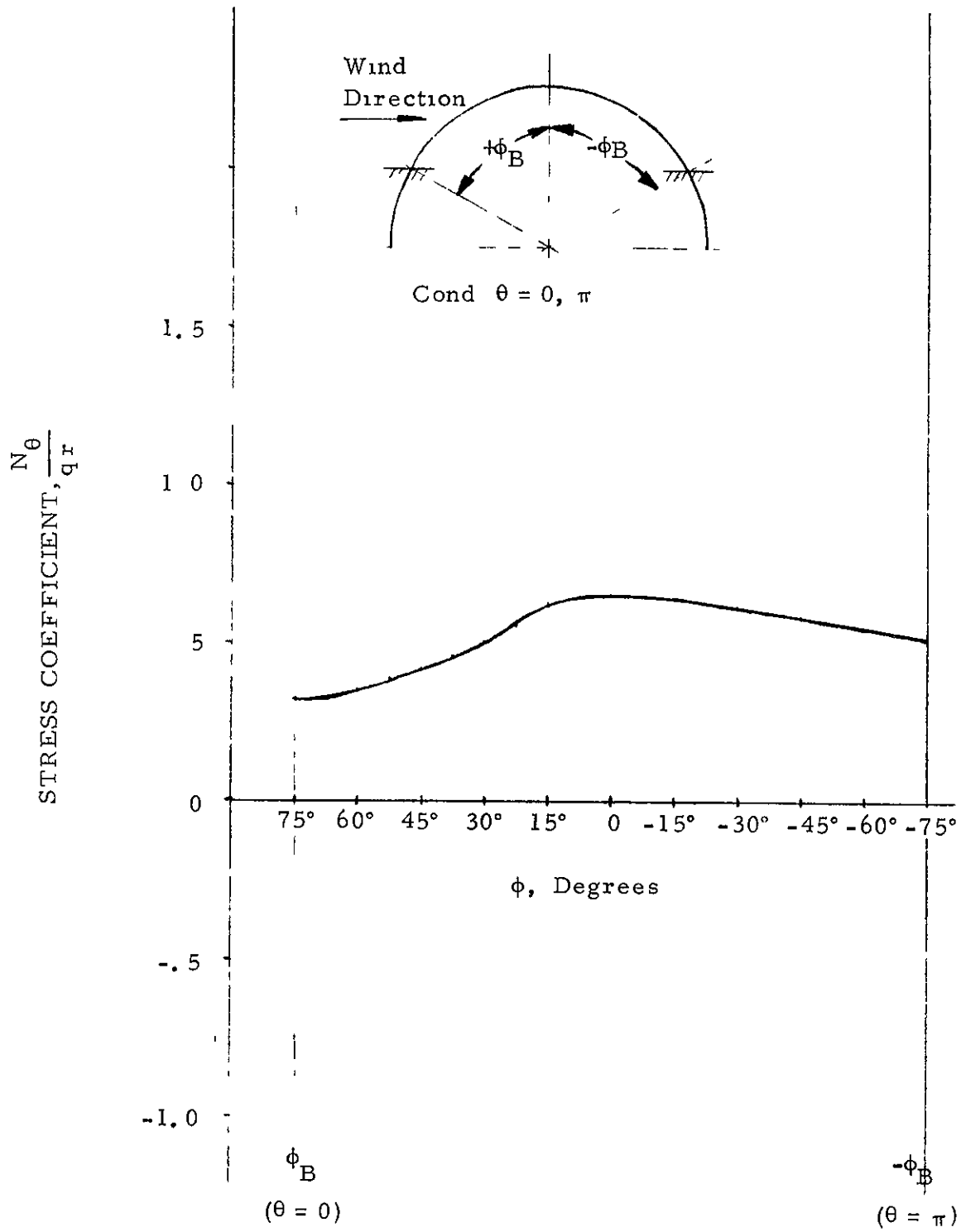

FIGURE 69 - TYPICAL MAXIMUM PERIPHERAL STRESS COEFFICIENT DISTRIBUTION, CYLINDRICAL - SPHERICAL END JUNCTION (INTERFACE) MODEL NO 8 - ALL TESTS - $\phi = 0°$ to $\pm\ \phi_B$

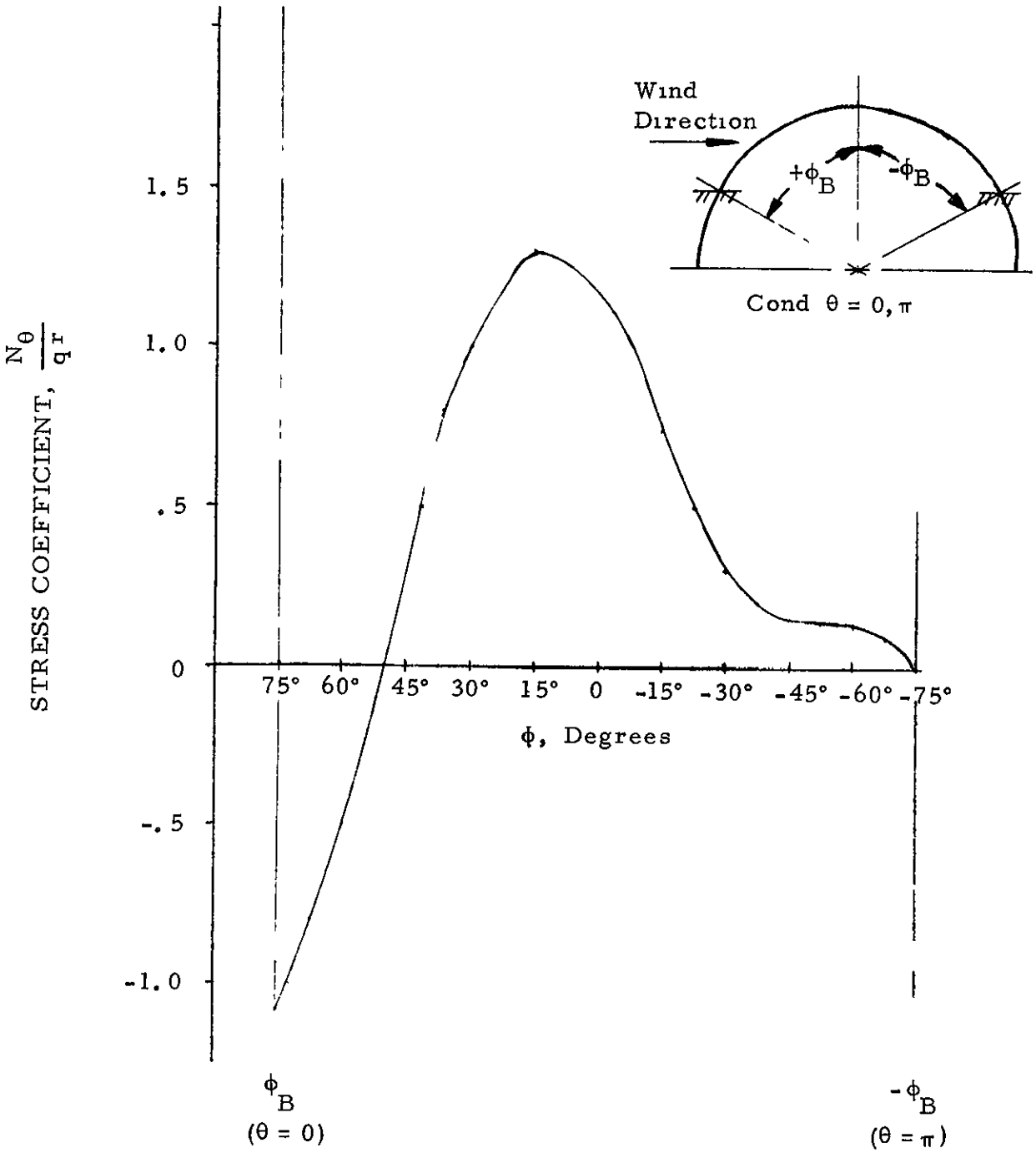

FIGURE 70. - TYPICAL MAXIMUM PERIPHERAL STRESS COEFFICIENT DISTRIBUTION, CYLINDRICAL-SPHERICAL END JUNCTION (INTERFACE) MODEL NO 8 - ALL TESTS - $\phi = 0°$ to $\pm \phi_B$

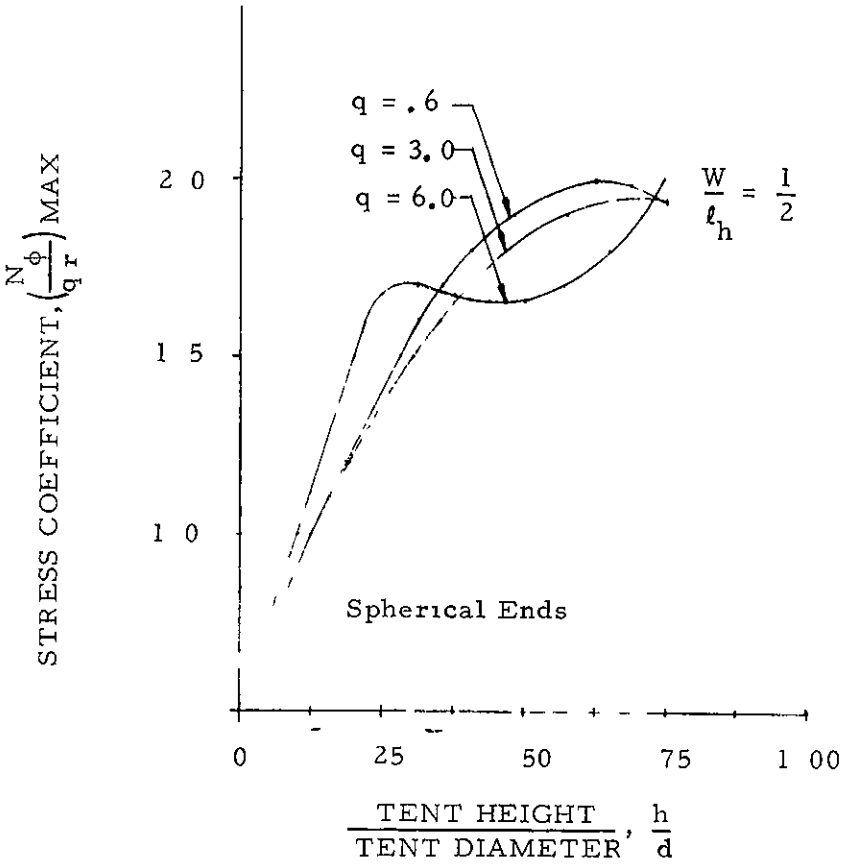

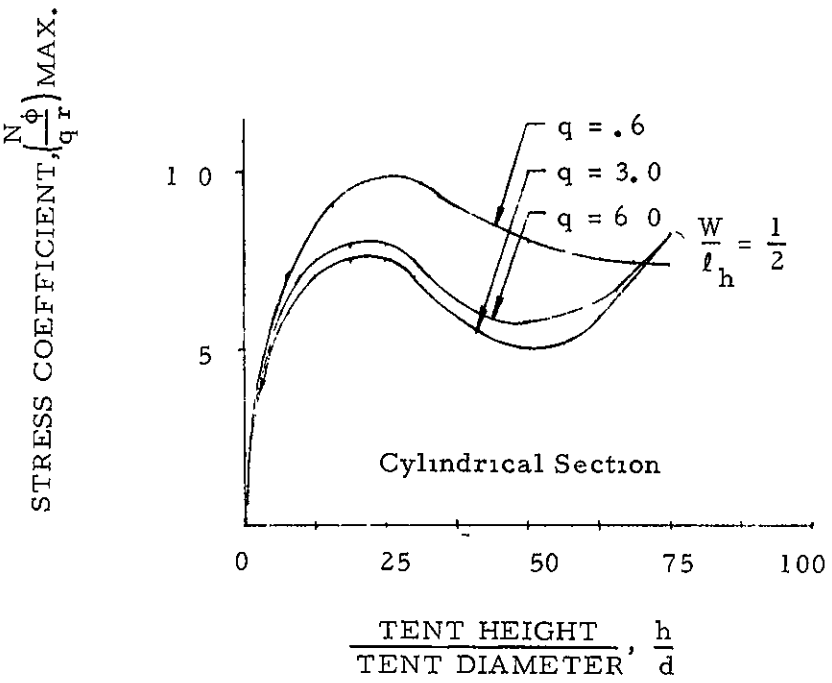

FIGURE 71 - MAXIMUM DESIGN STRESS COEFFICIENT-SPECIFIC DYNAMIC PRESSURE

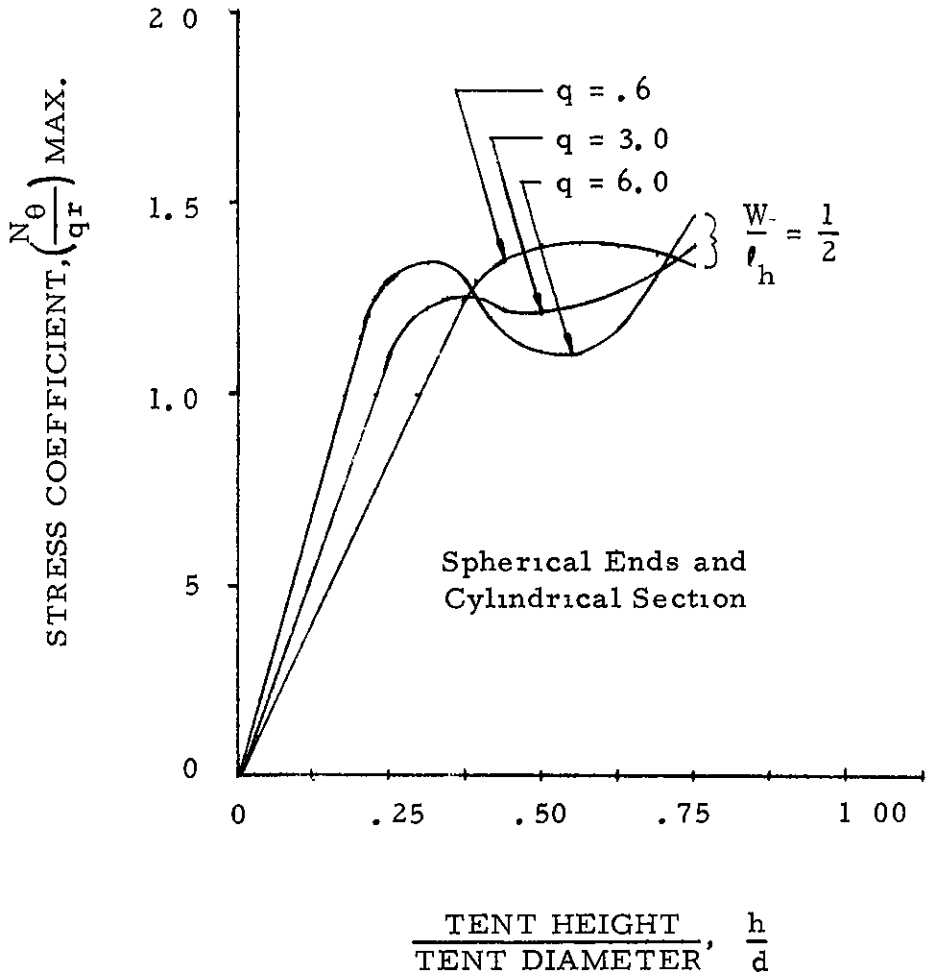

FIGURE 72. - MAXIMUM DESIGN STRESS COEFFICIENT - SPECIFIC DYNAMIC PRESSURE

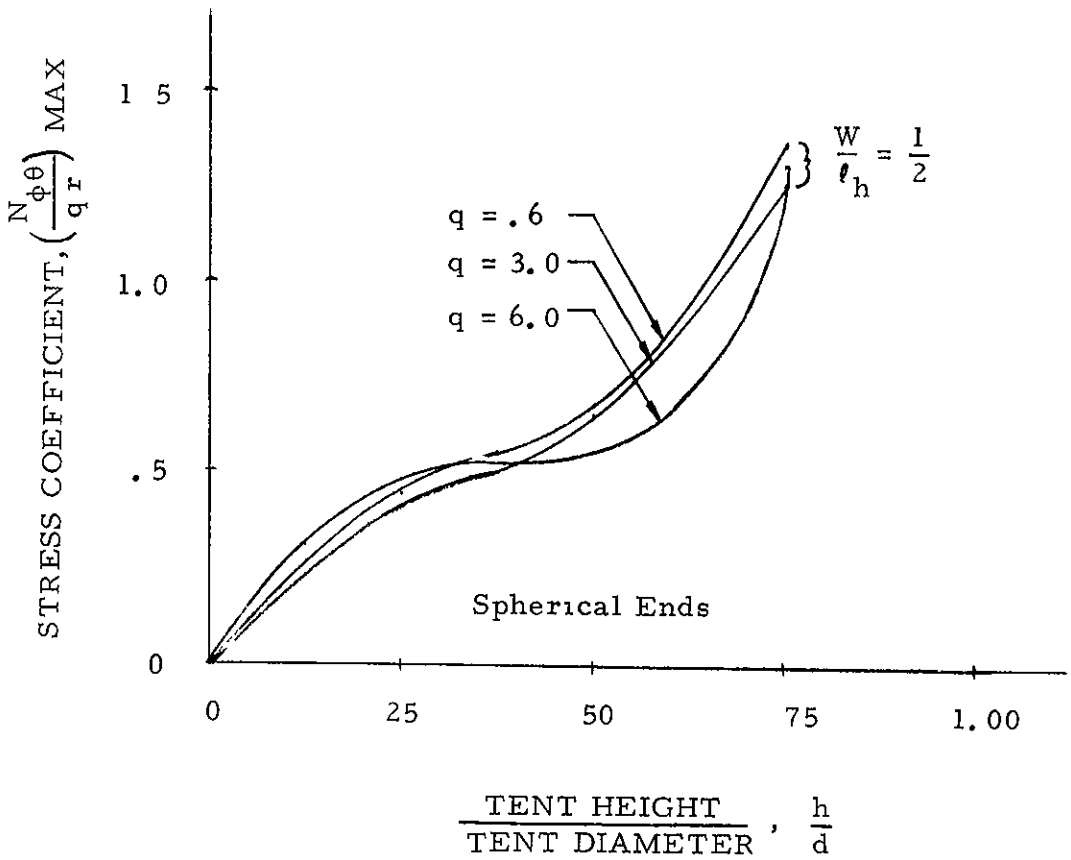

FIGURE 73. - MAXIMUM DESIGN STRESS COEFFICIENT
SPECIFIC DYNAMIC PRESSURE

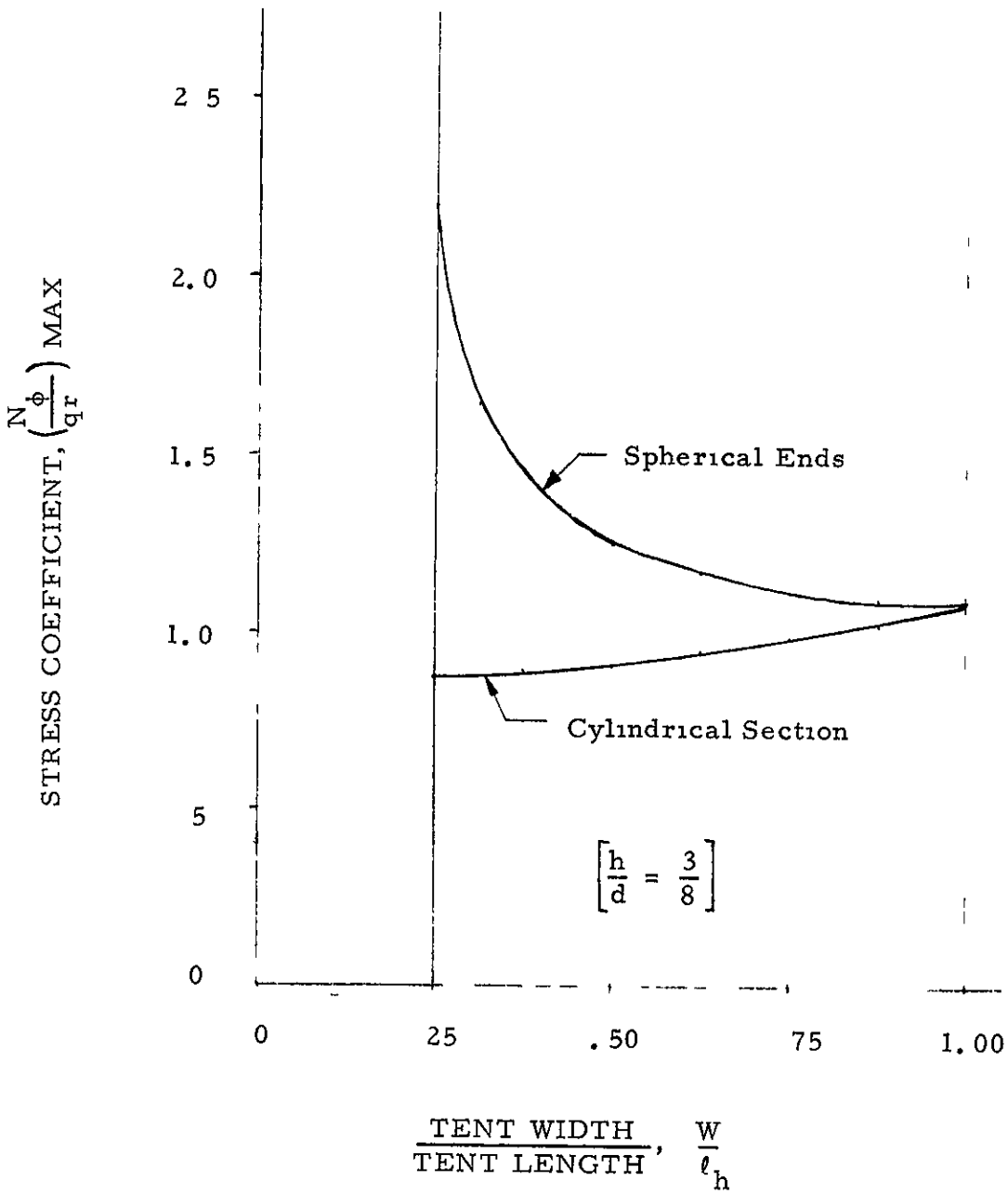

FIGURE 74. - MAXIMUM DESIGN STRESS COEFFICIENT - DYNAMIC PRESSURE LIMIT (q - 6.0) CONSTANT h/d - W/ℓ_h RANGE W/ℓ_h = .25 to 1 00)

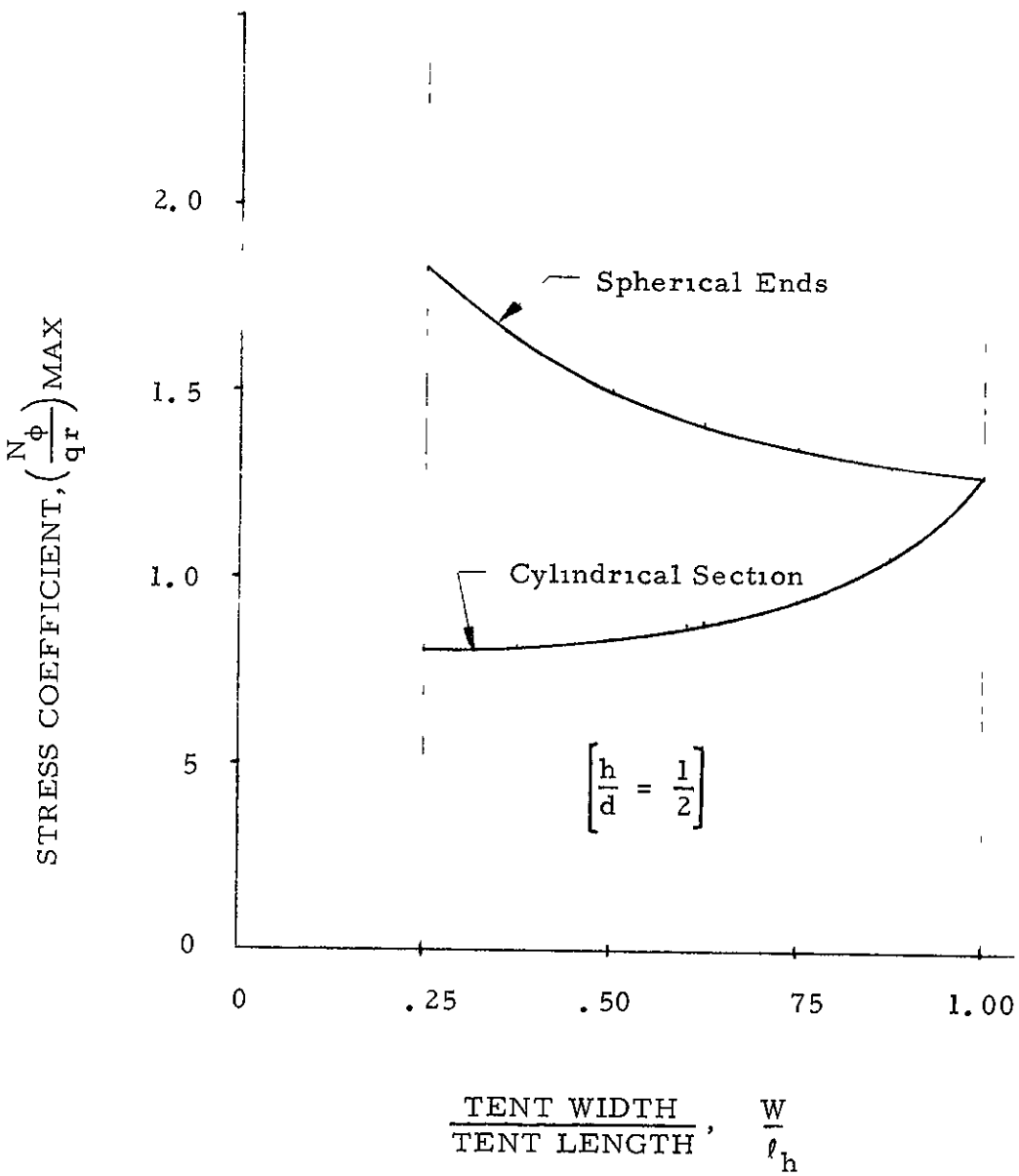

FIGURE 75 - MAXIMUM DESIGN STRESS COEFFICIENT - DYNAMIC PRESSURE LIMIT (q = 6 0) CONSTANT h/d - W/ℓ_h RANGE (W/ℓ_h = 25 to 1 00).

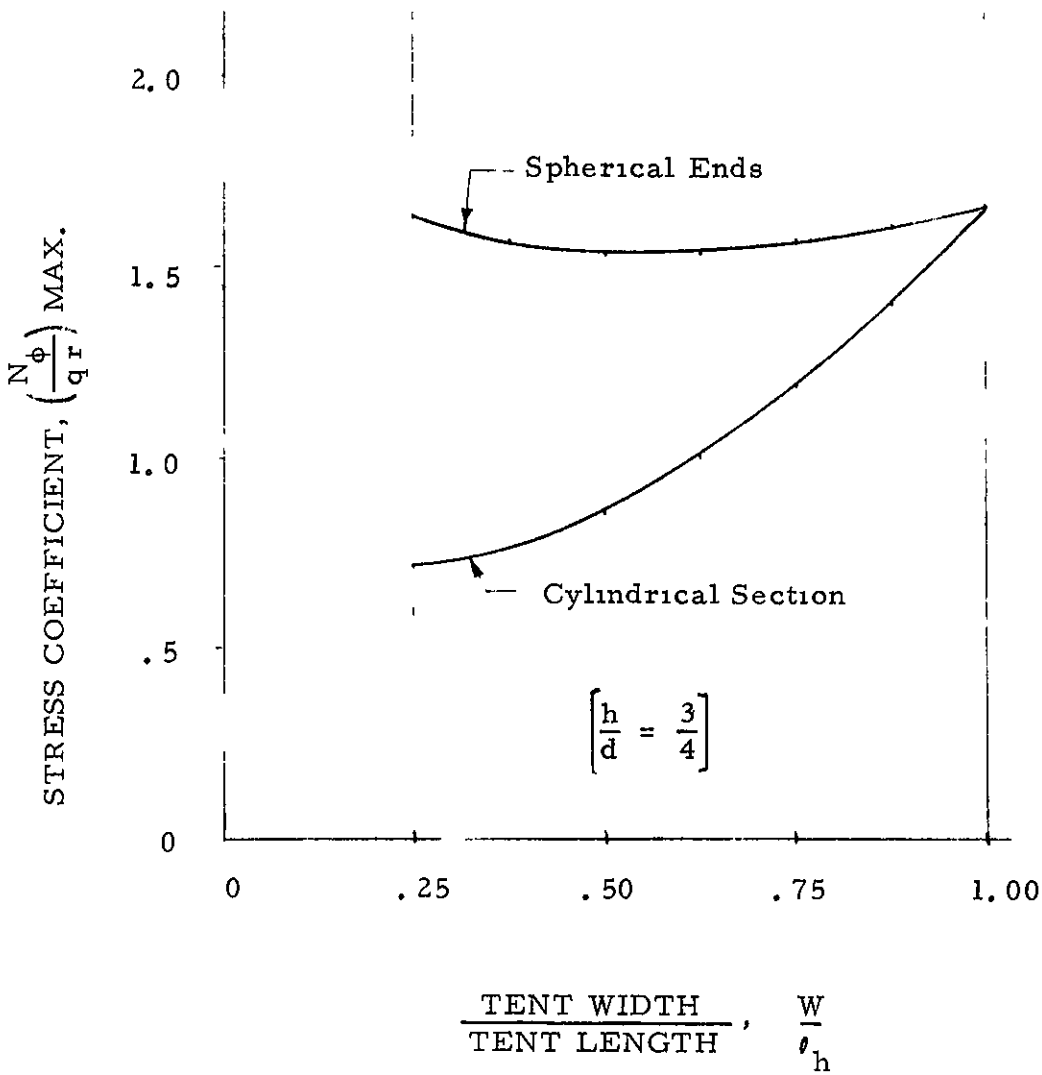

FIGURE 76 - MAXIMUM DESIGN STRESS COEFFICIENT - DYNAMIC PRESSURE LIMIT (q = 6.0) CONSTANT h/d - W/ℓ_h RANGE (W/ℓ_h = .25 to 1.00)

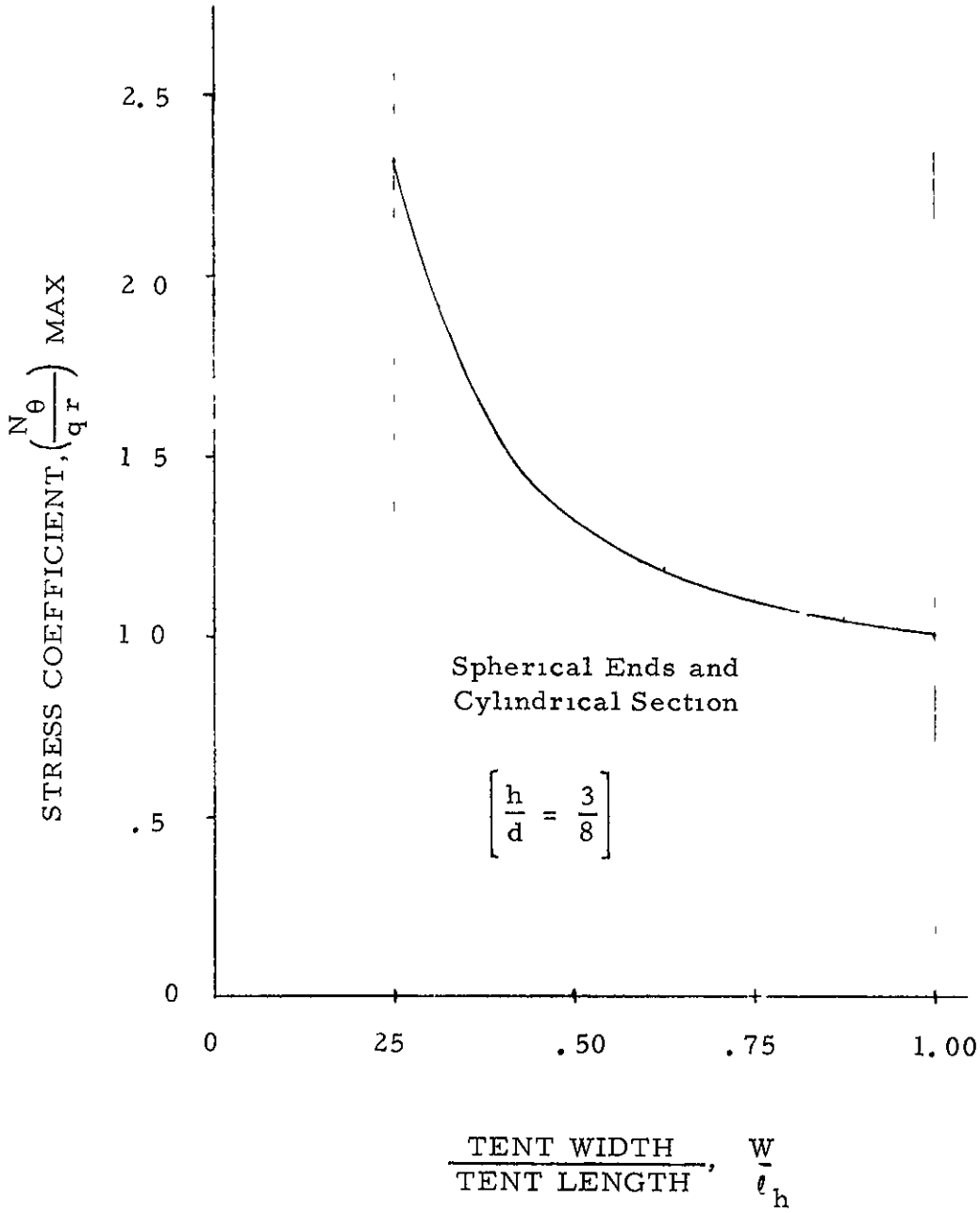

FIGURE 77. - MAXIMUM DESIGN STRESS COEFFICIENT - DYNAMIC PRESSURE LIMIT (q = 6 0) CONSTANT h/d - W/ℓ_h RANGE (W/ℓ_h = 25 to 1 00)

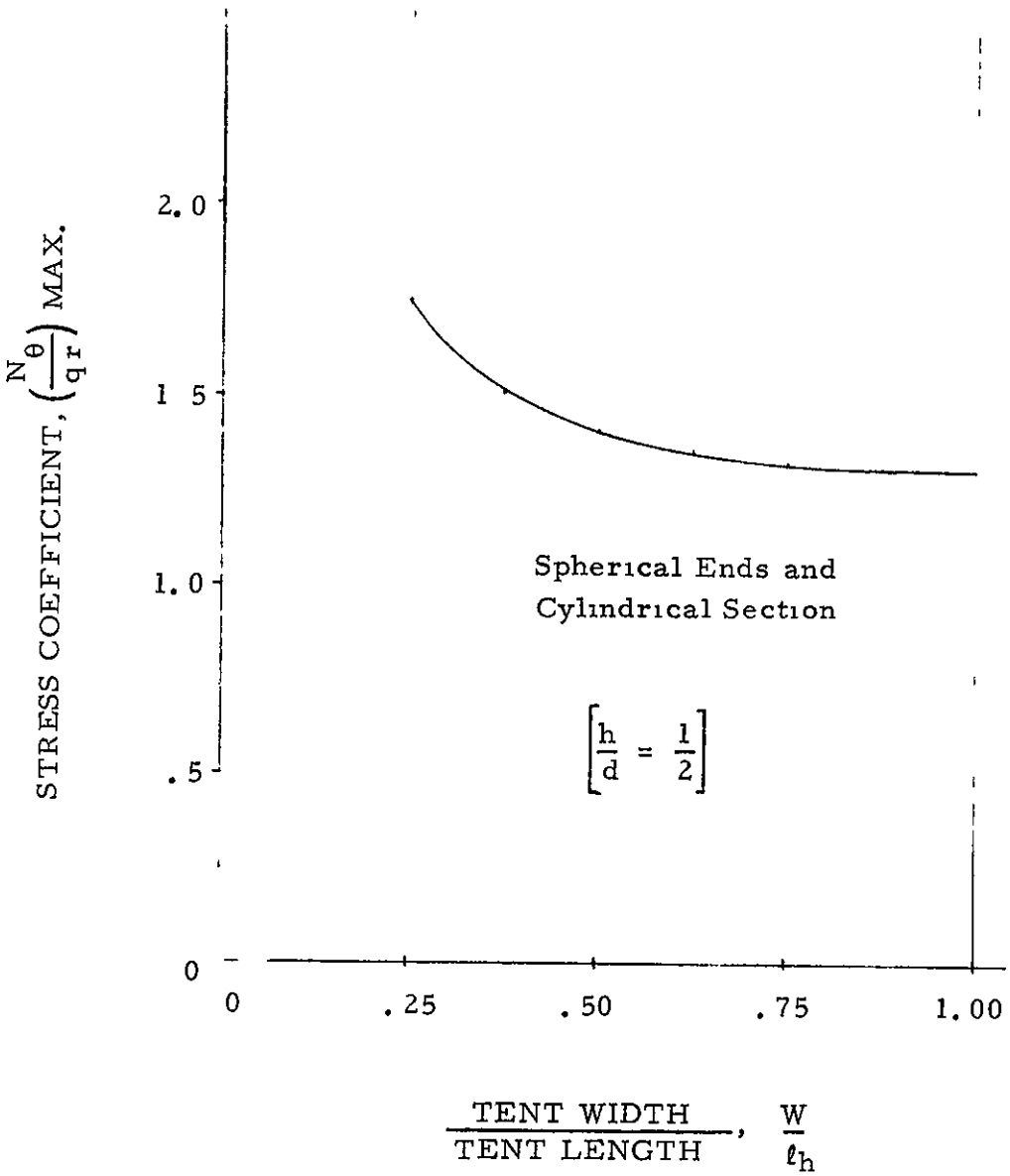

FIGURE 78. - MAXIMUM DESIGN STRESS COEFFICIENT - DYNAMIC PRESSURE LIMIT (q = 6.0) CONSTANT h/d - W/ℓ_h RANGE (W/ℓ_h = .25 to 1.00)

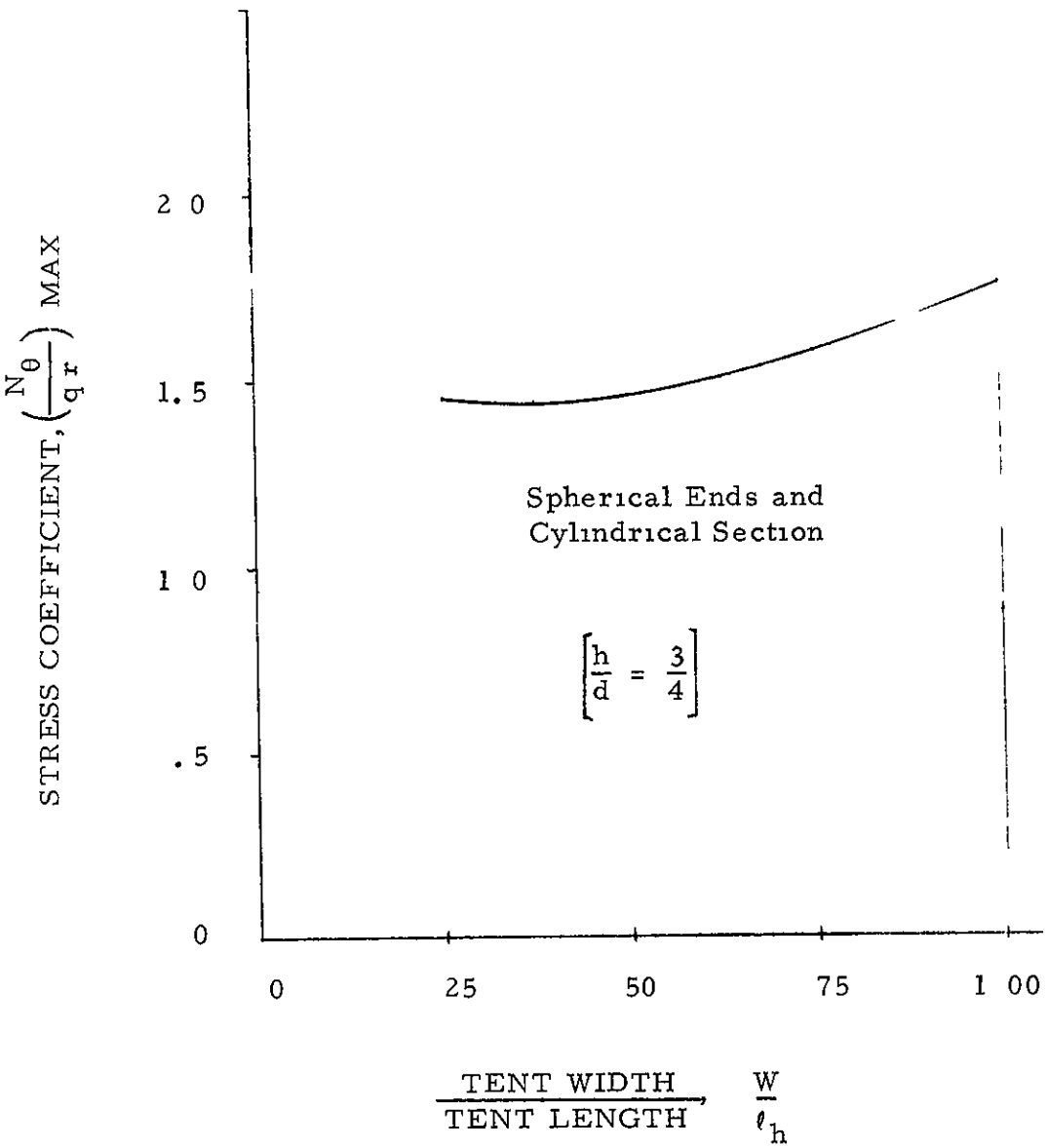

FIGURE 79. - MAXIMUM DESIGN STRESS COEFFICIENT - DYNAMIC PRESSURE LIMIT (q = 6 0) CONSTANT h/d - W/ℓ_h RANGE (W/ℓ_h = . 25 to 1 00)

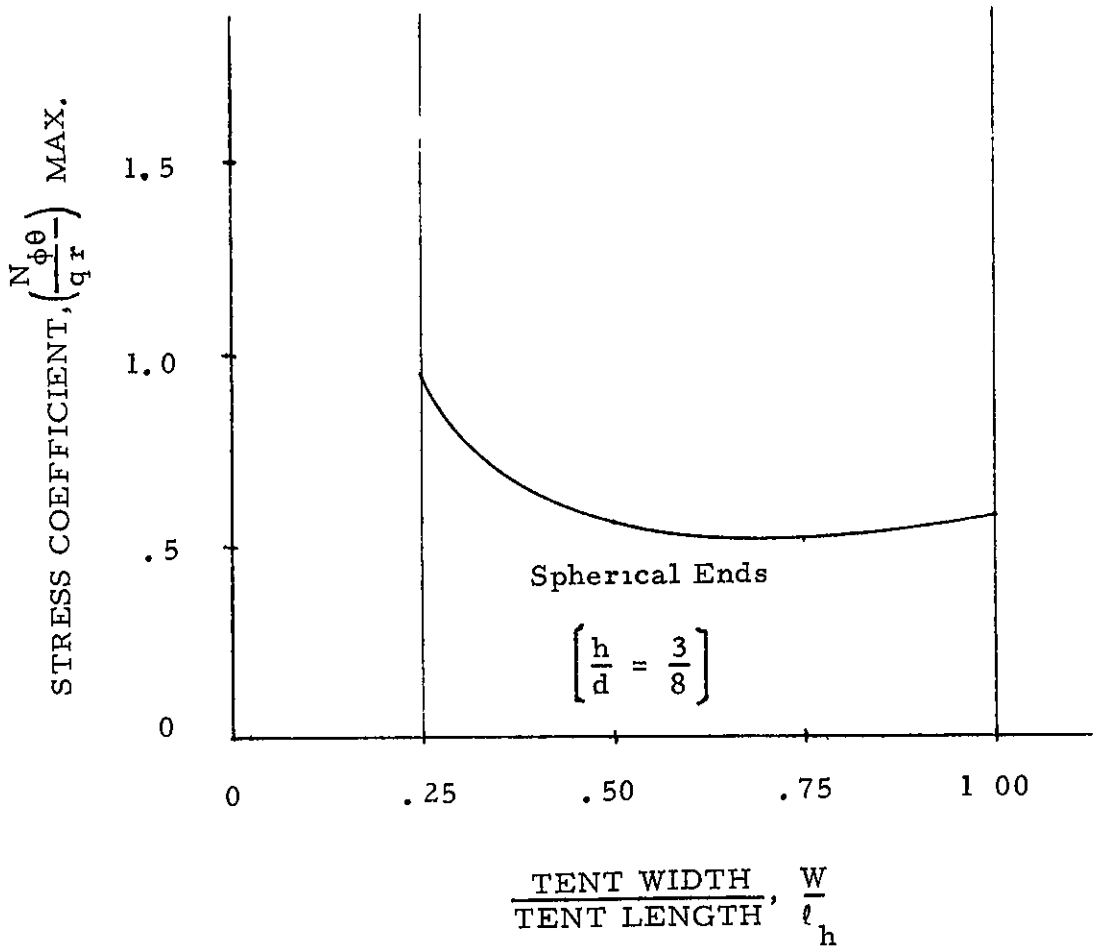

FIGURE 80. - MAXIMUM DESIGN STRESS COEFFICIENT - DYNAMIC PRESSURE LIMIT (q = 6.0) CONSTANT h/d - W/ℓ_h RANGE (W/ℓ_h = 25 to 1.00)

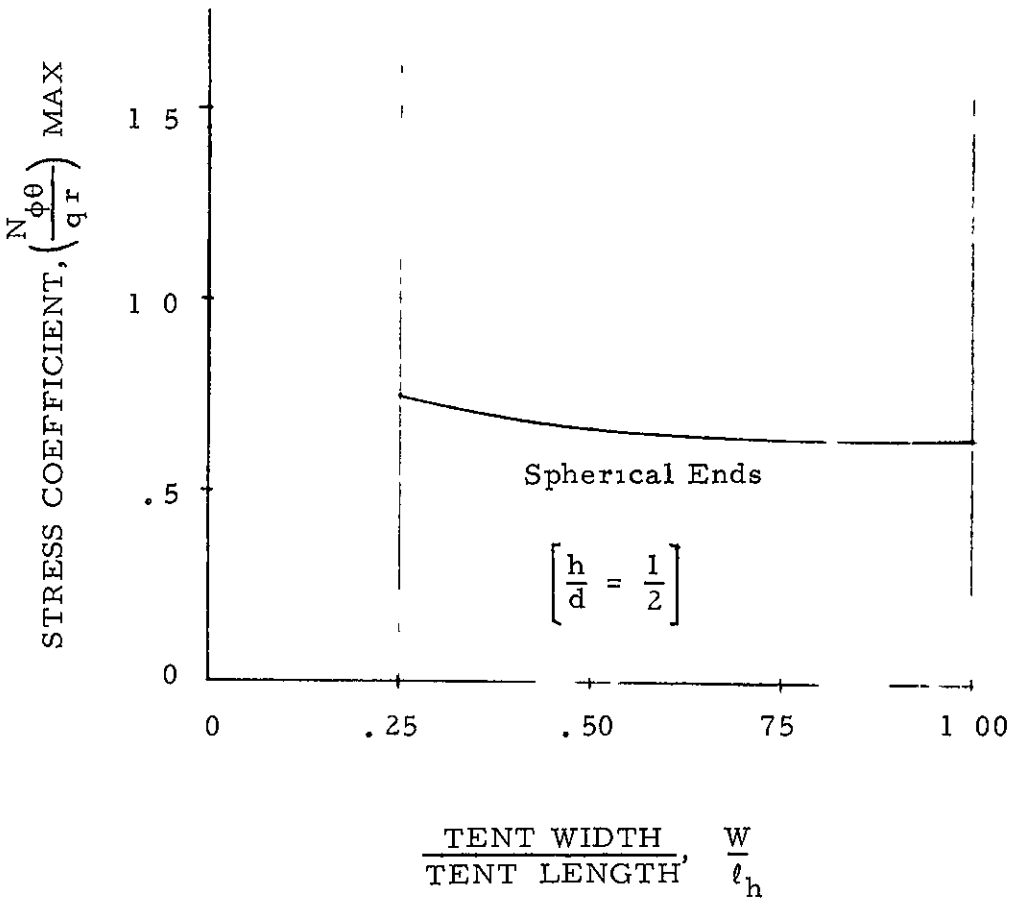

FIGURE 81. - MAXIMUM DESIGN STRESS COEFFICIENT - DYNAMIC PRESSURE LIMIT (q = 6 0) CONSTANT h/d - W/ℓ_h RANGE (W/ℓ_h = 25 to 1 00)

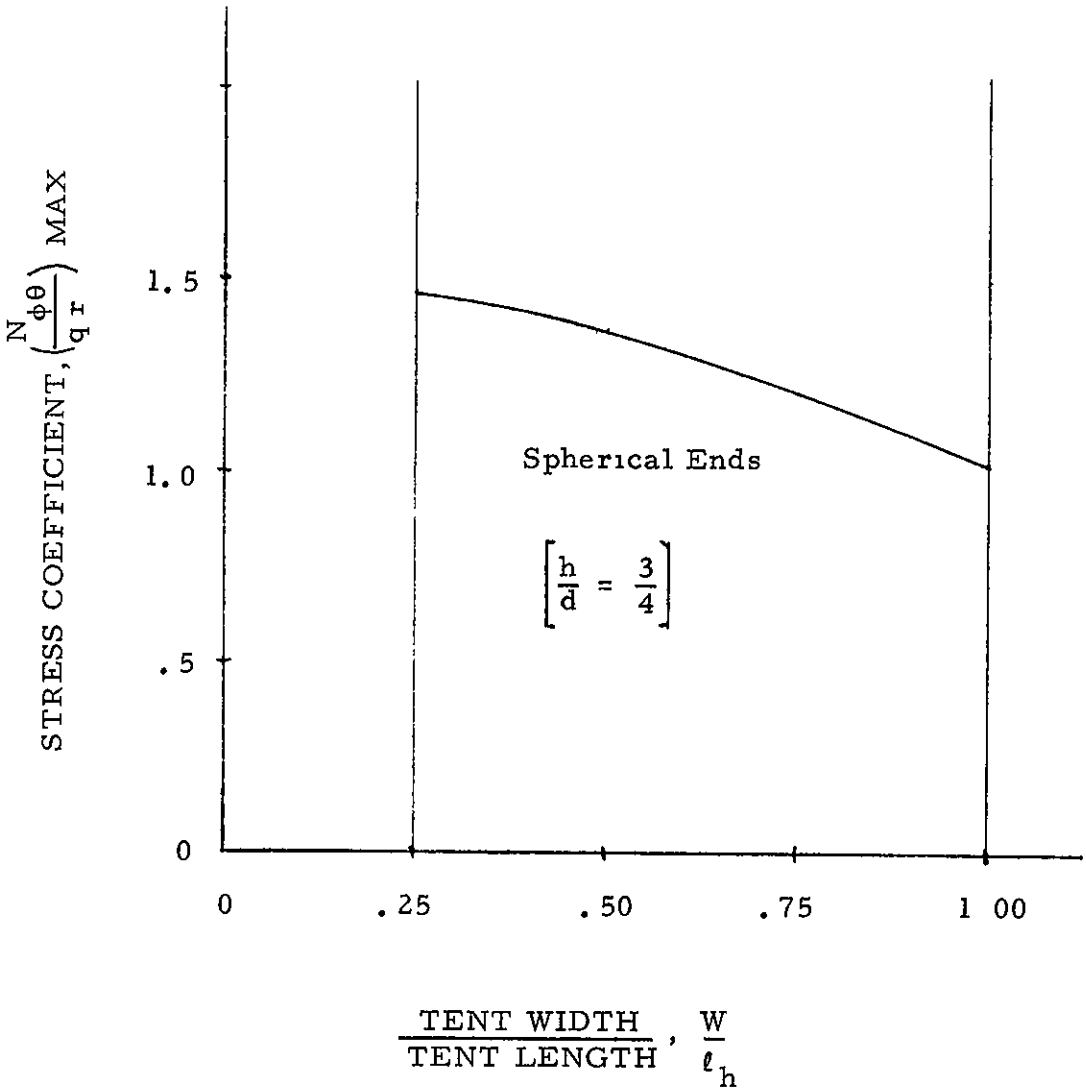

FIGURE 82. - MAXIMUM DESIGN STRESS COEFFICIENT - DYNAMIC PRESSURE LIMIT (q = 6.0) CONSTANT h/d - W/ℓ_h RANGE (W/ℓ_h = 25 to 1 00)

Model No 1
3/4 Sphere
Radius 13 5"
Height 20 3"
Width 27 0"

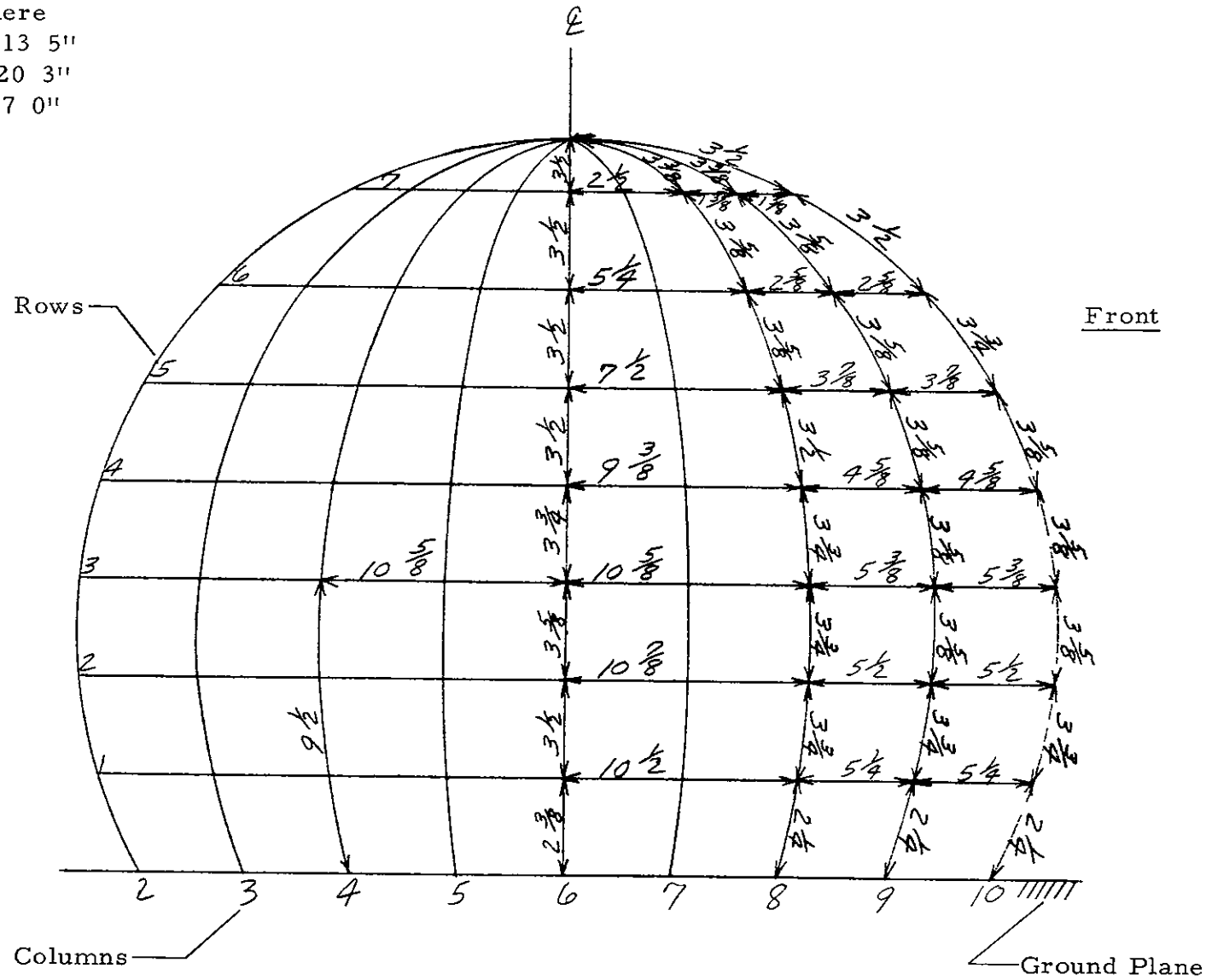

Figure 83 - Model No 1, Pressure Tap Locations

Model No 17
3/4 Cylinder $W/\ell_h = 1/1$
Radius 11 2"
Height 16 8"
Width 22 4"

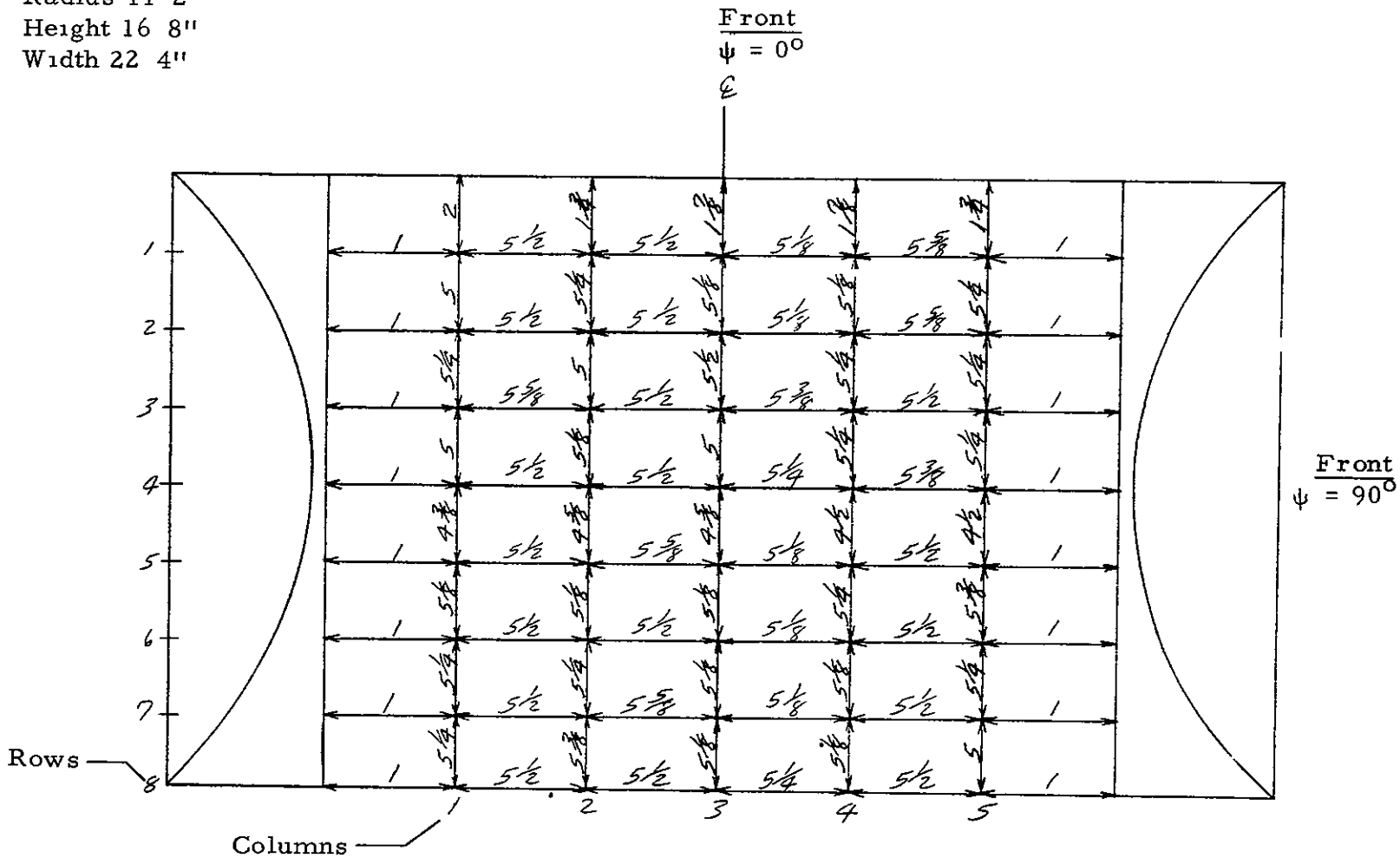

Figure 84 - Model No 17, Pressure Tap Locations

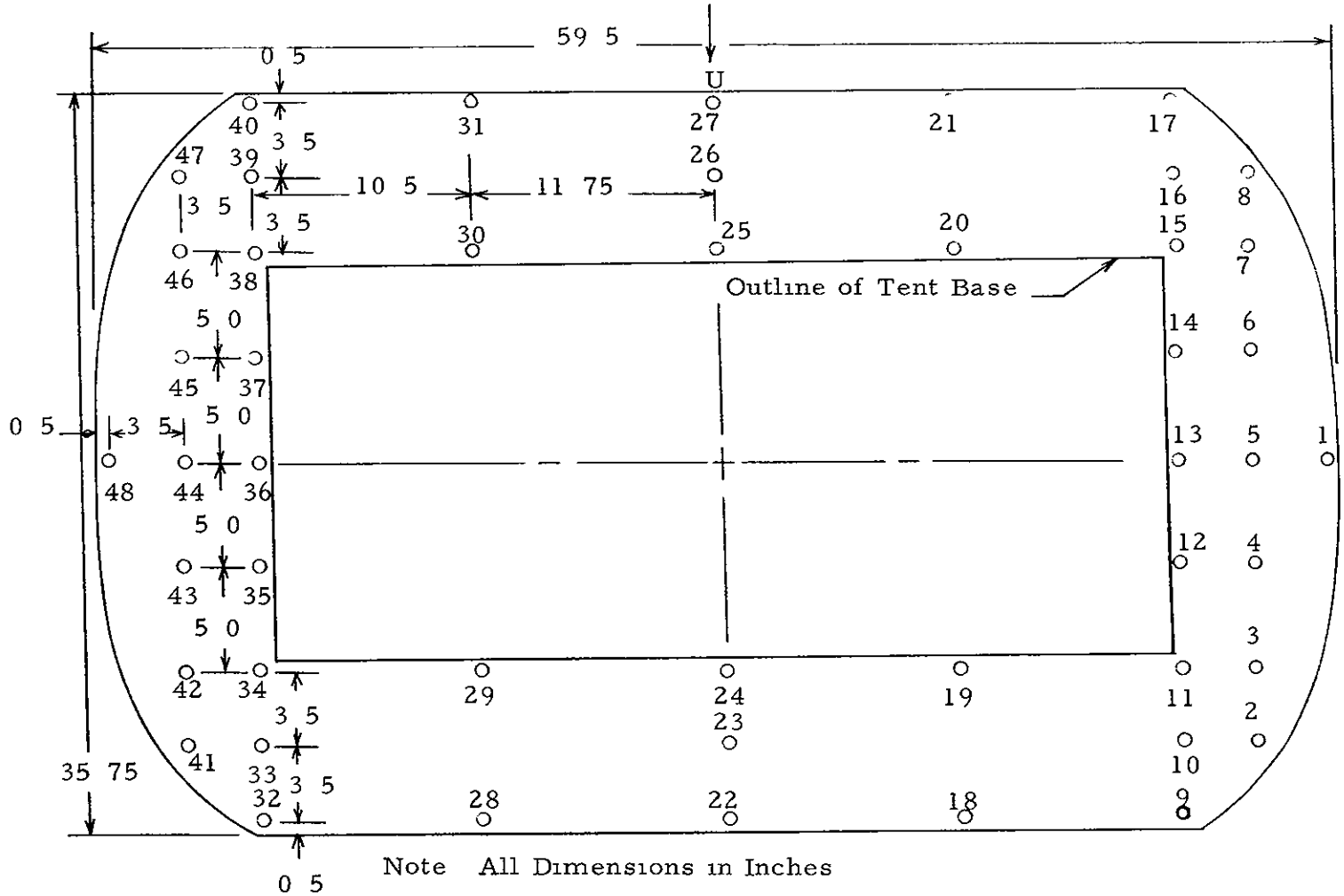

FIGURE 85 - PICKUP LOCATIONS FOR PRESSURE DISTRIBUTION MEASUREMENT ON MODEL BASE FOR MODEL NO 19

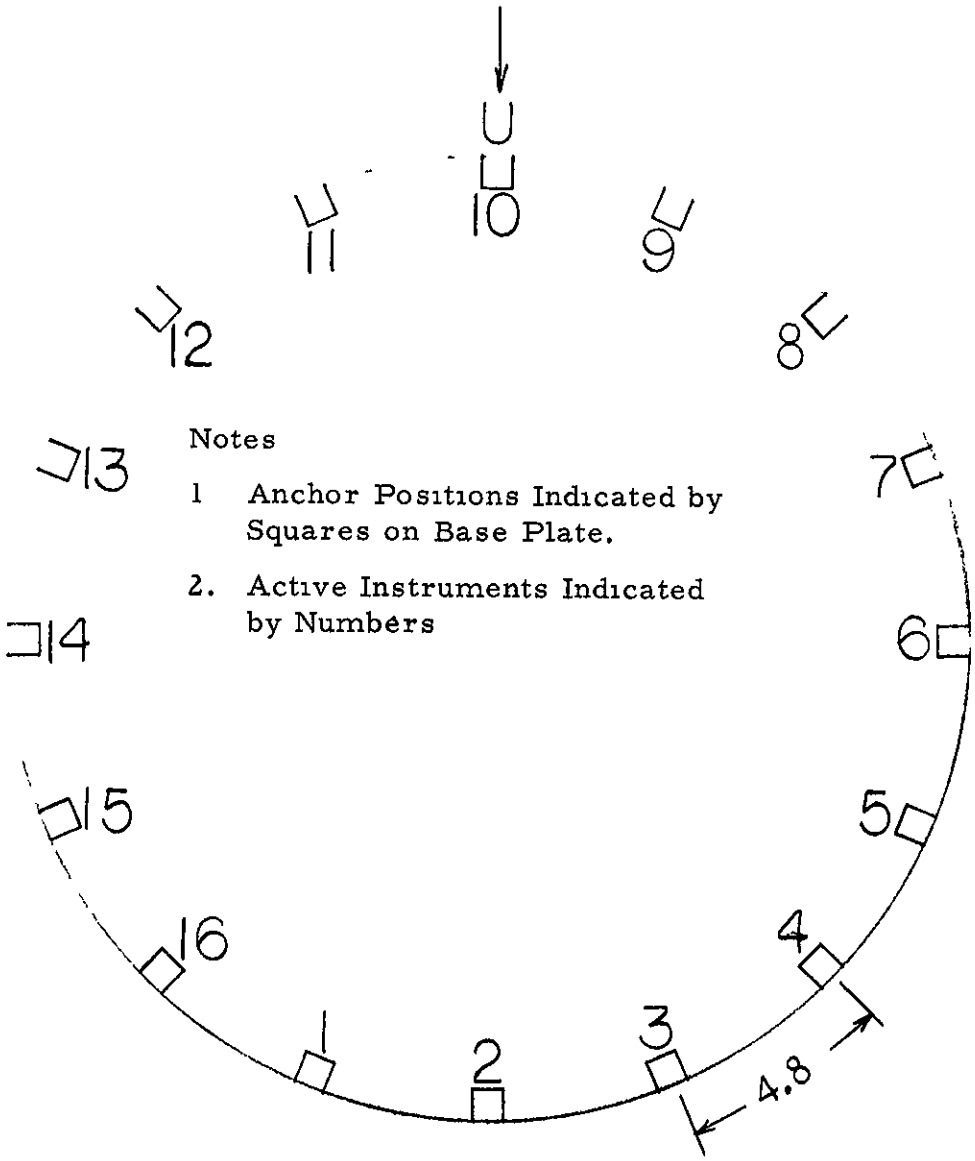

Figure 86. - Model No. 1, Strain Gage Locations

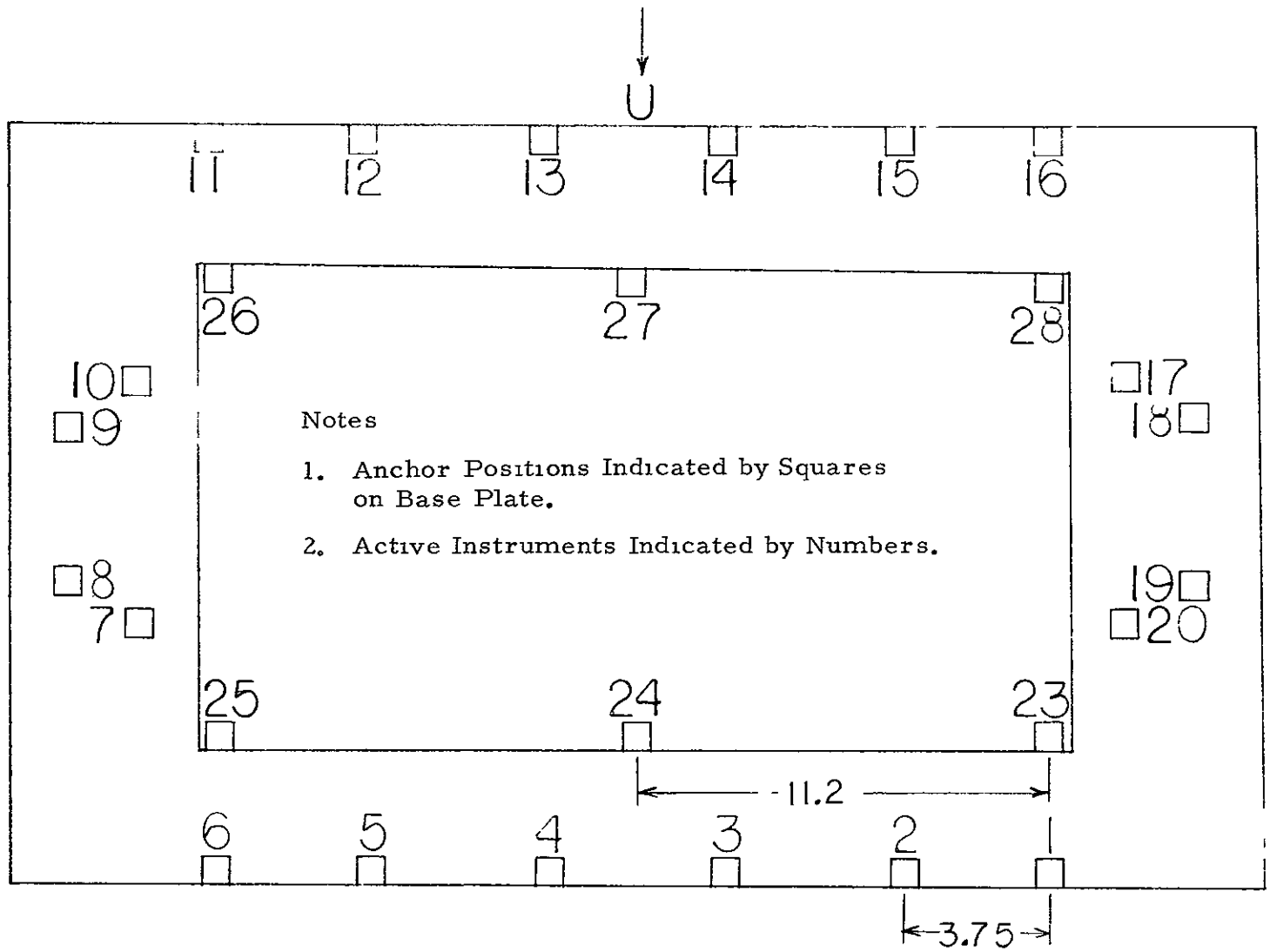

Figure 87. - Model No. 17, Strain Gage Locations

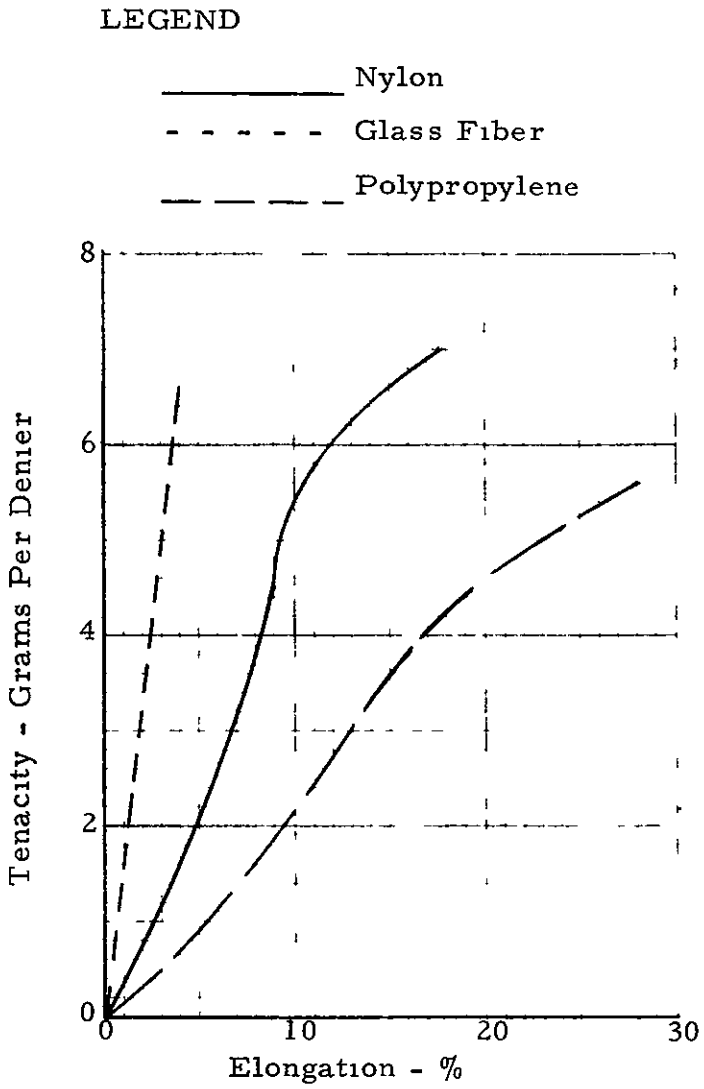

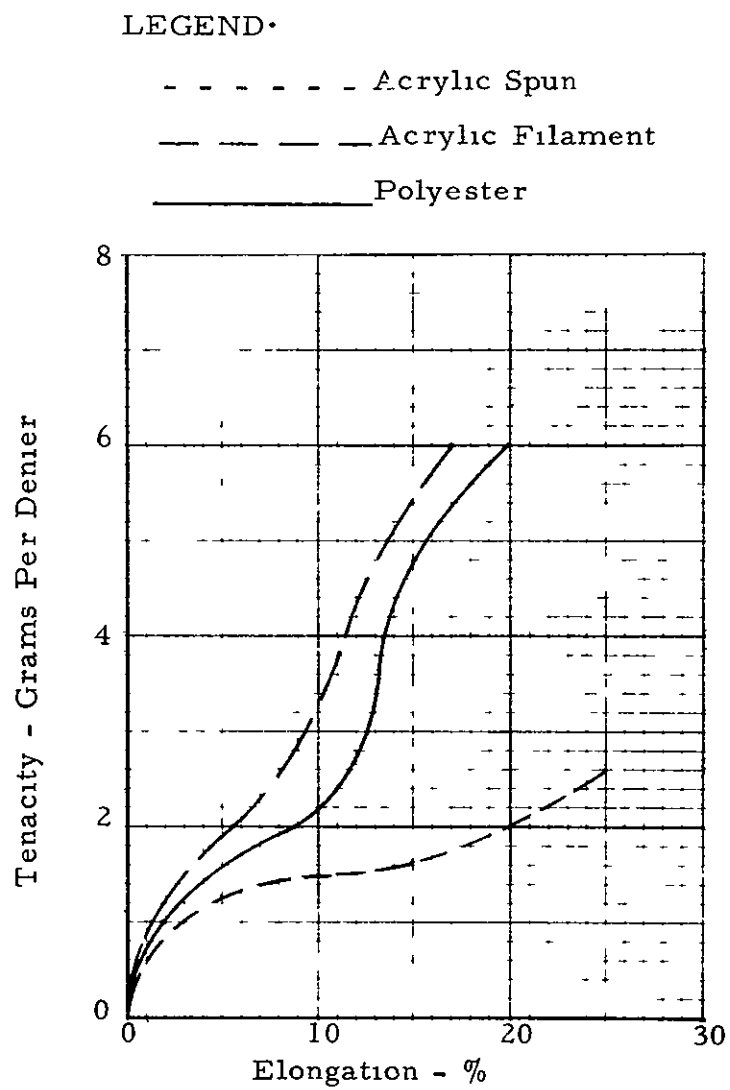

Figure 88. - Tenacity vs. Elongation Diagram of Fiber.

POLYESTER

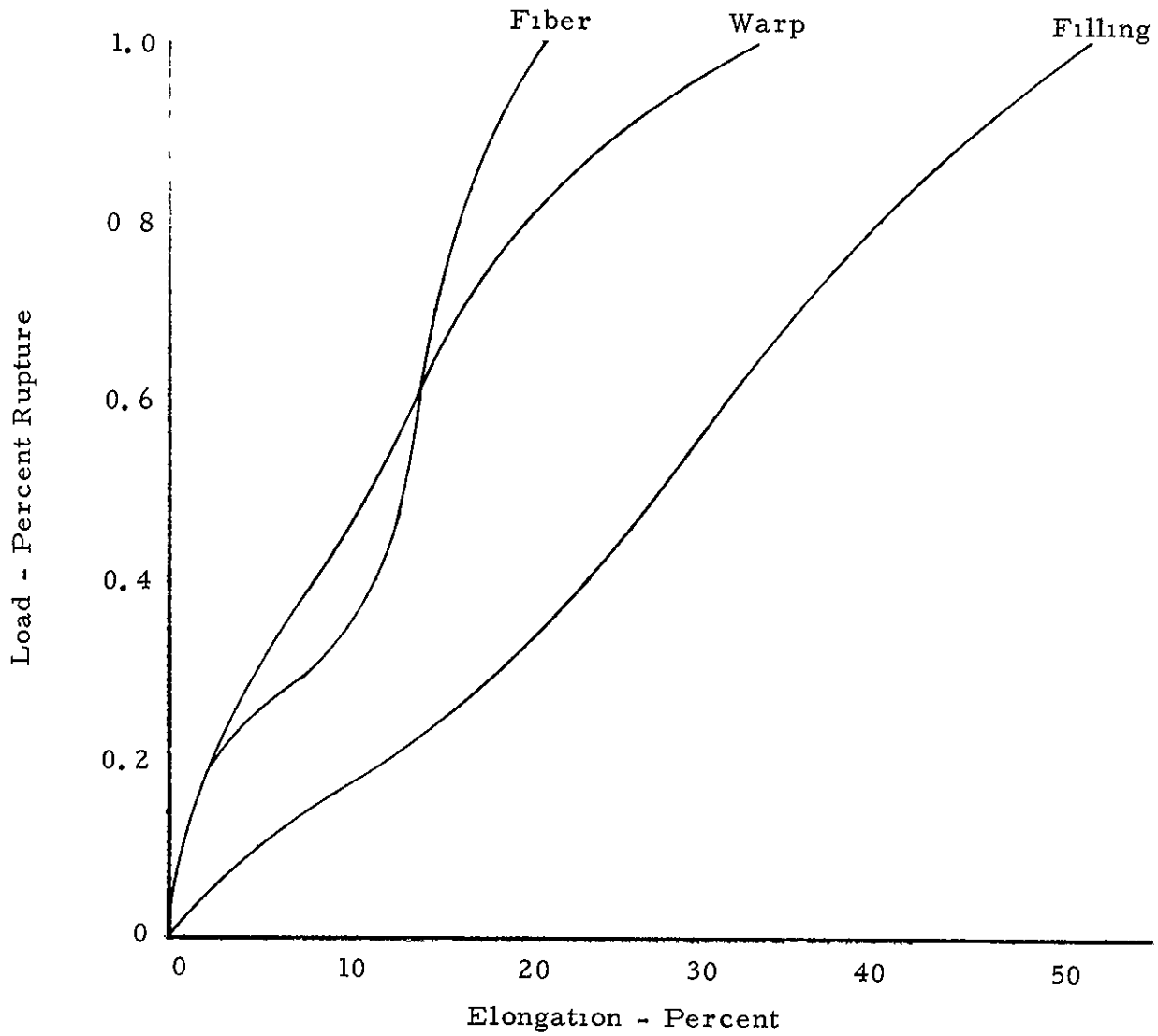

Figure 89. - Load - Elongation Diagram of Fiber and Plain Weave Fabric.

NYLON

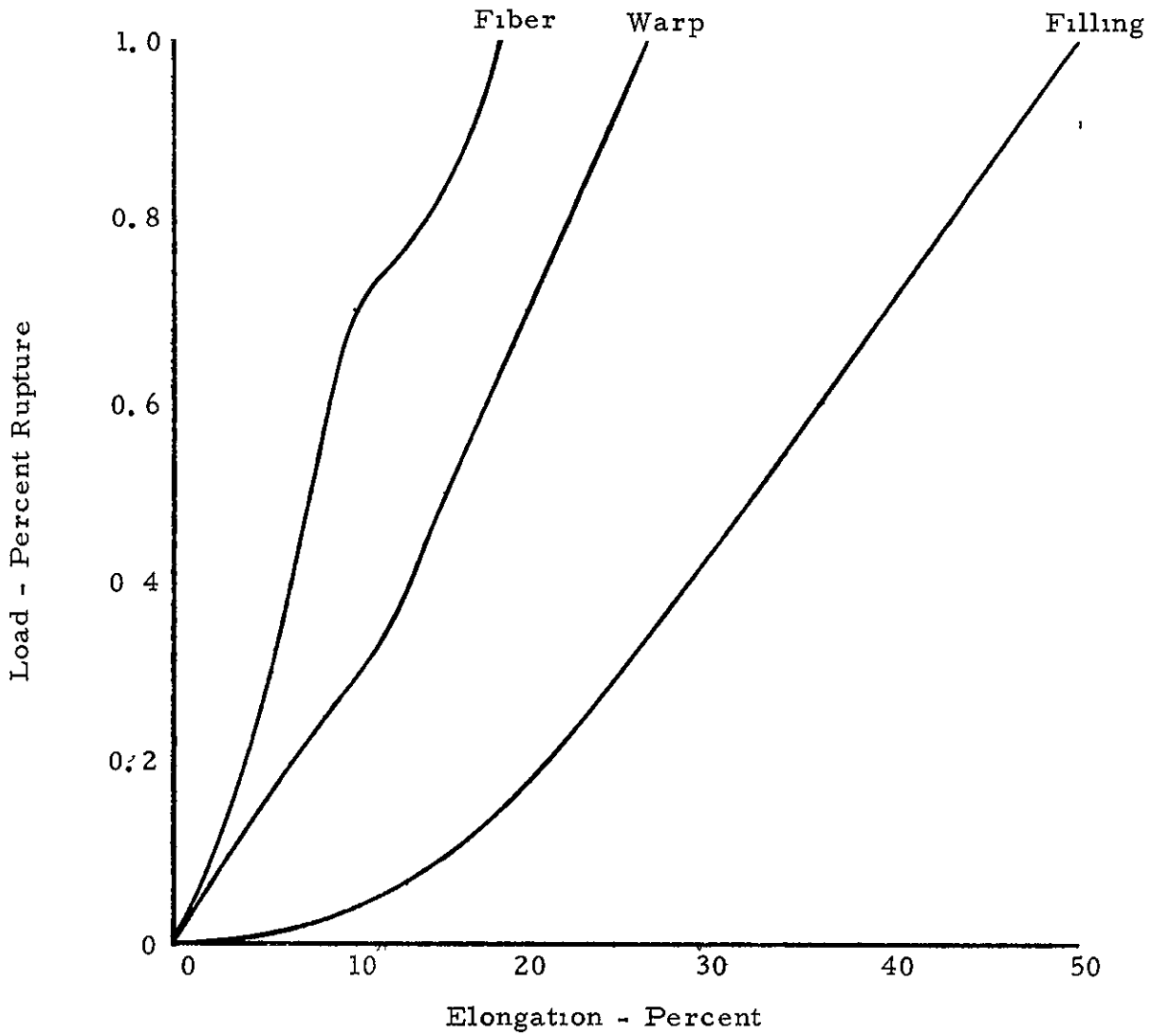

Figure 90. - Load - Elongation Diagram of Fiber and Plain Weave Fabric.

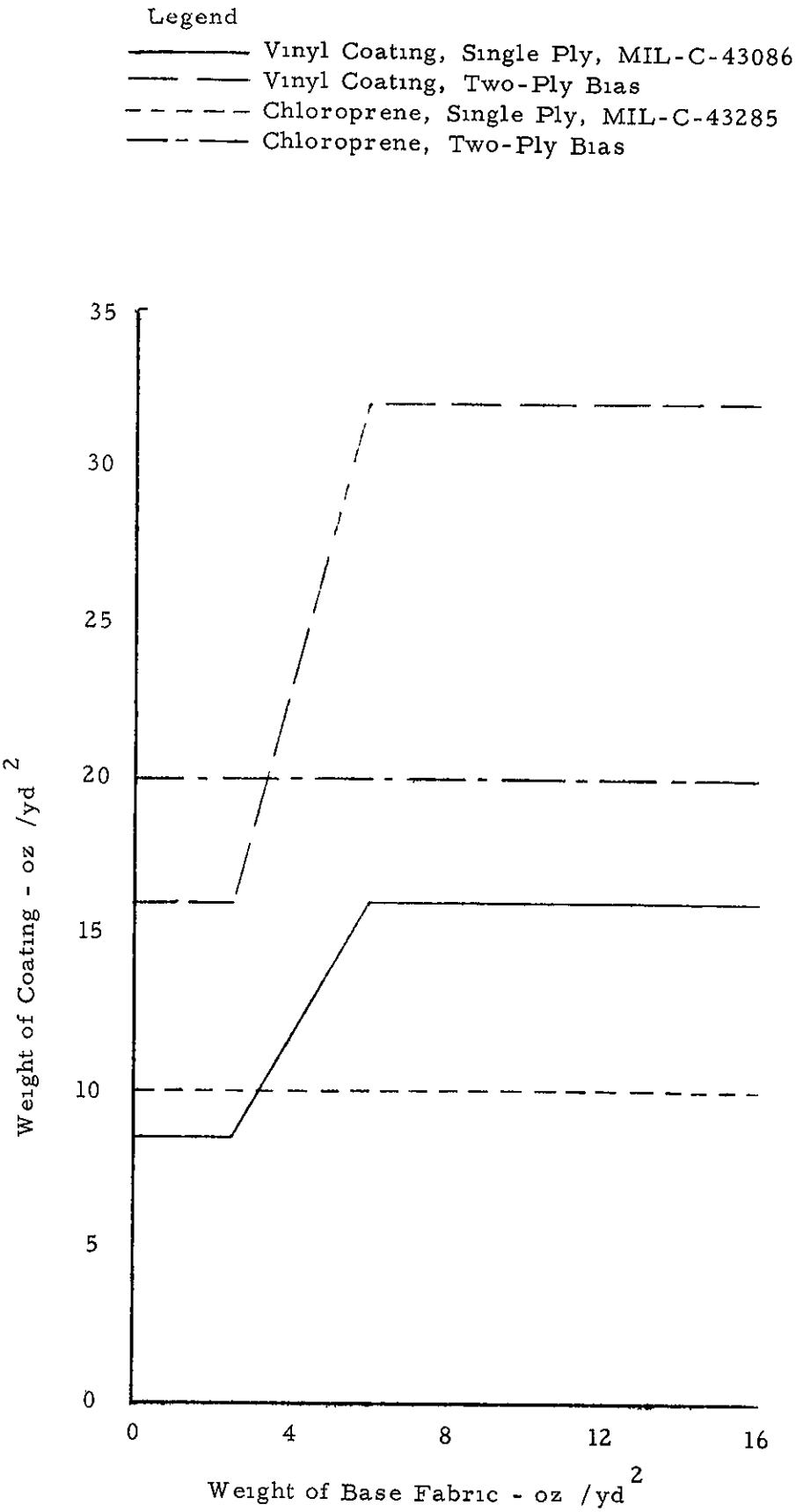

Figure 91 - Weight of Coating For Single And Two Ply Coated Fabric

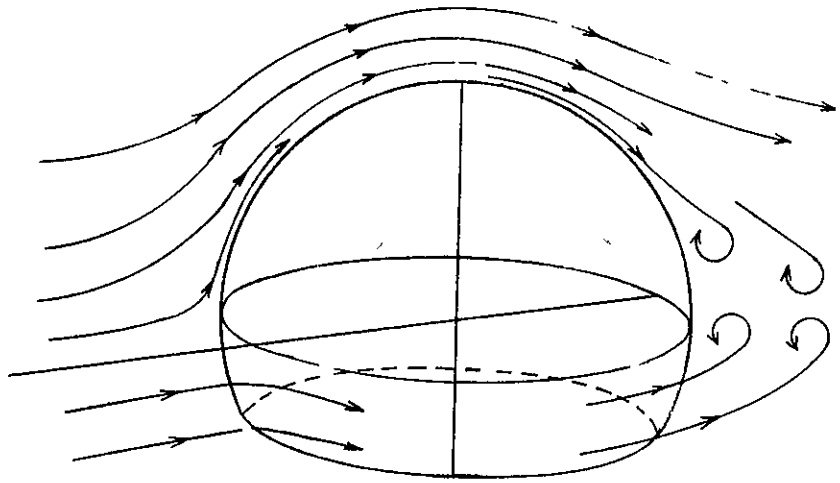

Typical Air Flow

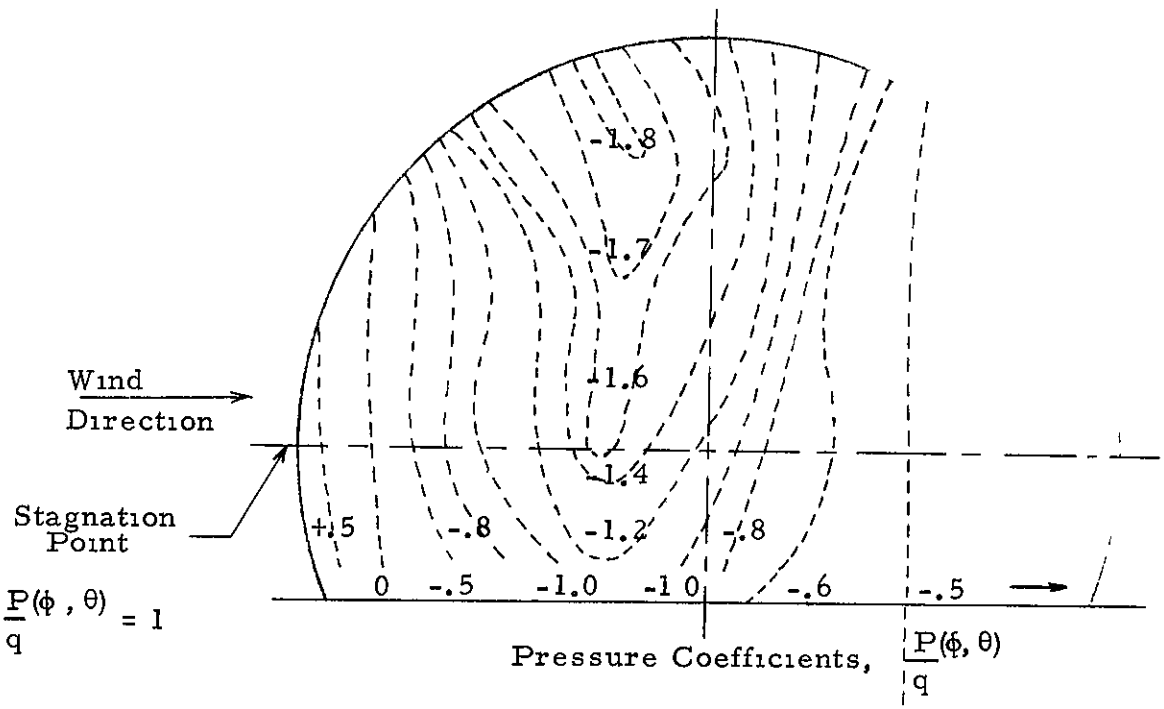

FIGURE 92. - TYPICAL PRESSURE DISTRIBUTION ON A SPHERICAL SHELL

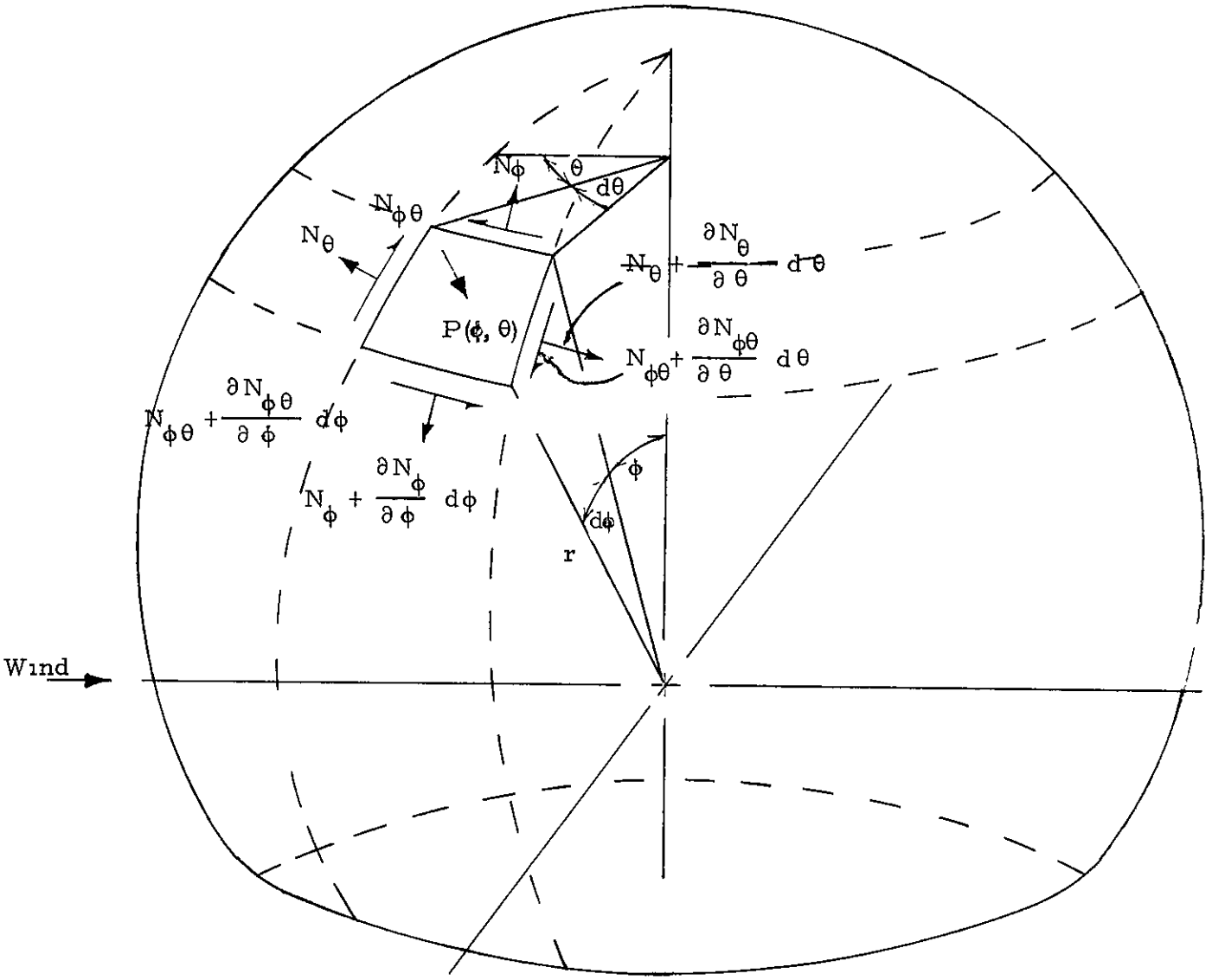

FIGURE 93. - COORDINATE SYSTEM AND MEMBRANE STRESSES FOR A TRUNCATED SPHERICAL SHELL

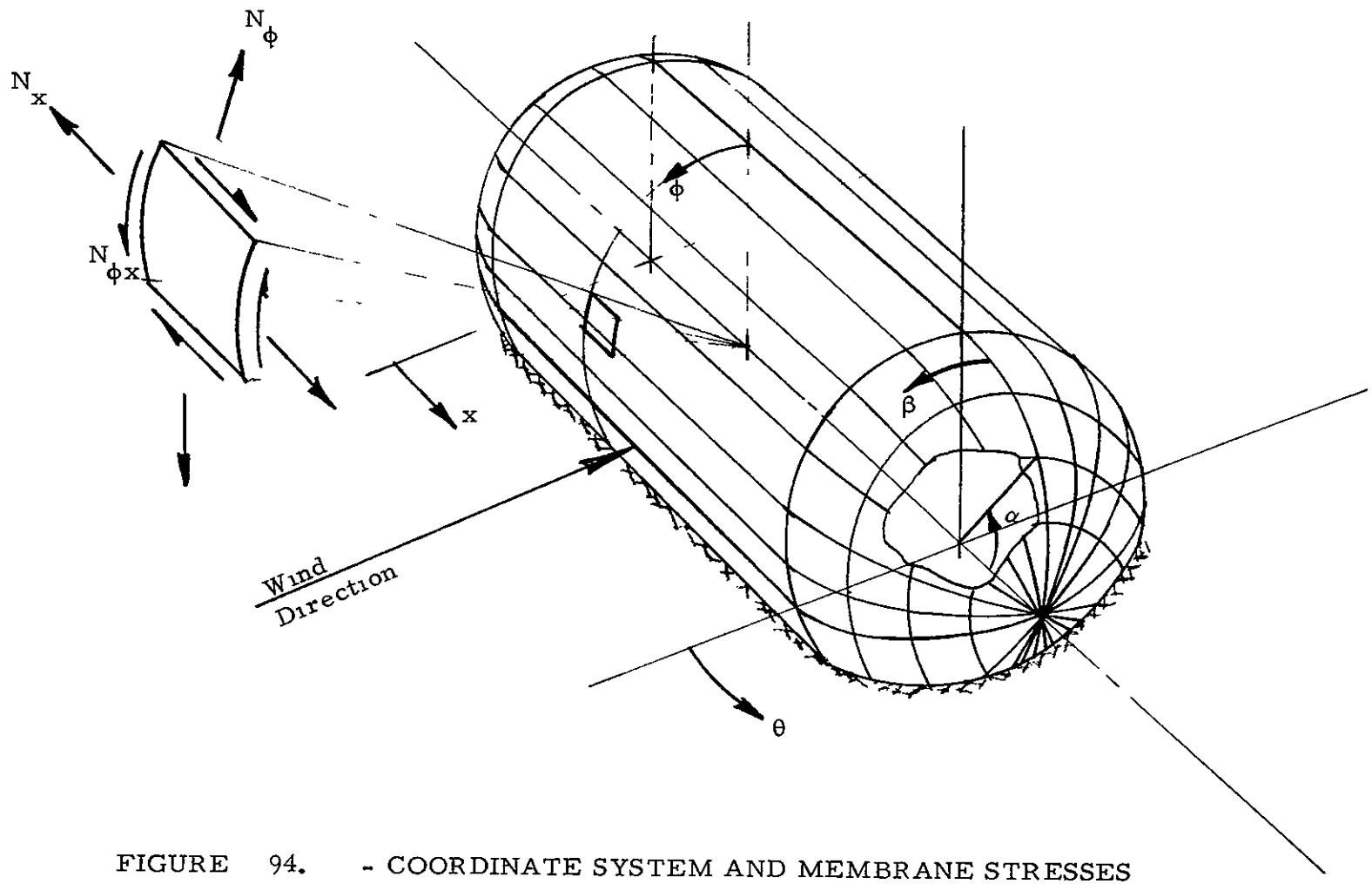

FIGURE 94. - COORDINATE SYSTEM AND MEMBRANE STRESSES FOR A CYLINDRICAL SHELL WITH HEMISPHERICAL ENDS

MAXIMUM TENT DEFLECTION
SINGLE WALL SPHERES

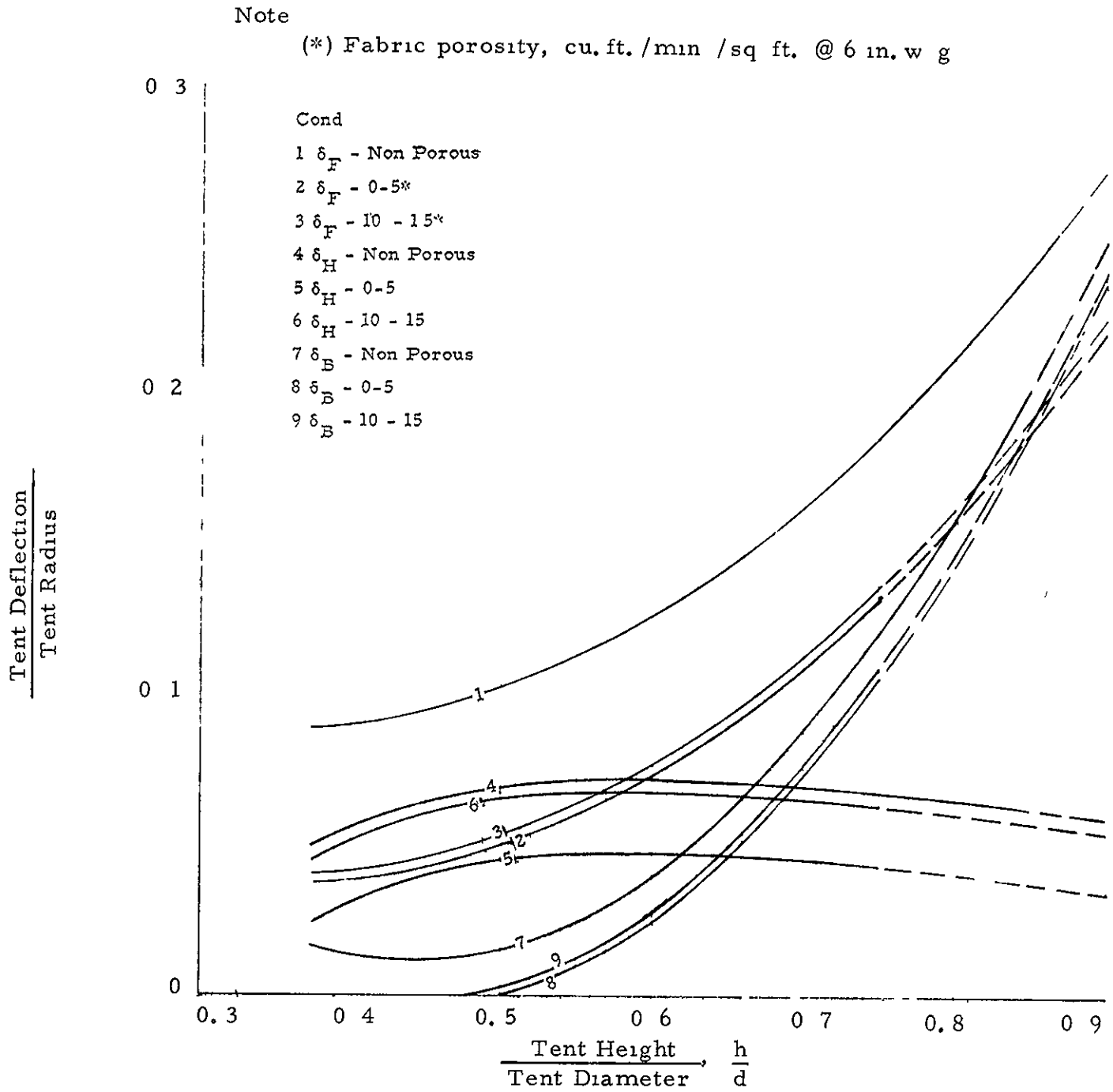

Figure 95 - Variation of Tent Deflection with Shape and Fabric Porosity (Spherical Single Wall Tents)

MAXIMUM TENT DEFLECTION
SINGLE WALL 1.2 CYLINDERS

Note

(*) Fabric porosity, cu. ft. /min. /sq. ft. @ 6 in w. g.

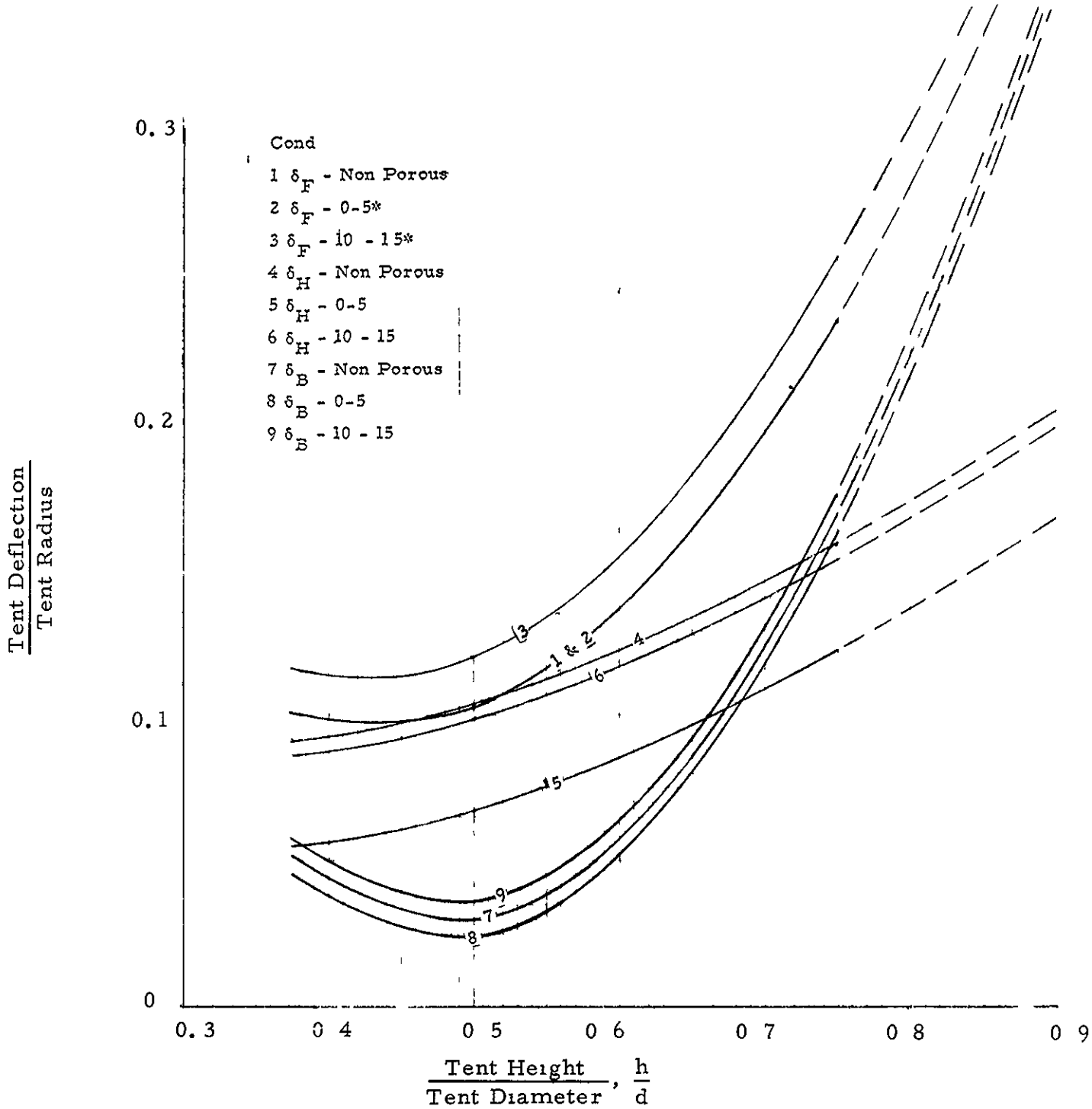

Figure 96. - Variation of Tent Deflection with Shape and Fabric Porosity (Cylindrical Single Wall Tents, 1.2 W/δ_h)

MAXIMUM TENT DEFLECTION
SINGLE WALL 1 4 CYLINDERS

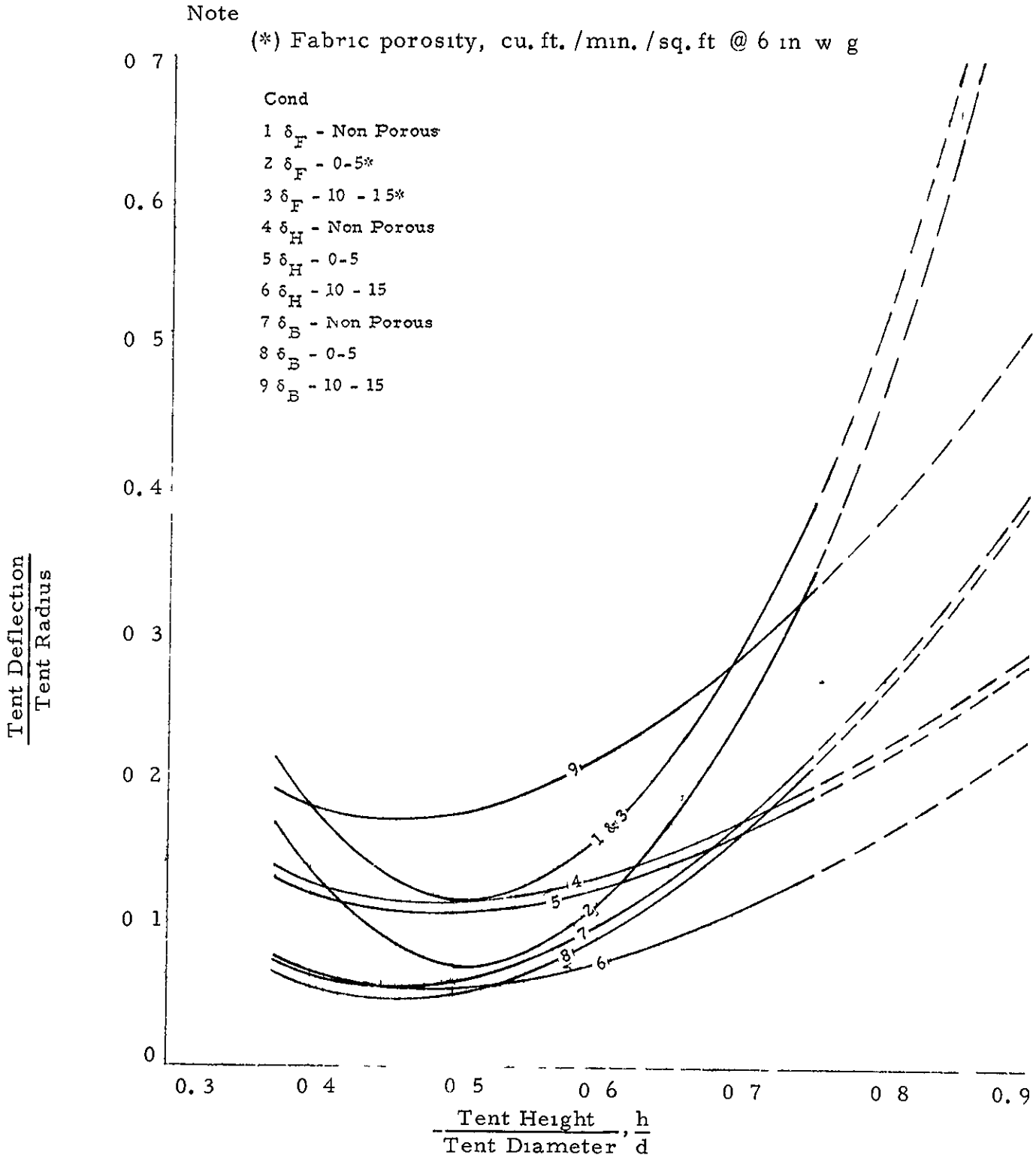

Figure 97. - Variation of Tent Deflection with Shape and Fabric Porosity (Cylindrical Single Wall Tents, 1 4 W/ℓ_h)

MAXIMUM TENT DEFLECTION
DOUBLE WALL CYLINDERS

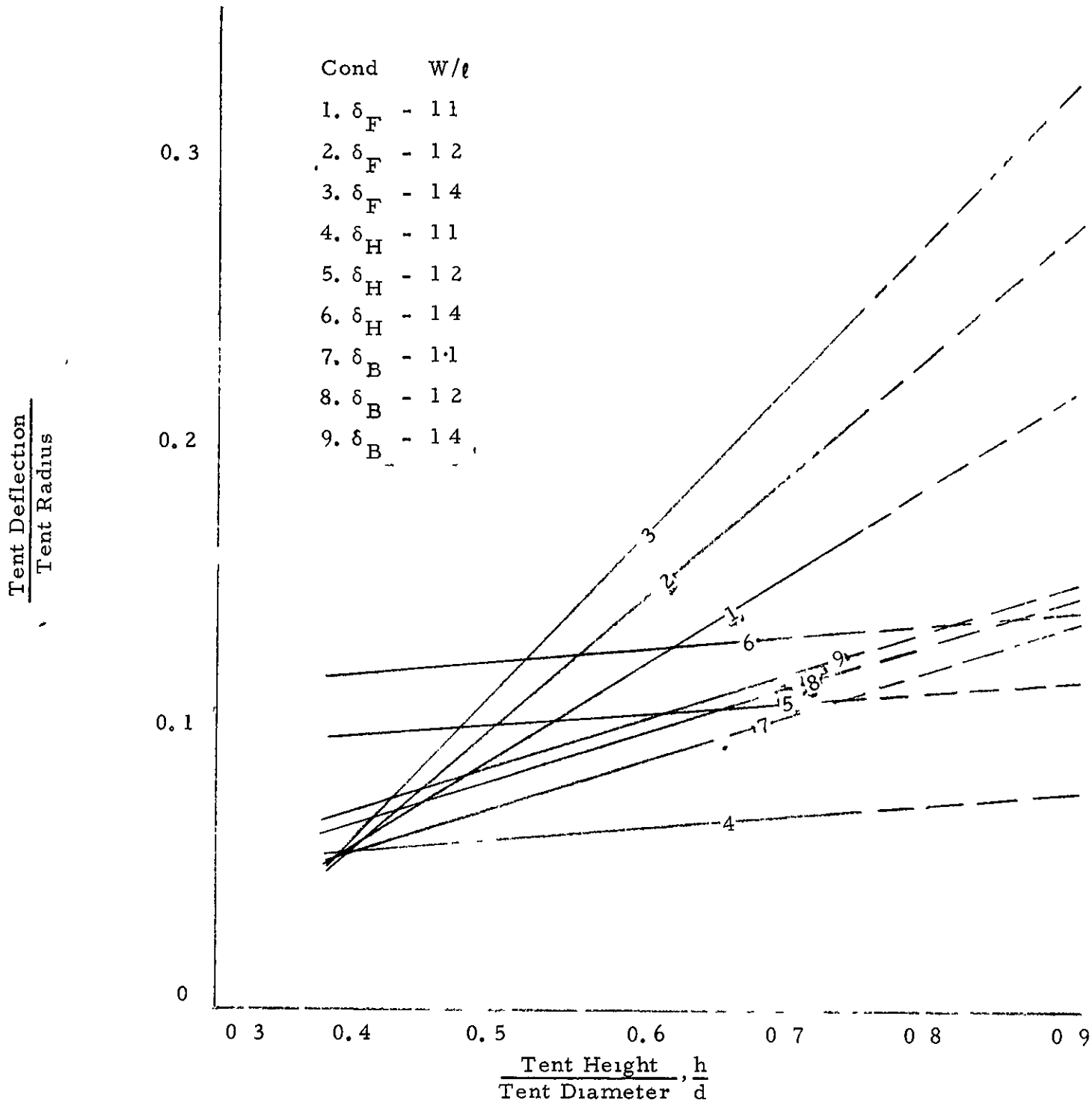

Figure 98 - Variation of Tent Deflection with Shape
(Double Wall Tents, 1 1, 1 2, 1 4, W/ℓ_h)

SUMMARY

The objective of this program is to provide tentage information based on wind tunnel test data that can be applied either to the evaluation and improvement of existing ground mounted air supported tents or to the design of such future structures The data presented are the results of a program conducted by the Hayes International Corporation of Birmingham, Alabama under Contract DA 19-129-AMC-129(N) for the U S Army Natick Laboratories, Natick, Massachusetts

The program consisted of study, test and analytical investigation phases which began in July 1963 and concluded in October 1966 During the study phase, a review was made of pertinent literature on experimental techniques, data and analyses applicable to determining maximum aerodynamic force on and stresses in fabric structures The wind tunnel investigations consisted of detailed testing of twenty-six tent models to include sixteen single wall tents (ten with non-porous and six with porous fabric) and ten double wall tents Tests were conducted at stabilized wind speeds up to 105 miles per hour in the Virginia Polytechnic Institute's 6' x 6' stability tunnel In the analytical phase, test data were used to develop fabric stress and aerodynamic coefficient data variation with tent parameters

The results of the wind tunnel investigations and the stress analyses have been incorporated into this manual and includes comprehensive, practical design data suitable for engineering reliable, stable, single and double-wall air-supported tents Data, in general, are presented in non-dimensional coefficient form, and therefore, are applicable to full scale tents within the range of parameters investigated Design information is presented as charts and tables on such items as tent aerodynamic force and moment coefficients, anchor and guy line coefficients, surface deflection, material stresses and specifications, usable volume, and weight

DISTRIBUTION LIST

Copies	
1	Commanding General, U.S. Army Materiel Command, Washington, D.C. 20315
1	Commanding General, U.S. Army Missile Command, Redstone Arsenal, Alabama
1	Commanding General, U.S. Army Mobility Command, Warren, Michigan
1	Commanding General, U.S. Army Munitions Command, Picatinny Arsenal, Dover, New Jersey
1	Commanding General, U.S. Army Supply and Maintenance Command, Washington, D.C. 20315
1	Commanding General, U.S Army Test and Evaluation Command, Aberdeen Proving Ground, Maryland
1	Commanding General, U.S Army Weapons Command, Rock Island Arsenal, Rock Island, Illinois
1	Commandant, U.S. Army War College, Attn Dir., Doctrine and Studies Division, Carlisle Barracks, Pennsylvania
1	Commanding Officer, U.S Army Combat Service Support Group, Ft Lee, Virginia
1	Commandant, U S. Army Command and General Staff College, Attn. Archives, Ft Leavenworth, Kansas
1	Chief, AMC Liaison Office, ASDL-8 Aeronautical Systems Division, Wright-Patterson Air Force Base, Ohio
1	Chief, Bureau of Supplies and Accounts, Dept. of the Navy, Washington, D.C.
1	Commander, Defense General Supply Center, Richmond, Virginia
1	U.S. Army Natick Laboratories Representative, Defense General Supply Center, Richmond, Virginia
1	National Research Council, 2101 Constitution Avenue, Washington, D.C.
1	Commandant, Industrial College of the Armed Forces, Ft. McNair, Washington, D.C.
1	Commandant, The QM School, Attn Library, Ft. Lee, Virginia
1	The Army Library, Pentagon Bldg., Washington, D.C.
1	~~Director, Joint Military Packaging Training Center, Toledo, Ohio~~
1	Commander, Letterkenny Army Depot, Chambersburg, Pennsylvania
1	Commander, New Cumberland Army Depot, New Cumberland, Pennsylvania
1	Commandant, U S. Army Logistics Management Center, Ft. Lee, Va.
1	Commander, U.S Army Major Items Supply Management Agency, Chambersburg, Pennsylvania
1	Commanding General, U.S. Army Mobility Equipment Center, St Louis, Missouri
1	Commanding General, Defense Personnel Support Center, 2800 South 20th Street, Philadelphia, Pennsylvania
1	Commanding Officer, U.S. Army General Equipment Test Activity, Ft Lee, Virginia
1	Senior Standardization Representative, U S. Army Standardization Group, Ottawa, Canada

DISTRIBUTION LIST CONT'D

Copies	
1	Senior Standardization Representative, U.S. Army Standardization Group, United Kingdom, London, England
1	Commanding Officer, U S Army Support Center, Philadelphia, Philadelphia, Pennsylvania
1	Commanding Officer, U.S. Army Support Center, Richmond, Virginia
1	President, U.S. Army Transportation Board, Fort Eustis, Virginia
1	Commanding Officer, Utah Army Depot, Ogden, Utah
1	Commanding Officer, U S Army Transportation Terminal Command, Gulf, New Orleans, Louisianna
1	Commanding Officer, Granite City Army Depot, Granite City, Illinois
1	Commanding Officer, U.S. Army Transportation Terminal Command, Atlantic, Brooklyn, New York
1	Commanding General, U.S. Army Transportation Terminal Command, Pacific, Ft Mason, California
1	Commanding Officer, Atlanta Army Depot, Forest Park, Georgia
1	Commanding Officer, Fort Worth Army Depot, Fort Worth, Texas
1	Commanding Officer, Memphis Army Depot, Memphis, Tennessee
1	Commanding Officer, Schenectady Army Depot, Schenectady, New York
1	Commanding Officer, Anniston Army Depot, Anniston, Alabama
1	Commanding Officer, Black Hills Army Depot, Igloo, South Dakota
1	Commanding Officer, Blue Grass Army Depot, Richmond, Kentucky
1	Commanding Officer, Erie Army Depot, Port Clinton, Ohio
1	Commanding Officer, Navajo Army Depot, Flagstaff, Arizona
1	Commanding Officer, Red River Army Depot, Texarkana, Texas
1	Commanding Officer, Savanna Army Depot, Savanna, Illinois
1	Commanding Officer, Seneca Army Depot, Romulus, New York
1	Commanding Officer, Sierra Army Depot, Herlong, California
1	Commanding Officer, Sioux Army Depot, Sidney, Nebraska
1	Commanding Officer, Tooele Army Depot, Tooele, Utah
1	Commanding Officer, Umatilla Army Depot, Hermiston, Oregon
1	Commanding Officer, Fort Wingate Army Depot, Gallup, New Mexico
1	Commanding Officer, Lexington Army Depot, Lexington, Kentucky
1	Commanding Officer, Sacramento Army Depot, Sacramento, California
1	Commanding Officer, Tobyhanna Army Depot, Tobyhanna, Pennsylvania
1	Commanding Officer, Charleston Army Depot, North Charleston, S.C
1	Commanding Officer, Rio Vista Army Depot, Rio Vista, California
1	Commanding Officer, Rock Island Army Depot, Rock Island Arsenal, Illinois
1	NASA Scientific and Technical Information Facility, College Park, Maryland

INTERNAL DISTRIBUTION

Copies	
35	Acting Director, General Equipment and Packaging Laboratory, NLABS
20	Chief, Technical Plans Office, NLABS (for transmittal to Defense Documentation Center)
8	Military Liaison Representatives Technical Plans Office, NLABS
2	Technical Library, NLABS

UNCLASSIFIED
Security Classification

DOCUMENT CONTROL DATA - R&D

(Security classification of title body of abstract and indexing annotation must be entered when the overall report is classified)

1 ORIGINATING ACTIVITY *(Corporate author)*
Hayes International Corporation
Birmingham, Alabama

2a REPORT SECURITY CLASSIFICATION
Unclassified

2b GROUP

3 REPORT TITLE
Wind Tunnel Tests and Analyses for Ground Mounted Air-Supported Structures

4 DESCRIPTIVE NOTES *(Type of report and inclusive dates)*
Wind Tunnel Report

5 AUTHOR(S) *(Last name first name initial)*
Dietz, A.B., Proffitt, R.B., and Chabot, R.S.

6 REPORT DATE
October 1966

7a TOTAL NO OF PAGES
174

7b NO OF REFS
26

8a CONTRACT OR GRANT NO DA19-129-AMC-129(N)

b. PROJECT NO 1K643303D546

c

d

9a ORIGINATOR S REPORT NUMBER(S)
67-36-ME

9b OTHER REPORT NO(S) *(Any other numbers that may be assigned this report)*

10 AVAILABILITY/LIMITATION NOTICES
Distribution of this document is unlimited.
Release to CFSTI is authorized.

11 SUPPLEMENTARY NOTES

12 SPONSORING MILITARY ACTIVITY
U.S. Army Natick Laboratories
Natick, Mass.

13 ABSTRACT

The objective of this program is to provide tentage information based on wind tunnel test data that can be applied either to the evaluation and and improvement of existing ground mounted air-supported tents or to the design of such future structures.

The program consisted of study, test and analytical investigation phases from July 1963 to October 1966. During the study phase, a review was made on pertinent literature on experimental techniques, data and analyses applicable to determining maximum aerodynamic force on and stresses in fabric structures. The wind tunnel investigations consisted of detailed testing of twenty-six tent models to include sixteen single wall tents (ten with non-porous and six with porous fabrics) and ten double-wall tents. Tests were conducted at stabilized wind speeds up to 105 miles per hour in the Virginia Polytechnic Institute's 6' x 6' stability tunnel. In the analytical phase, test data were used to develop fabric stress and aerodynamic coefficient data variation with tent parameters.

Results of the wind tunnel investigations and stress analyses have been incorporated and includes comprehensive, practical design data suitable for engineering reliable, stable, single and double-wall air-supported tents. Data, in general, are presented in non-dimensional coefficient form, and therefore, are applicable to full scale tents within the range of the parameters investigated. Design information is presented as charts and tables on tent aerodynamic force and moment coefficients, anchor and guy line coefficients, structural deflection, material stresses and packaged volume, and weight.

DD FORM 1 JAN 64 1473

UNCLASSIFIED
Security Classification

14 KEY WORDS	LINK A ROLE	LINK A WT	LINK B ROLE	LINK B WT	LINK C ROLE	LINK C WT
Testing	8					
Inflatable structures	8,9		4			
Tents	8,9		4			
Air-supported	0					
Wind tunnels	10					
Armed Forces equipment	4		4			
Evaluation			8			
Physical properties			9			
Flexibility			9			
Low-temperature			0			
Dielectric constant			9			
Weight			6,9			
Tensile properties			7,9			
Fabrics			9			
Fibers			9			

INSTRUCTIONS

1 ORIGINATING ACTIVITY Enter the name and address of the contractor, subcontractor, grantee, Department of Defense activity or other organization *(corporate author)* issuing the report

2a REPORT SECURITY CLASSIFICATION Enter the overall security classification of the report Indicate whether "Restricted Data" is included. Marking is to be in accordance with appropriate security regulations

2b GROUP Automatic downgrading is specified in DoD Directive 5200 10 and Armed Forces Industrial Manual Enter the group number Also when applicable, show that optional markings have been used for Group 3 and Group 4 as authorized

3. REPORT TITLE Enter the complete report title in all capital letters Titles in all cases should be unclassified If a meaningful title cannot be selected without classification, show title classification in all capitals in parenthesis immediately following the title

4 DESCRIPTIVE NOTES. If appropriate, enter the type of report, e g , interim, progress summary annual, or final Give the inclusive dates when a specific reporting period is covered

5 AUTHOR(S) Enter the name(s) of author(s) as shown on or in the report Enter last name, first name, middle initial If military, show rank and branch of service. The name of the principal author is an absolute minimum requirement

6. REPORT DATE. Enter the date of the report as day, month, year or month year. If more than one date appears on the report, use date of publication

7a TOTAL NUMBER OF PAGES The total page count should follow normal pagination procedures i.e , enter the number of pages containing information.

7b NUMBER OF REFERENCES. Enter the total number of references cited in the report

8a CONTRACT OR GRANT NUMBER If appropriate, enter the applicable number of the contract or grant under which the report was written.

8b, 8c, & 8d PROJECT NUMBER Enter the appropriate military department identification such as project number subproject number system numbers, task number, etc

9a ORIGINATOR'S REPORT NUMBER(S) Enter the official report number by which the document will be identified and controlled by the originating activity This number must be unique to this report

9b OTHER REPORT NUMBER(S) If the report has been assigned any other report numbers *(either by the originator or by the sponsor)* also enter this number(s)

10 AVAILABILITY/LIMITATION NOTICES Enter any limitations on further dissemination of the report other than those imposed by security classification, using standard statements such as

(1) "Qualified requesters may obtain copies of this report from DDC."

(2) "Foreign announcement and dissemination of this report by DDC is not authorized."

(3) "U S Government agencies may obtain copies of this report directly from DDC Other qualified DDC users shall request through _____ "

(4) "U S military agencies may obtain copies of this report directly from DDC. Other qualified users shall request through _____ "

(5) "All distribution of this report is controlled. Qualified DDC users shall request through _____ "

If the report has been furnished to the Office of Technical Services, Department of Commerce, for sale to the public, indicate this fact and enter the price, if known.

11 SUPPLEMENTARY NOTES Use for additional explanatory notes

12 SPONSORING MILITARY ACTIVITY Enter the name of the departmental project office or laboratory sponsoring *(paying for)* the research and development Include address

13 ABSTRACT Enter an abstract giving a brief and factual summary of the document indicative of the report even though it may also appear elsewhere in the body of the technical report If additional space is required a continuation sheet shall be attached

It is highly desirable that the abstract of classified reports be unclassified Each paragraph of the abstract shall end with an indication of the military security classification of the information in the paragraph represented as *(TS), (S) (C), or (U)*

There is no limitation on the length of the abstract However the suggested length is from 150 to 225 words

14 KEY WORDS Key words are technically meaningful terms or short phrases that characterize a report and may be used as index entries for cataloging the report Key words must be selected so that no security classification is required Identifiers such as equipment model designation trade name military project code name geographic location may be used as key words but will be followed by an indication of technical context The assignment of links rules and weights is optional